βαββββ-module-containing proteins in metabolism and resistance of *Pseudomonas aeruginosa*

Von der Fakultät für Lebenswissenschaften

der Technischen Universität Carolo-Wilhelmina zu Braunschweig

zur Erlangung des Grades einer

Doktorin der Naturwissenschaften

(Dr. rer. nat.)

genehmigte

D i s s e r t a t i o n

von Monika Anita Popp

aus Münchberg

1. Referent:	Prof. Dr. Wulf Blankenfeldt
2. Referentin:	Prof. Dr. Susanne Engelmann
eingereicht am:	22.08.2018
mündliche Prüfung (Disputation) am:	08.11.2018

Druckjahr 2018

Vorveröffentlichung der Dissertation

Teilergebnisse aus dieser Arbeit wurden mit Genehmigung der Fakultät für Lebenswissenschaften, vertreten durch den Mentor der Arbeit, in folgenden Beiträgen vorab veröffentlicht:

Tagungsbeiträge

Popp, M., Vit, A., Blankenfeldt, W.: βαββββ-module-containing proteins in resistance and metabolism of *Pseudomonas aeruginosa*. 19th Heart of Europe Bio-Crystallography Meeting, Burg Warberg, Germany, September 2016

Popp, M., Sadana, P., Schwemmlein, N.: (Towards) Elucidating molecular mechanisms of pathogens using X-rays. 6th Annual Retreat of the Helmholtz International Graduate School for Infection Research (GS-FIRE), Braunschweig, Germany, June 2015

Popp, M., Klingen, T.: The benefits of structural information for functional and evolutionary analysis. 7Th Annual Retreat of the Helmholtz International Graduate School for Infection Research (GS-FIRE), Goslar-Hahnenklee, Germany, June 2016

Posterbeiträge

Popp, M., Vit, A., Blankenfeldt, W.: βαββββ-module proteins in resistance and metabolism of *Pseudomonas aeruginosa.* 5th Annual Retreat of the Helmholtz International Graduate School for Infection Research (GS-FIRE), Goslar-Hahnenklee, Germany, May 2014

Popp, M., Vit, A., Blankenfeldt, W.: βαββββ-module proteins in resistance and metabolism of *Pseudomonas aeruginosa*. 7th International PhD Symposium of the Helmholtz International Graduate School for Infection Research (GS-FIRE), Braunschweig, Germany, December 2014

Popp, M., Vit, A., Blankenfeldt, W.: βαββββ-module-containing proteins in resistance and metabolism of *Pseudomonas aeruginosa*. 23rd Annual Meeting of the German Crystallographic Society (DGK), Germany, March 2015

Popp, M., Vit, A., Blankenfeldt, W.: βαββββ-module proteins in resistance and metabolism of *Pseudomonas aeruginosa*. 8th International PhD Symposium of the Helmholtz International Graduate School for Infection Research (GS-FIRE), Braunschweig, Germany, December 2015

Popp, M., Vit, A., Blankenfeldt, W.: Towards the function of βαββββ-module-containing proteins in *Pseudomonas aeruginosa*. 16th International Conference on Pseudomonas, Liverpool, UK, September 2017

Table of Contents

Abbreviations

2S-αKGO	α-keto acid dependent oxygenase
A_{280}	absorption at 280 nm
AIEX	anion exchange chromatograph
Amp	ampicillin
APS	ammonium persulfate
B. cepacia	*Burkholderia cepacia*
B. circulans	*Bacillus circulans*
B. fuscum	*Brevibacterium fuscum*
BAT	bleomycin N-acetyltransferase
BESSY	Berliner Elektronenspeicherring-Gesellschaft für Synchrotronstrahlung
BME	β-mercaptoethanol
CBZ-PRO	N-benzyloxycarbonyl-L-proline
CF	cystic fibrosis
CHES	N-cyclohexyl-2-aminoethanesulfonic acid
Cm	chloramphenicol
DESY	Deutsches Elektronen-Synchrotron
DHBD	2,3-dyhydroxybyphenyl 1,2-dioxygenase
DLS	dynamic light scattering
DP	differential thermal power
DTT	dithiothreitol
E. coli	*Escherichia coli*
F_{norm}	normalized fluorescence
FS	fragment screening
G3P	glyceraldehyde 3-phophate
GAPN	glyceraldehyde 3-phosphate dehydrogenase
Gfa	glutathione-dependent formaldehyde-activating enzyme
Glo1/Glx1	glyoxalase 1

Gm	gentamicin
GOI	gene of interest
GSH	glutathione reduced
GUI	graphical user interface
HMS	hydroxymandelate synthase
HPCD	homoprotocatechute 2,3-dioxygenase
HPPD	4-hydroxyphenylpyruvate dioxygenase
HZB	Helmholtz-Zentrum Berlin
HZI	Helmholtz Centre for Infection Research
IEX	Ion exchange chromatography
IL	interleukin
IMAC	immobilized metal ion affinity chromatography
IPTG	isopropyl β-D-1-thiogalactopyranoside
IR	infrared
K. pneumoniae	*Klebsiella pneumoniae*
K_a	association constant
K_D	dissociation constant
LB	lysogeny broth
LN_2	liquid nitrogen
MES	2-(N-morpholino)ethanesulfonic acid
Mex	multidrug efflux
MM	master mix
MMCE	methylmalonyl-CoA epimerase
MPI	Max Planck Institute
MST	microscale thermophoresis
MW	molecular weight
MWCO	molecular weight cut-off
OD	optical density

Opr	outer membrane protein
P. aeruginosa	*Pseudomonas aeruginosa*
P. agglomerans	*Pantoea agglomerans*
PCR	polymerase chain reaction
Pd	*Paracoccus denitrificans*
PDB	protein databank
PETRA	Positron-Elektron-Tandem-Ring-Anlage
pg	prep grade
pI	isoelectric point
PM	Phenotype MicroArray™
POI	protein of interest
PSI	Paul Scherrer Institute
RSCC	real-space correlation coefficient
S. lavendulae	*Streptomyces lavendulae*
S. verticillus	*Streptomyces verticillus*
SAD	single-anomalous diffraction
SAM	S-adenosyl methionine
SDS	sodium dodecyl sulfate
SDS-PAGE	sodium dodecyl sulfate polyacrylamide gel electrophoresis
SEC	size exclusion chromatography
SLIC	sequence and ligation independent cloning
SLS	Swiss Light Source
SOC	super optimal broth with catabolite repression
SouR	sarcosine oxidation and utilization regulator
Str	streptomycin
TA	toxin-antitoxin
TB	terrific broth
TEMED	tetramethylethylenediamine

Tet	tetracycline
THF	tetrahydrofolate
TLR	Toll-like receptor
T_m	melting temperature
TSA	thermal shift assay
VOC	vicinal oxygen chelate
XRE	xenobiotic response element

Three and single letter abbreviations of amino acids were used as recommended by the International Union of Pure and Applied Chemistry (IUPAC) and the International Union of Biochemistry and Molecular Biology (IUBMB).

Summary

The opportunistic pathogen *Pseudomonas aeruginosa* is an increasing threat in human health care, since multi-resistant strains are on the rise. One protein family that was found to participate in a variety of resistance mechanisms is the βαββ-module-containing protein family. They have a highly conserved fold but a diverse set of functions. *P. aeruginosa* contains 22 of these proteins. Conserved active site residues subdivide them into three classes. Class I contains at least three conserved metal-complexing residues, and most characterized members catalyze the breakdown of toxic compounds. In class II, two aromatic side chains complex toxic aromatics to mediate resistance. The remaining proteins lack the conserved residues and were assigned to class III.

In this study, the physiological roles of class III proteins PA1358, PA1672, PA2721, PA4183 and PA4518 were investigated with microbiological, biophysical and X-ray crystallography methods. This revealed that PA1672 has a low affinity to chlorpromazine and promethazine. At the same time, PA1672 seems to play a role during swarming motility and biofilm formation. A ligand structure of PA2721 revealed the binding with N-benzyloxycarbonyl-L-proline and that a proposed active site cysteine residue is covalently modified by the antimicrobial compounds dichlofluanid and captan. *P. aeruginosa* mutants of *PA1358, PA4183* and *PA4518* revealed an altered sensitivity to a variety of distinct antimicrobial compounds.

Furthermore, a high-resolution crystal structure of the class III protein PA4183$^{16\text{-}155}$ was determined, as well as structures of the proteins PA1359, PA2722 and PA2723, which are encoded in the same operon as class III proteins. The structures showed that the C-terminal domain of PA1359 has a cupin-like and that PA2722 has a Gfa/CENP-V-like fold. PA2723 was the first protein that solely consists of an R3H-like domain. However, no functional annotations could be derived from these structures.

Overall, this study identified undetermined protein structures and gave specific starting points for the functional characterization of PA2721 and PA1672. The results from the chemical sensitivity assays seem to support the assumption that at least some class III βαββ-module proteins participate in resistance mechanisms.

1 Introduction

1.1 *Pseudomonas aeruginosa*

Pseudomonas aeruginosa is a versatile Gram-negative γ-proteobacterium. The soil-dwelling bacterium has simple growth requirements, which allows it to adopt to a variety of environmental conditions (Silby *et al.*, 2011). For example it was found to survive in distilled water (Favero *et al.*, 1971) and to be able to degrade "non-biodegradable" synthetic plastics such as low density polythene (Kyaw *et al.*, 2012). Pathogenic strains infect several organisms including plants or mammals (Silby *et al.*, 2011). In humans, they can cause fatal chronic and acute, nosocomial infections, for example in the urinary tract, on burn wounds or in the respiratory system of immunocompromised patients. In cystic fibrosis (CF) patients, the human pathogen causes severe pneumonia and is the main cause for morbidity and mortality (Figure 1A) (Moradali *et al.*, 2017). Increasing levels of antimicrobial resistant strains raise the need for new cures to overcome an upcoming public health crisis and prevent the prophesies of a post-antibiotic future, in which infectious diseases will be responsible for millions of deaths (Pendleton *et al.*, 2013).

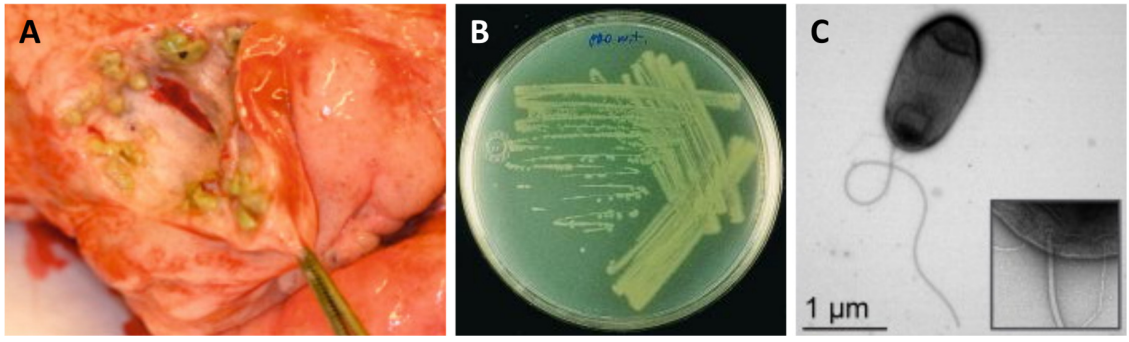

Figure 1: *Pseudomonas aeruginosa.* A) Biofilm in the lungs from a CF patient. Reprinted from Alhede *et al.*, 2014, Copyright (2014), with permission from Elsevier Inc. B) Phenazine production by *P. aeruginosa* PAO1 strain. The figure was reprinted from Mavrodi *et al.*, 2001. C) Monoflagellated bacterial cell with a magnification of the cell pole (right square). The figure was reprinted from van Ditmarsch *et al.*, 2013.

1.1.1 Virulence factors

The pathogenicity is based on various virulence factors that are produced and secreted in the extracellular environment or directly injected into the host cell via distinct secretion systems, of which *P. aeruginosa* encodes at least six different types (Bleves *et al.*, 2010). Virulence fac-

tors can either be recognized by receptors of the immune cells and modulate the immune response or they are cytotoxic compounds, proteins or enzymes that induce apoptosis of host or bacterial cells. This triggers inflammation, weakens host antibacterial mechanisms or kills competing bacterial species to gain a growth advantage (Hall *et al.*, 2016; Michalska and Wolf, 2015). One well-studied example is the redox-active, organic phenazine compound pyocyanin. It is one of the most abundant secondary metabolites from *P. aeruginosa* and is, among others, responsible for the characteristic greenish pigmentation of the bacterial colonies, because it has a blue color in the oxidized state (Figure 1 A/B) (Mavrodi *et al.*, 2006; Pierson & Pierson, 2010). It is secreted via the type II secretion system machinery into the extracellular space (Hall *et al.*, 2016). Based on its redox properties it is able to induce the emergence of highly reactive superoxide and H_2O_2, which cause unspecific oxidative damage (Mavrodi *et al.*, 2006). The most toxic, enzymatically active virulence factor is exotoxin A, which is also secreted through the type II secretion system. It induces its phagocytic uptake and release into the host cell cytosol, where it enzymatically alters a specific translation elongation factor on the ribosome, causing the inactivation of the host cell protein biosynthesis and the induction of apoptosis (Michalska & Wolf, 2015). The cell appendices of *P. aeruginosa* that are crucial for the bacterial motility, such as the polar flagellum and type IV pili, are also considered as virulence factors (Josenhans & Suerbaum, 2002). Non-motile cells are unable to cause a successful infection (Feldman *et al.*, 1998) and besides, the flagellum proteins are recognized by the host immune cells and also influence the immune response (Haiko & Westerlund-Wikström, 2013).

1.1.2 Motility and acute infections

Highly motile lifestyle forms initiate the acute infection (Klockgether & Tümmler, 2017). Different motility types, such as swimming, swarming or twitching, allow the bacteria to spread and colonize larger surface areas in the host and further enable the chemotactic movement away from toxic environments or towards favorable substrates (Josenhans & Suerbaum, 2002). The main motor for swimming and swarming is the single polar flagellum. The rotation of this organelle alone allows the bacteria to swim through liquid and low viscosity media (Jarrell & McBride, 2008). Swarming describes the movement over high viscosity, semisolid

surfaces. In contrast to swimming, which is performed by individual bacteria, swarming is a multicellular behavior that further requires the secretion of surface-active agents (surfactants) that are amphiphilic wetting agents to decrease the surface tension between the bacteria and the environment and allow them to move. Swarming further requires the presence of type IV pili. Type IV pili are appendages that are distributed at the bacterial surface. They have adhesive function that allow the attachment to and the sensing of other cells (Kearns, 2010). The suggested role of type IV pili during swarming is to mediate the interaction between the bacterial cells to control their collective movement (Anyan *et al.*, 2014). Type IV pili alone are responsible for twitching. In this case, the retractability of the pili filaments plays an important role. They are elongated, adhere and are retracted, which drags the cell towards the side of adherence (Kearns, 2010). The pili and the flagellum are also crucial for initial adherence to biotic or abiotic surfaces for switching to the sessile lifestyle, since non-motile mutants are not able to form a biofilm (O'Toole & Kolter, 1998).

1.1.3 Biofilms and persistence

Biofilms consist of cellular aggregates of non-motile cells that are embedded in a hydrated matrix of extracellular polymeric substances such as exopolysaccharides, extracellular DNA or polypeptides (Figure 2 A) (Rasamiravaka *et al.*, 2015). The biofilm builds a barrier that shields the bacterial cells from being attacked by the immune system of the host and by antimicrobial compounds. This limits the effective eradication of the bacterial population independently of specific antibiotic resistance mechanism and enables the establishment of chronic infections (Rybtke *et al.*, 2011). Distinct subpopulations with various metabolic activity within the biofilm further complicate the total elimination of bacterial cells, especially if persister cells are among them. During persistence, the cell enters a dormant lifestyle in which cellular processes such as proliferation or metabolism are arrested. The arrest is triggered by the stringent response upon all kinds of stressful conditions such as in the presence of toxic compounds, by oxidative stress and under nutrient starvation. The transformation towards persister cells is driven by genetically encoded, bicistronic toxin-antitoxin (TA) systems (Moradali *et al.*, 2017). They are widely distributed among bacteria and archaea and six distinct types of TA systems are identified at present that are distinguished by the identity of

the labile antitoxin, which can be a protein or RNA, while stabile toxins are always proteins (Page & Peti, 2016; Unterholzner *et al.*, 2013). So far, only type I and especially type II TA-system were discovered to influence persister cell formation (Figure 2 B).

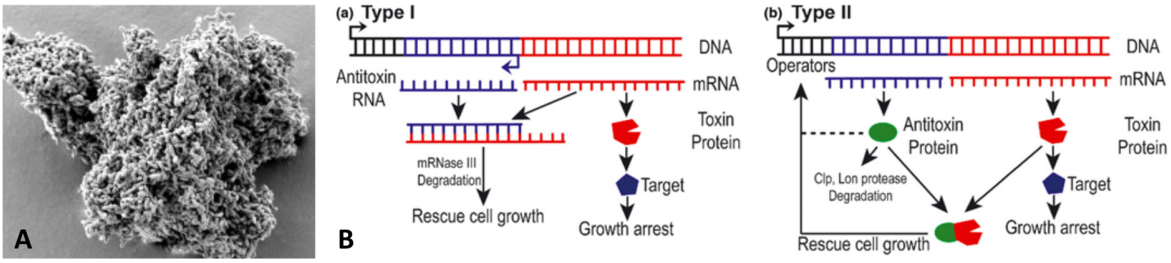

Figure 2: Biofilms and persistence of *P. aeruginosa.* A) *P. aeruginosa* Biofilm. Reprinted from Alhede *et al.*, 2014, Copyright (2014), with permission from Elsevier Inc. B) Mechanisms of type I (a) and type II (b) toxin-antitoxin systems. Reprinted from Wen, Y., Behiels, E. & Devreese, B., *Toxin-Antitoxin systems: their role in persistence, biofilm formation, and pathogenicity*, (2014). *Pathog. Dis.* 70, 240–249, Copyright (2014), with permission of Federation of European Microbiological Societies.

In the type I TA system, the antitoxin is a small RNA that is complementary to a portion of the mRNA that codes for the toxin and therefore inhibits the translation of the toxin. In type II systems, the antitoxin is a protein that detoxifies the toxin by protein-protein interaction (Unterholzner *et al.*, 2013). Under favorable conditions, toxin and antitoxin are present at comparable level and the antitoxin prevents the toxic effect. Under stress conditions, the stringent response also triggers the expression of specific proteases or RNases that degrade the respective antitoxin. This liberates the toxins, which inhibit basic cellular processes such as DNA replication or protein translation resulting in growth arrest (Page & Peti, 2016). Functionally characterized TA systems from *P. aeruginosa* include the type II HigB/HigA and HicA/HicB systems. HigB and HicA are the respective toxins with RNase activity. Both systems are widely distributed among clinical *P. aeruginosa* isolates and it is suggested that persister cells are one reason that make it difficult to eradicate chronic infections with antibiotics, since the persisters reawaken after the treatment is finished and transform back into normal growing cells that can reestablish the infection (Moradali *et al.*, 2017).

1.1.4 Antibiotic resistance

Single bacterial cells can combat antibiotic treatment by different intrinsic resistance mechanisms. They express several enzymes that are able to catalyze the breakdown and inactivation of antibiotics, such as β-lactam or fosfomycin, which actively target dividing bacteria by

inhibiting cell wall synthesis enzymes (Kong *et al.*, 2010; Silver, 2017). Enzymes that target β-lactam antibiotics are called β-lactamases. 120 of them were identified in different clinical isolates that detoxify all types of β-lactam antibiotics, such as cephalosporins, which are detoxified by AmpC-like enzymes, or like carbapanems, which are degraded by carbapenemases (Zhao & Hu, 2010). Fosfomycin is hydrolyzed by the enzyme FosA, which belongs to the βαβββ-module-containing protein family (Bernat *et al.*, 1997; Rife *et al.*, 2002). Indirect mechanisms involve the reduced permeability of the membrane for antimicrobials (Moradali *et al.*, 2017). The membrane is semipermeable to supply the cell with nutrient molecules. Molecules up to a size of 500 Da can pass the membranes by passive diffusion through porins (Nikaido, 2003). The expression of porins such as the outer membrane protein F (OprF) or OprD is reduced if the bacterium is exposed to antimicrobials so that their uptake is limited and the bacterium becomes resistant (Pendleton *et al.*, 2013). Harmful effects of antibiotics that have nevertheless reached the interior of the cell can be avoided by actively exporting them out of the cytoplasm again. This is achieved by increased levels of multidrug efflux pumps (Mex) with distinct substrate specificity. MexXY pumps, for example, transport several antibiotics, like fluoroquinolones, aminoglycosides, tetracycline or chloramphenicol (Lister *et al.*, 2009). The MexAB-OprM pump is further able to export other toxic compounds, such as biocides or detergents, in addition to the classic antibiotics such as β-lactams or sulfonamides (Lister *et al.*, 2009). Other resistance mechanisms are based on mutations in the antimicrobial target. Fluoroquinolone antibiotics, for instance, target DNA gyrase and topoisomerase IV and therefore prevent replication and inhibit bacterial growth (Drlica, 1999). Mutational changes in the respective targets render the antibiotic ineffective and mediate resistance (Lee *et al.*, 2005).

1.1.5 Genome

The wide spectrum of mechanisms that were developed by *P. aeruginosa* to optimize the survival under all kinds of adverse circumstances is reflected by the large genome size, which, with more than 6 Mbp, encodes roughly 6000 open reading frames (ORFs) (Moradali *et al.*, 2017; Valot *et al.*, 2015). Albeit a large amount of genes were functionally annotated in the past there are still around 35 % of hypothetical and unknown proteins that are without functional predictions (Winsor *et al.*, 2016).

1.2 βαββββ-module-containing proteins

22 genes of one large protein family were recently discovered in the genome of *P. aeruginosa* PAO1. They are predicted to encode members of the functionally diverse βαββββ-module-containing protein family (Vit, 2015). βαββββ-module proteins are abundant in all kingdoms of life and participate in the detoxification of compounds with antimicrobial functions, but only eight members of the 22 βαββββ-module proteins from *P. aeruginosa* were functionally characterized (Bernat *et al.*, 1997; Kalawy-Fansa, 2010; Sukdeo *et al.*, 2004; Vit, 2015; Yu, 2009). Since the functionally unknown proteins are assumed to mediate resistance mechanisms like their relatives, shedding light on those unrevealed functions might identify new and interesting mechanisms.

1.2.1 Overview of βαββββ-module-containing proteins

The βαββββ-module-containing protein family is also termed glyoxalase I/bleomycin resistance protein family and vicinal oxygen chelate (VOC) domain superfamily. The distinct denominations are attributed to the diverse functions that are mediated by the members of this protein family. Albeit sequence similarities are low the core fold of these proteins is highly conserved. The fold originates in the βαββββ-module. One module has four β-strands that form a β-sheet. The strands have the order and polarity of $\beta_1\uparrow\ \beta_4\uparrow\ \beta_3\downarrow\ \beta_2\uparrow$. One α-helix connects β_1 and β_2 (Figure 3) (Bergdoll *et al.*, 1998). Four of these modules assemble to the stable and fully functional βαββββ-module containing protein (Figure 4). In this assembly, the α-helices from two modules, which interact with each other via so-called back-to-back contacts. The β-sheets of two modules are connected via edge-to-edge contacts and form one big, eight-stranded U-shaped or half barrel-like β-sheet (Figure 4).

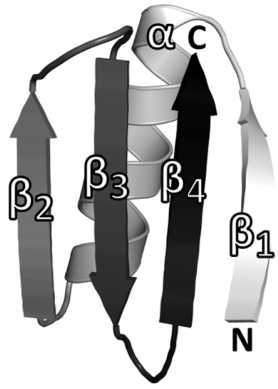

Figure 3: Structure of a βαββββ-module colored from white to black (N- to C-terminus).

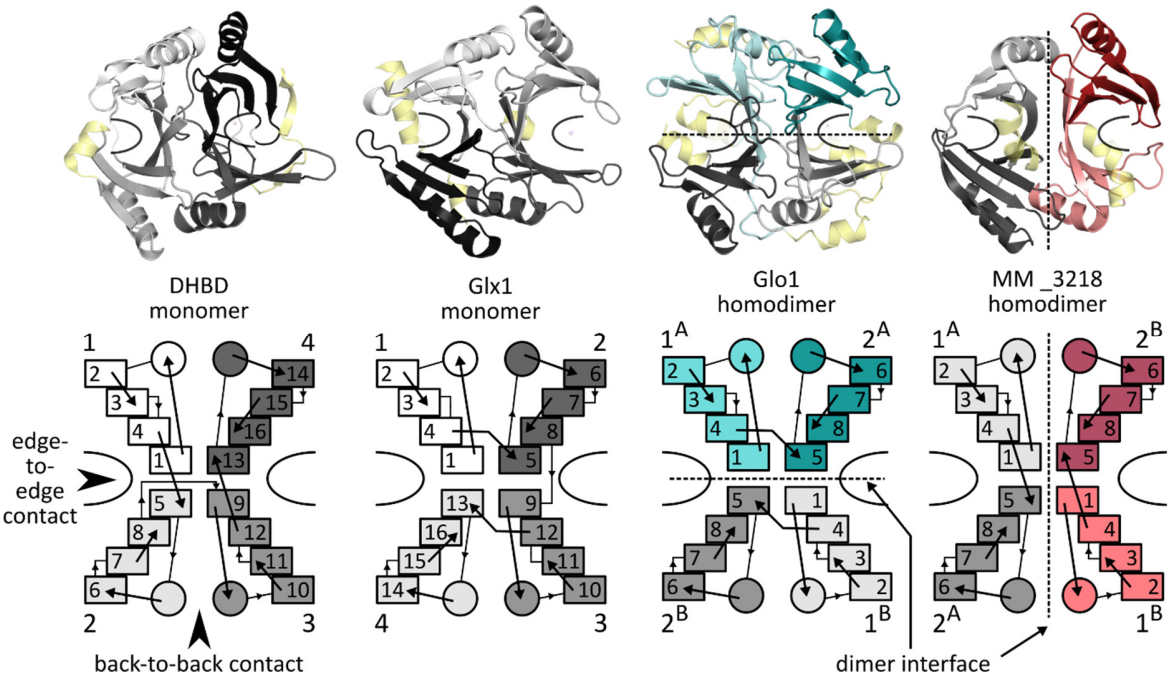

Figure 4: Assembly of βαββββ-module-containing proteins DHBD from *B. cepacia* LB400 (PDB-ID: 1HAN, Han *et al.*, 1995), glyoxalase 1 (Glx1) from *Zea mays* (PDB-ID: 5D7Z, Turra *et al.*, 2015), human glyoxalase 1 (Glo1) (PDB-ID: 1FRO, Cameron *et al.*, 1997) and the hypothetical protein MM_3218 from *Methanosarcina mazei* (PDB-ID: 3R6A, Eswaramoorthy *et al.* to be published). The upper panel shows the crystal structures. Secondary structure elements that are not part of the core βαββββ-fold are yellow. The lower panel shows the schematic arrangement of βαββββ-modules in the distinct monomeric and homodimeric βαββββ-module proteins. Homodimers can be established via edge-to-edge (teal) or back-to-back (red) contacts. The circles represent α-helices and the rectangles β-sheets. They are numbered from N- to C-terminus. The connections between the secondary elements are indicated by arrows and may contain additional secondary elements besides the core fold. The schematic representation is adapted from Bergdoll *et al.*, 1998. The βαββββ-modules that belong to one protein chain have different shades of the same color. The U-shapes indicate the location of the conserved active or binding sites. Dashed lines represent the homodimer interfaces.

The arrangement of the tertiary structure is dependent on how many βαββββ-modules are encoded in one protein chain. On the one hand, there are monomeric proteins that encode four modules, which can assemble in two distinct ways as depicted in Figure 4. On the other, there are proteins that encode two βαββββ-modules per chain and form homodimers in two different ways. The dimerization can either be mediated by edge-to-edge contacts, where the half barrel is formed between two protein chains or by back-to-back contacts, where each of the half barrels is made up by one protein chain (Figure 4) (Bergdoll *et al.*, 1998). Since the half-barrel is the conserved location for the active site, the homodimers contain two identical sites, while the monomeric βαββββ-module-containing proteins can have two distinct sites (Figure 4). Further, βαββββ-module-containing proteins also exist as higher order oligomers, like the 2,3-dihydroxybiphenyl 1,2-dioxygenase (DHBD) from *Burkholderia cepacia* LB400

(Han *et al.*, 1995), which encodes four βαββββ-modules per protein chain (Figure 4) and assembles into an octamer (Figure 5). Another example is the tetrameric homoprotocatechuate 2,3-dioxygenase (HPCD) from *Brevibacterium fuscum* (Figure 5) (Oberthuer *et al.*, 2017). There are also multidomain proteins such as the bleomycin N-acetyltransferase (BAT) from *Streptomyces verticillus* (Oda *et al.*, 2010). This enzyme consists of an N-terminal acetyltransferase domain that mediates the catalytic activity and a C-terminal βαββββ-module domain with two modules that mediate the dimerization of the protein (Figure 5).

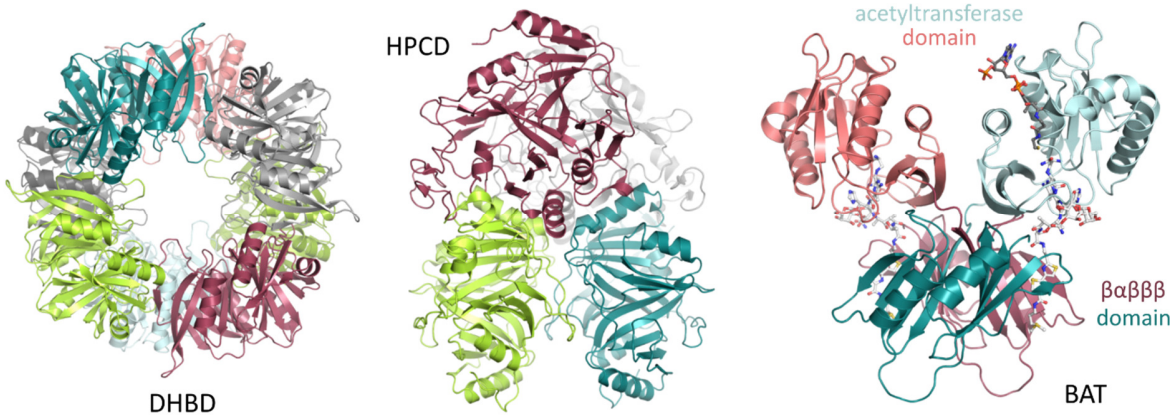

Figure 5: Examples for higher order oligomers and multidomain βαββββ-module-containing proteins. Octamer assembly of DHBD monomers (differently colored) from *B. cepacia* LB400 (PDB-ID: 1HAN, Han *et al.*, 1995). Tetrameric assembly of HPCD monomers (differently colored) from *B. fuscum* (PDB-ID: 5TRX, Oberthuer *et al.*, 2017). Multidomain bleomycin N-acetyltransferase (BAT) from *S. verticillus* (PDB-ID: 2ZW7, Oda *et al.*, 2010) in complex with bleomycin (white) and coenzyme A (grey). Each protein chain (different shades of teal or red) contains an N-terminal acetyltransferase domain and two C-terminal βαββββ-modules. The homodimer of BAT is formed by edge-to-edge dimerization of the C-terminal βαββββ-module domains.

The structural diversity is reflected in different functions that βαββββ-module-containing proteins fulfill. The VOC family of βαββββ-module-containing proteins share three to four amino acid residues in the active site that complex a divalent metal ion. The metal ion bidentate coordinates substrates and reaction intermediates with vicinal oxygen atoms and serves as catalytic center in different reaction mechanisms (He & Moran, 2011). Two general enzyme groups can be distinguished, namely the dioxygenase and the non-dioxygenase groups. The later catalyzes non-redox active reactions. In this group, the divalent metal center is important for electrophilic activation of the substrate and/or for stabilization of a transition state or an intermediate to catalyze isomerization reactions or to open oxirane rings by nucleophilic addition. Isomerizations are carried out in similar fashion by glyoxalase I (GlxI) and

methylmalonyl-CoA epimerases (MMCE), which coordinate several divalent metal ions by four active site residues and are widely distributed in all kingdoms of life (Figure 6). MMCE catalyzes the epimerization of (2*R*)-methylmalonyl-CoA to (2*S*)-methylmalonyl-CoA, which is an essential reaction during the breakdown of odd-chain fatty and branched amino acids. GlxI are lactoylglutathione lyases that catalyze a step during the detoxification pathway of the toxic side-product methylglyoxal. Methylglyoxal spontaneously reacts with glutathione (GSH) to a hemithioacetal product that serves as substrate for GlxI and is converted to *S*-D-lactoylglutathione (Figure 6) (He & Moran, 2011; Silva *et al.*, 2013). Nucleophilic additions were discovered in fosfomycin resistance proteins, which complex Mn^{2+} or Mg^{2+} ions by three amino acid side chains in the active site (Figure 6 B). Fosfomycin is an epoxide antibiotic that inhibits bacterial cell wall synthesis by inactivation of the UDP-N-acetylglucosamine-enolpyruvyltransferase MurA, which catalyzes the first step in peptidoglycan synthesis (Silver, 2017). Three classes of fosfomycin resistance proteins have been discovered by now. FosA and FosB catalyze the addition of respectively GSH or cysteine to fosfomycin, while FosX hydrolyses the antibiotic. These reactions result in the opening of the epoxide ring and thus inactivate fosfomycin. Fosfomycin binding is exemplified for FosA from *P. aeruginosa,* which additionally uses the monovalent ion K^+ not present in FosB and FosX (Figure 6 B). The general reaction mechanism is displayed in Figure 6 A. The dioxygenase group of VOC enzymes catalyzes the oxidative cleavage of carbon-carbon bonds using molecular O_2 as substrate. Most of them complex Fe^{2+}, but also Mn^{2+}-dependent enzymes were discovered (Armstrong, 2000; Fenwick *et al.*, 2011). All discovered βαβββ-fold dioxygenases are monomeric with two distinct sites of whom only one is occupied by a metal, complexed by three residues (Figure 6 B). Distinct substrate specificities and O_2 activation mechanisms distinguish type I aromatic ring-cleaving extradiol dioxygenases, two-substrate α-keto acid dependent oxygenases (2S-αKGO) and toxoflavin lyases. Extradiol dioxygenases, such as HPCD from *B. fuscum* (Figure 6 B), catalyze the O_2 transfer to single or double ring aromatic compounds with a benzene-1,2-diol moiety to yield the respective 2-hydroxymuconic semialdehyde derivatives (Figure 6 A). 2S-αKGOs are 4-hydroxyphenylpyruvate dioxygenases (HPPD) and hydroxymandelate synthases (HMS),

which catalyze the oxidative decarboxylation of 4-hydroxyphenylpyruvate to 2,5-dihydroxyphenylacetate or to hydroxymandelate as intermediate steps during tyrosine catabolism, respectively (Armstrong, 2000; He & Moran, 2009, 2011). Toxoflavin lyases, such as TflA from *Paenibacillus polymyxa,* catalyze the Mn^{2+}-dependent oxidative detoxification of toxoflavin (Fenwick *et al.*, 2011), which is produced by several bacteria (Jeong *et al.*, 2003; Levenberg & Linton, 1966), to yield peroxytoxoflavin (Philmus *et al.*, 2012) (Figure 6).

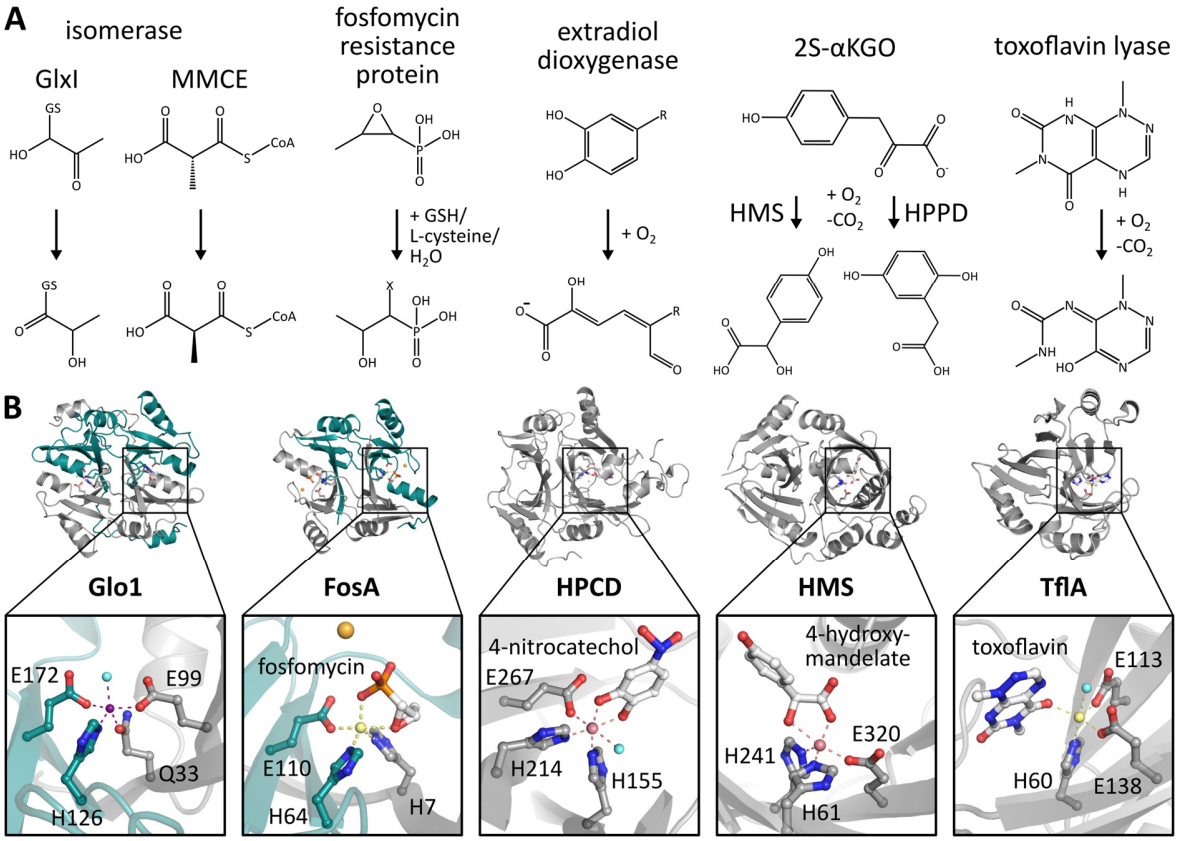

Figure 6: VOC family of βαβββ-module-containing proteins. A) Reactions catalyzed by distinct VOC family members. B) Examples for enzymes from the VOC family. Protein chains are colored differently. The boxes are magnifications of the active sites with the metal-complexing residues and the substrate (fosfomycin, toxoflavin), substrate analogue (4-nitrochatechol) or reaction product (4-hydroxmandelate) (white). The spheres represent Zn^{2+} (purple), Mn^{2+} (yellow), K^{+} (orange), Co^{2+} (pink) and H_2O (blue). Glo1: human isomerase (PDB-ID: 1FRO, Cameron *et al.*, 1997). FosA: fosfomycin resistance protein from *P. aeruginosa* PAO1 (PDB-ID: 1LQP, Rife *et al.*, 2002). HPCD: extradiol dioxygenase from *B. fuscum* (PDB-ID: 3OJK, Fielding *et al.*, 2011). HMS: 2S-αKGO from *Amycolatopsis orientalis* (PDB-ID: 2R5V, Fielding *et al.*, 2011). TflA: toxoflavin lyase from *P. polymyxa* (PDB-ID: 3PXK, Fenwick *et al.*, 2011).

There are also various metal-independent βαβββ-module-containing proteins. All the metal-independent proteins that have been characterized until now do not catalyze an enzymatic reaction. Many of them have two opposing aromatic amino acid residues in the conserved

βαββββ-module protein binding site, which mediate the complexation of small aromatic, heterocyclic compounds. Examples are the mitomycin C resistance protein MRD from *Streptomyces lavendulae*, which complexes mitomycin C, EhpR from *Pantoea agglomerans,* which binds the phenazine griseoluteic acid, and PA0803 from *P. aeruginosa*, which binds the self-produced pyocyanin (Figure 7). A more complex binding mode has been identified in bleomycin resistance proteins, which is a consequence of the relatively large size of their ligands. One example is the bleomycin resistance determinant (BLMT) from *Klebsiella pneumoniae* (Figure 7), where many residues stabilize the compounds in the binding site via salt bridges and H-bonds. Two aromatic side chains (W35, W99) in the binding site interact with an aromatic moiety of bleomycin in a similar fashion as seen in MRD, EhpR and PA0803 in complex with their respective ligands (Figure 7).

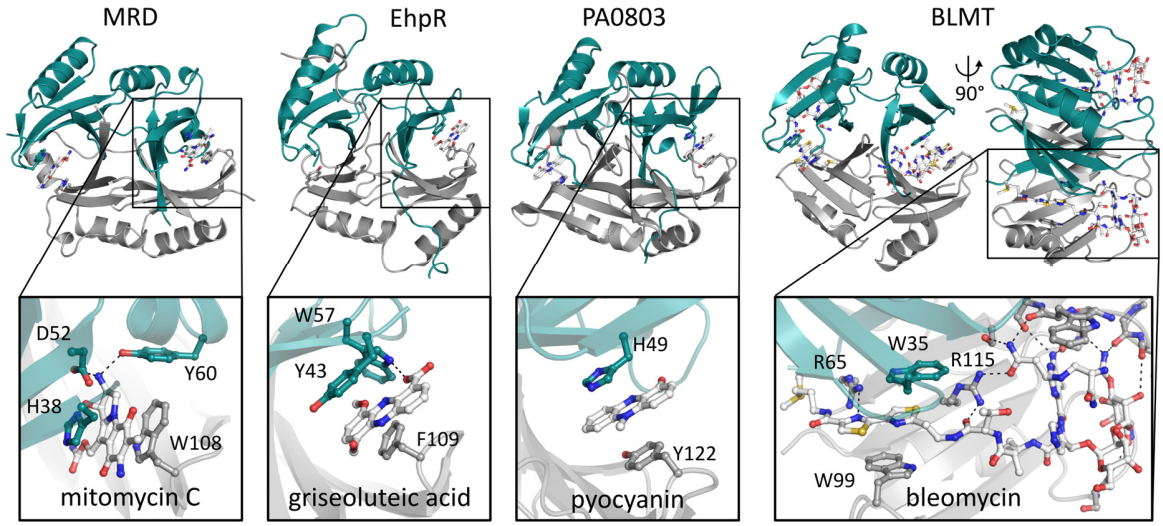

Figure 7: Metal-independent βαββββ-module-containing ligand binding proteins. The top panel shows the overall structure of the homodimeric binding proteins (chain A in grey, chain B in teal). The lower panel highlights the ligand-binding site and the ligand (white). Dashed lines represent H-bonds with a maximum distance of 3.2 Å. MRD from *S. lavendulae* in complex with mitomycin C (PDB-ID: 1KLL, Martin *et al.*, 2002), EhpR from *P. agglomerans* with griseoluteic acid (PDB-ID: 3SK2, Yu *et al.*, 2011), PA0803 from *P. aeruginosa* PAO1 (Vit, 2015), BLMT from *K. pneumoniae* (PDB-ID: 1EWJ, Maruyama *et al.*, 2001).

These binding proteins render the bacteria self-resistant to cope with the cytotoxic activity of endogenous secondary metabolites, such as mitomycin C, phenazines or bleomycin. This way, it is hypothesized that the respective compound is safely transported through the cell until it is exported to the environment and that the βαββββ-module protein might directly interact with a respective exporter (Martin *et al.*, 2002; Vit, 2015; Yu *et al.*, 2011).

Besides, another βαββββ-module-containing protein Rv0577 from *Mycobacterium tuberculosis* was recently structurally characterized. It is monomeric with different binding sites that are both metal-independent. One site, however, has two opposing tryptophan residues, similar to BLMT and other aromatic compound binding βαββββ-module proteins (Figure 7), that are not present in the second site (Buchko *et al.*, 2017). It is overexpressed and secreted into the host during infection (Huard *et al.*, 2003; Rosenkrands *et al.*, 2000) and was shown to interact with human Toll-like receptor 2 (TLR2), thereby interfering with the human immune response (Byun *et al.*, 2012). The molecular function is not clear, but it seems to be a virulence factor of this pathogenic bacterium and is therefore considered as a potential new drug target (Buchko *et al.*, 2012). The structurally undefined protein KbpA from *Streptomyces coelicolor* is homologous to Rv0577 (Buchko *et al.*, 2017). KbpA was shown to participate in the negative regulation of actinorhodin production, which is a secondary metabolite with antibiotic function. KbpA directly interacts with the serine/threonine kinase AfsK, which inhibits its autophosphorylation and thus the signal transduction pathway that would lead to the transcription of the actinorhodin synthesis genes (Umeyama & Horinouchi, 2001).

1.2.2 βαββββ-module-containing proteins of *P. aeruginosa*

The overall sequence similarity between the 22 βαββββ-module-containing proteins that are encoded in the genome of *P. aeruginosa* PAO1 is very low, but some distinct conserved residues enabled the identification of different protein classes (Figure 8) (Vit, 2015). Class I βαββββ-module proteins all possess three conserved metal-complexing residues in the binding site (HIS, HIS, GLU) that coordinate divalent metal cations as exemplified for FosA (Figure 6 B) (Bernat *et al.*, 1997; Rife *et al.*, 2002). Further functionally characterized representatives are the glyoxalases GloA1 (PA3524), GloA2 (PA0710) and GloA3 (PA5111), which all contain the fourth metal-complexing glutamate that is conserved among glyoxalases (Figure 6 B, Figure 8) (Sukdeo *et al.*, 2004). The two proteins with four βαββββ-modules per protein chain, PA0242 and PA0856 also contain the conserved metal-complexing residues and are therefore assigned to class I.

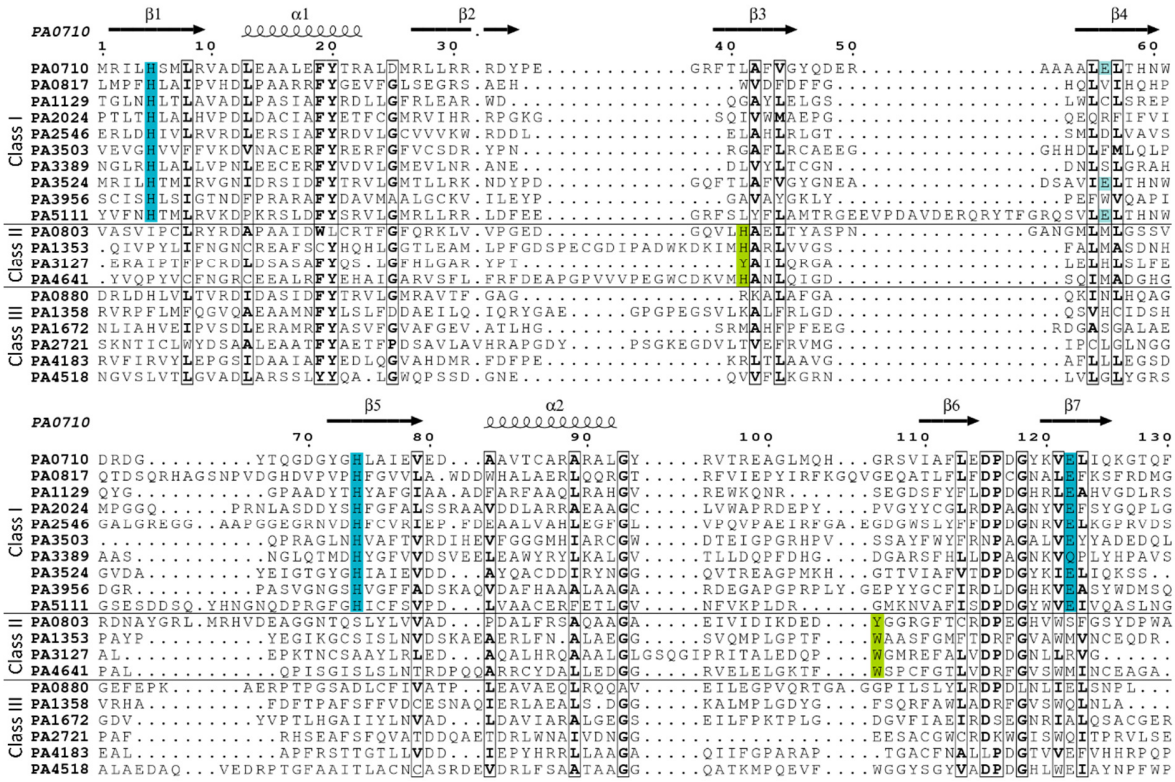

Figure 8: Excerpt from the structure-based sequence alignment of βαββ-module-containing proteins from *P. aeruginosa* performed with PROMALS3D (Pei *et al.*, 2008) and colored with ESPript 3.0 (Robert & Gouet, 2014). The figure was adapted from Vit, 2015. Conserved metal-complexing residues among all class I βαββ-module proteins are highlighted in teal and additional conserved metal-complexing residues in glyoxalases are highlighted in light teal. Conserved aromatic compound binding residues from class II βαββ-module proteins are highlighted in green.

Proteins that have two conserved aromatic residues in their binding pocket are assigned to class II βαββ-module-containing proteins (Vit, 2015). PA0803, PA1353 and PA4641 are catalytically inactive, unspecific phenazine binding proteins and suspected to mediate resistance to self-produced compounds like pyocyanin (Figure 7) (Kalawy-Fansa, 2010; Vit, 2015; Yu, 2009). PA3127 is suggested to be a two domain bleomycin N-acetyltransferase that catalyzes the detoxification of bleomycin (Vit, 2015). The enzymatic reaction is catalyzed by the C-terminal acetyltransferase domain (Vit, 2015). The N-terminal βαββ-module domain probably assists in the proper binding of an aromatic moiety of bleomycin, mediated by the two conserved aromatic side chains also found in the other class II βαββ-module proteins (Popp, 2013; Vit, 2015). The class III βαββ-module-containing protein family comprises six proteins that lack both the conserved metal complexing and aromatic residues in the binding pocket (Vit, 2015).

1.2.3 Class III βαββββ-module-containing proteins in *P. aeruginosa*

Class III βαββββ-module-containing proteins from *P. aeruginosa* are PA0880, PA1358, PA1672, PA2721, PA4183 and PA4518 (Vit, 2015). They are conserved among several *P. aeruginosa* strains, such as PAO1 and PA14 (Valot *et al.*, 2015). Except for PA4183, the crystal structures of all class III βαββββ-module proteins have been determined (Figure 9).

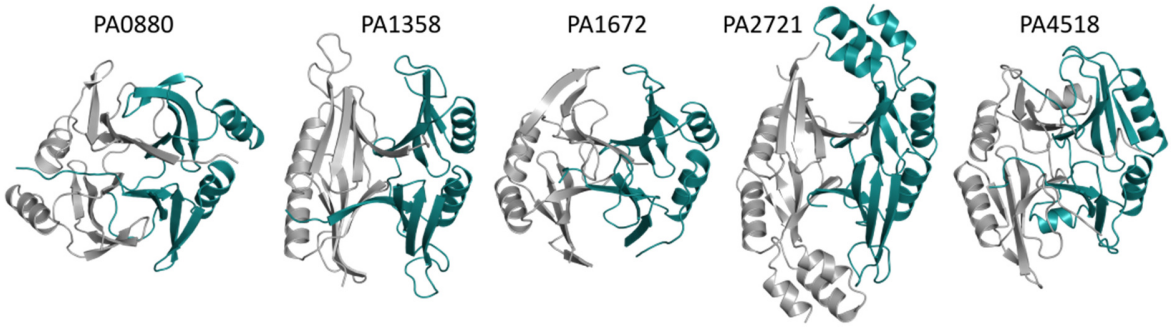

Figure 9: Crystal structures of class III βαββββ-module-containing proteins. The distinct protein chains of the homodimeric proteins are colored in grey and teal. PA0880, PA1672, PA4518 (Vit, 2015). PA1358 (PDB-ID: 1U7I, Osipiuk *et al.*, to be published). PA2721 (PDB-ID: 1U69, Nocek *et al.*, 2006).

They are homodimers that are formed via edge-to-edge contacts (Vit, 2015; Nocek *et al.*, 2006; Osipiuk *et al.*, to be published). Besides the core βαββββ-module-containing protein fold and a lack of the conserved residues of class I and class II βαββββ-proteins, they only have little similarity. They have sequence identities below 30 % and do not share conserved residues in their active sites indicating that they are not functionally homologous to each other (Sievers *et al.*, 2011). Based on the available structures of class III proteins, no functional predictions were possible, because the sequence identities with functionally characterized βαββββ-family members are very low (Nocek *et al.*, 2006; Vit, 2015) or the structures have not been further analyzed as in the case of PA1358 (PDB-ID: 1U7I, Osipiuk *et al.*, to be published). Only PA0880 is suspected to participate in itaconate metabolism, since it is encoded in the same operon as genes that code for itaconate degradation enzymes (Sasikaran *et al.*, 2014). However, even for this protein, an actual substrate could not be identified until now (Vit, 2015).

2 Research Objectives

Pseudomonas aeruginosa is an opportunistic human pathogen, which causes infections that are difficult to treat with current antibiotics. For better understanding of *P. aeruginosa* infections, its virulence, resistance mechanisms and regulatory pathways, it is crucial to characterize previously unknown proteins to support the identification of new drug targets and the development of effective antimicrobial strategies.

P. aeruginosa encodes 22 members of the βαββββ-module-containing protein family. These proteins are abundant in all kingdoms of life and all so far functionally characterized proteins mediate resistance towards toxic compounds. The 22 βαββββ-module proteins from P*. aeruginosa* are distinguished in metal-binding (class I), aromatic compound-binding (class II) and functionally uncharacterized proteins (class III) (Vit, 2015). Since aromatic compound-binding proteins mediate resistance against small aromatic compounds, such as the self-produced pyocyanin (Kalawy-Fansa, 2010; Vit, 2015; Yu, 2009) and most of the metal-binding representatives mediate resistance towards extrinsic antibiotics such as fosfomycin (Bernat *et al.*, 1997), class III proteins are also assumed to participate in resistance mechanisms.

Therefore, the structural and functional characterization of the class III βαββββ-module-containing proteins PA1358, PA1672, PA2721, PA4183 and PA4518 was in the focus of this study. The physiological and molecular functions of class III βαββββ-module proteins were supposed to by characterized. The physiological roles were investigated using comparative microbiological assays with *P. aeruginosa* wild type strains and transposon insertion mutants of the respective genes to identify conditions that caused altered phenotypes in the mutants. For this, the bacteria were exposed to distinct antibiotics, incubated on different carbon sources and they were grown on solid and liquid media. Besides, the genomic background of class III genes was investigated to find further evidence towards a potential function of proteins that are encoded in the same operon as the class III βαββββ-module-containing proteins. Detailed information on molecular level were gained with biophysical methods and protein X-ray crystallography using the recombinant proteins.

3 Materials and Methods

3.1 Materials

3.1.1 Chemicals, media, buffer and solutions

All chemicals were purchased from Acros Organics (Geel, Belgium), Alfa Aeser (Haverhill, Massachusetts (MA), USA), AppliChem GmbH (Darmstadt, Germany), Becton Dickinson and Company (Franklin Lakes, New Jersey, USA), Biolog (Hayward, CA, USA), Carl Roth GmbH & Co. (Karlsruhe, Germany), Cayman Chemicals (Ann Arbor, Michigan, USA), Merck KGaA (Darmstadt, Germany), MP Biomedicals, LLC (Santa Ana, California, USA), Thermo Fisher Scientific (Waltham, MA, USA) and Sigma-Aldrich (St. Louis, Missouri, USA). The QIAquick® PCR Purification and Gel Extraction Kit as well as the QIAprep® Spin Miniprep Kit were purchased from Qiagen (Hilden, Germany).

Media, buffers and buffer stock solutions were prepared in MilliQ®-H_2O. Buffers and stock-solutions were sterilized by filtration, while media were autoclaved. Buffers for protein purification and ITC experiments were also degassed. Antibiotic stock solutions were dissolved in MilliQ®-H_2O (ampicillin, gentamicin) or 70 % Ethanol (chloramphenicol, tetracycline). Final antibiotic concentrations were 100 µg/ml ampicillin (Amp) and 34 µg/ml chloramphenicol (Cm) for *E. coli* strains, 20 µg/ml Amp for *P. aeruginosa* PA14 and PAO1 wild type strains and 20 µg/ml gentamicin (Gm) or 60 µg/ml tetracycline (Tet) for *P. aeruginosa* transposon mutants. 50 µg/ml Gm were used for PA14 wt strains transformed with pHERD30T plasmids.

Media

Lysogeny broth (LB)	10 g/l tryptone, 7 g/l NaCl 5 g/l yeast extract
LB agar	10 g/l tryptone, 7 g/l NaCl, 5 g/l yeast extract, 15 g/l agar
Terrific broth (TB)	12 g/l tryptone, 24 g/l yeast extract, 4 % (v/v) glycerol, 17 mM KH_2PO_4, 72 mM K_2HPO_4
Super optimal broth with catabolite repression (SOC)	20 g/l trypton, 5 g/l yeast extract, 10 mM NaCl, 2.5 mM KCl, 10 mM $MgCl_2$, 10 mM $MgSO_4$, 20 mM glucose
M9-medium	6 g/l Na_2HPO_4, 3 g/l KH_2PO_4, 0.5 g/l NaCl, 1 g/l NH_4Cl, 1 mM $MgSO_4$, 0.1 mM $CaCl_2$, 0.4 % (w/v) glucose

Swarming agar	0.5 % (w/v) agar, 6 g/l Na_2HPO_4, 3 g/l KH_2PO_4, 0.5 g/l NaCl, 2 mM $MgSO_4$, 0.2% (w/v) glucose, 0.5 % (w/v) casamino acids
Swimming agar	0.3 % (w/v) agar, 6 g/l Na_2HPO_4, 3 g/l KH_2PO_4, 0.5 g/l NaCl, 1 mM $MgSO_4$, 0.2% (w/v) glucose, 0.5 % (w/v) casamino acids

Buffers for protein purification

Buffer A	50 mM Na_2HPO_4/NaH_2PO_4 pH 8.0, 300 mM NaCl
Buffer B	Buffer A with 500 mM imidazole, pH 8.0
Protease cleavage buffer	20 mM Tris/HCl pH 8.0, 150 ml NaCl, 4 mM β-mercaptoethanol (BME) or 2 mM dithiothreitol (DTT)
SEC buffer	20 mM Tris/HCl pH 8.0, 150 ml NaCl
Low salt buffer	20 mM Tris/HCl pH 8.0, 20 mM NaCl
High salt buffer	20 mM Tris/HCl pH 8.0, 1 M NaCl

Solutions for Phenotype MicroArrays™

IF-0a GN/GP Base inoculating fluid (1.2x)	Biolog, Inc., Hayward, California, USA
IF-10a GN Base inoculating fluid (1.2x)	Biolog, Inc., Hayward, CA, USA
Biolog Redox Dye mix A (100x)	Biolog, Inc., Hayward, CA, USA

Other solutions

TAE buffer (1x)	40 mM Tris pH 8.0, 20 mM acetic acid, 1 mM EDTA
0.8 % (w/v) agarose gel	0.8 g agarose in 100 ml 1xTAE buffer, 5 µl Roti®-GelStain (Carl Roth, Karlsruhe, Germany)
DNA gel loading dye (6x)	30% (v/v) glycerol, 0.25% (w/v) bromophenol blue
DNA ladder	GeneRuler DNA Ladder Mix, #SM0333 (Thermo Fisher Scientific, Waltham, MA, USA)
Amino acid mix	0.1 g/l Lys, Phe, Thr, 0.05 g/l Ile, Leu, Val
Stacking gel buffer (4x)	0.5 M Tris/HCl pH 6.8, 0.4 % (w/v) SDS
Stacking gel (5 %)	1x stacking gel buffer, 5 % (w/v) acrylamide (stock: 30 % (w/v) 37.5:1), 0.1 % (w/v) ammonium persulfate (APS), 0.001 % (v/v) tetramethylethylenediamine (TEMED)
Resolving gel buffer (4x)	1.5 M Tris/HCl pH 8.8, 0.4 % (w/v) SDS
Resolving gel (15 %)	1x resolving gel buffer, 15 % (w/v) acrylamide (stock: 30 % (w/v) 37.5:1), 0.1 % (w/v) APS, 0.001 % (v/v) TEMED

Resolving gel (18 %)	1x resolving gel buffer, 18 % (w/v) acrylamide (stock: 30 % (w/v) 37.5:1), 0.1 % (w/v) APS, 0.001 % (v/v) TEMED
SDS-loading buffer (5x)	50 mM Tris/HCl pH 6.8, 500 mM BME, 50 % (v/v) glycerol, 10 % (w/v) SDS, 0.05 % (w/v) bromophenol blue
Protein standard	PageRuler™ Plus Prestained Protein Ladder, #26620 (Thermo Fisher Scientific, Waltham, MA, USA)
SDS-running buffer (10x)	Rotiphorese® 10x SDS-PAGE (Carl Roth, Karlsruhe, Germany)
Staining Solution	InstantBlue™ Protein Stain (expedeon, Cambridge, UK)

3.1.2 Enzymes

All restriction endonucleases used in this study (NdeI, XhoI, BamHI, DpnI, NcoI, HindIII), Phusion® High-Fidelity DNA-Polymerase, T4 DNA Ligase and Antarctic Phosphatase were purchased from New England Biolabs (NEB, Ipswich, MA, USA). KAPA HiFi polymerase was from Kapa Biosystems (Wilminton, MA, USA). Taq DNA polymerase was purchased as 2x VWR Red Taq DNA-polymerase Master Mix from VWR (VWR International, Haasrode, Belgium). Proteases for the cleavage of purification-tags (Tobacco etch virus (TEV)- and SUMO-protease) were purified by Claudia Hanko, Petra Büssig, Tobias Bock, Ute Widow or Vanessa Hering. All proteases were expressed with at least a hexa-histidine tag (His_6) and purified by Ni(II)-immobilized metal ion affinity chromatography (Ni-IMAC) followed by size exclusion chromatography (SEC).

3.1.3 Oligonucleotides, plasmids and bacterial strains

Oligonucleotides for the amplification of open reading frames (ORF) of interest were designed using OligoCalc (Kibbe, 2007) and are displayed in Table 1. For this, DNA-sequences of *P. aeruginosa* strain PAO1 were taken from the *Pseudomonas* Genome Database (Winsor *et al.*, 2016). Oligonucleotides for cloning were created with 5' overhangs containing recognition sites for restriction endonucleases. Oligonucleotides were ordered from Eurofins MWG Operon LLC (Ebersberg, Germany).

Table 1: Oligonucleotides

Oligonucleotide name[#]	sequence 5'→ 3' [¥]	source
1358_*NdeI*_s	AAGACACATATGAGCGCACGCGTACGACC	this study
1358_*XhoI*_as	ATATTCTCGAGTCAGGCCAGATTGAGCTGC	this study
1358_SLIC_*NcoI*_s	AAGAAGGAGATATACATACCCATGAGCGCACGCGTACGACCC	this study
1358_SLIC_*HindIII*_as	TAAAACGACGGCCAGTGCCAAGCTTTCAGGCCAGATTGAGCTGCCAGG	this study

1359-CTD_*NdeI*_s	AATGTCCATATGGCCACCGACCGCTCGC	this study
1359-CTD_*XhoI*_as	ATATTCTCGAGCTAGCTCACCACGTTGCGG	Vit, 2015
1359_SLIC_ *NcoI*_s	AAGAAGGAGATATACATACCCATGGAAGAGGTCCGGCAGTGGGAAG	this study
1359_SLIC_ *HindIII*_as	TAAAACGACGGCCAGTGCCAAGCTTCTAGCTCACCACGTTGCGGGTG	this study
1672_*NdeI*_s	AATGTCCATATGAACCTGATCGCGCACGTG	Vit, 2015
1672_*XhoI*_as	ATATACTCGAGTCACGGCCGCTCTCCGCA	Vit, 2015
2721_*NdeI*_s	AATGTCCATATGAACAGCAAGAACACCATC	Vit, 2015
2721_*XhoI*_as	ATGTCCTCGAGTCATCAGCCCTTGAAG	Vit, 2015
2722_*NdeI*_s	AATGTCCATATGGATCGATTCACCGGCG	this study
2722_*XhoI*_as	ATAACACTCGAGTCACTCTTCGCTGCG	this study
2723_*NdeI*_s	AATATACATATGGACGAACTGTTCGAAGAG	this study
2723_*XhoI*_as	ATAACACTCGAGTCAGAGCAGTACGG	this study

#Oligonucleotide names contain the name of the respective restriction endonuclease in italics. ¥Recognition sites for the respective restriction endonucleases are underlined.

The plasmids for recombinant protein expression in *E. coli* as well as for protein expression in *P. aeruginosa* that were used and generated in this study are listed in Table 2. The plasmids generated during this study were sequenced at Eurofins MWG Operon LLC (Ebersberg, Germany) or at the Genome Analytics Facility (GMAK) of the HZI to verify the insertion of the correct DNA sequence in comparison to the sequence from the *Pseudomonas* Genome Database (Winsor *et al.*, 2016).

Table 2: Plasmids¥

plasmid	description	source
pET19m	Vector for expression of N-term. His_6-tagged protein with TEV-protease cleavage site	MPI Dortmund
pET-SUMO	Vector for expression of N-term. His_6-SUMO-tagged protein with SUMO-protease cleavage site	MPI Dortmund
pHERD30T	*E. coli/Pseudomonas* shuttle vector for protein expression in *P. aeruginosa*	Qiu *et al.*, 2008
pET19m_*PA1358*	pET19m containing full-length *PA1358*	Vit, 2015
pET19m_*PA1359*	pET19m containing full-length *PA1359*	Vit, 2015
pET19m_*PA1359*-CTD	pET19m containing a *PA1359* construct, coding for the C-terminal domain (CTD, aa108-218) of PA1359	this study
pET19m_*PA2721*	pET19m containing full-length *PA2721*	this study
pET19m_*PA2722*	pET19m containing full-length *PA2722*	this study
pET19m_*PA2723*	pET19m containing full-length *PA2723*	this study
pET19m_*PA4183* $^{16\text{-}155}$	pET19m containing a *PA4183* construct, coding for N-term. truncated (aa 16-155) PA4183	Vit, 2015
pET19m_*PA4518*	pET19m containing full-length *PA4518*	Vit, 2015
pET-SUMO_*PA1358*	pET-SUMO containing full-length *PA1358*	this study
pET-SUMO_*PA1672*	pET-SUMO containing full-length *PA1672*	this study
pHERD30T_*PA1358*	pHERD30T containing the full-length *PA1358*	this study
pHERD30T_*PA1359*	pHERD30T containing the full-length *PA1359*	this study

¥ pET19m and pETSUMO are vectors for IPTG inducible protein expression in *E. coli* with Amp^r, pHERD30T is a vector for arabinose inducible protein expression in *P. aeruginosa* with Gm^r.

E. coli strains (Table 3) were used for plasmid amplification and recombinant protein expression. *P. aeruginosa* PA14 transposon insertion mutants from the non-redundant mutant library (Liberati *et al.*, 2006) or PAO1 transposon mutants from the two-allele library (Held *et al.*, 2012) were used for microbiological experiments (Table 3). The bacteria were stored at -80 °C in 20 % (v/v) glycerol. To confirm the presence of the transposon insertions, the respective gene was amplified by PCR (3.2.1.2) and the PCR product was sequenced at Eurofins MWG Operon LLC (Ebersberg, Germany).

Table 3: Bacterial strains

Strain	Genotype or description[†]	source
E. coli		
DH5α	F– Φ80*lac*ZΔM15 Δ(*lac*ZYA-*arg*F) U169 *rec*A1 *end*A1 *hsd*R17 (rK–, mK+) *pho*A *sup*E44 λ– *thi*-1 *gyr*A96 *rel*A1	Invitrogen
Top10	F– *mcr*A Δ(*mrr-hsd*RMS-*mcr*BC) Φ80*lac*ZΔM15 Δ*lac*X74 *rec*A1 *ara*D139 Δ(*ara leu*) 7697 *gal*U *gal*K *rps*L **(Str^r)** *end*A1 *nup*G	Invitrogen
XL1blue	recA1 endA1 gyrA96 thi-1 hsdR17 supE44 relA1 lac [F´ proAB lacIq ZΔM15 Tn10 **(Tet^r)**]	Stratagene
OmniMAX^{TM} 2	F´ [proAB lacI^q lacZΔM15 *Tn10* **(Tet^r)** Δ(ccdAB)] *mcrA* Δ(*mrr-hsd*RMS-*mcr*BC) Φ80(*lac*Z)ΔM15 Δ(*lac*ZYA-*arg*F)U169 *end*A1 *rec*A1 *sup*E44 *thi*-1 *gyr*A96 relA1 tonA panD	Invitrogen
BL21(DE3)	F– *ompT hsdS*$_B$(r_B^- m_B^-) *gal dcm* (DE3)	Novagen
Rosetta (DE3) pLysS	F– *ompT hsdS*$_B$(r_B^- m_B^-) *gal dcm* (DE3) pLysSRARE **(Cm^r)**	Novagen
Rosetta2 (DE3)	F– *ompT hsdS*$_B$(r_B^- m_B^-) *gal dcm* (DE3) pRARE2 **(Cm^r)**	Novagen
P. aeruginosa[*]		
PAO1 wt	wild type	
PAO1 *PA1359*::Tn	*PA1359*::IS*phoA*/hah; **Tet^r**, PAO1 transposon mutant 41250	Held *et al.*, 2012
PAO1 *PA2721*::Tn	*PA2721*::IS*lacZ*/hah; **Tet^r**, PAO1 transposon mutant 21211	Held *et al.*, 2012
PAO1 *flgK*::Tn	*flgK*::IS*lacZ*/hah; **Tet^r**, PAO1 transposon mutant 17288	Held *et al.*, 2012
PA14 wt	wild type	Liberati *et al.*, 2006
PA14 *PA1358*::Tn	*PA14_46720*::*MAR2xT7*; **Gm^r**, PA14 transposon mutant 43400[#]	Liberati *et al.*, 2006
PA14 *PA1672*::Tn	*PA14_42870*::*MAR2xT7*; **Gm^r**, PA14 transposon mutant 27951	Liberati *et al.*, 2006
PA14 *PA4183*::Tn	*PA14_09780*::*MAR2xT7*; **Gm^r**,PA14 transposon mutant 36793	Liberati *et al.*, 2006
PA14 *PA4518*::Tn	*PA14_58620*::*MAR2xT7*; **Gm^r**, PA14 transposon mutant 31441	Liberati *et al.*, 2006
PA14 *flgK*::Tn	*flgK*::*MAR2xT7*; **Gm^r**, PA14 transposon mutant 56704	Liberati *et al.*, 2006
PA14 *rhlR*::Tn	*rhlR*::*MAR2xT7*; **Gm^r**,PA14 transposon mutant 37943	Liberati *et al.*, 2006
PA14 wt pHERD30T	PA14 wt transformed with the empty pHERD30T vector, **Gm^r**	this study
PA14 wt pHERD30T_*PA1358*	PA14 wt transformed with the pHERD30T plasmid containing the ORF of *PA1358*, **Gm^r**	this study
PA14 wt pHERD30T_*PA1359*	PA14 wt transformed with the pHERD30T plasmid containing the ORF of *PA1358*, **Gm^r**	this study

[†]Antibiotic resistance genes are highlighted in bold (Str: streptomycin, Cm: chloramphenicol, Tet: tetracycline, Gm: gentamicin). [*] *P. aeruginosa* strains were provided by the collaborator S. Häußler (HZI). [¥]PAO1 transposon mutants are numbered according to the two-allele library (Held *et al.*, 2012). [#]PA14 transposon mutants are numbered according to the non-redundant mutant library (Liberati *et al.*, 2006).

3.1.4 Chromatography columns

HisTrap™ HP 5 ml	GE Healthcare, Munich, Germany
HiTrap™ Q HP 5 ml	GE Healthcare, Munich, Germany
HiLoad™ 75 16/600 Superdex™ prep grade (pg)	GE Healthcare, Munich, Germany
HiLoad™ 75 26/600 Superdex™ pg	GE Healthcare, Munich, Germany
Superdex™ 75 10/300 GL	GE Healthcare, Munich, Germany

3.1.5 Screens and Phenotype MicroArrays™ (PM)

The Phenotype MicroArrays™ (PM) PM1 and PM2 MicroPlate™ for screening carbon sources and the plates for testing chemical sensitivity PM11C, PM12B, PM13B, PM14A, PM15B, PM16A, PM17A, PM18C, PM19 and PM20B were purchased from Biolog, Inc. (Hayward, CA, USA). The Helmholtz-Zentrum Berlin (HZB, Berlin, Germany) provided the HZB immobilized fragment-screen version 2. Crystallization screens were purchased from Hampton Research (Aliso Viejo, CA, USA), Molecular Dimensions (Newmarket, Suffolk, UK) and Qiagen (Hilden, Germany). Silver Bullets™ and Silver Bullets Bio™ additive screens are from Hampton Research.

3.2 Methods

3.2.1 Molecular biology

3.2.1.1 Isolation of genomic *P. aeruginosa* DNA

The genomic DNA (gDNA) from *P. aeruginosa* strain PAO1 for cloning was isolated by A. Vit (Vit, 2015). The gDNA from *P. aeruginosa* PAO1 and PA14 transposon insertion mutants for verifying the transposon insertion was either isolated by chloroform/phenol extraction as described in Vit, 2015 or by the protocol “Procedure for sequencing the transposon insertion site” (Filloux and Ramos, 2014).

3.2.1.2 Polymerase chain reaction (PCR)

Polymerase chain reactions (PCR) were performed to amplify the DNA sequences of the genes of interest (GOI). gDNA from *P. aeruginosa* (Table 3) or plasmid DNA (Table 2) served as DNA templates. For colony PCR (cPCR) single bacterial colonies were suspended in 5 µl ddH_2O and

1 µl of the cell suspension was used as template in PCR reactions with a total volume of 50 µl. The Phusion polymerase was used for DNA amplification and the Taq polymerase Master Mix (MM) was used for cPCR. The Taq polymerase MM and the KAPAHiFi were used to verify the transposon insertions. PCR reactions were prepared as described in Table 4. The optimal annealing temperature for the KAPAHiFi polymerase was determined by gradient PCR. PCR cycling programs were performed as described in Table 4.

Table 4: Composition of PCR reactions and PCR cycling programs

PCR reactions					
Component		**Phusion**	**KAPAHiFi**	**Taq Master Mix**	**Final conc.**
Buffer		Phusion GC (5x) 10 µl	KAPAHiFi GC (5x) 10µl	Taq Master Mix (2x) 25 µl	1x
dNTPs (10 mM)		1 µl	0.75 µl	included in MM	0.2 – 0.3 mM
Primer fw (10 µM)		2.5 µl	0.75 µl	2.5 µl	0.3 - 0.5 µM
Primer rv (10 µM)		2.5 µl	0.75 µl	2.5 µl	0.3 - 0.5 µM
Template	gDNA	50 – 250 ng	10 – 100 ng	10 – 500 ng	As required
	Plasmid	1 pg – 10 ng	0.1 – 1 ng	0.1 – 1 ng	
DMSO (100 %)		2 µl	0-1 µl	1 µl	0-4 %
Polymerase		0.5 µl	1 µl	included in MM	1 – 5 U
PCR grade H_2O		ad 50 µl	ad 25 µl	ad 50 µl	

PCR cycling programs							
Step	**Cycle**	**Phusion**		**KAPAHiFi**		**Taq Master Mix**	
		T [°C]	**T [s]**	**T [°C]**	**T [s]**	**T [°C]**	**T [s]**
Initial denaturation	1	98	60	95	300	95	120
Denaturation	30	98	20	98	20	95	20
Annealing¥		T_m -5	20	T_m +/- 5	15	T_m -5	20
Extension		72	30/kb	72	30/kb	72	60/kb
Final extension	1	72	600	72	60/kb	72	600

¥ Annealing temperatures for Phusion and Taq polymerase were set 5 K below the melting temperature (T_m) of the primer with the lower T_m. The most efficient annealing temperature for KAPAHiFi polymerase was determined with temperature gradient PCR.

3.2.1.3 Agarose gel electrophoresis and DNA extraction

Agarose gel electrophoresis was performed in agarose gels (0.8 % (w/v)) supplemented with Roti®-GelStain to visualize nucleotides under UV light. The PCR reactions were supplemented with DNA loading dye (6x), loaded on the gel and separated by size in comparison to the GeneRuler DNA Ladder Mix by applying a voltage of 80 V. The DNA fragments with the expected size were cut out under UV light and purified with the QIAquick® Gel Extraction Kit (Qiagen) according to the manufacturer's manual.

3.2.1.4 Determination of nucleic acid concentrations

Nucleic acid concentrations were determined with a NanoDrop2000 spectrophotometer (Thermo Scientific) by measuring the UV absorption at the maximum absorption wavelength of nucleic acids at 260 nm. An absorption value of 1 corresponds to a double stranded DNA (dsDNA) concentration of 50 µg/ml.

3.2.1.5 Restriction digest of DNA and purification of linear DNA

To generate single stranded 3' overhangs in the PCR products and in the plasmid DNA, both were treated with specific restriction endonucleases (NEB, Table 1). PCR products for sequence and ligation independent cloning (SLIC, 3.2.1.7) were only digested with DpnI to remove the template DNA. Plasmids were simultaneously dephosphorylated at the 5'-DNA ends with Antarctic Phosphatase (NEB) to limit the probability for relegation. Double digestion reactions were prepared with plasmid DNA (> 1µg) and PCR product (500 - 600 ng). The reaction with the plasmid DNA contained the respective endonuclease (1 µl), Cut Smart buffer (10x, 4 µl), Antarctic Phosphatase (1 µl, NEB) and Antarctic Phosphatase reaction buffer (10x, 4 µl). The total reaction volume (40 µl) was reached by adding ddH_2O. The reaction with the PCR product contained Cut Smart buffer (10x, 4 µl) and the respective endonucleases (1 µl). The reactions were incubated at 37 °C for 30 min, followed by heat inactivation of the enzymes at 65 °C for 20 min. The linear DNA was purified with the QIAquick PCR Purification Kit (Qiagen) according to the manufacturer's manual.

3.2.1.6 Ligation

The ligation of PCR fragments with linearized plasmids was performed with T4 DNA Ligase. The reactions were prepared in a total volume of 10 µl by combining 6 µl of insert DNA, 2 µl of plasmid DNA, 1 µl of T4 DNA Ligase buffer (10x) and 1 µl T4 DNA Ligase. The reactions were incubated overnight at 16 °C followed by heat inactivation for 20 min at 65 °C and directly used for transformation of *E. coli* cells (4.2.1.7).

3.2.1.7 Sequence and ligation independent cloning (SLIC)

SLIC (Li and Elledge, 2007) was performed to insert the *PA1358* and *PA1359* genes into the pHERD30T plasmid. The genes were amplified as described in section 3.2.1.2 with the respective SLIC primers (Table 1), digested and purified as described in section 3.2.1.5. The pHERD30T plasmid was linearized with HindIII and NcoI and purified as described in section 3.2.1.5. SLIC was performed with the Quick-Fusion Cloning Kit (Biotool) according to the vendor's protocol. Afterwards the SLIC reaction was transformed into *E. coli* cells (4.2.1.7).

3.2.1.8 Preparation of competent bacterial cells

Ca^{2+}-competent *E. coli* cells for heat shock transformation were produced by Claudia Hanko at the Helmholtz Centre for Infection Research. Electrocompetent *P. aeruginosa* PA14 cells were prepared according to the protocol "Gene Transfer: Transformation/Electroporation" (Filloux and Ramos, 2014).

3.2.1.9 Transformation of competent bacterial cells

Plasmids were transformed into competent bacterial cells (Table 3) for plasmid amplification or protein production. For heat shock transformation, up to 100 ng of DNA were mixed with 50 µl of chemically competent *E. coli* cells and incubated on ice for 30 min. The heat shock was performed for 90 s at 42 °C. After 10 min incubation on ice, the cells were supplemented with 1 ml LB or SOC medium and incubated at 37 °C for 30 min. The cells were pelleted for 1 min at 15700 *g*, plated on LB agar that was supplemented with appropriate antibiotics and incubated at 37 °C overnight. Electrocompetent *P. aeruginosa* cells were transformed by electroporation as described in the protocol "Gene Transfer: Transformation/Electroporation" (Filloux & Ramos, 2014).

3.2.2 Protein expression

3.2.2.1 Recombinant expression of target proteins

Proteins were recombinantly expressed in different *E. coli* strains (Table 3/4). The cells were transformed with the expression plasmids (Table 5) and a single colony was used for inoculation of LB media supplemented with the respective antibiotics. The cell density of bacterial liquid cultures was determined by measuring the absorption at a wavelength of 600 nm

(OD_{600}). LB cultures were incubated for 16 h at 37 °C while shaking at 130 rpm. The precultures were used to inoculate fresh medium, supplemented with the respective antibiotics, to an OD_{600} of 0.05. After the main cultures were grown to an OD_{600} of 0.6 at 37 °C, the incubation temperature was reduced to 20 °C and the cells were supplemented with 0.5 mM isopropyl β-D-1-thiogalactopyranoside (IPTG) to induce the expression of the target protein. After incubation of 16-18 h at 20 °C, the cells were harvested at 6774 *g* and 10 °C for 10 min. The cell pellet was either directly used for protein purification or shock frozen in liquid nitrogen (LN_2) and stored at -80 °C until usage.

Table 5: Recombinant protein expression conditions.

Protein	Plasmid	Bacterial strain	Medium[#]
His_6-SUMO-PA1358	pETSUMO_*PA1358*	Rosetta (DE3)pLysS	TB
His_6-PA1359-CTD[¥]	pET19m_*PA1359*-CTD	Rosetta 2(DE3)	TB
His_6-SUMO-PA1672	pETSUMO_*PA1672*	Rosetta (DE3)pLysS	TB
His_6-PA2721	pET19m_*PA2721*	Rosetta (DE3)pLysS	TB
His_6-PA2722	pET19m_*PA2722*	Rosetta 2(DE3)	TB
His_6-PA2723	pET19m_*PA2723*	BL21 (DE3)	LB
His_6-PA4183$^{16-155}$	pET19m_*PA4183*$^{16-155}$	BL21 (DE3)	TB

[¥]CTD: C-terminal domain. [#]TB: terrific broth; LB: lysogeny broth.

3.2.2.2 Expression of selenomethionine-labelled protein

For experimental phasing of PA4183$^{16-155}$ the two MET residues of the protein were replaced with selenomethionine (SEM). The pET19m_*PA4183*$^{16-155}$ plasmid was transformed into BL21 (DE3) cells. A single colony of the transformed cells was used to inoculate 100 ml LB medium. The preculture was incubated overnight at 37 °C under vigorous shaking (130 rpm) before cells were harvested and resuspended in 100 ml prewarmed M9-minimal medium. The cells were incubated for 1 h at 37 °C under vigorous shaking, while M9-minimal medium for the main culture was prewarmed to 37 °C and aerated under vigorous shaking (130 rpm). The main culture was inoculated to an OD_{600} of 0.05 and grown at 37 °C until the OD_{600} reached 0.5. Then the amino acid mix (0.1 g/l Lys, Phe, Thr, 0.05 g/l Ile, Leu, Val) was added to inhibit the natural methionine biosynthesis while the incubation temperature was lowered to 20 °C. After 30 min of further incubation, 60 mg/l L-selenomethionine and 0.5 mM IPTG were added to induce protein expression. After 16 h of incubation at 20 °C under vigorous

shaking (130 rpm), the cells were harvested at 6774 *g* and 10 °C for 10 min. The cell pellet was directly used for protein purification (3.2.3).

3.2.3 Protein purification

All proteins in this study were purified at 4-10 °C using the ÄKTA purifier FPLC-system (GE Healthcare) for all chromatography steps described below. The untagged and unlabelled protein PA4183$^{16\text{-}155}$ was purified by Allegra Vit in a previous study (Vit, 2015). PA4518 used in this study was purified by Vanessa Hering according to the protocol described by Vit, 2015. The purification of PA1672 and PA2721 was described before (Nocek *et al.*, 2006; Vit, 2015; Weber, 2011). Purification of the other proteins (PA2722, PA2723, PA1359-CTD) was described first in this study.

3.2.3.1 Cell disruption

Bacterial cell pellets (3.2.2) were resuspended in buffer A containing BME (2 mM), $MgSO_4$ (2 mM), DNase (0.8 mg/l, Roche Life Science) and a cOmplete™ mini EDTA-free protease inhibitor cocktail tablet (Roche Life Science). Cells were disrupted with an Emulsiflex-C3 homogenizer (Avestin) or by sonification (Bandelin Electronic™ SONOPLUS HD3200) at 4 °C and centrifuged at 37000 *g* for 45 min at 4°C to remove insoluble cell debris, while the supernatant was used to isolate the target protein (3.2.3.2).

3.2.3.2 Ni^{2+}-immobilized metal ion affinity chromatography (Ni^{2+}-IMAC)

Since all proteins were expressed with a His_6-tag, the first purification step was a Ni^{2+}-IMAC. The supernatant of the cell lysate (3.2.3.1) was loaded onto a 5 ml HisTrap™ HP column (GE Healthcare Life Sciences) charged with Ni^{2+} to separate the tagged protein of interest (POI) from *E. coli* proteins. The column was washed with buffer A and 2 % of buffer B to elute unspecifically bound proteins. The His_6-tagged protein was eluted with an imidazole gradient from 2-50 % buffer B in 2 ml fractions. The total protein amount was monitored by recording the absorption at 280 nm (A_{280}) to analyze the purification process. The protein-containing fractions were analyzed by SDS-PAGE (3.2.3.6). Fractions that contained the POI were united for dialysis and protease cleavage if required (3.2.3.3).

After protease cleavage, a second Ni^{2+}-IMAC was performed to remove the His_6-tag, the protease and undigested protein. The Ni^{2+}-charged HisTrap™ HP column (GE Healthcare Life Sciences) was equilibrated with SEC buffer before loading the protein sample. The protein was collected in 2 ml fractions and analyzed by SDS-PAGE (3.2.3.6). The fractions containing the isolated target protein were combined, concentrated by ultrafiltration with Vivaspin® centrifugal concentrators (PES membrane with 3 or 10 kDa MWCO, Sartorius AG, Göttingen) and used for size exclusion chromatography (3.2.3.5).

3.2.3.3 Dialysis and protease cleavage

The combined fractions from the Ni^{2+}-IMAC were dialyzed in SnakeSkin™ dialysis membrane with a 3.5 kDa cutoff (Thermo Scientific) to remove the imidazole. The dialysis was performed overnight at 4 °C under stirring conditions against a buffer volume that was 50x exceeding the volume in the dialysis membrane. Since the His_6-tagged version of $PA4183^{16-155}$ was not pure after Ni^{2+}-IMAC it was dialyzed against a low salt buffer to prepare it for anion exchange chromatography (AIEX, 3.2.3.4). The other proteins were dialyzed against SEC buffer. To remove the purification tags during dialysis, the POI was incubated with the respective protease and the buffer was supplemented with a reducing agent (Table 6). After dialysis the protein was further purified by AIEX (3.2.3.4), size exclusion chromatography (3.2.3.5) or a second Ni^{2+}-IMAC (3.2.3.2).

Table 6: Protease cleavage conditions of expressed proteins to yield the final protein after cleavage. ¥

Expressed protein	MW [kDa]	ε_{280} [M^{-1} cm^{-1}]	Reducing agent	Protease#	Final protein	MW [kDa]	ε_{280} [M^{-1} cm^{-1}]
His_6-SUMO-PA1358	28.28	18450	1 mM DTT	SUMO	PA1358	14.84	15470
His_6-PA1359-CTD	14.44	27960	4 mM BME	TEV	PA1359-CTD	12.87	26470
His_6-SUMO-PA1672	26.89	7450	1 mM DTT	SUMO	PA1672	13.55	4470
His_6-PA2721	19.43	33460	2 mM DTT	TEV	PA2721	17.55	31970
His_6-PA2722	16.71	18450	4 mM BME	TEV	PA2722	14.84	16960
His_6-PA2723	12.41	12950	4 mM BME	TEV	PA2723	10.54	11460
His_6-$PA4183^{16-155}$ MSE	17.46	11460	4 mM BME	TEV	$PA4183^{16-155}$ MSE	15.58	9970
His_6-$PA4183^{16-155}$	17.46	11460	-	-	His_6-$PA4183^{16-155}$	17.46	11460
His_6-PA4518	17.22	32430	4 mM BME	TEV	PA4518	15.35	30940

¥The molecular weight (MW) and the extinction coefficient at A_{280} (ε_{280}) were calculated with the ExPASy program ProtParam (Gasteiger *et al.*, 2005). #Proteases were applied to the cleavage reaction in molar ratios of 1:100 protein to SUMO- and 1:25 protein to TEV-protease.

3.2.3.4 Ion exchange chromatography (IEX)

Ion exchange chromatography (IEX) was performed to separate proteins by their total charge. This was required for His_6-PA4183$^{16-155}$, as it was not pure after Ni^{2+}-IMAC. The theoretical isoelectric point (pI) of His_6-PA4183$^{16-155}$ is 5.8 according to ProtParam (Gasteiger *et al.*, 2005), such that the protein is negatively charged at pH 8. Therefore, an anion exchange chromatography (AIEX) was performed with a 5 ml HiTrap™ Q HP column (GE Healthcare, Munich). The protein in low salt buffer (3.2.3.3) was loaded on the column that was equilibrated with the same buffer. The column was washed with low salt buffer to remove unspecific proteins, before the target protein was eluted with a flat NaCl gradient by increasing the concentration of the high salt buffer (20 mM Tris/HCl pH 8, 1 M NaCl) from 0 to 50 %. The eluate was collected in 2 ml fractions, while the elution of the protein was visualized by monitoring the change in A_{280}. The protein-containing fractions were analyzed by SDS-PAGE (3.2.3.6) and pure target protein fractions were combined and concentrated by ultrafiltration with Vivaspin® centrifugal concentrators (PES membrane with 3 or 10 kDa MWCO, Sartorius AG, Göttingen) for size exclusion chromatography (3.2.3.5).

3.2.3.5 Preparative size exclusion chromatography

The final purification step was size exclusion chromatography (SEC) to separate aggregates, oligomerization states and further impurities. Depending on the amount of protein, the protein solutions were either loaded onto a HiLoad™ 75 16/600 Superdex™ pg or onto a HiLoad™ 75 26/600 Superdex™ pg (GE Healthcare, Munich) column equilibrated with the respective SEC buffer (Table 7). The final purity of the protein fractions (1-2 ml) was analyzed by SDS-PAGE (3.2.3.6). The pure and homogenous protein fractions were combined, concentrated by ultrafiltration with Vivaspin® centrifugal concentrators (PES membrane with 3 or 10 kDa MWCO, Sartorius AG, Göttingen), flash frozen in LN_2 and stored at -80 °C. A summary of the protein purification steps, storage buffers and the final yields is displayed in Table 7. The identity of the proteins was confirmed by mass spectrometry (MS) (3.2.4.6).

Table 7: Protein purification summary.

Final protein	Purification steps[#]	Storage buffer	Yield[¥] (mg/l)
PA1358	1st Ni, 2nd Ni, SEC	SEC	16
PA1359-CTD	1st Ni, 2nd Ni, SEC	SEC	24
PA1672	1st Ni, 2nd Ni, SEC	SEC	20
PA2721	1st Ni, 2nd Ni, SEC	SEC	21
PA2722	1st Ni, 2nd Ni, SEC	SEC	11
PA2723	1st Ni, 2nd Ni, SEC	SEC	8
SEM-PA4183$^{16-155}$	1st Ni, 2nd Ni, SEC	SEC, 2 mM DTT	19
His_6-PA4183$^{16-155}$	1st Ni, AIEX, SEC	SEC	15

[#]Ni: Ni^{2+}-IMAC, SEC: size exclusion chromatography, AIEX: aion exchange chromatography. [¥]The yield refers to the amount of protein in mg after SEC that was purified from 1 l of cell culture.

3.2.3.6 SDS-PAGE

SDS-PAGE was performed to identify and characterize the purity of the POI (Laemmli, 1970). Protein samples were mixed with SDS-loading buffer (5x), denatured for 5 min at 95 °C and electrophoretically separated by their size on polyacrylamide gels (stacking gel: 5 % acrylamide, resolving gel: 15 or 18 % acrylamide) in SDS running buffer (1x). Proteins were visualized with InstantBlue™ protein staining solution (expedeon, Cambridge).

3.2.3.7 Determination of protein concentrations

Protein concentrations were determined at the NanoDrop™ 2000 spectrophotometer (Thermo Scientific) by measuring the UV absorption at a wavelength of 280 nm (A_{280}) based on Lambert-Beer's law (1). Based on the protein sequence, the MW and ε_{280} (Table 6) were calculated with the ExPASy program ProtParam (Gasteiger *et al.*, 2005).

$$A_{280} = c \cdot d \cdot \varepsilon_{280} \quad (1)$$

A_{280} – UV absorption at a wavelength of 280 nm, c – protein concentration (M), d – path length (cm), ε_{280} – extinction coefficient at A_{280} (M^{-1} cm^{-1})

3.2.4 Biochemical methods

3.2.4.1 Dynamic light scattering (DLS)

The oligomerization state of proteins was determined with dynamic light scattering (DLS) experiments using a DynaPro Titan DLS device (Wyatt Technology Corp.). The solutions of PA2722 (1 mg/ml), PA2723 (1 mg/ml), PA4183$^{16-155}$ (2 mg/ml) and PA1359-CTD (2 mg/ml) in

SEC buffer were centrifuged at 17000 *g* at 4 °C for 15 min prior to the measurements. Intensities of the scattered light were collected 100 times for 20 s at 25 °C. The DYNAMICS program (Wyatt Technology Corp.) calculated the MW of each protein.

3.2.4.2 Analytical size exclusion chromatography

Analytical SEC was used as another method to identify the oligomerization state of proteins. The MW of proteins can be derived from a calibration curve, which is obtained by plotting the partition coefficients (K_{av}) of known calibration standard proteins against the logarithm of their molecular weight. The K_{av} can be calculated after equation (2).

$$K_{av} = \frac{(V_e - V_0)}{(V_c - V_0)} \quad (2)$$

K_{av} – partition coefficient, V_e – elution volume, V_0 – void volume, V_c – column volume

The Superdex™ 75 10/300 GL column (V_c: 24 ml, GE Healthcare) was equilibrated with SEC buffer before the samples were loaded onto the column. The elution volume V_e of all proteins was determined at the peak absorption monitored at A_{280}. The calibration standard from the LMW Gel Filtration Calibration Kit (GE Healthcare), which contained aprotinin, ribonuclease A, carbonic anhydrase and conalbumin (100 µl 3 mg/ml each), was applied onto the column. The void volume V_0 was determined with Blue Dextran 2000 (100 µl, 1 mg/ml). The V_e of PA2723 (100 µl, 300 µM) was determined to identify its oligomerization state. To identify a possible complex formation between PA1358 and PA1359-CTD, an equimolar mixture of both proteins (100 µl, 100:100 µM) was incubated for 10 min at RT and loaded onto the column. As reference, two independent runs with PA1358 and PA1359-CTD (100 µl, 100 µM) were performed.

3.2.4.3 Thermal shift assay (TSA)

Fluorescence-based thermal shift assays (TSA) were performed to characterize the melting temperature (T_m) of proteins. The technique was mainly applied to screen for molecules that cause a shift in thermal stability upon protein binding. The principle of TSA is based on a fluorescent SYPRO™ Orange dye (Invitrogen) whose fluorescence is quenched in aqueous solutions. Upon temperature dependent protein denaturation, hydrophobic patches of the protein core are exposed, generating a nonpolar environment in which the fluorescence of the

dye is enhanced. Therefore, the increase in fluorescence serves as measure for protein unfolding. By plotting the fluorescence intensity against the temperature, a sigmoidal curve is obtained before the signal decreases again, caused by protein precipitation and aggregation (Figure 10 A). The T_m at the inflection point of this unfolding curve is defined as 50 % of denatured protein. It can be calculated by fitting the non-linear part of the sigmoidal curve with the Boltzmann equation (Niesen *et al.*, 2007; Huynh & Partch, 2015, Figure 10 A):

$$y = I_{min} + \frac{(I_{min} - I_{max})}{1 + exp\left(\frac{T_m - x}{a}\right)} \quad (3)$$

y – fluorescence intensity, x – temperature, a – slope, I_{min} and I_{max} – minimum and maximum fluorescence intensity, T_m – melting temperature

Alternatively the T_m can be derived from the minimum of the first derivative of the fluorescence emission as a function of the temperature (-dF/dT) (Niesen *et al.*, 2007; Huynh & Partch, 2015) (Figure 10 B).

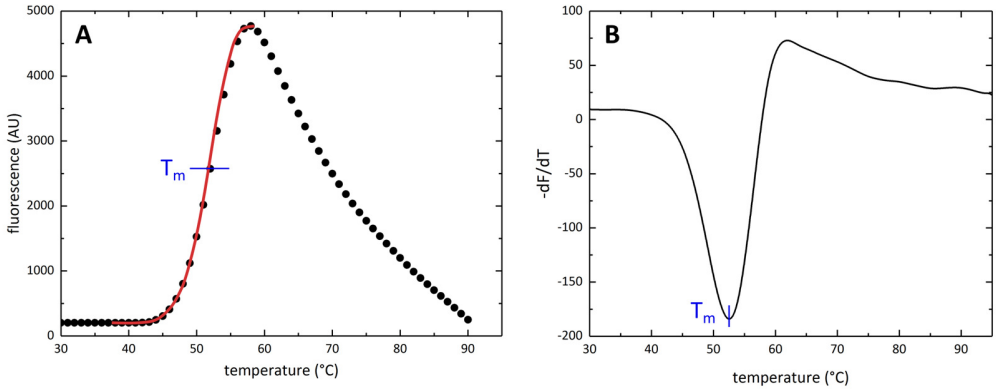

Figure 10: Determination of the protein melting temperature (T_m) by a thermal shift assay (TSA). A) Fluorescence emission upon protein unfolding. T_m is determined at the inflection point of the unfolding transition by non-linear fitting (red line) of the sigmoidal part of the unfolding curve with the Boltzmann equation (3). B) T_m determination at the minimum of the first derivative of the fluorescence emission as a function of the temperature (-dF/dT) (Huynh & Partch, 2015).

The assay was performed in a CFX96 real time PCR system connected to a C1000 thermal cycler (Bio-Rad Laboratories, Inc., Hercules, CA, USA). The solutions were pipetted in a 96-well PCR Multiplate™ (Bio-Rad) and sealed with optically clear sealing film (Bio-Rad). A temperature was applied from 4 to 95 °C, with increments of 1 K, with 15 s hold at each temperature, while the fluorescence signal was monitored (excitation: 492 nm, emission: 610 nm). T_m-values were calculated with the CFX Manager™ 2.0 software (Bio-Rad). TSA to determine the thermal stability of proteins were set up with SYPRO™ Orange (50x, 5 µl), the respective

protein (2 mg/ml, 5 µl) and SEC buffer (40 µl). The TSA compound screens were set up with SYPRO™ Orange (50x, 5 µl), the respective protein (2 mg/ml, 5 µl), buffer (35 µl) and the respective compound (Table 8, 5 µl). The measurement of chlorpromazine and promethazine with PA1672 was performed in 50 mM HEPES pH 7, 150 mM NaCl. All other experiments were conducted in SEC buffer. Control samples contained no ligands but the same buffer and DMSO concentration (Table 8). Three independent experiments were performed for each condition.

Table 8: Final compound and DMSO concentrations in TSA compound screens.

Compound	c[compound] (µM)	c[DMSO] (% (v/v))	Protein*
2-nitroimidazole	130	1	PA1672
2-phenylpenol	130	1	PA1358, PA1672, PA4183$^{16-155}$
8-hydroxyquinoline	130	1	PA1672, PA2721
Acetic acid	150	-	PA1672
Adenosine	150	-	PA1672
Azlocillin	130	-	PA1358, PA1672, PA4183$^{16-155}$, PA4518
Captan	100	2.5	PA2721
$CdCl_2$	130	-	PA2721
Cefsoludin	130	-	PA1672
Chlorodinitrobenzene	130	1	PA1672, PA2721, PA4183$^{16-155}$, PA4518
Chloroxylenol	130	1	PA1358, PA1672, PA4183$^{16-155}$, PA4518
Chlorpromazine	150	-	PA1672
$CoCl_2$	130	-	PA2721
Dichlofluanid	100, 130, 130	2.5, 1, 1	PA2721, PA1672, PA4518
Domiphen bromide	120	-	PA2721
Enoxacin	130	1	PA1358, PA1672, PA4183$^{16-155}$
Gallic acid	120	1	PA2721
Glycerol	150	-	PA1672
L-Arginine	150	-	PA1672
L-Aspartic acid	150	-	PA1672
Lauryl sulfobetaine	130	-	PA1358, PA1672
L-Lactic acid	150	-	PA1672
L-Valine	150	-	PA1672
Malonic acid	150	-	PA1672
Sodium caprylate	130	-	PA1672
Nafcillin	130	-	PA1672, PA4183$^{16-155}$
Oxacillin	130	-	PA1358
Patulin	120	1	PA2721
Procaine	130	-	PA1672
Proflavin	130	-	PA2721
Promethazine	150	-	PA1672
Semicarbazide HCl	130	-	PA1672, PA2721
Succinic acid	150	-	PA1672
Sulfanilamide	130	1	PA1672
Tobramycin	130	-	PA1358, PA1672, PA4183$^{16-155}$, PA4518

* Final protein concentrations: PA1358: 13.4 µM, PA1672: 14.8 µM, PA2721: 11.2 µM, PA4183$^{16-155}$: 12.8 µM PA4518: 13 µM

3.2.4.4 Microscale thermophoresis (MST)

3.2.4.4.1 Principles of MST

Thermophoresis describes the movement of particles in a temperature gradient. It is used to determine the interaction of molecules, because the movement in the temperature gradient is dependent on different properties of the molecules, such as the hydration shell, size or charge. These properties vary between the bound and the unbound state of a protein, which leads to an altered movement in the temperature gradient (Figure 11 B/C, Jerabek-Willemsen *et al.*, 2014). Figure 11 A/B shows the experimental set up of a microscale thermophoresis (MST) experiment in which up to 16 capillaries are filled with a serial dilution of the ligand and a constant concentration of the labelled molecule. The fluorescence of the labelled molecule is detected, while an infrared (IR) laser induces a local temperature gradient. Changes in fluorescence are recorded as a measure of the molecule movement and plotted against the time (Figure 11 B). The thermophoresis of the fluorescent molecule changes upon ligand binding, which results in altered time traces. The experiment is evaluated by plotting the change in normalized fluorescence (ΔF_{norm}) against the ligand concentration. ΔF_{norm} is defined as 1000x F_{cold}/F_{hot} (Figure 11 C). F_{cold} is an average value of the initial fluorescence measured between defined areas. F_{hot} corresponds to an average value of the fluorescence after the steady state is established in the temperature gradient measured between defined areas. By plotting ΔF_{norm} against the ligand concentration a sigmoidal binding curve is obtained that can be fitted to derive the binding constant (K_D) based on the law of mass action in equation (4) (Figure 11 D).

$$f(c) = U + \frac{(B - U) \cdot (c_{lig} + c_{prot} + K_D - \sqrt{(c_{lig} + c_{prot} + K_D)^2 - 4 \cdot c_{lig} \cdot c_{prot}}}{2 \cdot c_{prot}} \quad (4)$$

U – response value of the unbound state, B – response value of the bound state, c_{prot} – concentration of the fluorescent molecule, c_{lig} – concentration of the titrated ligand, K_D – dissociation constant

Response curves for a cooperative binding event were fitted with the Hill-equation (5). The *EC50* describes the effective ligand concentration that gives 50 % of the maximum response. The Hill coefficient depends on the steepness of the curve and is a measure for the cooperativity.

$$f(c) = U + \frac{B - U}{1 + \left(\frac{EC50}{c_{lig}}\right)^{Hill\ coefficient}} \quad (5)$$

U – response value of the unbound state, B – response value of the bound state, c_{lig} – concentration of the titrated ligand

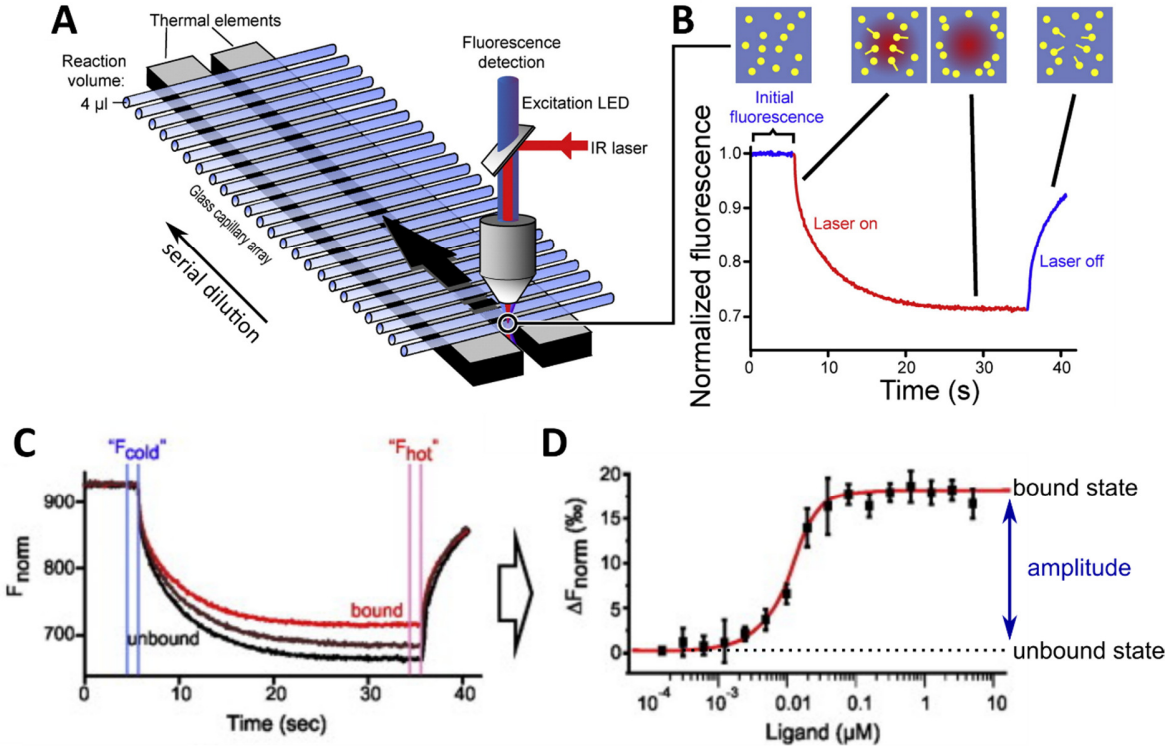

Figure 11: Principles of MST. Figures A/B are reprinted from Alexander *et al.*, 2014, Copyright (2014), with permission from Elsevier B.V. Figures C/D are reprinted from Jerabek-Willemsen *et al.*, 2014. A) MST experimental set up. Capillaries are filled with a serial dilution of the potential binding partner and a fixed concentration of the fluorescent protein. The IR-laser creates a local temperature gradient. The movement of the fluorophore in the gradient is followed by measuring the emittance of the fluorophore after its excitation. B) The movement of the fluorescent molecule (yellow dots) is detected over time until a steady state is reached. C) Altered thermophoretic movement of molecules upon ligand binding. F_{cold} and F_{hot} correspond to the average values measured between the areas that are defined by the blue respective red lines. D) Response curve which can be fitted to obtain the K_D- or EC50- value after equation 4 or 5. (Jerabek-Willemsen *et al.*, 2011, 2014; Seidel *et al.*, 2012).

Initial fluorescence for K_D determination

Besides using thermophoresis as a measure for ligand binding, in some cases the initial fluorescence signal can be used directly for K_D determination. This is possible if the ligand specifically quenches or enhances the signal of the fluorescent dye, which might be caused by changing the electrostatic surrounding of the dye (Jerabek-Willemsen *et al.*, 2011). In this case the initial fluorescence signal can be plotted against the ligand concentration. The obtained binding curve can be fitted with equation (4) for K_D determination.

To make sure that the fluorescence change is caused by specific protein-ligand binding and not by an unspecific interaction between the dye and the protein or by a loss of the fluorescent molecule due to aggregation, a SDS denaturation (SD)-test has to be performed. In this test, the difference in fluorescence of the labelled molecule in bound form (with a high ligand concentration) and in unbound form (with a low or zero ligand concentration) is compared to the fluorescence of the denatured labelled molecule with a high and a low ligand concentration. If the change in fluorescence is caused by the binding event, the fluorescence intensities of the bound and unbound sample should be the same after the protein is denatured. If the change in fluorescence has other reasons, the difference in fluorescence intensity remains after denaturation.

3.2.4.4.2 Experimental set up

MST experiments were performed with a NanoTemper Monolith NT.115 (NanoTemper Technologies, Munich, Germany) at 20 °C using the standard glass capillaries and evaluated with the MO.Affinity Analysis software v2.15 (NanoTemper Technologies GmbH). Proteins with primary amines (PA1672, PA2721, PA2722 and PA4518) were labeled with Amersham™-Cy™5 Mono NHS Ester dye (GE Healthcare) according to the manual of the Monolith Protein Labeling Kit RED-NHS (NanoTemper Technologies GmbH). In the case of $PA4183^{16-155}$, the His_6-tagged protein was labelled with the Monolith His-Tag Labeling Kit RED-tris-NTA (NanoTemper Technologies).

MST screens were performed to identify possible binding partners. Two capillaries were filled with the same sample, containing the protein (Table 9) and a high concentration of ligand (>1 mM) to ensure that the protein is saturated in case of binding (bound state). Two other capillaries were filled with the protein in identical buffer but without the ligand as a reference (unbound state). ΔF_{norm} was measured and the amplitude between the reference (unbound state) and the sample containing the ligand (bound state) was determined (Figure 11 D). Labelled PA1672 was excited with 20 % LED-power, while the other fluorescent molecules were excited with 30 % LED-power.

Table 9: Reaction conditions for screening of potential binding partners by MST.

Ligands	c[ligand] (mM)	c[DMSO] (% (v/v))
PA1672		
100 nM NHS-labelled in SEC buffer, 0.5 mg/ml BSA		
nafcillin, azlocillin, procaine	4	-
tobramycin, lauryl sulfobetaine	1	-
dichlofluanid	1	25
chloroxylenol	1.5	10
8-hydroxyquinoline	1.7	10
gallic acid	1	2.5
PA2721		
100 nM NHS-labelled in SEC buffer, 0.5 mg/ml BSA		
patulin	4	10
8-hydroxyquinoline	3.4	10
gallic acid	1	2.5
dichlofluanid, captan	1	25
PA4518		
100 nM NHS-labelled in SEC buffer, 0.5 mg/ml BSA		
dichlofluanid	1	25
His_6-PA4183		
50 nM His-labelled in SEC buffer		
cholin, DMG, sarcosine, glyphosate, betaine aldehyde, GB, GLY, SER, pyruvate, tobramycin, nafcillin, azlocillin	5	-
Tetrahydrofolate (THF)	2.3	50
enoxacin, chloroxylenol, chlorodinitrobenzene, 2-phenylphenol	2.5	25

Actual MST experiments were performed to determine the binding constant of potential ligands. For this purpose, the ligands were titrated in 1:1 serial dilutions against the proteins (Table 10). Serial dilutions of ligands that were soluble in aqueous solutions were prepared with the respective buffers (Table 10). Other ligands were dissolved in 100 % (v/v) DMSO. Serial dilutions were prepared in 100 % (v/v) DMSO and then diluted in the respective reaction buffers to reach the final concentrations given in Table 10. The mixtures were incubated for 10 min before they were transferred into the capillaries. All reactions were performed with 20 and 40 % MST power. LED power for fluorescence excitation was 20 % for labelled PA1672 and 30 % for the other proteins.

Table 10: Final conditions for MST experiments.

Ligands	c[ligand] (mM)*	c[DMSO] (% (v/v))
PA1672		
100 nM NHS-labelled in SEC buffer, 0.5 mg/ml BSA		
nafcillin, procaine	1	-
chloroxylenol	2	20
8-hydroxyquinoline	1	10
gallic acid	1	2.5
PA2721		
100 nM NHS-labelled in SEC buffer, 0.5 mg/ml BSA		
patulin	4	10
8-hydroxyquinoline	3.4	10
gallic acid	1	2.5
dichlofluanid, captan	1	25, 10
$CdCl_3$, $CoCl_2$	1	-
PA2721		
200 nM NHS-labelled in 50 mM Tris/HCl. pH 7.4, 150 mM NaCl, 0.5 mg/ml BSA		
N-benzyloxycarbonyl-L-proline	0.05 & 5	10
PA2722		
250 nM NHS-labelled in SEC buffer, 0.05 % (v/v) Tween20		
GSH	2	-
Formaldehyde	1 & 10	-
PA4518		
100 nM NHS-labelled in SEC buffer, 0.5 mg/ml BSA		
dichlofluanid	1	25
His_6-PA4183		
50 nM His-labelled in SEC buffer		
cholin, glyphosate, GLY, SER, tobramycin	1	-
sarcosine	1 & 25	-
2-phenylphenol	1	10
enoxacin	1 & 50	10 & 50

*c[ligand] (mM): highest ligand concentration of the dilution series

During MST-screening with chlorpromazine and promethazine, the fluorescence intensity of NHS-labelled PA1672 was significantly quenched. An SD-test was performed to find out if the quenching is specifically caused by the ligands binding to the protein. The labelled protein was mixed with 0, 1 and 20 mM of both compounds in HEPES pH 7, 150 mM NaCl, 0.5 mg/ml BSA. For each concentration, two independent mixtures were centrifuged for 10 min at 17000 *g* to remove precipitated protein and mixed 1:1 with 2x SD-mix (4 % SDS, 40 mM DTT) and denatured at 95 °C for 5 min. The fluorescence signal was detected after excitation with 40 % LED-power. The fluorescence signal was restored for the mixture containing 1 mM lig-

and, the fluorescence difference persisted in the mixture containing 20 mM ligand. This indicated that the fluorescence is specifically quenched upon ligand binding to the protein but only until a certain ligand concentration is exceeded. To identify the critical concentration at which promethazine and chlorpromazine start to interact unspecifically with the dye, a measurement was conducted that contained 100 nM free dye titrated against both ligands in a 1:1 dilution series with a highest concentration of 20 mM. For this, a buffer without BSA (125 mM HEPES, pH 7, 150 mM NaCl) was used to prevent the reaction of the free dye with the primary amines of BSA. For determining the binding constant of chlorpromazine and promethazine, three independent measurements were conducted. The ligands were titrated in a 1:1 dilution series (highest concentration: 20 mM) against 300 nM of the NHS-labelled PA1672 in 125 mM HEPES, pH 7, 150 mM NaCl, 0.5 mg/ml BSA. The fluorescence was excited with 40 % LED-power at a temperature of 25 °C.

3.2.4.5 Isothermal titration calorimetry (ITC)

3.2.4.5.1 Principles of ITC

Isothermal titration calorimetry (ITC) is a method to characterize interactions between molecules by detecting changes in enthalpy that occur during formation of complexes such as between two proteins or between small molecules and proteins. An ITC calorimeter contains a reference cell filled with water and the sample cell in an adiabatic jacket (Figure 12 A). The sample cell is filled with the macromolecule in the desired buffer, while its interaction partner (titrant) is filled in a syringe in the same buffer and titrated into the sample chamber under constant stirring. The reference and sample cells are connected to heaters that establish the desired reaction temperature. A sensor connecting both chambers detects if heat is generated (exothermal binding) or absorbed (endothermal binding) upon interaction of the titrant and the macromolecule. The heat change in the sample cell is compensated by the heaters through applying the necessary differential thermal power (DP in µcal/sec) until the temperature balance is restored. The DP is measured throughout the titration experiment, in which the protein is increasingly saturated as the molar ratio between the protein and the titrant is gradually elevated. When the saturation increases, less binding events occur.

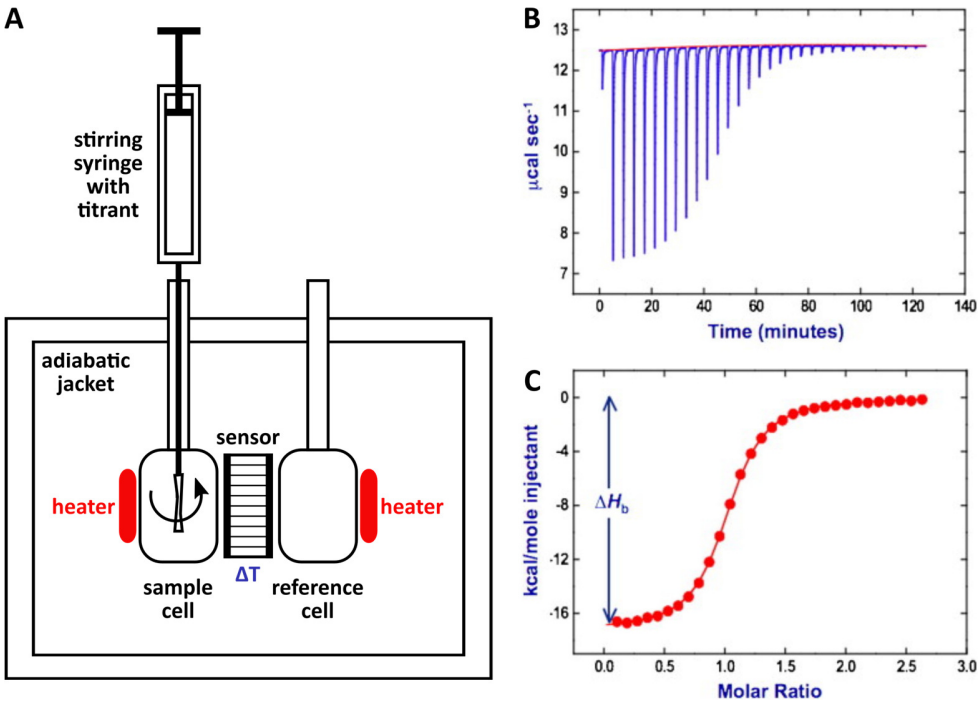

Figure 12: Principles of isothermal titration calorimetry (ITC). A) Schematic representation of an isothermal titration calorimeter. It consists of an adiabatic jacket that encloses the reference cell, filled with water and the sample cell, filled with the macromolecule. A syringe is filled with the ligand and titrated to the sample under constant stirring. The heat change (ΔT) between sample and reference cell, upon a binding event is detected by a sensor. The sensor gives feedback to a heater that compensates the heat change by applying a certain differential power (DP). B) ITC raw data. The DP in µcal sec^{-1} that is necessary to keep the cells at equal temperatures is plotted over time. C) Evaluation of ITC data. The integral of the DP (kcal/mole injectant) is plotted against the molar ratio of titrant and macromolecule. By fitting the experimental sigmoidal curve, the association constant K_a and the stoichiometry n can be derived from the inflection point and the enthalpy ΔH (kcal/mol) corresponds to the amplitude. B) and C) are reprinted from Buurma & Haq, 2007, Copyright (2007), with permission from Elsevier Inc.

Therefore, the DP decreases until the protein is saturated (Figure 12 B). The DP is integrated and plotted against the molar ratio between the titrant and the protein (Figure 12 C), which gives a sigmoidal curve. The association constant K_a and the stoichiometry *n* can be derived from the inflection point of the curve and the enthalpy ΔH (kcal/mol) corresponds to the amplitude. The entropy ΔS (kcal/mol) can be calculated after equation (6).

$$\Delta G = -RT \cdot \ln K_a = \Delta H - T \cdot \Delta S \qquad (6)$$

ΔG – Gibbs free energy (kcal/mol), R – ideal gas constant (8.3144598 J/(mol·K)), K_a – *association constant,* ΔH – enthalpy (kcal/mol), T – temperature (K), ΔS – entropy (kcal/mol)

To derive reliable thermodynamic data from the ITC curve it is important to utilize appropriate concentrations of the binding partners. They can be determined by calculating the C-value (equation (7)) that ideally ranges between 10 and 1000 (Buurma & Haq, 2007; Jelesarov & Bosshard, 1999).

$$C = \frac{c_{prot}}{K_D} \quad (7)$$

c_{prot} – protein concentration, K_D – dissociation constant (K_a^{-1})

3.2.4.5.2 Experimental set up

ITC experiments were performed with a MicroCal™ VP-ITC System (GE Healthcare). Titration experiments were performed at 25 °C with a stirring speed of 307 rpm. An ITC experiment was conducted to verify a possible interaction of PA1358 with PA1359-CTD, which were both diluted in SEC buffer. PA1359-CTD was provided in the sample cell at a concentration of 0.1 mM, while 1 mM of PA1358 was injected with a volume of 8 µl at 0.5 µl/s with spacing times of 240 s between injections. The reference power was 10 µCal/s.

The interaction of PA1672 with promethazine and chlorpromazine was also analyzed with ITC. The sample cell was filled with 0.1 mM PA1672 in 50 mM HEPES pH 7, 150 mM NaCl. 2 mM of each compound that was diluted in the identical buffer was injected with a volume of 4 µl at 0.5 µl/s with spacing times of 240 s. The reference power was 3 µCal/s. The buffer reference was measured by titrating the compounds with identical parameters, into the sample cell containing the protein-free buffer. ITC data were analyzed and plotted in Origin® v7.0 (OriginLab, Northampton, MA, USA).

3.2.4.6 Mass spectrometry (MS) analysis

Mass spectrometry (MS) analysis was performed by the staff of the HZI mass analysis facility in the CPRO department. MALDI-TOF experiments of protein bands digested with trypsin, which were isolated from SDS gels after SDS-PAGE (3.2.3.6), were done to approve the identity of the POI. To analyze a potential covalent modification of PA2722 with glutathione, a MALDI analysis with the undigested protein was performed. For this, 10 µl of a 2 mM PA2722 solution in SEC buffer were incubated with 4 mM GSH or GSSG for 30 min at room temperature. The sample was stored overnight in the fridge before the MS measurement was conducted. A control sample that contained no ligands was treated equally.

3.2.5 Microbiological methods

Several microbiological assays were performed to identify the physiological function of the class III βαββββ-proteins. The phenotypes of *P. aeruginosa* strains with transposon insertions in the respective GOI were compared to the wild type (wt) reference strain (Table 3).

3.2.5.1 Planktonic growth assays of *P. aeruginosa*

For planktonic growth assays of the transposon mutants (Table 3) bacteria from glycerol stocks were streaked on LB agar plates supplemented with the respective antibiotics and were incubated overnight at 37 °C. LB media (5 ml) without antibiotics were inoculated and incubated at 37 °C for at least 18 h under vigorous shaking. Fresh LB medium (40 ml) was inoculated with the overnight culture to an OD_{600} of 0.05. The culture was incubated at 37 °C under vigorous shaking while the OD_{600} was measured regularly.

The expression of PA1358 and PA1359 from pHERD30T plasmids in the PA14 wt background, together with an empty vector control, was performed with the respective PA14 strains, listed in Table 3. They were handled as described for the transposon mutants above but the LB medium (50 ml) for the main cultures was supplemented with gentamycin (50 mg/ml). After inoculation, the cultures were incubated for 180 min at 37 °C under vigorous shaking. After 180 min they were split into subcultures (25 ml). Of each culture one subculture was induced with arabinose (0.1 % (w/v)) and one not. All subcultures were further incubated at 37 °C and the OD_{600} was measured regularly.

3.2.5.2 Motility assays

In plate-based assays, the swimming and swarming motility of PAO1 and PA14 transposon insertion mutants were compared with the behavior of the wt and swimming and swarming deficient negative control strains (Table 3). For both assays, the bacteria were streaked from glycerol stocks on LB agar supplied with appropriate antibiotics and incubated overnight. LB medium (5 ml) was inoculated with a single colony and grown overnight at 37°C under vigorous shaking (200 rpm). The next day the overnight bacterial cultures were normalized to an OD_{600} of 1 by dilution with fresh LB medium and subsequently used for the inoculation of the swimming and swarming agar plates.

The swimming assay was performed as described in the protocol "Plate-Based Assay for Swimming Motility in *Pseudomonas aeruginosa*" (Filloux & Ramos, 2014). For this assay, the 0.3 % agar swimming plates were dried under the clean bench for ~ 3h. The inoculated plates were incubated at 37°C for 19 h. The swarming assay was conducted on 0.5 % agar swarming plates according to the protocol "Plate-Based Assay for Swarming Motility in *Pseudomonas aeruginosa*" (Filloux & Ramos, 2014) apart from the following changes. After the plates were dried under the clean bench for 3-4 h, they were inoculated by pipetting 1 µl of the normalized cell culture on the center of the plate. The plates were then incubated at 37°C for 18 h.

3.2.5.3 Phenotype MicroArrays™ (PM)

High-throughput phenotyping of *P. aeruginosa* transposon insertion mutants was performed with the commercially available OmniLog® Phenotype MicroArray™ system (Biolog, Inc., Hayward, CA, USA). It enables to simultaneously monitor and compare phenotypic changes between several strains that were cultured under different conditions. It provides preconfigured 96-well microtiter plates that contain different compounds in dehydrated form. In this study, the PM plates PM1 and PM2 for measuring the respiration activity on different carbon sources and the PM11-20 plates for testing the sensitivity of cells towards different chemicals were used. A reporter system that is based on the redox properties of a tetrazolium dye was used to follow the phenotypic changes. If cell respiration is possible in a condition, NADH is produced. NADH induces the reduction of the tetrazolium salt to a purple formazan dye, whose absorption can be followed over time serving as a reporter for cell respiration (Bochner, 1989, 2009).

Phenotypic changes were studied in *P. aeruginosa* strains carrying transposon insertions in the genes that are coding for class III βαβββ-module proteins PA1358, PA1672, PA2721, PA4183 and PA4518 (Table 3). For PA2721 the PAO1 mutant strain (PAO1 *PA2721*::Tn) was compared with the respective PAO1 wild type as a reference. For all others the PA14 mutants (PA14 *PA1358*::Tn, PA14 *PA1672*::Tn, PA14 *PA4183*::Tn, PA14 *PA4518*::Tn) were compared with the respective PA14 wild type reference. All strains were streaked from frozen glycerol stocks and grown overnight at 37°C on LB agar supplied with appropriate antibiotics. Single bacterial colonies were transferred onto antibiotic-free LB agar plates and grown overnight

at 37°C. Following the manufactures protocol "PM procedures for *E. coli* and other GN bacteria" (Biolog, Inc., Hayward, CA, USA), all cells were suspended in IF-0a minima medium. The cell suspensions were either diluted with IF-0a medium supplemented with dye mix A (PM1 and PM2 plates) or with IF-10a medium plus dye mix A (PM11-20 plates). Each well was inoculated with 100 µl of cell suspension. For achieving the highest possible comparability, same plate types were directly inoculated with cell suspensions of the different strains after each other. The PM plates were incubated in the OmniLog® at 37°C and increasing levels of purple dye were automatically monitored with the OmniLog® PM Software by measuring its absorbance (490 nm) every 15 min over a period of 48 h. The phenomic data were extracted and plotted with the DuctApe software suite (Galardini *et al.*, 2014) by comparing the respiration curve of each mutant with the respective reference. Plates PM1 and PM2 each contained a negative control well. Their absorption was subtracted from the remaining 95 wells. The preparation of cell suspensions and the OmniLog® PM measurements were carried out under assistance of Elisabeth Majer in the department of Prof. Dr. Dietmar Schomburg, who granted access to the OmniLog® PM system at Braunschweig Integrated Centre of Systems Biology (BRICS).

3.2.6 Protein X-ray crystallography

3.2.6.1 Principals of protein X-ray crystallography

X-ray crystallography is a high-resolution technique that indirectly images protein structures at molecular level, which is crucial for understanding their function. To localize the positions of single atoms, distances of at least 0.15 nm (length of a C-C bond) have to be resolved. The optical resolution limit is dependent on the wavelength (λ) used for imaging objects. Two objects can only be distinguished as two separate objects if their distance is at least λ/2. Only the wavelength of X-rays is small enough (10 - 0.01 nm) to achieve this high resolution. The dependence on X-rays raises two major problems. First, lenses are not able to refocus the scattered rays to the image of the sample like in a microscope. The second problem is that only undetectable amounts of X-rays are scattered at a single protein, because X-rays are weakly interacting with organic materials. To circumvent the latter, protein crystals that are

constituted by many systematically ordered proteins are used. The X-rays are diffracted by the sum of electrons in the crystal delivering a detectable diffraction pattern if the waves positively interfere with each other. The distribution of the electrons can be recalculated from the diffraction pattern to create a model of the protein sample (Figure 13) (Rupp, 2009; Rhodes, 2006).

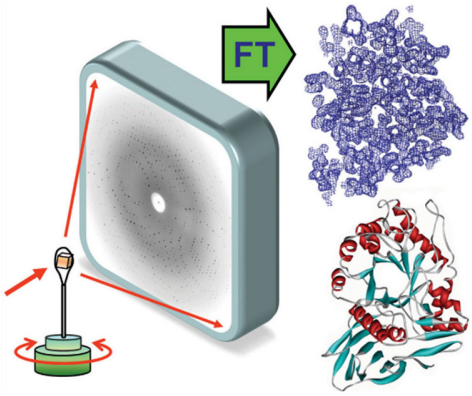

Figure 13: Principles of protein X-ray crystallography. X-rays are scattered on the electrons of the proteins in a crystal. Diffracted X-rays that positively interfere with each other can be detected. The distribution of the electrons in three-dimensional space can be recalculated from the diffraction pattern with a Fourier transform (FT) and used to create a model of the protein sample. The image is reproduced with permission from Biomolecular Crystallography by Bernhard Rupp, © 2009-2014 Garland Science/Taylor & Francis LLC.

3.2.6.1.1 Protein crystallization

During protein crystallization the molecules from an aqueous solution assemble into a periodically arranged crystal lattice, when the solution is brought into supersaturation. In this case the proteins undergo a phase transition that can be illustrated by a typical crystallization phase diagram, which is compartmentalized in four zones (Figure 14 A). In the unsaturated zone the protein is fully dissolved and will not crystalize. In the area of high supersaturation, precipitation occurs. Spontaneous nucleation will take place in the moderate supersaturation zone (nucleation zone). The formation of crystal nuclei is fundamental for crystal growth. The growth takes place in the metastable zone, an area of lower supersaturation, where crystals are stable. The transition from the nucleation to the metastable zone ideally happens as the protein concentration in the solution automatically drops during the assembly of the molecules. To induce the transition from the undersaturated aqueous protein solution into saturation, several methods have been implemented. Only the most widely used vapor diffusion

method (Figure 14 B) will be discussed. Here the protein solution is combined with a precipitant solution, either as hanging or sitting drop and equilibrated against a reservoir that contains a precipitant solution with a higher concentration than in the drop. In the sealed system vapor diffuses from the droplet to the reservoir to compensate the concentration gradient. This way, the concentration of protein and/or precipitants are increased, lowering the solubility of the protein. This might eventually lead to a supersaturated state in the nucleation phase, which can continue in crystal growth until an equilibrium is established. (Chayen, 2004; Chayen & Saridakis, 2008)

Unfortunately, it is unpredictable which precipitants lead to a successful crystallization process, making the screening for the right conditions inevitable. Commercially available 96-well matrix screens that are constituted of different combinations of precipitants including salts, organic solvents, long-chain polymers or organic compounds allow a high-throughput screening to identify initial crystals. One important factor to increase the probability of crystal growth is a highly pure protein solution with a high concentration (~ 20 mg/ml) but below the solubility limit. (McPherson & Gavira, 2013)

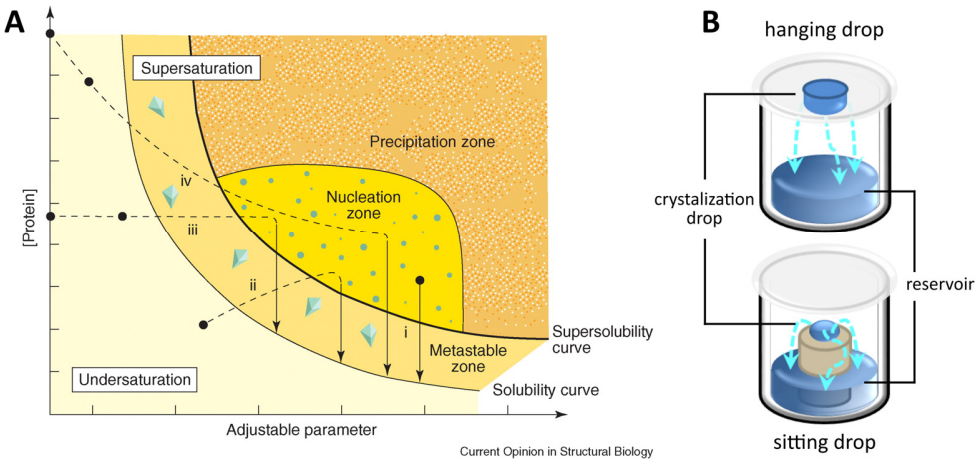

Figure 14: Protein crystallization process. A) Schematic illustration of the protein crystallization phase diagram. Adjustable parameters are the precipitant or additive concentrations, pH and temperature. This diagram represents the path of four crystallization methods: microbatch (i), vapor diffusion (ii), dialysis (iii) and free interface diffusion (iv). Grey dots represent the initial condition. Reprinted from Chayen, 2004, Copyright (2004), with permission from Elsevier Ltd. B) Experimental set up of hanging and sitting drop vapor diffusion methods. Light blue dashed lines indicate water diffusion.

3.2.6.1.2 Diffraction

The diffraction of X-rays results from the interaction of electromagnetic radiation with periodically arranged molecules in the protein crystal. Protein crystals can be described as repetitive assemblies of small building blocks, the so-called unit cell. A unit cell contains the protein that is edged by the unit lattice, which is defined by three vectors **a**, **b** and **c** that come from a common origin 0 and the angles α, β and γ between them (Figure 15A).

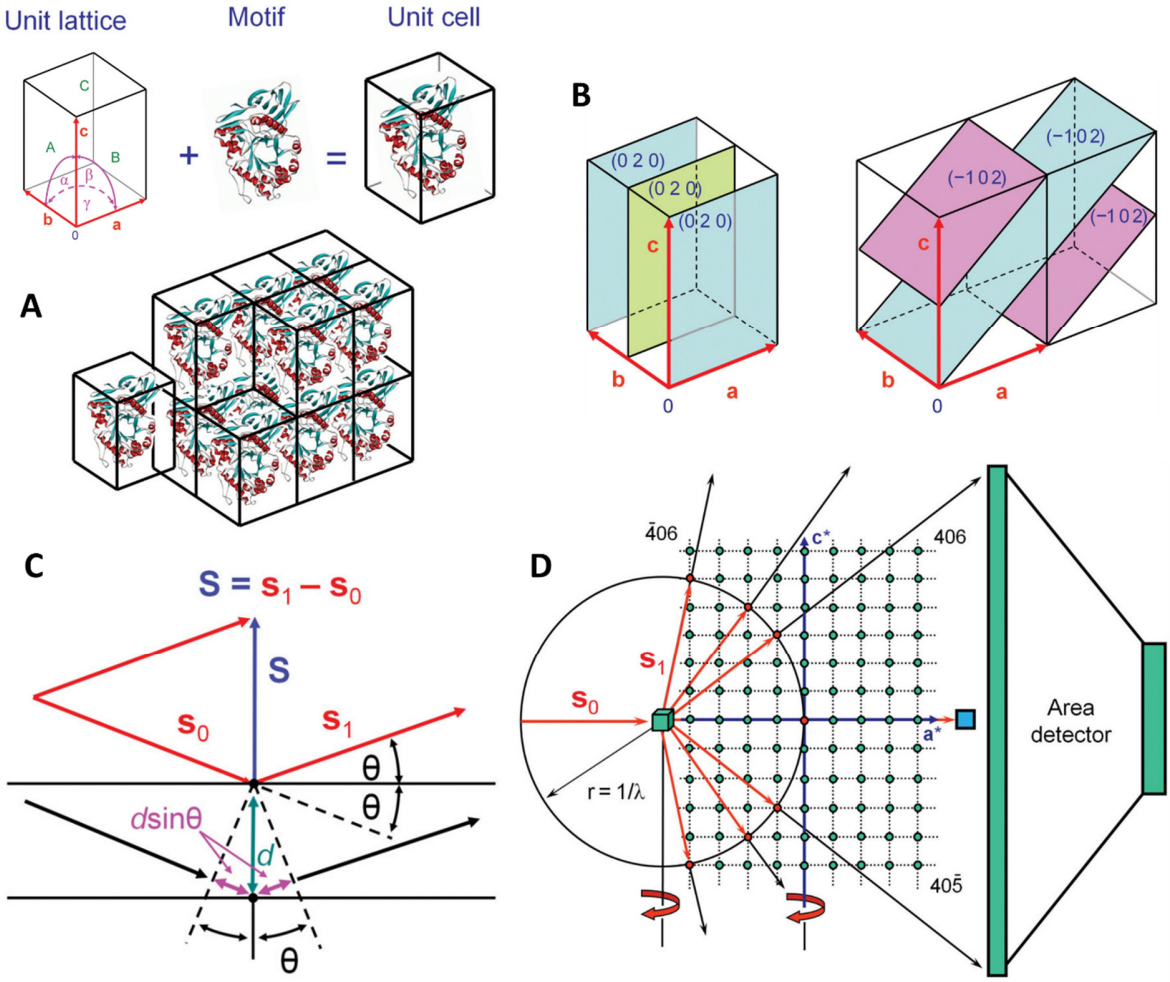

Figure 15: Principles of crystal assembly and X-ray diffraction. A) Description of a crystal by periodical arrangements of unit cells, which contain the protein motif and the unit lattice. B) Lattice planes that slice the unit lattice. They are described by the Miller indices hkl, which define in how many pieces the planes intersect the lattice planes. C) Geometrical construction of Bragg's law. In Bragg's law, the X-ray diffraction is treated as reflection from lattice planes. D) 2D representation of the Ewald construction. The green sphere is the crystal, which is the center of the Ewald Sphere with a radius of 1/λ. A detectable X-ray reflection (red arrows) occurs if a reciprocal lattice point lies on the Ewald sphere. The blue square is the beam stop and lies at the center of the reciprocal lattice. By rotating the protein crystal during the measurement, the reciprocal lattice is also rotated, and other lattice points hit the Ewald sphere resulting in other reflections. The figures are adapted and reproduced with permission from Biomolecular Crystallography by Bernhard Rupp, © 2009-2014 Garland Science/Taylor & Francis LLC.

If the electromagnetic wave hits an atom, the interaction with the electrons deviates it. The scattering of the X-rays by the electrons results in detectable diffraction if the scattered rays sum up by positive interference. The requirements that have to be fulfilled for constructive interference can be described by the Bragg equation (8) and visualized by the geometric construction in Figure 15 C.

$$n\lambda = 2 \cdot d_{hkl} \cdot \sin\theta \quad (8)$$

n – integer, λ – wavelength, d_{hkl} – distance between lattice planes, θ – scattering angle

Here, X-ray diffraction is interpreted as a reflection from lattice planes. These planes periodically intersect the unit lattice. One set of perpendicular planes with equal spacing is described by the Miller indices *hkl*, which define in how many slices the unit cell vectors a, b and c are divided by the planes (Figure 15B). The distance of the planes is d_{hkl}. Figure 15 C describes how electromagnetic waves with the same wavelength hit different planes, are scattered with the same angle θ but have to travel distinct distances. Only if this distance is a positive multiple integer of λ, the X-rays constructively interfere and add up to a strong diffracted beam. Otherwise, they are destructively interfering and no or a weaker signal is detected. Besides, the intensity of the resulting reflection is always dependent on the amount of electron density that lies on a particular set of planes. To understand how a typical protein X-ray diffraction pattern (Figure 13) is obtained, one has to enter the mathematically constructed reciprocal space, which is inverse to the real space. In reciprocal space a reciprocal lattice exists, in which each lattice point *h, k* and *l* is defined by the lattice vector $\mathbf{d}^*_{hkl}$. Bragg's law can be rewritten and related to the reciprocal space after equation (9).

$$\boldsymbol{d}^*_{hkl} = \frac{1}{\boldsymbol{d}_{hkl}} = \frac{2 \cdot \sin\theta}{\lambda} \quad (9)$$

$\boldsymbol{d}^*_{hkl}$ – lattice vector in reciprocal space, $\boldsymbol{d}_{hkl}$ – real space interplanar spacing vector, θ – diffraction angle, λ – wavelength

A condition that results in diffraction can be described with the Ewald construction (Figure **15** D). Here, Bragg's scattering diagram is overlaid with the Ewald sphere, which is drawn around the protein crystal with a radius of 1/λ, representing the X-rays in reciprocal space. The origin of the reciprocal lattice is where the incident X-ray beam travels through the crystal

and hits the Ewald sphere. Only where the reciprocal lattice points collide with the Ewald sphere, Bragg's law is fulfilled and the constructive interference can be measured as a reflection point on an X-ray detector. The rotation of the crystal also leads to the rotation of the reciprocal lattice, which causes different lattice points to lie on the Ewald sphere. The position of each reflection in the reciprocal space can be assigned with the indices h, k and l from the origin (hkl = 000) of the centrosymmetric diffraction pattern. The central reflection is not measurable because it would be overlaid by the unscattered X-ray beam, which is shielded by the beam stop. The beam stop prevents that the beam hits the detector and is positioned behind the crystal. (Rhodes, 2006; Rupp, 2009)

3.2.6.1.3 Fourier transformation and the phase problem

Every spot on the diffraction pattern is caused by an electromagnetic wave that is the sum of scattering events from all electrons in the unit cell. Electromagnetic waves are periodic functions that can be represented in the complex number plane as a vector with a real and an imaginary part (Figure 16 A). They can be described as in equation 10, using basic trigonometry and Euler's formula.

$$\boldsymbol{F} = A + iB = |\boldsymbol{F}|(cos\varphi + isin\varphi) = |\boldsymbol{F}| \cdot e^{i\varphi} \tag{10}$$

$\boldsymbol{F}$ – electromagnetic wave vector, $|\boldsymbol{F}|$ – amplitude of the vector $\boldsymbol{F}$, A – real part, iB – imaginary part B, φ – phase angle

In the complex number plane, the summation of waves can be described by vector addition (Figure 16 B) where the resulting wave **F** is the sum of all contributing waves as defined in equation 11 (Rupp, 2009).

$$\boldsymbol{F} = \sum_{j=1}^{n} |\boldsymbol{F}_j| \cdot e^{i\varphi_j} \tag{11}$$

F – sum of n waves, $|\boldsymbol{F}_j|$ – amplitude of each partial wave $\boldsymbol{F}_j$, φ_j – phase angle of partial wave j

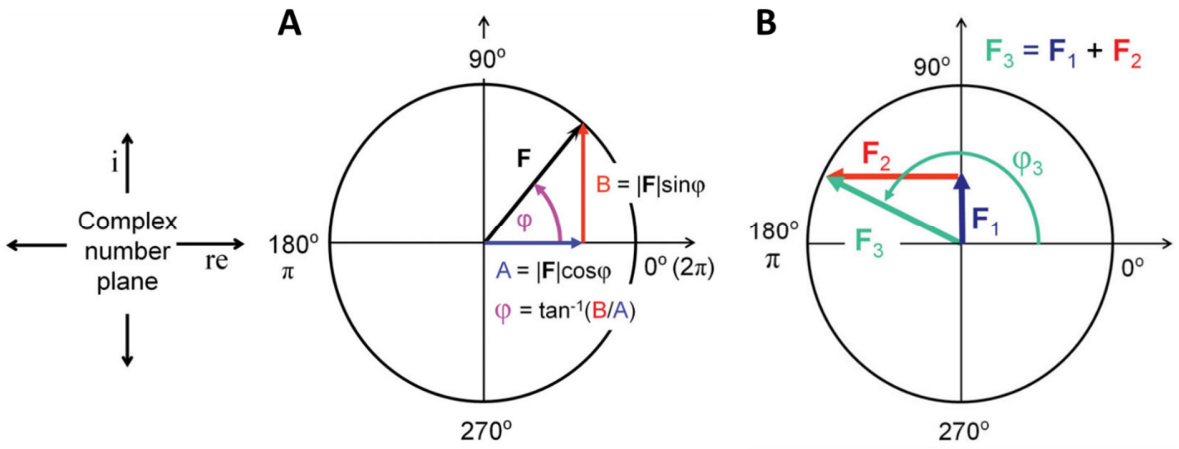

Figure 16: Representation (A) and addition of waves (B) in the complex number plane, which is spanned by the real part axis (re) and the imaginary part axis (i). A) The vector **F** is defined by its real part A = |**F**|cosφ and the imaginary part B = |**F**|sinφ. B) Vector addition of waves $\mathbf{F_1}$ and $\mathbf{F_2}$ results in the new wave $\mathbf{F_3}$, with the amplitude |$\mathbf{F_3}$| and phase angle φ_3. The figures are adapted and reproduced with permission from Biomolecular Crystallography by Bernhard Rupp, © 2009-2014 Garland Science/Taylor & Francis LLC.

A reflection *hkl* on the diffraction pattern is the sum of scattered waves from the atoms in the crystal and can be described by a vector sum that is called the complex structure factor $\mathbf{F}_{hkl}$ (Equation (12)). It is the Fourier transform of the electron density. Equation (12) describes the structure factor $\mathbf{F}_{hkl}$ that is proportional to the sum of diffraction contributions from all atoms *j* in the unit cell that contains a total of *n* atoms. In detail, it is the sum of all partial waves from each single atom at position (xyz) with each individual scattering factor f_j. The scattering factor is a function that describes the atom as an electron density sphere and is different for each element depending on the element's amount of electrons.

$$\boldsymbol{F}_{hkl} = \sum_{j=1}^{n} f_j e^{2\pi i(hx_j + ky_j + lz_j)} \tag{12}$$

F_{hkl} – complex structure factor, n – number of atoms in the unit cell, f_j – individual scattering factor of atom j

For calculating the electron density ρ(xyz) from the diffraction pattern, an inverse Fourier transform is operated according to equation (13). It describes the electron density as a transform of the structure factors $\mathbf{F}_{hkl}$ in the directions (hkl) for the whole volume of the unit cell. Here, the structure factor is expressed as a complex vector in Euler's formula (14).

$$\rho(xyz) = \frac{1}{V} \sum_{h} \sum_{k} \sum_{l} |\boldsymbol{F}_{hkl}| \cdot e^{i\alpha_{hkl}} \cdot e^{-2\pi i(hx+ky+lz)} \quad (13)$$

$$\boldsymbol{F}_{hkl} = |\boldsymbol{F}_{hkl}| \cdot e^{i\alpha_{hkl}} \quad (14)$$

ρ(xyz) – electron density at position xyz, V – volume of the unit cell, $|\boldsymbol{F}_{hkl}|$- amplitude of the complex structure factor, α_{hkl} – phase angle of the complex structure factor, $\boldsymbol{F}_{hkl}$ – complex structure factor

The structure factor amplitude $|\mathbf{F}_{hkl}|$ is proportional to the measured intensities I_{hkl} of the collected reflections *hkl* ($I_{hkl} = |\mathbf{F}_{hkl}|^2$). The amplitude can be determined from the diffraction experiment, but the information for the phase angle is lost. This results in the phase problem as the phase information is crucial for calculating the electron density (Rhodes, 2006).

3.2.6.1.4 Solution of the phase problem using molecular replacement and anomalous scattering atoms

Several methods have been developed to overcome the phase problem and to calculate interpretable electron density. Molecular replacement (MR) is a method that requires the determined structure of a protein with a similar architecture (search model). The phases of the search model are used as initial estimates for the unknown phases of the target protein structure. For this, the search model has to be placed into the unit cell in the same location as the target protein. At first, a rotation search is performed to find the right orientation followed by a translational search to identify the correct position. The correct position is identified by calculating the search model's structure factors at every position and by comparing their amplitudes with the actual amplitude derived from the diffraction experiment with the target protein. The search model is correctly positioned if the structure factors have the highest possible consistency so that the computed phases can be used to solve the phase problem and to calculate the initial electron density of the target protein.

In cases where suitable MR search models are not available, the phases have to be determined experimentally. One method for experimental phasing is the heavy-atom method that uses the anomalous scattering properties of those atoms. This usually requires the introduction of heavy atoms into the protein crystal that have a higher atomic number regarding lighter elements like C, N or O. Heavy atoms can be introduced to the protein crystal by soaking or by crystallizing proteins that have heavy atoms incorporated. One possibility here is to

use a protein that was produced with selenomethionine (MSE) substituting the naturally occurring methionine (MET). In addition, intrinsic catalytically or structurally relevant ions like zinc or iron can be used. The single-wavelength anomalous diffraction (SAD) phasing method was the only heavy-atom method used in this study. SAD requires the collection of only one dataset of the heavy-atom containing protein crystal. The dataset is measured with X-rays that exhibit a wavelength at the characteristic absorption peak of the introduced heavy-atom (Figure 17A), which entails the breakdown of Friedel's law.

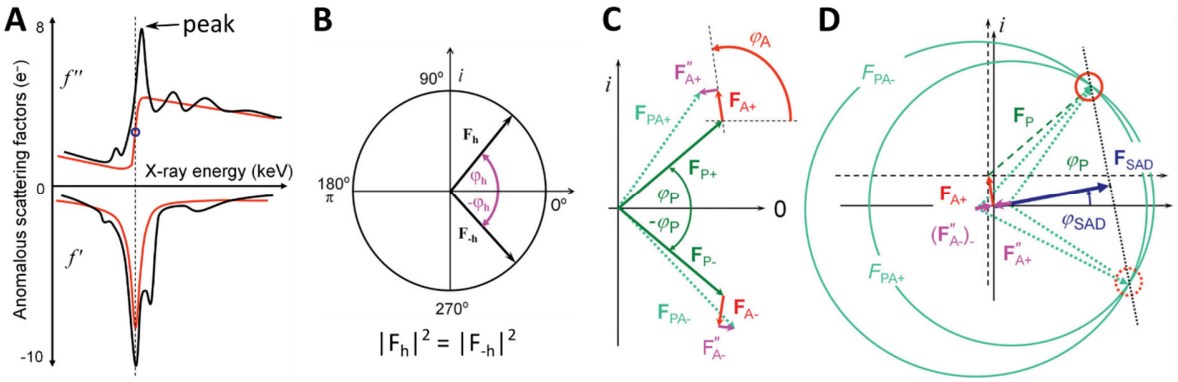

Figure 17: A) X-ray edge scan. f'' schematically represents the structure of an experimental absorption edge. f' is derived from f'' by a mathematical transformation (Kramers-Kronig transform). SAD measurements are conducted at the absorption peak wavelength, where the signal of f'' and thus the anomalous differences are maximal. B) Friedel pair in the complex number plane. Two centrosymmetrically related reflections at hkl and -h-k-l, have identical identities ($|F_h|^2=|F_{-h}|^2$) but inverse phases φ. C) Breakdown of Friedel's law through anomalous scattering. Friedel pairs have different intensities ($F_{PA-} \neq F_{PA+}$), caused by a phase shift because of the anomalous scattering at heavy atoms. D) Harker construction for SAD phasing. Anomalous differences allow the identification of heavy-atom structure factors (F_{A+}). Two possible phase angles (φ_p) for the protein are found at the intersection of circles with a radius that corresponds to the amplitudes of F_{PA+} und F_{PA-} and originate at the respective vector origins. The figures are adapted and reproduced with permission from Biomolecular Crystallography by Bernhard Rupp, © 2009-2014 Garland Science/Taylor & Francis LLC.

Friedel's law is based on the centrosymmetry of the reciprocal space or the diffraction pattern and it states that two centrosymmetrically related reflections (Friedel's pairs) have identical intensities but inverse phases (Figure 17 B). If the X-rays wavelength is near the absorption edge of the introduced heavy-atom, part of the scattering will have an anomalous phase shift of π/2 compared to the normal scattering events. This leads to the breakdown of Friedel's law because it alters the intensities of otherwise corresponding Friedel's pairs that now have different intensities (Figure 17 C). The anomalous differences allow the extraction of the heavy-atom contributions (Figure 17 D), which in turn enables the identification of the location of the anomalous scattering atoms in the unit cell with the Patterson method. This

method is independent of the phase information and only requires the measured intensities to get initial phase information. Therefore, it enables the solution of the heavy-atom substructure. This information can be used to calculate an initial electron density map of the whole protein (Rupp, 2009; Taylor, 2010; Terwilliger *et al.*, 2016).

3.2.6.2 Experimental set up

3.2.6.2.1 Crystal screening and optimization

The sitting drop vapor diffusion method was used with commercially available crystallization screens (3.1.5) to identify initial crystallization conditions. The solutions were dispensed at 20 °C with a Honeybee (Zinsser Analytic) or at 4 °C with an OryxNano (Douglas Instruments) robot in 96-3 high profile Intelli-Plates® (Art Robins Instruments). The crystallization drops consisted of different concentrated protein solutions (0.2 µl) and reservoir solution (0.2 µl). The drops were equilibrated against 60 µl reservoir. All plates were sealed and incubated at 20 °C in the automated Rock Imager system (Formulatrix).

To improve the diffraction quality and the shape of initial crystals, the composition of crystallization conditions regarding the pH and the concentration of the ingredients as well as the protein concentration were optimized in grid screens, using either sitting or hanging drop vapor diffusion method. The crystals were optimized in the sitting drop format as described for the initial screening. Here the Formulator liquid handler (Formulatrix) premixed the reservoir solutions. The hanging drop vapor diffusion method was performed in 24-well grid screen format using 24-well VDXm™ plates (Hampton Research). The reservoir was filled with 500 µl of reservoir solution. The reservoir solution (1 µl) was mixed with protein solution (1 µl) on a glass slide that was used to seal the reservoirs. These plates were also incubated at 20 °C but the drops were monitored manually under a microscope. A summary of the initial and final crystallization conditions, as well as the applied protein concentrations are listed in Table 11. Additive screens with Silver Bullets™ and Silver Bullets Bio™ screen (Hampton Research) were performed to improve the diffraction quality of PA2723 crystals. For this, the additive screen was added to the reservoir solution (0.3 M $CaCl_2$, 19 % (w/v) PEG3350) in a

ratio of 1:10. This screen was set up in 96-3 high profile Intelli-Plates® (Art Robins Instruments) using the Honeybee (Zinsser Analytic) robot that mixed the protein solution (0.2 µl) with the reservoir solution (0.2 µl).

Table 11: Crystallization conditions.

Protein	Initial hit condition	Method	c[protein] (mg/ml)	Final condition	Cryo (% (v/v))
PA1359-CTD	0.1 M Tris pH 8.5, 8 % (w/v) PEG8000 (JCSGII, A12)	X	20	initial hit	10 % 2R,3R-butanediol
PA2721	30 % PEG6000, 0.1 M MES pH 5 (JCSG IV, G6)	96-well sitting drop†	20	0.1 M MES pH 5.7, 28 % (w/v) PEG6000	10 % 2R,3R-butanediol
PA2722	0.1 M MES pH 6.5, 12 % (w/v) PEG20000 (JCSGII, D11)	24-well hanging drop	20/15*	0.1 M MES pH 6.3, 14 % (w/v) PEG20000	20 % glycerol
PA2723	0.2 M $CaCl_2$, 20 % (w/v) PEG3350 (PEG-I , E7)	24-well hanging/96-well sitting drop‡	1.5	19% (w/v) PEG3350, 0.3 M $CaCl_2$, 0.2% (w/v) caffeine/cytosine/nicotinamide/gallic acid · H_2O/tetrasodium pyrophosphate · $10H_2O$, 0.02 M HEPES pH 6.8	20 % glycerol
$PA4183^{16\text{-}155}$ SEM	1 M K/Na tartrate, 0.2 M $LiSO_4$, 0.1 M CHES pH 9.5 (JCSG IV, A5)	X	30	initial hit	20 % glycerol
$PA4183^{16\text{-}155}$	x	24-well hanging drop	15	0.7 M K/NA tartrate, 0.2M $LiSO_4$, 0.1 M CHES pH 9.6	20 % glycerol

*The crystal obtained in the initial screen used for Zn^{2+}-phasing of PA2722 grew at 20 mg/ml, while the optimized crystal grew at 15 mg/ml. †Dispensed with OryxNano (Douglas Instruments). ‡Dispensed with the Honeybee (Zinsser Analytic).

3.2.6.2.2 Cryoprotection of crystals

The crystals were cryoprotected in the reservoir solution supplemented with a cryoprotectant (Table 11). They were harvested with a nylon loop and subsequently flash cooled in LN_2.

3.2.6.2.3 Soaking and cocrystallization

To obtain protein-ligand complex structures, the ligands were either soaked into crystals or cocrystallized with the protein. For soaking experiments, well-diffracting crystals were transferred with a nylon loop into a drop that consisted of 80 % (v/v) reservoir solution, 10 % (v/v)

cryoprotectant (2R,3R-butanediol) and 10 % (v/v) of the ligand (Table 12). For soaking crystals of PA2722 a soaking solution was prepared that contained the reservoir solution (0.1 M MES pH 6.5, 14 (w/v) PEG20000), 10 mM GSH and 20 % (v/v) glycerol. The crystals were soaked for several minutes to 24 h in hanging or sitting drop format equilibrated against 500 µl or 60 µl of reservoir solution, respectively.

Table 12: Soaking conditions.

Crystal‡	Ligand*	Condition	Soaking time	hit
PA2721 (20, 25) in SEC buffer	proflavine, $CoCl_2$, $CdCl_2$, (15) chlorodinitrobenzene^D (2.5)	0.1 M MES pH 5.7, 28 % (w/v) PEG6000	24h	no
	dichlofluanid^D, captan^D (1.5)		24 h	yes
PA2722 (15, 20) in SEC buffer	GSH (10)	0.1 M MES pH 6.5, 14 % (w/v) PEG20000	1, 4.5, 24 h	no

‡*Values in parentheses refer to the initial protein concentration in mg/ml (Crystal) or to the final ligand concentration in mM (Ligand). ^{D}The soaking condition for this compound additionally contained 10 % (v/v) DMSO.

If soaking was not possible cocrystallization experiments were performed. For this, protein solutions were incubated with a 10-times higher concentration of the ligand for 10 min at RT before initial crystallization screens were carried out as described in 3.2.6.2. Crystals were harvested as described in 3.2.6.2.2.

Table 13: Cocrystallization conditions.

Protein‡	Ligands*	Condition	Cryo	Hit
PA1672 (20 mg/ml) in 50 mM HEPES pH 7, 150 mM NaCl	promethazine (15)	No xtals in JCSG+, PACT, pH clear II, Morpheus®		
	chlorpromazine (15)	1 M $LiCl_2$, 30 % (w/v) PEG6000, 0.1 M bicine pH 9	10 % (v/v) 2R,3R-butanediol	No diffraction
PA2722 (20 mg/ml) in SEC buffer	GSH (5)	0.2 M NaCl, 20 % (w/v) PEG8000, 0.1 M CAPS pH 10.5	20 % (v/v) glycerol	3.7 Å, no ligand
	GSH/GSSG (10/0.1)	No xtals in JCSG I-IV, Morpheus®, Index™, ComPAS, MIDAS™, PGA-LM™ Screens		

‡Protein was mixed 1:1 with the crystallization condition. *Values in parentheses refer to the final ligand concentration in mM.

3.2.6.2.4 Diffraction data collection

All diffraction experiments were performed at 100 K. The diffraction of crystals was first analyzed at the home source, which is a MicroMax™ 007 HF rotating Cu-anode X-ray (λ = 1.54187 Å) generator (Rigaku, Tokyo, Japan) with a Saturn 944+ CCD detector (Rigaku, Tokyo, Japan). High resolution and SAD data were collected at synchrotrons as described in Table 14.

Table 14: Diffraction data collection.

Protein	Method	Wavelength (Å)	Synchrotron*	Beamline	Detector
PA2723	high resolution	1.033	PETRA III, DESY, Hamburg, Germany	P11	Pilatus 6M
PA2722	high resolution	1	SLS, PSI, Villigen, Switzerland	X06DA	Pilatus 2M
PA1359-CTD	high resolution				
PA4183$^{16\text{-}155}$ SEM	Se-SAD	0.97901			
PA4183$^{16\text{-}155}$	high resolution	0.91841	BESSYII, HZB, Berlin, Germany	BL14.2	MarCCD
PA2722	Zn-SAD	1.282416		BL14.1	Pilatus 6M

*PETRA: Positron-Elektron-Tandem-Ring-Anlage. DESY: Deutsches Elektronen-Synchrotron. SLS: Swiss Light Source. PSI: Paul Scherrer Institut. BESSY: Berliner Elektronenspeicherring-Gesellschaft für Synchrotronstrahlung. HZB: Helmholtz-Zentrum Berlin.

3.2.6.2.5 Data processing and phasing

All datasets were indexed and integrated with XDS (Kabsch, 2010) and scaled with Aimless (Evans & Murshudov, 2013) from the CCP4 program suite (Winn *et al.*, 2011). The content of the asymmetric unit was estimated with the Matthews_Coef tool from the CCP4 suite (Winn *et al.*, 2011). The SAD data for PA2722 and PA4183$^{16\text{-}155}$ SEM were used for experimental phasing with AutoSol from the PHENIX program suite (Adams *et al.*, 2010). The program identified the sites of anomalous scatterers, carried out the phasing, density modification and built an initial model. The native high-resolution structures of PA2722 and PA4183$^{16\text{-}155}$ were phased by MR with Phaser from the PHENIX suite (Adams *et al.*, 2010) using experimentally determined search models. PA1359-CTD was phased with the MR pipeline BALBES (Long *et al.*, 2008) using the structure from PDB entry 1Y9Q (sequence identity 18.5 %) as a search model. PA2723 was phased *ab initio* with the program Arcimboldo LITE (Rodríguez *et al.*, 2009). Arcimboldo uses Phaser (McCoy *et al.*, 2007) for a MR approach that places small structure fragments like α-helices. Based on a secondary structure prediction of PA2723 (Figure S6), Arcimboldo (Rodríguez *et al.*, 2009) was advised to search for 3 helices. Second the main-chain auto tracing program SHELXE (Thorn & Sheldrick, 2013) extended the successfully placed helices. That partial model of PA2723 was further extended by the AutoBuild program of the PHENIX suite (Adams *et al.*, 2010).

3.2.6.2.6 Structure refinement and analysis

The initial structure models after phasing were improved by alternating cycles of manual refinement in COOT (Emsley *et al.*, 2010) and automated refinement with phenix.refine (Adams

et al., 2010). Restraints for ligands were created with phenix.eLBOW (Moriarty *et al.*, 2009). Figures of structure models were created with PyMOL (DeLano, 2002). Chemical structures of ligands were drawn with ChemDraw Professional 17.0 (PerkinElmer Informatics, Inc., Waltham, MA, USA). Protein-ligand interactions were analyzed with Discovery Studio Visualizer v16.1. (Dassault Systèmes BIOVIA Corp, San Diego, CA, USA) or UCSF Chimera (Pettersen *et al.*, 2004).

3.2.6.2.7 Crystallographic fragment screening of PA2721 crystals

Crystallographic fragment screening (FS) was performed with an updated version of the recently published HZB 96-compound library (Huschmann *et al.*, 2016) and optimized PA2721 crystals that were obtained as described in 3.2.6.2. The fragment library was provided by the HZB in a 96-3 low profile Intelli-Plate® (Art Robins Instruments). The fragments were immobilized in two wells per reservoir. The soaking solution was prepared by mixing the crystallization condition (0.1 M MES pH 5.7, 28 (w/v) % PEG6000) with 2*R*,3*R*-butanediol as cryoprotectant (10 % (v/v) final concentration) and DMSO (10 % (v/v) final concentration) to dissolve the fragments. The reservoirs were supplemented with 60 µl of soaking solution. To reach a final fragment concentration of 100 mM, 0.3 µl of the soaking solution were pipetted to each well. At least two optimized PA2721 crystals were transferred with a loop to each well and soaked for 24 h at 20 °C with the respective compound. Crystals soaked with fragments 100, 121 and 123 did not diffract after 24 h. For those, diffracting crystals were obtained by reducing the soaking time to 1 h for fragment 100 and to 5 h for fragment 121 and by decreasing the concentration of fragment 123. The crystals were observed under the microscope during the soaking time to monitor possible changes in crystal shape. Crystals were harvested in nylon loops and flash frozen in LN_2. Diffraction datasets were collected at the home source (3.2.6.2.4) or on beamline BL14.2 at BESSY II (λ=0.9184 Å, (Mueller *et al.*, 2012, 2015). The data collected at BESSYII were processed with XDSAPPv2.99 or v2.0 GUI (Krug *et al.*, 2012; Sparta *et al.*, 2016) in space group P1 or $P2_1$. The phase problem was solved by MR with the published PA2721 model (PDB-ID: 1U69; Nocek *et al.*, 2006) for one high resolution dataset in each space group. The respective structures were refined without waters (3.2.6.2.6) and used as search models for the automated HZB refinement pipeline. The pipeline performed

molecular replacement and refinement with PHENIX (Adams *et al.*, 2010). The home source data were processed and phased as explained in 3.2.6.2.5. The resulting electron density maps were manually inspected in COOT (Emsley *et al.*, 2010) to identify difference electron density caused by the presence of bound fragments. Hits were refined as described under 3.2.6.2.6.

4 Results and Discussion

4.1 Open reading frames PA2721 – PA2723

The previously published crystal structure of class III βαββββ-module-containing protein PA2721 builds a homodimer by edge-to-edge contacts (Bergdoll *et al.*, 1998; Nocek *et al.*, 2006). In contrast to all other known βαββββ-module-containing proteins, PA2721 has an additional three-helix bundle. The three helices close the characteristic U-shaped binding site to form a tunnel together with a flexible loop that is only visible in one monomer (Figure 18 A).

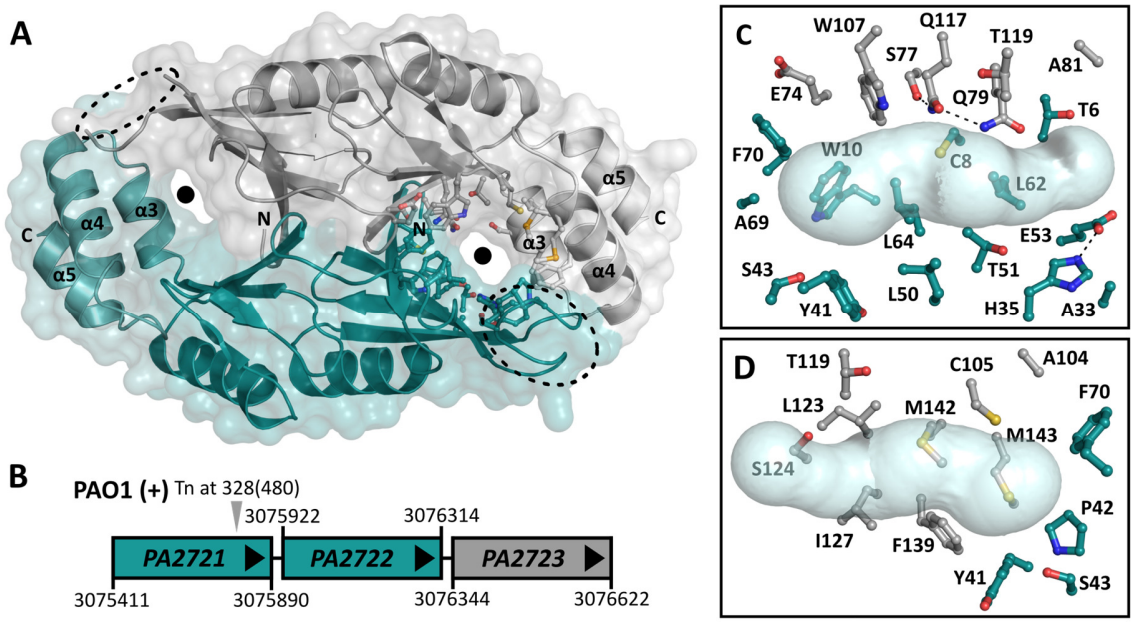

Figure 18: A) Crystal structure of PA2721 (PDB-ID: 1U69, Nocek *et al.*, 2006). Displayed is the homodimer with differently colored monomers in cartoon and surface representation. The black dots highlight the location of the potential binding tunnels. The amino acid side chains flanking one tunnel are shown in balls and sticks representation. The dashed lines indicate a flexible loop region. Members of the three-helix bundle are numbered according to their location on the peptide chain. B) Operon organization and genomic localization of open reading frames PA2721-PA2723 in PAO1 as derived from pseudomonas.com (Winsor *et al.*, 2016). Genes colored in teal are part of one operon. The transposon insertion site (Tn) of the PAO1 *PA2721*::Tn mutant is indicated by a grey arrow. The position of the insertion in the ORF is given in units of bp. The total length of the gene is given in brackets. C/D) Magnification of the potential binding/active site in different orientations. The flanking amino acid side chains are represented as balls and sticks. Oxygen (O), nitrogen (N) and sulfur (S) atoms are colored in red, blue or yellow. Dashed lines represent H-bonds with a maximum distance of 3.2 Å. The surface of the potential binding tunnel is shown in light blue as visualized with Caver3.0 (Chovancova *et al.*, 2012).

A closer look at the amino acid side chains that point into the tunnel reveals many potential residues that might contribute to the function of PA2721 (Figure 18 B), such as the side chains of H35 and E53, which are in H-bonding distance to each other and belong to the amino acids that are most frequently found in catalytic centers of proteins (Bartlett *et al.*, 2002). Both often

serve as acid-base catalysts and also participate in the stabilization of transition states or act as nucleophiles (Holliday *et al.*, 2009). The two cysteine residues C8 and C105 might also be of functional importance, as their thiol side chains can also participate in general acid/base catalysis but also in covalent catalysis by forming disulfide bridges (Bartlett *et al.*, 2002; Holliday *et al.*, 2009). C105 is of special interest as it is surrounded by M142 and M143. Though MET residues are not crucial in protein catalysis (Bartlett *et al.*, 2002; Holliday *et al.*, 2009), they can serve as antioxidants through forming methionine sulfoxide (Kim *et al.*, 2014). This way, MET residues were shown to serve as endogenous protection of residues that are essential for catalysis (Reddy *et al.*, 1994; Levine *et al.*, 1996; Kim *et al.*, 2014). A comparable protective mechanism might be mediated by M142 and M143 to keep the potentially relevant C105 reduced and functional. The coordinates of the structure were input for the 3D search for protein sites (SPRITE) server. It scans the protein and compares its surface residues to a database of 3D side chain arrangements from sites and motifs with characterized function to identify conserved functionally relevant motifs independent of structure and sequence similarities (Nadzirin *et al.*, 2012). This search did not discover any relevant patterns in the potential binding tunnel so no hint towards a potential function of PA2721 was derived from the structure.

The gene that codes for PA2721 is expressed in an operon with the downstream gene *PA2722* (Figure 18 C) according to a transcriptome analysis (Wurtzel *et al.*, 2012). A protein sequence-based BLAST (Altschul *et al.*, 1997) and InterPro (Hunter *et al.*, 2009) analysis predicted PA2722 to be a Glutathione-dependent formaldehyde-activating enzyme/centromere V protein. A Phyre^2-prediction modelled 81 % of the protein with a confidence of 99.9 % to a reliable structure with a glutathione-dependent formaldehyde-activating enzyme/centromere V protein fold. The template with the highest sequence coverage (80 %) was the crystal structure of the glutathione-dependent formaldehyde-activating enzyme (Gfa) from *Paracoccus denitrificans* (*Pd.* Gfa), which contains two zinc centers (PDB-ID: 1X6M, Neculai *et al.*, 2005). As the cysteine residues that complex the zinc ions are conserved in PA2722 (Figure 32, lower panel), it was assumed that the target protein can also bind Zn^{2+}-ions. To confirm the protein fold, the structure of PA2722 was determined and biochemical data were collected to find evidence for a Gfa-like function. The adjacent gene *PA2723* was also part of the investigations in this study. A ho-

mology-based structure prediction with the Phyre^2-server (Kelley *et al.*, 2015) gave no reliable output as only 13% of the protein residues were modelled with 24 % confidence. Besides, a protein sequence-based BLAST analysis (Altschul *et al.*, 1997) could not identify conserved domains in PA2723 so the protein could not be assigned to a known protein family. Therefore, the focus for this was the identification of the structure with the intention to discover a new, previously undescribed protein fold.

4.1.1 PA2721

4.1.1.1 Phenotyping of a PAO1 *PA2721*::Tn mutant

The transposon insertion in the gene coding for *PA2721* (PAO1 PA2721::Tn) was introduced by Held *et al.*, 2012 and the respective strain was kindly provided by Prof. S. Häußler from the HZI. The insertion of the IS*lacZ*/hah transposon was confirmed by PCR and sequence analysis after bp 328 as stated by the manufacturer (Held *et al.*, 2012) (Figure 18 C). To identify the physiological relevance of PA2721 the phenotype of PAO1 *PA2721*::Tn was compared to the wt strain in motility and planktonic growth assays as well as under distinct growth conditions in Phenotypic MicroArrays^{TM}.

4.1.1.1.1 Motility and planktonic growth

In addition to planktonic growth, motile bacteria like *P. aeruginosa* can migrate over different surfaces and colonize distinct environments. This enables them to colonize larger areas and invade host tissues to establish an infection (Gellatly & Hancock, 2013; Josenhans & Suerbaum, 2002). Swimming motility is a flagellum-dependent movement of individual bacterial cells through liquid or low viscosity media. Swarming motility is a multicellular behavior on semisolid surfaces that also requires a functional flagellum but is also dependent on type IV pili and the secretion of surface-active agents (surfactants). Surfactants are amphiphilic wetting agents that are secreted by the bacteria to reduce the surface tension and facilitate the bacterial movement (Kearns, 2010). The swimming and swarming motility assays conducted here revealed that the PAO1 *PA2721*::Tn mutant had no deficiencies in comparison to the wt, since both strains were able to migrate equally through a low viscosity swimming agar (Figure 19 B/D) or

over the semisolid swarming agar (Figure 19 C/E). Similar phenotypes were also discovered in planktonic growth assays (Figure 19 A).

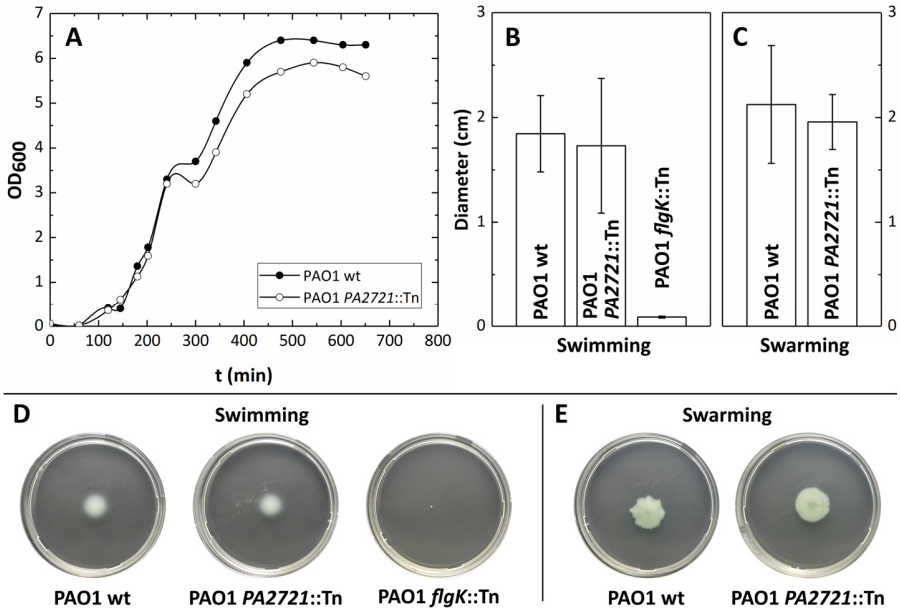

Figure 19: Phenotypic characterization of a *P. aeruginosa* PAO1 PA2721 mutant (PAO1 *PA2721*::Tn) in comparison to the PAO1 wt and a swimming deficient mutant (PAO1 *flgK*::Tn). A) Planktonic growth curves of the mutant and the wt. Displayed is the increase in optical density over time (t (min)) as measured from the cell cultures in regular intervals at 600 nm (OD_{600}). The bacteria were incubated in LB-medium under shaking conditions at 37 °C. B/C) The diameter of swimming and swarming colonies were determined from three independent experiments (Figure S2/S3), after incubation for 19 h (swimming) and 18 h (swarming) at 37 °C. Error bars represent the deviation calculated from the mean triplicates. D/E) Examples of the respective swimming and swarming colonies.

Those findings indicate that the PA2721 protein does not participate in the basic cellular functions that are involved in these processes. Moreover, no morphological differences occurred. Colonies of the wt and the mutant exhibited the same shape on LB agar plates and developed comparable levels of green color when reaching high cell densities during solid and planktonic growth. Since the coloration of *P. aeruginosa* is caused by the production of the most abundant phenazines pyocyanin and pyoverdine (Pierson & Pierson, 2010), one can conclude that the disruption of the *PA2721* gene does not interfere with the production and secretion of these secondary metabolites.

4.1.1.1.2 Phenotype MicroArrays™

Phenotype MicroArrays™ (PM) were performed to monitor the phenotypic response of the mutants to distinct conditions and use differences to the wt as starting points for functional characterization. Instead of cell growth, the respiration rate of the cells is measured trough a

reporter system. This system is based on the reduction of a tetrazolium dye with NADH that is produced during cell metabolism. This creates a purple color which can be measured colorimetrically (Bochner, 2009). Like growth curves, the respiration curves are sigmoidal with a lag phase in which the cell proteome is adopted to the growth conditions and an exponential phase until the stationary phase is reached. The respiration curves have no death or decline phase since the reduction of the dye is irreversible and remains even if the cellular metabolism stopped after the nutrient source is consumed (Bochner, 2009). Since the βαβββ-module proteins were suspected to participate in resistance mechanisms, PMs were the method of choice for functional characterization as they enable the parallel high-throughput screening of 240 compounds with antibacterial activity provided in four different concentrations. The participation of βαβββ-module proteins in carbon source metabolism was also tested by applying PMs with 190 different compounds as sole carbon source. The comparative analysis of PAO1 *PA2721*::Tn with the PAO1 wt revealed coinciding respiration curves on most conditions (Figure S5). One significant change occurred when the dipeptide Gly-Pro served as the sole carbon source (Figure 20 A). In this case, the maximum respiration rate in the stationary phase of *PA2721*::Tn was reduced by approximately 50 %. Interestingly, no deficiency was detected if similar compounds, such as proline or hydroxyproline were available as sole carbon sources (Figure 20 B/C).

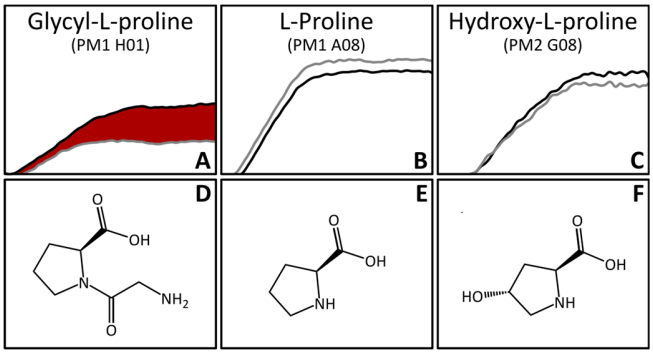

Figure 20: Carbon source utilization Phenotype MicroArrays™ of PAO1 *PA2721*::Tn. A, B, C: Displayed are the respiration curves of *PA2721*::Tn (grey) in comparison to the PAO1 wt strain (black) for cells that were incubated on three proline derivatives that served as sole carbon sources in the Phenotype MicroArrays™. The red color highlights the reduced phenotype of the mutant. The values in parentheses describe the number of the respective Phenotype MicroArray™ and of the wells containing the compound. The respiration curves were obtained by plotting the measured absorbance in arbitrary units from 0-400 detected at 490 nm (y-axes) against the incubation time from 0-48 h (x-axes). To highlight the growth deficiency of the mutant, the area between the respiration curves was colored red D,E,F: Chemical structures of the proline derivatives were obtained from the PubChem database (Kim *et al.*, 2016) and visualized with ChemDraw Professional 17.0.

This means that the mutant can generate energy from glycyl-l-proline but not as effective as from other proline derivatives. A possible explanation is that PA2721 directly participates in the catabolism of glycyl-L-proline in a pathway upstream of the catabolism of L-proline and hydroxyl-L-proline. It is also possible that PA2721 detoxifies compounds that emerge from the breakdown of glycyl-L-proline but not from the other derivatives, which is not possible in the mutant and kills the bacteria after accumulation of the toxic compound. Further studies are required to proof the intervention of PA2721 in the glycyl-L-proline metabolism.

In the chemical sensitivity assays, several phenotypic changes occurred (Figure 21). Since the manufacturer of the PM plates does not provide the exact compound concentrations, the results were evaluated qualitatively. PAO1 *PA2721*::Tn was more susceptible to 13 compounds and more resistant to six. They mediate diverse antimicrobial effects by targeting distinct sites in the bacterial cell. The diversity of these compounds makes it very challenging to suggest a clear physiological role of PA2721 that could explain all the observed phenotypes. Nafcillin is for example a β-lactam antibiotic that inhibits the synthesis of the cell wall (Wright, 1999), while serine hyrdoxamate is a serine analogue that inhibits the seryl-tRNA synthase and thus protein synthesis (Tosa & Pizer, 1971*b*,*a*). Further, monothioglycerol inhibits bacterial growth by accepting the methyl group from the central methyl donor S-adenosyl methionine (SAM) and thus lowers its concentration and prevents crucial metabolic functions that require SAM (Javor, 1983). Further, the heteroaromatic acridines, acriflavine, proflavine and 9-aminoacridine intercalate into DNA, interfere with DNA replication and lead to problems during reproduction. They also release ROS under UV light, which leads to increased oxidative stress in the cell (Gatasheh *et al.*, 2017; Wainwright, 2001). The interpretation of the results towards a PA2721 function was further complicated by the fact that some compounds are supposed to target the same bacterial process induce contrary phenotypes, such as the detergent domiphen bromide and the polymyxin antibiotic colistin. Despite their distinct chemical structures (Figure 21), they are both amphiphilic compounds with positive charges and lipophilic moieties that act on the cell membranes. They cause the disruption of both membranes, leading to cell leakage and death (Biswas *et al.*, 2012; McDonnell & Russell, 1999).

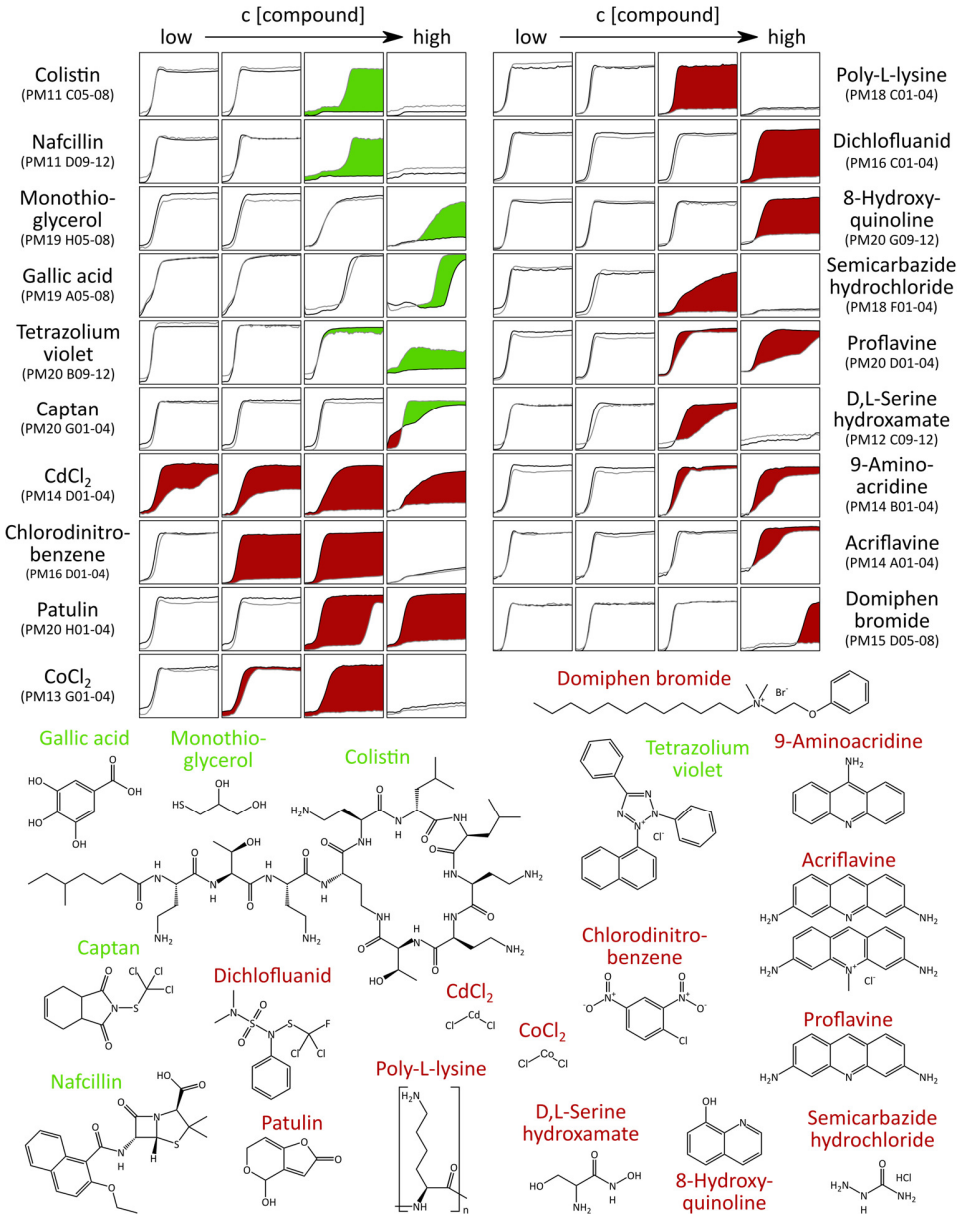

Figure 21: Chemical sensitivity Phenotype MicroArrays™ of *PA2721*::Tn. Respiration curves of the wt (black) and the mutant (grey). They were incubated on four concentrations of antimicrobial compounds. Displayed are the results for compounds that induced significant changes between the respiration rate of the wt and the mutant. The values in parentheses describe the number of the respective Phenotype MicroArray™ and of the wells containing the compound. The respiration curves were obtained by plotting the measured absorbance in arbitrary units from 0-400 detected at 490 nm (y-axes) against the incubation time from 0-48 h (x-axes). To highlight the differences, the area between the respiration curves was colored green if the mutant respired better than the wt or red if the respiration of the mutant was inhibited. The chemical structures were obtained from the PubChem database (Kim *et al.*, 2016) and visualized with ChemDraw Professional 17.0.

Other compounds that are active against the cell membrane of gram-negative bacteria and increase the permeability are poly-L-lysine (Hyldgaard *et al.*, 2014) as well as the phenolic compounds gallic acid (Borges *et al.*, 2013) and 8-hydroxyquinoline (Prachayasittikul *et al.*, 2013).

Phenolic compounds are known to induce several antimicrobial effects and can also inhibit cytoplasmic proteins and enzymes (McDonnell & Russell, 1999), which is also suspected for 8-hydroxyquinoline and gallic acid. A large group of compounds that induced reduced phenotypes (Figure 21) cause the increase of oxidative stress in bacteria. This group includes the toxic cations $CdCl_2$ and $CoCl_2$ (Blundell & Wild, 1969; Nies, 1999), patulin (Puel *et al.*, 2010), chlorodinitrobenzene (Habig *et al.*, 1974; Vuilleumier, 1997) and dichlofluanid (Schuphan *et al.*, 1981). Dichlofluanid is a perhalogenmethylmercapto fungicide and is structurally and functionally related to captan (Schuphan *et al.*, 1981), yet these two compounds induce contrary phenotypes (Figure 21). The increase of oxidative stress caused by the before mentioned compounds is based on their reactivity against sulfhydryl groups. They can react with GSH and lead to the depletion of the glutathione pool (Habig *et al.*, 1974; Nies, 1999; Puel *et al.*, 2010; Rahden-Staroń *et al.*, 1994; Schuphan *et al.*, 1981; Vuilleumier, 1997). As GSH is an important compound during detoxification of ROS by what its depletion indirectly increases oxidative stress and might lead to cell death (Masip *et al.*, 2006). Some of them are even able to covalently modify active site cysteine residues of enzymes (Puel *et al.*, 2010) or replace catalytically active metals (Nies, 1999), which might inhibit important metabolic functions. Besides that, captan and dichlofluanid also exhibit a mutagenic effect in prokaryotes introducing severe DNA damage (Barrueco and de la Peña, 1988; Rahden-Staroń *et al.*, 1994). The complexity of these findings indicates that further studies are required to make a statement about the intervention of PA2721 in the detoxification of the identified compounds.

4.1.1.2 Analysis of interactions between PA2721 and compounds that lead to chemical sensitivity

To find out if the discovered phenotypic changes indicate a precise function, the interaction of the change inducing compounds with the recombinantly expressed PA2721 (159 aa, 17.4 kDa) (Figure S1) protein was tested. For a fast screen the protein was utilized in a TSA to identify compounds that affect the melting temperature (T_m) of the protein upon binding. The compounds that induced a shift in thermal stability (Figure 22 A) were forwarded to an MST-screen.

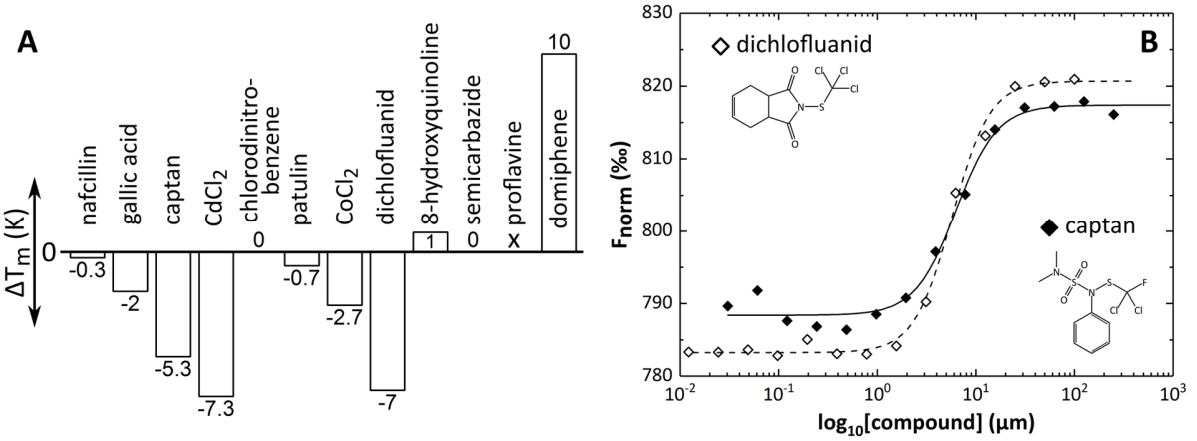

Figure 22: Interaction of PA2721 with antimicrobial compounds that induced significant changes in the chemical sensitivity PMs. A) Changes in thermal stability (ΔT_m) of PA2721 (T_m: 61°C) as measured with a TSA. ΔT_m were determined by averaging 3 independent experiments. B) MST dose-response curves were derived by plotting the thermophoresis signal F_{norm} (‰) against the compound concentration in µM. For the MST experiment 100 nM Cy5-labelled PA2721 were titrated against a 1:1 dilution series of dichlofluanid (◊) with a starting concentration of 100 µM and of captan (♦) with a starting concentration of 250 µM. MST data were collected at 293 K in standard capillaries with 30 % LED-power and 40 % MST-power. The final reaction conditions contained 20 mM Tris/HCl pH 8, 150 mM NaCl, 0.5 % BSA, 10 % (v/v) DMSO. From the curve fit after the Hill-equation (5) an EC50 of 5.7 ± 0.3 µM for dichlofluanid and 6.3 ± 0.6 µM for captan was calculated.

Significant changes in the thermophoretic behavior of PA2721 were discovered if the protein was incubated with gallic acid (MST response amplitude: 0-6), captan (MST response amplitude: ~15) and dichlofluanid (MST response amplitude: 10). To verify possible binding MST titration experiments were performed. This showed that gallic acid does not bind to PA2721 under the tested conditions. However, a sigmoidal binding curve as obtained for the related compounds captan and dichlofluanid (Figure 22 B/C). The curves were well fitted with the Hill-equation (5), leading to similar Hill-coefficients of 2.1 (captan) and 2.3 (dichlofluanid), indicative of positive cooperativity in both binding events (Cattoni *et al.*, 2015). The EC50 derived from these curves was 6.3 ± 0.6 µM for captan and 5.7 ± 0.3 µM for dichlofluanid.

4.1.1.3 Dichlofluanid and captan covalently modify PA2721

To get a detailed insight into the binding of captan and dichlofluanid, both ligands were soaked into PA2721 crystals (Figure 24). Furthermore, proflavine was soaked because its fluorescence properties did not allow interaction studies with a TSA or MST experiment. However, proflavine was not discovered in the structure and might not bind there. The full processing and refinement statistics for the soaks with dichlofluanid and captan are displayed in Table S1. In both cases the electron density map revealed no mFo-DFc difference density that would have been

interpretable with a ligand. However, one of the potential active site residues C105 (Figure 23 B/C/F/G) showed extra density caused by a covalent modification.

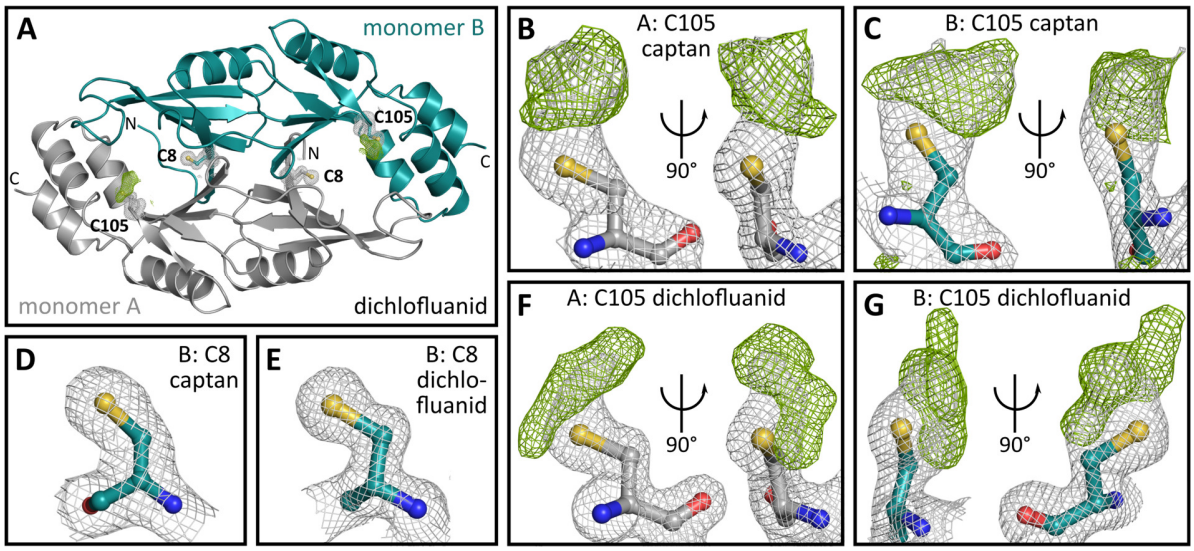

Figure 23: Cysteine modification in PA2721 after soaking the crystals in reservoir solution (0.1 M MES pH 5.7, 28 % (w/v) PEG6000), supplemented with 1.5 mM captan or dichlofluanid, 10 % (v/v) DMSO and 10 % (v/v) butane diol. A) Overall structure of the PA2721 dimer soaked with dichlofluanid. The positions of the modified CYS in the potential binding site are highlighted. B/C/F/G) Modified C105 in both monomers of a PA2721 crystal soaked with captan (B/C) and dichlofluanid (F/G). D/E) Examples of an unmodified C8 from monomer B from crystals soaked with captan (D) and dichlofluanid (E). The crystal soaked with captan diffracted to 2.1 Å and the one soaked with dichlofluanid to 1.46 Å. Full processing and refinement statistics are displayed in Table S1. The mFo-DFc difference electron density is displayed in green and contoured at 2.5 σ. The 2mFo-DFc is displayed in grey contoured at 1 σ. Monomer A is colored in grey and monomer B in teal. CYS residues are represented as balls and sticks. The oxygen atoms are red, the nitrogen atoms are blue, and the sulfurs are yellow.

It is likely that this modification was specifically introduced to C105 upon the contact with the ligand, as the other solvent exposed cysteine (C8) in the binding site was unmodified (Figure 23 D/E). Further, it is very unlikely that the extra density of C105 was caused by oxidization, as such a modification was unique to the crystals soaked with captan and dichlofluanid. In addition, no modification of C105 was discovered in reference crystals soaked with the same amount of DMSO (10 % (v/v)), which was required for dissolving the compounds or in the almost 100 crystals that were analyzed during the fragment screening campaign (4.1.1.4). Taken the results from both experiments together, one can conclude that PA2721 is covalently modified upon the incubation with captan and dichlofluanid in a concentration dependent manner at the specific amino acid C105. *In vitro* studies of enzyme-free reactions with dichlofluanid and free cysteine identified that a disulfide bridge is formed between the side chain of the cysteine and the flourodichlormethylthio moiety of dichlofluanid (Schuphan *et al.*, 1981), which could

also be the case for the C105 in PA2721. Unfortunately, the covalent modification of the protein does not allow to determine K_D-values from the MST experiment, as the covalently attached molecule does not dissociate of the protein. However, the EC50 defines that at a captan concentration of 6.3 ± 0.6 µM and at a dichlofluanid concentration of 5.7 ± 0.3 µM 50 % of the protein molecules are occupied, making them equally effective in the modification of PA2721. These findings could suggest that PA2721 might be able to catalyze the breakdown of dichlofluanid and captan over a covalent intermediate that must be transferred to a cosubstrate for further metabolism of the compound and to release the CYS for a new reaction cycle.

Since captan and dichlofluanid are agricultural fungicides, they were released into the environment where they possibly came into contact with soil-dwelling bacteria such as *P. aeruginosa.* Another soil-dwelling human pathogen is *Bacillus circulans*, which was identified to utilize captan as sole energy source (Megadi *et al.*, 2010). From a cell-free extract of *B. circulans* the activity of a captan hydrolase was identified, which is supposed to catalyze the first step in a proposed captan degradation pathway (Megadi *et al.*, 2010). Although the respective gene from *B. circulans* was not identified by now and therefore cannot be compared with PA2721 it is possible that *P. aeruginosa* also developed a specific resistance mechanism towards these agricultural compounds but further investigations are necessary to support this hypothesis. However another study identified that captan is hydrolyzed in H_2O so it should be considered that one of its hydrolysis products could be CYS reactive and responsible for the modification seen in PA2721 (Wolfe *et al.*, 1976).

4.1.1.4 Fragment screening of PA2721 with the HZB 96-compound library

A crystallographic fragment screening was performed with PA2721 to identify ligands in the potential binding site to derive ideas about the chemical structure of potential substrates. PA2721 is a very suitable target for such an approach as PA2721 rod shaped crystals are highly reproducible in amount, diffraction quality and resolution limits (Figure 24).

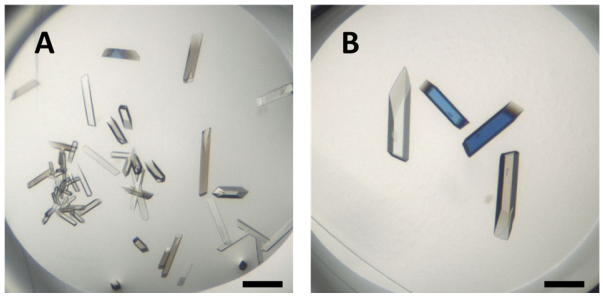

Figure 24: A/B) PA2721 crystals grown in 28 % (w/v) PEG6000, 0.1 M MES pH 5.7 for soaking the HZB 96-fragment library. Scale bar 300 µm.

An updated, immobilized version of the published 96-fragment library from HZB was chosen for individual soaking into the crystals, because the library offers a broad diversity with compounds from five chemical classes, namely buffer ingredients, carbohydrates and their derivatives, nucleotides, amino acid- and peptide-like fragments and various organic, drug-like compounds (Huschmann *et al.*, 2016). The compounds are small fragments ranging from 101 to 549 Da with an average MW of 205 Da. The crystals were individually soaked with the library and used for diffraction data collection. The diffraction data were processed in triclinic space group P1 or in monoclinic $P2_1$. Crystals in the P1 space group contained 8 monomers per ASU and data set 19 was used as the search model for the phasing pipeline. Full processing and refinement statistics for data set 19 can be found in Table S4 and Table S5. The pipeline phased and refined all 46 data sets from SG P1 that were collected at BESSY II (HZB), giving R_{free} values from 19 % to 37 % (Table S2). $P2_1$ SG crystals contained one homodimer in the ASU, which resembled the oligomerization state of the protein in solution. Data set 90 was chosen as pipeline input model for SG $P2_1$ (Table S4/S5). The 39 data sets collected at BESSYII (HZB) and processed in SG $P2_1$ were phased and refined to R_{free} values from 18.3 to 30.9 % (Table S3). Ten data sets were collected at the rotating anode X-ray source at the HZI. One was processed in SG P1 and the rest in $P2_1$. They were phased "manually" and refined to R_{free} values in the range of 22.5 to 34 % (Table S2/S3). The resolution limits of all data sets were between 1.04 and 2.2 Å. Taken together, the fragment screening campaign yielded well interpretable electron density maps.

4.1.1.4.1 Quality of fragment screening hits

The difference density map of crystals that were soaked with fragments 8, 10, 61 and 100 revealed clear electron density that was interpretable with the respective fragments (Figure 25

A/C/D/F/I), which are bis-tris propane, N-benzyloxycarbonyl-L-proline (CBZ-Pro), 4-nitrochatechol and barbituric acid. Full processing and refinement statistics of all data sets are displayed in Table S4 and Table S5. With real space correlation coefficients (RSCC) between 0.91 and 0.95 (Table 15) most of the protein-ligand models had a good quality according to the validation values of Deller & Rupp, 2015, who stated that ligands fit the electron density well if RCSSs are between 0.9 and 1 (Deller & Rupp, 2015). Only the complex of F10 with one binding site (site 1) of PA2721 was of lower quality with a RSCC of 0.83.

Table 15: Refined occupancies and real-space correlation coefficients (RSCC)[#] of FS hits, named by the fragment ID and the chemical name.

ID	Name	Occupancy	RSCC
8[‡]	bis-tris propane	0.72	0.95
10 site 1	N-benzyloxycarbonyl-L-proline	0.92	0.83
10 site 2		0.96	0.91
61	4-nitrocatechol	0.79	0.95
100	barbituric acid	0.73	0.93

[#]Occupancy refinement and calculation of RSCC was carried out with PHENIX.refine (Adams *et al.*, 2010). [‡]Fragment 8 has two alternate conformations with occupancies of 0.52 and 0.31 respectively, while RSCC did not differ.

Figure 25 A shows the binding of bis-tris propane with two alternate conformations for most of the hydroxyl groups of the two tris moieties. The refined occupancies of the individual conformations are 52 % and 31 % (Table 15). Both conformations are stabilized by a variety of H-bonds formed either directly between the protein and the fragment or mediated by H_2O (Figure 25 A). In this case, amino acids of three symmetry-related PA2721 homodimers contribute to the binding of bis-tris-propane (Figure 25 B). The difference electron density of 4-nitrocatechol was clearly interpretable with one conformation of the fragment (Figure 25 F). It had an occupancy of 79 % (Table 15). This fragment is complexed between two symmetry-related homodimers via three direct H-bonds (Figure 25 H). The fragment is further stabilized by π-alkyl interactions established by two ALA and one ARG side chain with the aromatic ring of the fragment (Figure 25 G). Barbituric acid is also bound between two symmetry-related homodimers (Figure 25 J). It reaches an occupancy of 76 % (Table 15). Direct and indirect H-bonds stabilize the interaction of protein and ligand (Figure 25 I).

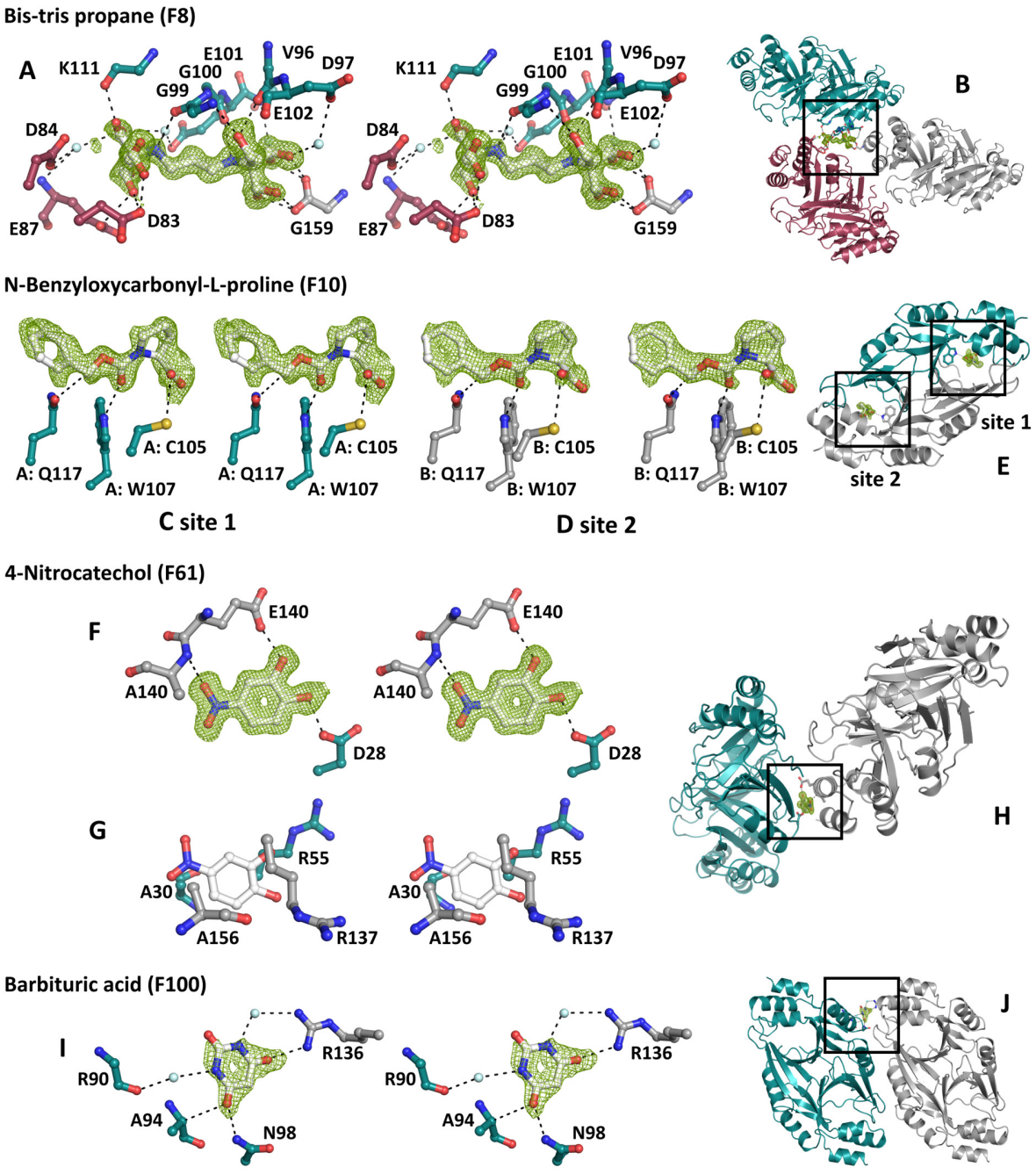

Figure 25: Binding mode of FS hits to PA2721. The left side (A, C, D, F&I) are stereo images of the unbiased mFo-DFc difference electron density contoured at 2.5 σ with the respective fragments and the amino acid residues that interact with the fragments. Amino acids of distinct protein chains are colored differently. Waters are represented as light blue spheres. H-bonds with a maximum distance of 3.2 Å are shown as black dashed lines. G) Amino acids that are participating in the binding of 4-nitrocatechol by alkyl interactions. The right side (B, E, H & J) displays the location of the fragments in the overall structure. Symmetry related homodimers of PA2721 have different colors (B, H&J). In E, each monomer of PA2721 is colored differently.

The only compound that was discovered in the potential binding site of PA2721 was N-benzyloxycarbonyl-L-proline. It occupied the equivalent binding tunnels of the protein dimer (Figure 25 E). Both ligands are complexed by equivalent residues and have similar occupancies. The occupancies for the fragment in site 1 was 92 % for the fragment in site 2 it was 96 % (Table 15). The strongest interactions are three H-bonds. They are formed between the W107 side chain and the fragment's carbonyl oxygen and between the C105 side chain and the carboxyl of the proline moiety. The third H-bond is formed between the side chain carbonyl of Q117 and the fragment (Figure 25 C/D). Since most fragments are complexed between symmetry-related protein chains that do not occur in solution their binding mode in the crystal likely is a crystallographic artefact and therefore not relevant. The only functionally relevant hit is CBZ-Pro that occupies the potential ligand-binding site of the protein.

4.1.1.4.2 Functional relevance of N-benzyloxycarbonyl-L-proline binding to PA2721

CBZ-Pro is the first ligand found to bind in the binding tunnel of PA2721, suggesting that this fragment has some chemical features of the protein's substrate. The fragment is complexed by equivalent residues in both binding tunnels such that only one site will be analyzed here (Figure 26). The side chain of the fragment's proline moiety is stabilized by alkyl-interactions mediated by the protein side chains L50 and L64 and by π-alkyl interactions with Y41. The benzene ring establishes only rather week hydrophobic interactions with the surrounding residues (M142, I127 and T119). One of the three H-bonds is formed between one proline carboxyl-oxygen and C105. Since this CYS residue might play a major role in the proteins function as discussed earlier (4.1, Figure 18 B), this interaction indicates a functional importance for the carboxyl-moiety of CBZ-Pro.

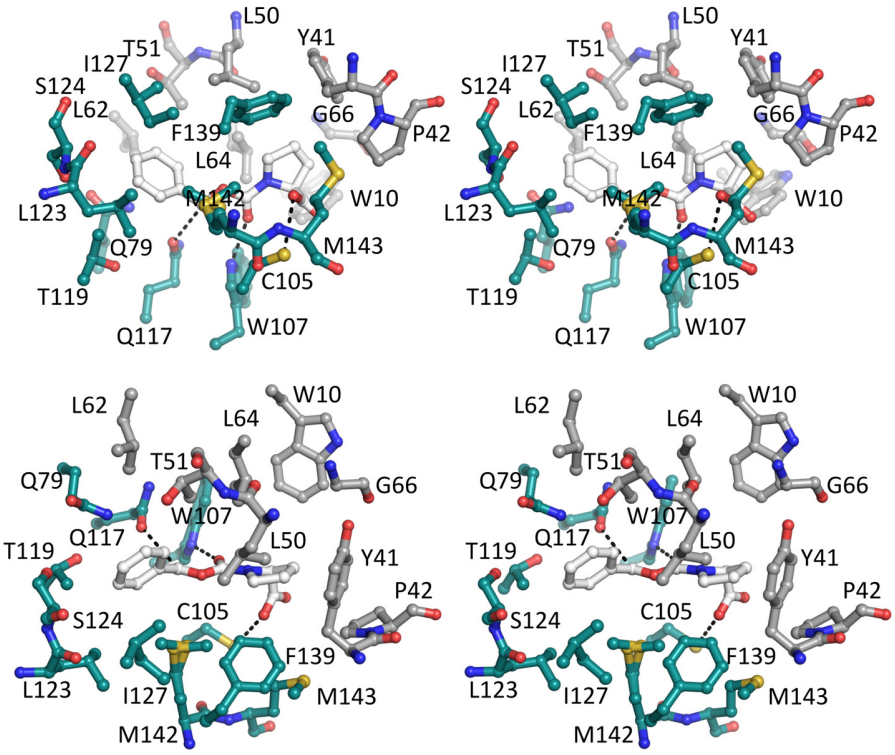

Figure 26: Stereo view of the potential binding site of PA2721 occupied with CBZ-Pro represented in different orientations. Amino acids surrounding the ligand (white) are displayed in balls and stick representation. The amino acids of chain A are colored in teal and the residues of chain B in grey. H-bonds with a maximum distance of 3.2 Å are shown as black dashed lines.

The HZB 96-fragment library contains four other proline derivatives (Figure 27) that were not discovered in the electron density. They all contain the carboxyl-oxygen of the proline-moiety that H-bonds with the C105 residue of the protein. The two smaller compounds 4-hydroxyl-L-proline and pyroglutamic acid have an additional hydroxyl- or carbonyl at the proline-ring, which might destroy the alkyl interaction between the proline and the protein. At the same time, there are no residues nearby that could form new H-bonds with the hydroxyl- or the carbonyl, such that the one possible H-bond that could be established seems to be insufficient for the complexation of these fragments. N-acetyl-L-proline and glycyl-L-proline still share the second carbonyl oxygen that mediates the H-bond with W107 and have no modifications at the proline, such that the alkyl interactions could also be preserved and the additional amino group in glycyl-L-proline might even be able to mediate the third H-bond with Q117. Nonetheless, both did not bind to the protein under the soaking conditions. This suggests that the aromatic benzyl-moiety is an important part of the compound. This indicates that longer molecules that occupy larger parts of the protein tunnel have a higher affinity to the protein and can bind.

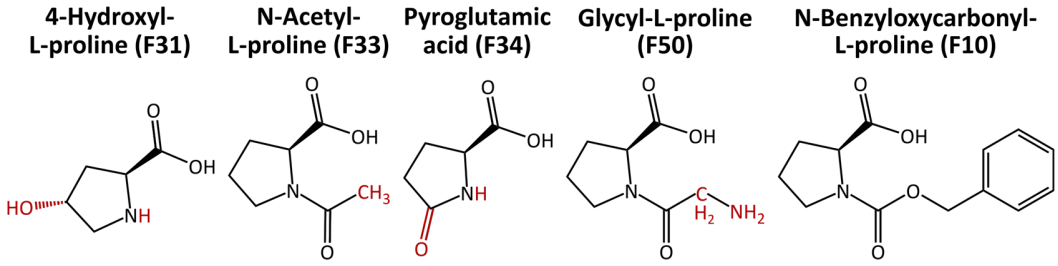

Figure 27: Proline derivatives from the HZB 96-fragment library with their fragment ID in brackets. Parts of the molecules that are different to N-benzyloxycarbonyl-L-proline are marked red.

MST-measurements for determining the dissociation constant (K_D) were conducted to determine the affinity of CBZ-Pro to PA2721 (Figure 28). The titration of CBZ-Pro from a maximum ligand-concentration of 5 mM did not result in a binding curve. This means that the K_D is either above 5 mM or the ligand only binds to the protein under the soaking conditions. Based on the chemical structure of the fragment one could search for similar natural compounds to perform a second screening to identify better binding ligands and get a better impression of the natural substrate.

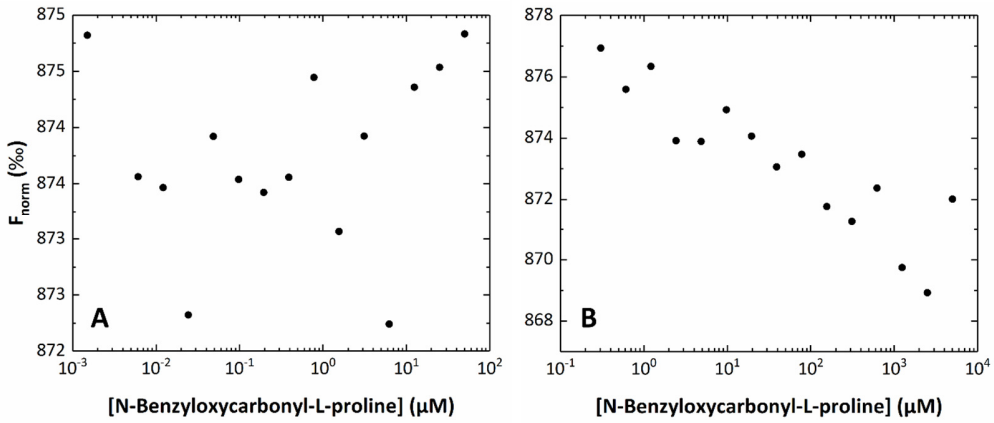

Figure 28: MST results of PA2721 with N-benzyloxycarbonyl-L-proline. The normalized fluorescence (F_{norm}) is plotted against the concentration of N-benzyloxycarbonyl-L-proline in µM. The measurement was conducted at 293 K as a 1:1 dilution series with highest ligand concentrations of 50 µM (A) and 5 mM (B) in standard capillaries. The buffer consisted of 50 mM Tis/HCl pH 7.4, 150 mM NaCl, 10 % (w/v) DMSO and 0.5 mg/ml BSA. The concentration of PA2721 was 200 nM. The LED- and MST-power were 20 %.

N-benzyloxycarbonyl-L-proline is a competitive substrate analogue inhibitor for human prolidase (King *et al.*, 1989; Lupi *et al.*, 2005). Prolidase is a metallo-peptidase that cleaves di-peptides with C-terminal proline or hydroxyproline in the final stages of protein catabolism. Prolidase inhibitors are used to simulate the effects caused by prolidase deficiency in humans that causes a variety of sever clinical symptoms (Myara *et al.*, 1984; Wilk *et al.*, 2017). The

comparison of prolidase active site and the N-benzyloxycarbonyl-L-proline binding site in PA2721 revealed no similarities. This indicates that PA2721 cannot fulfill the function of metallo-peptidases that are also able to interact with N-benzyloxycarbonyl-L-proline.

4.1.2 PA2722

4.1.2.1 Protein purification

The predicted Gfa PA2722 is a 130 aa protein with a theoretical MW of 14.6 kDa (Winsor *et al.*, 2016) and was first purified in this study. It was expressed in soluble form in *E. coli* with an N-terminal His_6-purfication tag and isolated via a three-step purification, during which the His_6-tag was removed by TEV-cleavage leaving two extra amino acids (GLY and HIS) at the N-terminus. The final yield was 11 mg of highly pure PA2722 per liter cell culture (Figure S1), suitable for crystallization and biochemical assays.

4.1.2.2 From crystallization to structure refinement

Good quality crystals grew in the initial screen (Figure 29 A). One of them was used to confirm the presence of the predicted Zn^{2+}-ions by an X-ray fluorescence scan (Figure S9). Based on this, Zn-SAD data were collected with reasonable overall diffraction (2.4 Å) and enough anomalous signal (3.4 Å) for phasing the structure of PA2722 (Table 16). Optimization enhanced crystal quality (Figure 29 B/C) and resulted in a high-resolution structure (1.25 Å).

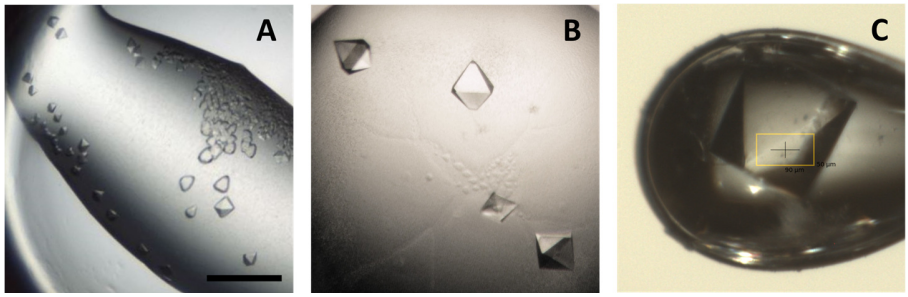

Figure 29: PA2722 crystals. A: Initial crystals in 0.1 M MES pH 6.5, 12 % (w/v) PEG20000 used for anomalous phasing at BESSYII. Scale bar: 300 µm. B: Optimized crystals in 0.1 M MES pH 6.3, 14 % (w/v) PEG20000. C: Optimized crystal during data collection at SLS.

Full data collection, processing and refinement statistics are listed in Table 16. Since the space group, cell parameters and structures were the same for the initial and the high-resolution model, only the latter was fully refined to a final R_{cryst} of 13.55 % and R_{free} of 15.12 %. The ASU

contained 8 molecules of PA2722, which corresponds with the calculated Matthews coefficient (Matthews, 1968) of 2.6 Å/Da and a solvent content of 53 %. The electron density was well interpretable so that all 130 amino acids of the eight protein chains in the ASU including the extra N-terminal residues GLY and HIS were modelled.

Table 16: PA2722 data collection and processing statistics at Zn-peak wavelength (Zn-SAD) and for high-resolution (Native) data as well as structure refinement statistics of the high-resolution data.

Data collection and processing	Zn-SAD*	Native	Structure refinement	Native
Beamline[†]	BL14.1, BESSYII	X06DA, SLS	**Resolution range (Å)**	47.79-1.25
Detector	Pilatus 6M	Pilatus 2MF	**Completeness (%)**	99.7
Wavelength (Å)	1.282416	1	**Final R_{cryst}**	13.22
Temperature (K)	100	100	**Final R_{free}**	14.75
Crystal-detector distance (mm)	313	135	**No. of reflections**	
Rotation range per image (°)	0.2	0.1	**Working set**	344867
Total rotation range (°)	1200	360	**Test set**	17486
Exposure time per image (s)	0.2	0.1	**No. of non-H atoms**	
Space group	$P2_12_12_1$	$P2_12_12_1$	**Protein**	8837
a, b, c (Å)	84.76 85.24 170.7	84.62 86.25 172.04	**Ion**	16
α, β, γ (°)	90 90 90	90 90 90	**Buffer molecule**	240
Mosaicity (°)[#]	0.17	0.05	**Water**	1960
Resolution range (Å)	47.32-2.48 (2.48-2.40)	47.79-1.25 (1.27-1.25)	**Total**	11053
			R.m.s. deviations	
Total No. of reflections	2145819 (186060)	4505463 (178863)	**Bonds (Å)**	0.011
No. of unique reflections	48303 (4349)	345072 (16564)	**Angles (°)**	1.224
Completeness (%)	98.4 (97.3)	99.8 (97.4)	**Average B-factor (Å²)**	
Multiplicity	44.4 (42.8)	13.1 (10.8)	**Protein**	16.58
Mean I/σ(I)	17.7 (2.9)	19.2 (2.6)	**Ion**	10.73
CC1/2[+]	99.9 (82.7)	99.8 (80.7)	**Buffer molecule**	27.43
R_{pim}[$]	4.3 (29.2)	2.2 (29.5)	**Water**	32.81
R_{meas}[¥]	28.6 (192.7)	7.9 (98.9)	**Ramachandran plot**	
Wilson B-factor (Å²)	29.9	10.1	**Favored regions (%)**	97.60
Phasing			**Outliers (%)**	0.0
Anom. Completeness	98.6 (97.4)		**MolProbity Score**[‡]	1.13
Anom. Multiplicity	23.0 (21.8)			

Values in parentheses are for the highest resolution shell, *Data collection statistics for unmerged Friedel pairs. [†]BESSYII (HZB, Berlin, Germany), SLS (PSI, Villigen, Switzerland), [#]Value as reported by *AIMLESS* (Evans & Murshudov, 2013). [+]CC1/2 as reported by (Karplus & Diederichs, 2012), [$]$R_{pim} = \Sigma_{hkl} (1/(N-1))^{1/2} \Sigma_i | I_i(hkl) - < I(hkl) > | / \Sigma_{hkl} \Sigma_i I_i(hkl)$; [¥]$R_{meas} = \Sigma_{hkl} (N/(N-1))^{1/2} \Sigma_i | I_i(hkl) - < I(hkl) > | / \Sigma_{hkl} \Sigma_i I_i(hkl)$, where N is the number of observations of the reflection with index hkl and I_i is the intensity of its i^{th} observation (Weiss, 2001). [‡]*MolProbity* score as reported by *MolProbity* (Chen *et al.*, 2010).

4.1.2.3 Topology and Oligomerization of PA2722

The crystal structure of one PA2722 monomer is dominated by a mixed, extremely curved eight-stranded β-sheet. A second antiparallel three stranded β-sheet (β_1-β_2-β_5) faces the anti-parallel arrangement (β_6-β_7-β_8-β_9) of the bigger β-sheet (Figure 30 A/B). This forms the core of the so called β-tent fold (Lupas *et al.*, 2015). This tent fold is stabilized by a conserved Zn-bind-

ing center. The Zn-binding center is at the top of the tent between two hairpin loops that connect the β_1- and β_2-strand and the β_7- and β_8-strand. This Zn^{2+} is tetrahedrally coordinated by CYS side chains with two being located on each hairpin (Figure 30 D).

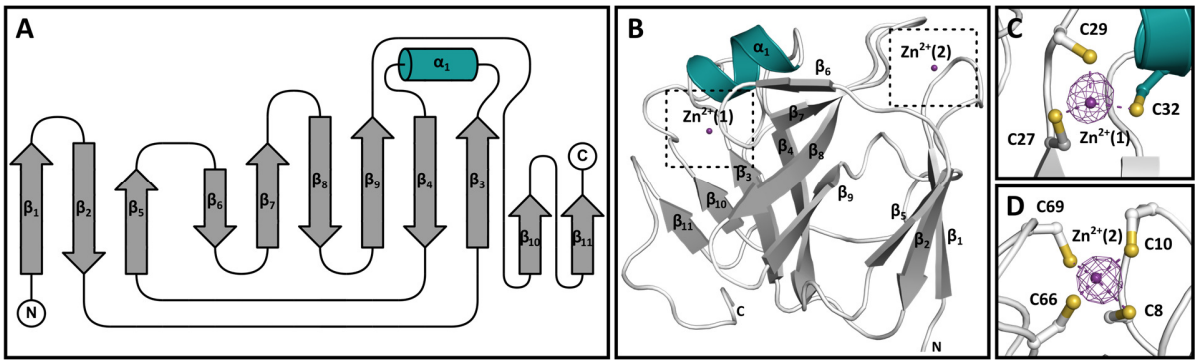

Figure 30: Topology of a PA2722 monomer. Secondary structure elements are numbered from N- to C-terminus. α-helices are colored in teal, β-strands are colored in grey and loop regions are white. Zn^{2+}-ions are colored purple. A) Schematically representation drawn with TopDraw (Bond, 2003). B) 3-D representation of the protein. C and D) are magnifications of both Zn^{2+}-binding centers with the complexing cysteine residues shown in ball and stick representation with sulfur atoms appearing in yellow. Dashed lines connect the Zn-ions with the complexing cysteine residues. Distances range from 2.29 to 2.36 Å. The anomalous Zn-electron density is shown in purple, contoured at 8 σ.

These CYS are usually found in two conserved CxxC-motifs, but PA2722 has a slightly modified CxC-motif on the first hairpin (Lupas *et al.*, 2015). Another conserved feature of β-tent fold proteins is a β-hairpin formed by β_3 and β_4 while extending the four-stranded β-sheet. The hairpin β-strands are connected by the only α-helix of PA2722 that is not part of the core β-tent fold. There, a second Zn-binding site is also tetrahedrally complexed by three CYS (Figure 30 B/C) and the additional N-terminal HIS side chain from a symmetry related monomer that remains from the purification tag after TEV-cleavage (Figure 31 C/D), suggesting a crystallographic artefact. As the tetrahedral coordination is the lowest possible for Zn^{2+} (Laitaoja *et al.*, 2013), the artificial HIS side chain must be replaced by another molecule *in vivo* to keep the Zn-binding site functional. In the simplest case the fourth ligand could be H_2O, which is in general the case for catalytically active Zn^{2+}-ions (Vallee & Auld, 1993). Next to that, the β_{10}- and β_{11}-strands not participating in the core tent-fold elongate the central β-sheet. A DLS experiment calculated a MW of 33.7 kDa for PA2722 in solution, which is consistent with the theoretical size of a dimer which would be 29.7 kDa. To identify the natural dimer among the 8 molecules in the ASU, the intermolecular contacts were evaluated and a analysis with the 'Protein interfaces, surfaces and assemblies' service PISA (Krissinel & Henrick, 2007) was performed.

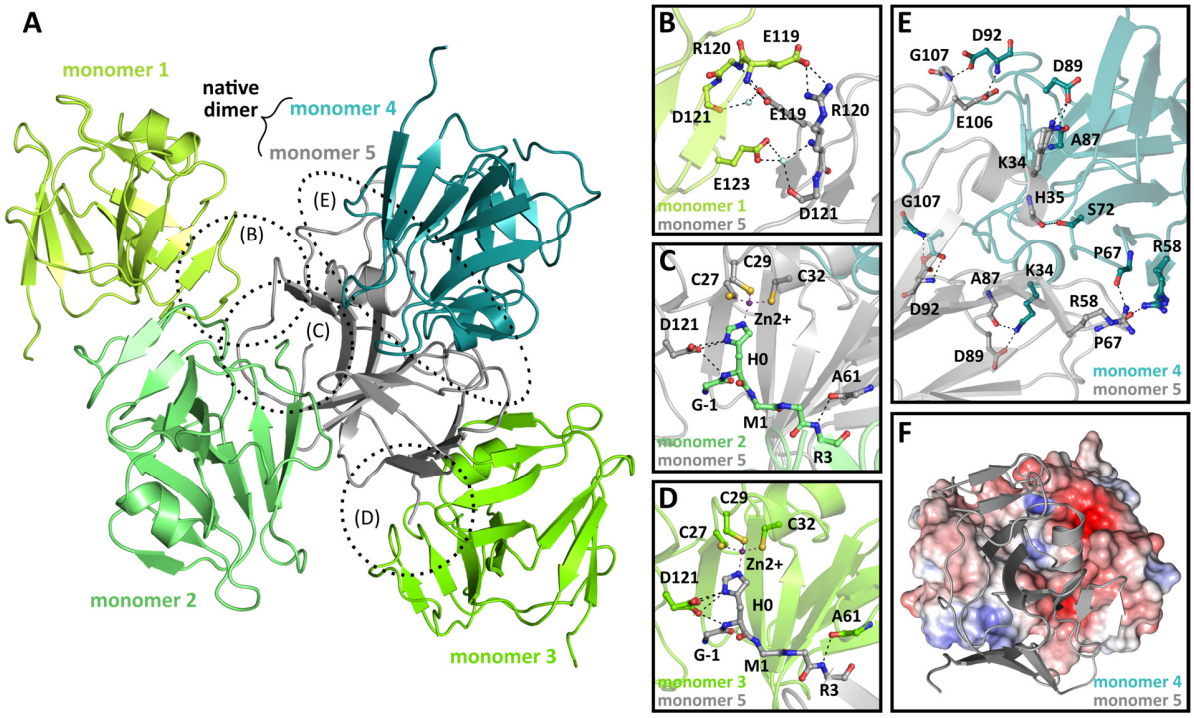

Figure 31: PA2722 monomers that contact each other in the ASU. A) Displayed are all four monomers 1-4 (different shades of green and teal) that interact with a central monomer 5 (grey). B-E) Representation of the interfaces that are encircled in A) but with rotated orientations. The parts of the residues that participate in H-bonds or salt-bridges are displayed as balls and sticks with oxygen atoms colored red, nitrogen blue and sulfur yellow. Black dashed lines are H-bonds or salt bridges with a maximum distance of 3.2 Å. Purple dashes connect the metal complexing residues with the Zn^{2+}-ion (purple sphere). Light blue spheres represent waters. F) Electrostatic potential from -5 (red) to 5 (blue) kT/e, as calculated by the PDB2PQR server Version 2.0.0 (Dolinsky *et al.*, 2004) of monomer 4 at the probable dimer interface between monomer 4 (teal) and monomer 5 (grey).

Each monomer contacts four other monomers (Figure 31). Interestingly, two of the contacts are mediated by the N-termini, especially by the interaction of the remaining nonnative G-1 and H0 of the purification tag. This includes the already mentioned complexation of the His-side chain with one of the Zn^{2+}-ions (Figure 31 C/D). While the third interface is only stabilized by indirect water-mediated and a few direct H-bonds (Figure 31 B) the fourth interface displays several H-bonds and salt bridges (Figure 31 E), together with a large uncharged interface (Figure 31 F). A PISA-analysis assigned the complex of monomer 4 and monomer 5 from Figure 31 A/E/F, as the only thermodynamically stable assembly in solution with a calculated value of 6.6 kcal/mol for the free energy of assembly dissociation (ΔG^{diss}), as ΔG^{diss}-values above zero determine assemblies as thermodynamically stable and with an interface of 1912 $Å^2$ that is four times larger than the next bigger interface. Therefore, monomer 4 and 5 most probably represent the native dimer in solution (Figure 31/32).

4.1.2.4 Comparison of PA2722 with Gfa/CENP-V like proteins

The newly identified PA2722 structure was compared to already characterized Gfa-like proteins to find evidence for a functional relation. A sequence-based BLAST analysis (Altschul *et al.*, 1997) revealed that PA2722 is highly conserved in the family of *Pseudomonadaceae* with more than 1000 genes coding for proteins similar to PA2722. Even the *P. aeruginosa* PAO1 strain itself has three more genes (*PA2702, PA4177, PA5465*) that encode predicted Gfa-like proteins, that share a protein sequence identity of 25-49 %. The PA2722 sequence is further conserved in prokaryotes like in other γ- (18 homologues), in α-proteobacteria (140 homologues) and in cyanobacteria (5 homologues).

Unfortunately, functional data are only available for more distantly related proteins, such as the already mentioned *Pd.* Gfa and the human centromere protein-V (CENP-V). Based on cellular studies *Pd.* Gfa (EC4.4.1.22) was declared as a carbon-sulfur lyase that was supposed to accelerate the spontaneous transfer of formaldehyde to reduced glutathione (GSH) to form S-hydroxymethylglutathione (HMG) as the first step of the formaldehyde detoxification pathway. This was hypothesized as a rather unusual mechanism where GSH is first covalently attached to the active site C56, thereby replacing the Zn^{2+}. However the actual reaction was supposed to occur at the detached Zn^{2+}, which becomes complexed by other glutathione molecules and the formaldehyde to polarize the respective bonds of formaldehyde and GSH to activate them for nucleophilic addition (Goenrich *et al.*, 2002; Neculai *et al.*, 2005). A later study could not find any evidence for the acceleration of this reaction through Gfa but confirmed the covalent modification of cysteine with glutathione (Hopkinson *et al.*, 2015). The centromere protein-V (CENP-V) is a two-domain protein with a C-terminal Gfa domain containing both conserved cysteine centers. CENP-V was found to be crucial for the hypercondensation of chromatin during mitosis (Tadeu *et al.*, 2008). Moreover, the mutation of its conserved catalytic site cysteine (Figure 32) inhibited the hypercondensation (Tadeu *et al.*, 2008) and confirmed the conserved functional importance of this residue in more distantly related Gfa-like proteins. Besides that, the importance of CENP-V for the directional motility of cells has been shown. It is based on protein-protein interactions between the Gfa-domain and microtubules (Honda *et al.*, 2009). These findings suggest that PA2722 might also be part of a protein-protein complex. However,

no structure of a CENP-V protein has been determined until now, such that the surface amino acid residues of PA2722 could not be compared with residues from the Gfa-like domain of CENP-V.

To search for structural homologs of PA2722 the structure similarity server PDBeFold (Krissinel and Henrick, 2004) was used. It identified only the *Pd.* Gfa and the functionally uncharacterized protein RSP_2168 from *Rhodobacter sphaeroides 2.4.1* (PDB-ID: 3FAC, to be published). A sequence alignment revealed that the sequences are non-homologous but that the Zn^{2+} complexing CYS residues are highly conserved. This includes the active site cysteine (C32 in PA2722) that was identified to play a crucial role for the activity of *Pd.* Gfa and hCENP-V and might therefore play an important role for the function of PA2722 as well. Despite the non-homologous sequences, the overall 3D-structure of the monomers are conserved. They share the characteristic β-tent core fold and PA2722 and the *Pd.* Gfa both contain the two additional β-sheets β_{10} and β_{11}. The location of both Zn-binding centers and the complexing cysteines are also conserved but no metal ions were implemented in the structure of RSP_2168. This stands in contrast to the F_o-F_c-electron density of RSP_2168, which revealed positive spots at the conserved metal binding sites. This indicates that metal ions were present in the structure but were not considered during refinement. In contrast to the conserved overall fold, the quaternary structures of PA2722 and *Pd.* Gfa are strikingly different. The Gfa from *P. denitrificans* is an experimentally confirmed dimer that has an alternative arrangement that is mediated by two additional α-helices in the C-terminal region (Figure 32). A consequence of this assembly is that the active sites of each monomer are facing each other and are combined to one big cavity. PA2722 and RSP_2168 are lacking the C-terminal helices and must thus assemble in an alternate way. The comparison shows that RSP_2168, which crystallized in the same space group and with a similar ASU content as PA2722, has the potential to form a similar dimer as PA2722 (Figure 32), however a PISA analysis (Krissinel & Henrick, 2007) stated that RSP_2168 appears to be a monomer in solution. As experimental data are lacking, no further statement upon the oligomerization state of RSP_2168 is possible. Either way, the potential active sites of RSP_2168 and PA2722 are independent on separate places of the protein dimer (Figure 32) or isolated in case of the monomeric state of RSP_2168 and are only half the size of the *Pd.* Gfa cavity.

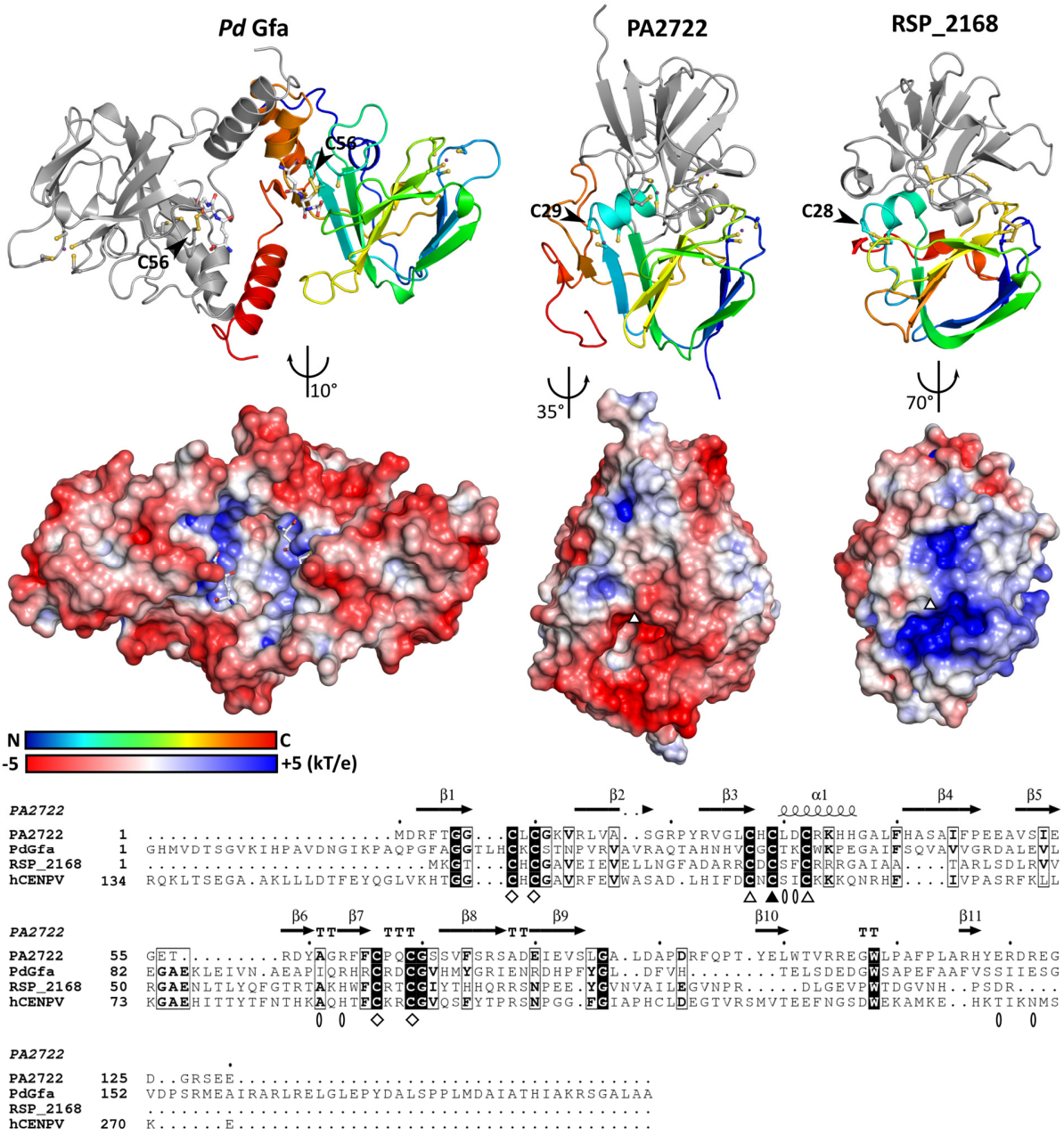

Figure 32: Comparison of PA2722 with other Gfa-fold proteins. The upper panel highlights the oligomerization forms of the Gfa from *P. denitrificans*, PA2722 and the possible, experimentally unconfirmed dimer of RSP_2168 in identical orientations. The monomer structures align with RSMD values of 2.7 Å for PA2722 vs. *Pd.* Gfa and with 2.4 Å for PA2722 vs. RSP_2168 (Holm & Laakso, 2016). One monomer is colored from blue to red (N- to C-term.) and the attached monomer in grey. Zn^{2+} are represented as violet spheres. The covalently attached glutathione in *Pd.* Gfa is represented as balls and sticks. The middle panel displays the electrostatic potential of the above proteins as calculated by the PDB2PQR server Version 2.0.0 (Dolinsky *et al.*, 2004). The triangles highlight the location of the potential active site cysteine. The lower panel shows the sequence alignment of the structural characterized proteins and the Gfa-like domain of hCENPV, as performed with Clustal Omega (Li *et al.*, 2015) and colored with ESPript 3.0 (Robert & Gouet, 2014). The secondary structure assignment is based on PA2722. Sequence identities between PA2772 and the other range from 24 % (hCENPV) to 18 % (RSP_2168). Diamonds highlight the structural relevant CYS and triangles highlight functional relevant CYS. The ovals mark the residues that are participating in *Pd.* Gfa glutathione binding.

4.1.2.5 Contraindications for a Gfa-like function of PA2722

As the *P. denitrificans* protein it is the only characterized Gfa from prokaryotes to date, it was the only lead to a functional prediction for PA2722. However, at first sight there are many differences, such as the dissimilar size and shape of the active/binding site cavities, which will most probably have a huge impact on the functionality (Figure 32, middle panel). Despite the obvious differences a detailed comparison of the potential active sites of *Pd.* Gfa and PA2722 with emphasis on the GS binding site was performed. The covalently attached GS is further stabilized by several H-bonds which are formed between GS and the side chains of S146, E149, T57, K58 and R98 and the main chain amine hydrogen of I94 (Figure 33 left).

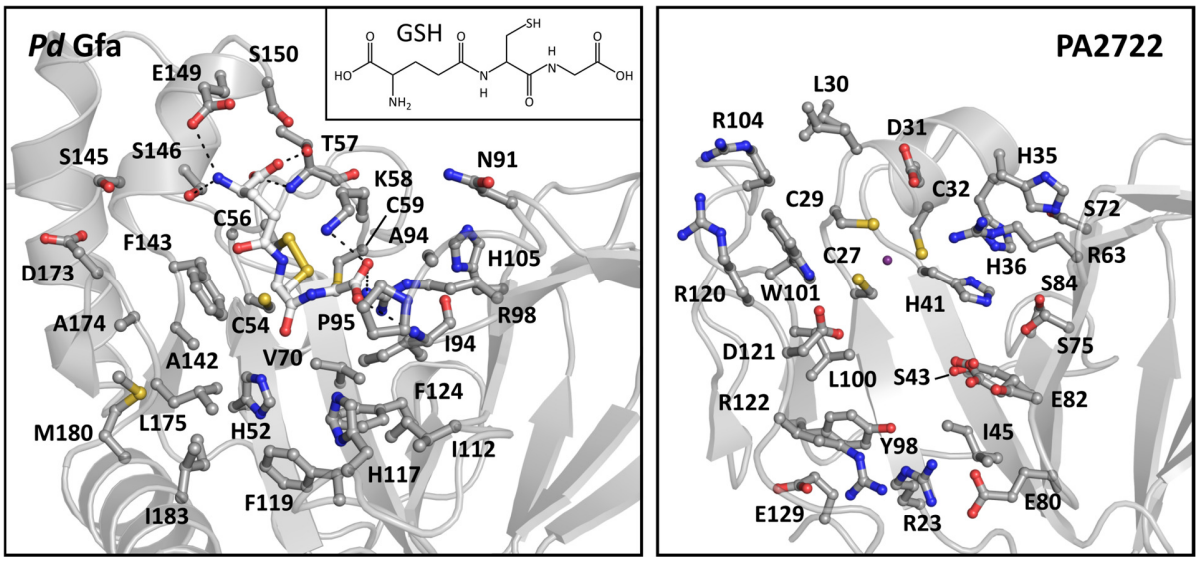

Figure 33: Potential active sites of *Pd.* Gfa monomer in glutathione (GSH) bound form (left panel, PDB-ID: 1XA8, Neculai *et al.*, 2005) and of a PA2722 monomer (right panel). The dashed lines in the left panel represent H-bonds with a maximal distance of 3.2 Å. The violet sphere represents the Zn^{2+}-ion. The residues in the binding cavity are shown as balls and sticks. Nitrogen atoms are blue, oxygen red and sulfur yellow.

From the sequence alignment, the only conserved GS binding residue was R98 (*Pd.* Gfa), which corresponds to R63 in PA2722. The position of these residues is also conserved in the 3D arrangement of the active site, as both are located at the N-terminal end of the β_7-strand. Since this remains the only similarity also with respect to the contrasting surface charges, (Figure 32, middle panel) it seems rather unlikely that GSH can interact with PA2722.

Nevertheless, several experiments were conducted to investigate if GSH and PA2722 can interact. A TSA gave some evidence to believe that GSH binds to PA2722, since the presence of GSH

increased the T_m of PA2722 (45 °C) by 1°, but MST measurements did not indicate any significant interaction. Besides, X-ray crystallography-based methods could not contribute in resolving the question of glutathione binding. The PA2722 crystals (Figure 29) were expected to be not suitable for soaking as the potential binding site was occupied by a buffer molecule and by the Zn^{2+}-coordinating H0 from a symmetry mate. Indeed, after soaking crystals with GSH no changes in the e^--density compared to unsoaked crystals were detected. Therefore, a cocrystallization experiment was set up that yielded weakly diffracting crystals only. The highest resolution obtained was 3.7 Å, which was not enough for an unambiguous identification of GSH in the electron density of the ligand-binding site. To find out if GSH can covalently modify PA2722 a MALDI mass spectrometry experiment was carried out. After the full-length protein was incubated with GSH (MW: 307.32 Da) it did not show a higher mass than the reference PA2722 not incubated with a ligand. Therefore, GSH did not covalently modify PA2722 under the tested conditions.

4.1.2.6 PA2722: from structure to function?

To derive a lead towards the potential function of PA2722 the protein's active site was examined. Extra mF_o-DF_c e^--density (Figure 34 A) was visible in the binding site. It was interpretable as two distinct molecules of 2-(N-morpholino)ethanesulfonic acid (MES) from the crystallization buffer. One MES molecule (MES1) is tightly complexed by several direct H-bonds. They are formed between two MES sulfate oxygen atoms and the sidechains of R234, R122 and Y98 and between the nitrogen and the oxygen of the morpholino part and the sidechains of E82 and C32 (Figure 34). The tight binding is reflected by the well interpretable e^--density (Figure 34 A) to which MES fits well with a RSCC of 0.99 and an occupancy of 100 %. A crystallographic artefact might cause the tight binding, because the non-native residues H0 and G-1 close the otherwise solvent exposed binding cavity and thereby enclose the MES molecule (Figure 34 C). The binding of MES1 in the active site could also assist in the mediation of this crystal contact as indicated by the H-bond that is formed between the N-terminal amine of G-1 and a sulfate oxygen atom of MES1 and thus promote the crystallization process (Figure 34 C).

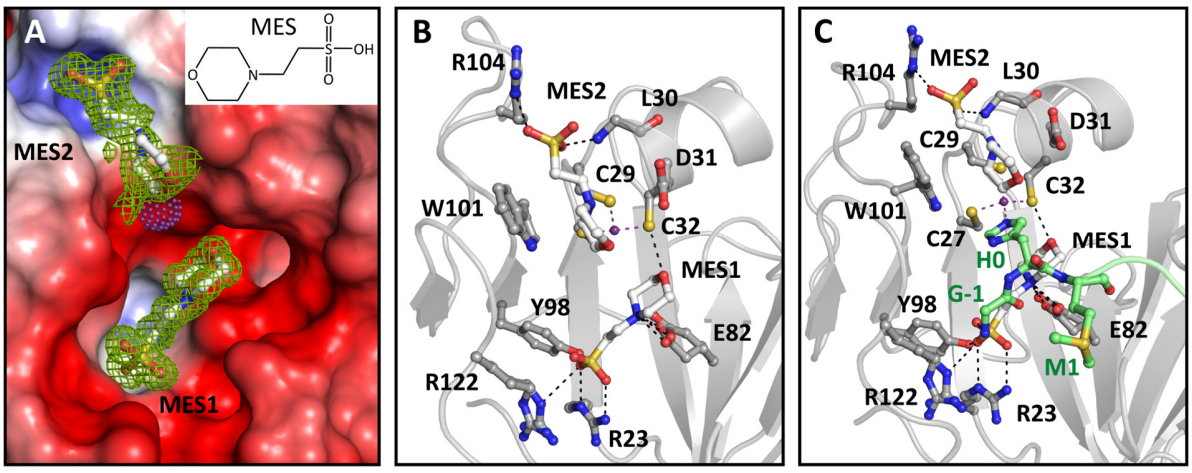

Figure 34: MES molecules in the potential binding site of PA2722. A) Electrostatic surface of the potential binding pocket of PA2722 with the unbiased mFo-DFc difference electron density contoured at 2.5σ that can be interpreted with MES molecules. The location of the Zn^{2+}-atom is marked by violet dots. B/C) Amino acids complexing MES molecules are shown as balls and sticks. Oxygen atoms are red, nitrogen are blue and sulfur are yellow. The violet sphere refers to Zn^{2+}. The violet dashes connect the Zn^{2+} with its complexing residues. Direct H-bonds between protein and ligand, with a maximum distance of 3.2 Å are shown as black dashed lines. C) The N-terminal part of a symmetry related monomer is displayed in green.

The other MES molecule (MES2) is only occupied by 75 %. It has a well interpretable e^--density for the ethanesulfonic acid part. It is stabilized by H-bonds that are formed between two sulfate oxygen atoms and the R104 side chain and the main chain nitrogen of L30 (Figure 34 A/B). The morpholino moiety is rather loosely bridged between W101 and D31 by π-cation interactions and attractive charges. Based on the close proximity of MES2 to H0 from a symmetry mate, the crystallization contact might also influence the interaction with the MES2 molecule (Figure 34 C). Nevertheless, the MES molecules probably share some chemical and structural properties with the actual binding partner of PA2722. Even if they do not provide a concrete image of the substrate they might assist in the identification of the real substrate.

4.1.3 PA2723

4.1.3.1 Protein purification and thermal stability

The *PA2723* gene codes for a 92 aa protein with an estimated molecular weight of 10.3 kDa (Winsor *et al.*, 2016). The purification of PA2723 was first described during this study and performed as for PA2722 (4.1.2). The final yield of PA2723 was 8 mg per liter of cell culture with a high final purity (Figure S1). Interestingly, the protein starts to precipitate at protein concentrations that exceed 3.4 mg/ml. Nevertheless, the protein was stable in the used buffer with a melting temperature of 59 °C as verified with a TSA (Figure S8).

4.1.3.2 From crystallization to structure refinement

Initial screening hits were optimized (Figure 35 A) but the crystals were still multi-layered and had an insufficient diffraction quality. The application of additive screens gave reasonable crystals and diffraction data quality. A crystal grown in 19% (w/v) PEG3350, 0.3 M $CaCl_2$ supplemented with 0.2% (w/v) caffeine/cytosine/nicotinamide/gallic acid monohydrate/sodium pyrophosphate tetrabasic decahydrate, 0.02 M Hepes pH 6.8 (Silver Bullets E1, Figure 35 B) diffracted best with a maximum resolution of 1.35 Å (Table 17).

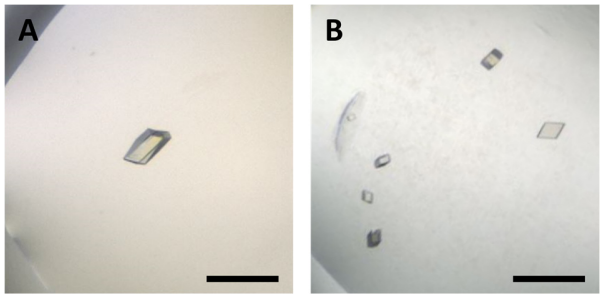

Figure 35: PA2723 crystals. A: Initial crystals in 0.2 M $CaCl_2$, 20 % (w/v) PEG3350. B: Optimized crystals in 19% (w/v) PEG3350, 0.3 M $CaCl_2$ supplemented with 0.2% (w/v) caffeine/cytosine/nicotinamide/gallic acid monohydrate/sodium pyrophosphate tetrabasic decahydrate, 0.02 M Hepes pH 6.8. Scale bar: 200 µm.

Since no homologous structures were available for PA2723, the phasing was done *ab initio* with the program Arcimboldo LITE (Rodríguez *et al.*, 2009). The crystal structure contained two molecules of PA2723 in the ASU and was refined to a final R_{cryst} of 15.91 % and an R_{free} of 18.02 % (Table 17). The Matthews coefficient (Matthews, 1968) for two molecules per ASU was calculated to a rather low value of 1.78 Å/Da, which corresponds to a solvent content of only 31 % indicating that PA2723 is rather densely packet. The electron density was well interpretable such that all 92 aa of both protein chains in the ASU including the extra N-terminal residues G-1 and H0 were modelled.

Table 17: PA2723 data collection, processing and refinement statistics

Data collection and processing	PA2723	Refinement	PA2723
Beamline[†]	P11, Petra III	**Resolution range (Å)**	39.39-1.35
Detector	Pilatus 6MF	**Completeness (%)**	94.03
Wavelength (Å)	1.033	**Final R_{cryst} (%)**	15.91
Temperature (K)	100	**Final R_{free} (%)**	18.02
Crystal-detector distance (mm)	172	**No. of reflections**	
Rotation range per image (°)	0.2	**Working set**	30262
Total rotation range (°)	288	**Test set**	1500
Exposure time per image (s)	0.2	**No. of non-H atoms**	
Space group	P1	**Protein**	1466
a,b,c (Å)	33.00 33.03 41.34	**Ion**	1
α,β,γ (°)	93.92 103.17 118.33	**Water**	255
Mosaicity (°)[#]	0.19	**Total**	1722
Resolution range (Å)	39.39-1.35 (1.37-1.35)	**R.m.s. deviations**	
Total No. of reflections	105451 (4731)	**Bonds (Å)**	0.009
No. of unique reflections	30273 (1508)	**Angles (°)**	1.243
Completeness (%)	94.0 (91.7)	**Average B factors (Å²)**	
Multiplicity	3.5 (3.1)	**Protein**	15.09
Mean I/σ(I)	17.7 (1.7)	**Ion**	20.07
CC1/2[+]	99.9 (73.1)	**Water**	28.81
R_{pim}[$]	2.3 (54.9)	**Ramachandran plot**	
R_{meas}[¥]	4.4 (100.1)	**Favored regions (%)**	97.28
Wilson B factor (Å²)	8.6	**Outliers (%)**	0
		MolProbity score[‡]	1.17

Values in parentheses are for the highest resolution shell, [†] Petra III (DESY, Hamburg, Germany), [#] Value as reported by *AIMLESS* (Evans & Murshudov, 2013). [+] CC1/2 as reported by (Karplus & Diederichs, 2012), [$] $R_{pim} = \Sigma_{hkl} (1/(N-1))^{1/2} \Sigma_i | I_i(hkl) - < I(hkl) > | / \Sigma_{hkl} \Sigma_i I_i(hkl)$ (Weiss, 2001); [¥] $R_{meas} = \Sigma_{hkl} (N/(N-1))^{1/2} \Sigma_i | I_i(hkl) - < I(hkl) > | / \Sigma_{hkl} \Sigma_i I_i(hkl)$, where N is the number of observations of the reflection with index hkl and I_i is the intensity of its i^{th} observation (Weiss, 2001). [‡] *MolProbity* score as reported by *MolProbity* (Chen *et al.*, 2010).

4.1.3.3 Architecture of PA2723

The overall structure of one PA2723 monomer revealed a central three-stranded antiparallel β-sheet (β1, β2, β3) flanked by three α-helices α1, α2 and α3 (Figure 36 A/B). The two molecules in the ASU are connected by a variety of H-bonds that are mediated between the two β_2-strands of monomer A and B and thus create a central six-stranded antiparallel β-sheet (Figure 36 C/D). Further, side chains and main chain atoms of β_2-strand amino acids are H-bonding with side chains that belong to α_2-helices of both monomers (Figure 36 F/G). Besides that, a dense H-bond network connects the amino acids at the N-terminal parts of both α_3-helices, the preceding loop regions as well as some amino acids of both β_2-strands and of β_3-strand of monomer A (Figure 36 E/H).

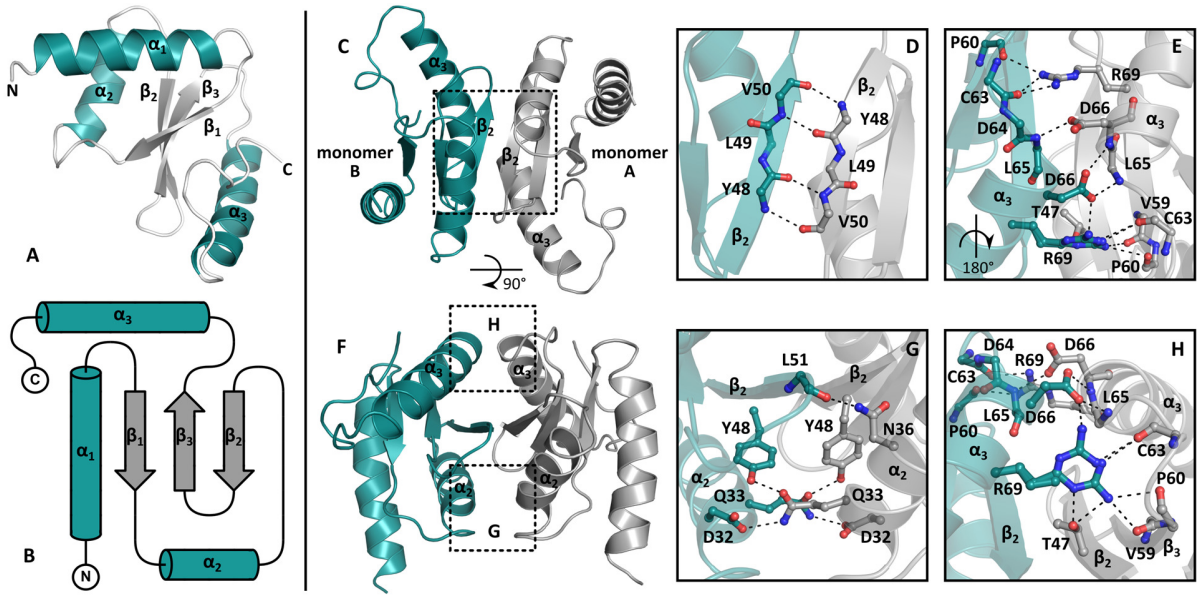

Figure 36: Architecture of PA2723. A/B) Topology of the monomer. Secondary structure elements are numbered from N- to C-terminus. Alpha helices are colored in teal, β-strands are colored in grey and loop regions are white. A) Representation of the 3D arrangement. B) Schematically representation drawn with TopDraw (Bond, 2003). C/F) Content of the ASU in different orientations. Monomer B is colored in teal and monomer A is colored grey. D/E/G/H) Enlargement of regions in which H-bonds are formed between both monomers in the ASU. H-bonds with a maximum distance of 3.2 Å are displayed as dashed lines. Oxygen atoms are colored red and nitrogen atoms are blue.

A vast number of interactions between the monomers in the ASU, which are not formed to other symmetry related proteins suggest that the molecules in the ASU represent the actual oligomerization state of PA2723. Unfortunately, it was not possible to verify the dimeric state of the protein in solution experimentally. DLS did not give a result because the protein sample was polydispers and the calculated MW from the analytical SEC was 15.1 kDa (Figure S7) which is right in between the monomer (10.5 kDa) and a possible dimer (21 kDa). A PISA analysis (Krissinel and Henrick, 2007) indicated that the content of the ASU may or may not be thermodynamically stable in solution, as the ΔG^{diss} had a slightly negative value of -0.6 kcal/mol.

4.1.3.4 Calcium binding site

The actual oligomerization state would also have a decisive influence on a potential metal binding site that is located between the N-terminal tips of the α_3-helices from both monomers in the ASU. There, a spherical mFo-DFc electron density could not be explained by a water molecule, as the electron density remained positive after refinement. The binding site is located at a negatively charged spot on the protein surface, suggesting that a cation binds there. Potential

candidates from the crystallization buffer (Table 11) were Na^+ and Ca^{2+}, but only Ca^{2+} had enough electrons to interpret the e^--density. The calcium is coordinated by seven atoms in an octahedral geometry. The carboxyl oxygen of D66 (chain B) mediates a bidentate interaction. A carboxyl oxygen of D64 (chain B) and of D66 (chain A) as well as three water molecules occupy the other coordination sites (Figure 37).

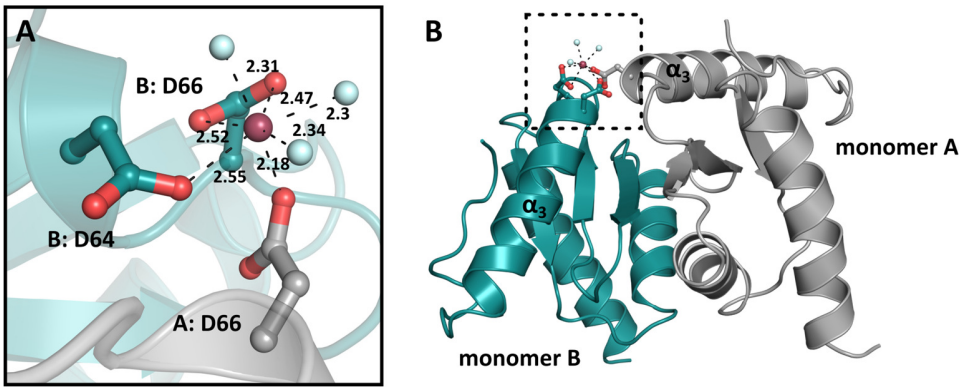

Figure 37: PA2723 Ca^{2+}-binding site. A) Close up of the amino acid side chains and waters (blue spheres) that are complexing the Ca^{2+} (red sphere). The distances are given in Å. B) Location of the Ca^{2+}-binding site on the overall structure.

The octahedral geometry of the Ca^{2+}-binding site, which is constituted by carboxylate side chain oxygen atoms, represents the typical environment of Ca^{2+}-ions complexed in protein structures (Zheng *et al.*, 2008) and supports the identity of the metal. The same accounts for the distances between the calcium and the carboxylate and the H_2O oxygen (Figure 37 A). A further analysis with the metal binding site validation server checkMyMetal (Zheng *et al.*, 2014, 2017) confirmed the identity of the metal as Ca^{2+}. It is not clear if the presence of a metal-ion in the PA2723 structure has any functional or structural relevance since the ion-binding site would be disrupted if PA2723 is a monomer in solution. It is also possible that the binding site is a crystallographic artefact, provoked by the high concentration of 300 mM $CaCl_2$ in the crystallization condition.

4.1.3.5 PA2723 adopts the R3H domain fold

The online structure alignment tool PDBeFold (Krissinel & Henrick, 2004) was applied to find homologous structures. It detected only the NMR structure of the R3H domain of human sperm-associated antigen 7 (aa 37 to 130 of full-length protein, 10.59 kDa, PDB-ID: 2CPM),

which had more than 70 % of matching secondary structure elements. Both structures shared the same topology (Figure 38 A) and the core fold aligns with an RMSD of 3.6 Å (Holm & Laakso, 2016) while the sequence identity is only 7 %.

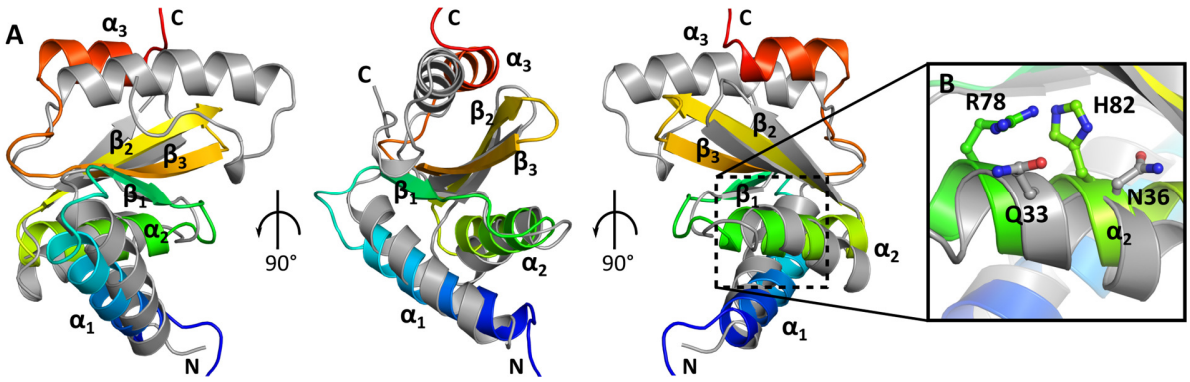

Figure 38: A) Overlay of a PA2723 monomer (grey) with the R3H-domain (rainbow coloring from the blue N-term. to the red C-term.) of human sperm-associated antigen 7 (PDB-ID: 2CPM) in different orientations. B) Enlargement of α_2-helices containing the conserved R3H-motif in the R3H-domain and the respective residues of PA2723 at the same position. Nitrogen atoms are blue and oxygen atoms are red.

R3H domains are named after their conserved R3H-motif on the α_2-helix. It consists of a conserved ARG- and HIS-residue that are separated by three other amino acids (Figure 38 B). R3H-domains are usually part of bigger protein complexes, where they mediate nucleic acid binding by the R3H-motif (Grishin, 1998; Jaudzems *et al.*, 2012). In PA2723 Q33 and N36 (Figure 38 B) replace the nucleic acid binding amino acids. This indicates that PA2723 does not have the same nucleic acid binding functions as other R3H-domains.

A further search conducted with DALI (Holm & Laakso, 2016; Holm & Rosenström, 2010) against the PDB archive revealed almost 500 hits with Z-scores above 3.0 and sequence identities between 3 and 16 %. The best hit (Z-score: 5.9) was the already described R3H-domain from sperm-associated antigen 7. Most of the other hits were either nucleic acid binding proteins or functionally uncharacterized and hypothetical proteins such that this search did not deliver new indications towards a potential function.

4.1.3.6 Protein surface mapping

To identify a potential active or ligand-binding cavity, the electrostatic surface of PA2723 was generated. The surface of the monomer and the dimer were analyzed separately since the oligomerization state is unclear (Figure 39 A/B).

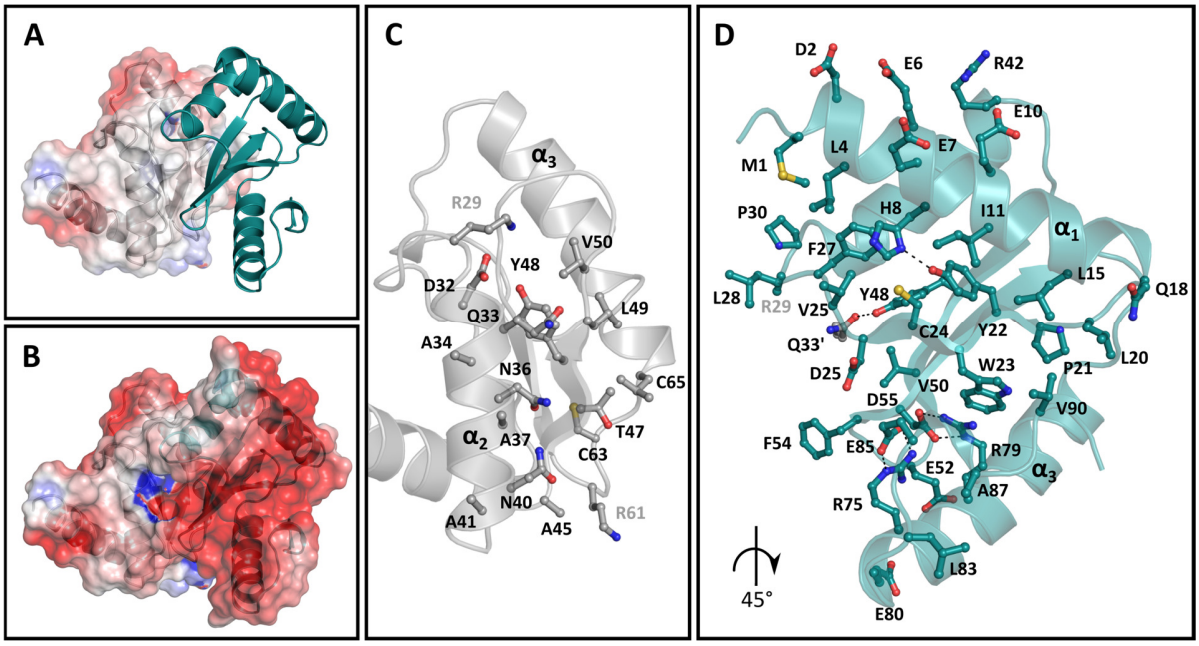

Figure 39: Surface mapping of PA2723. The monomers in the ASU are colored in gray and teal. The electrostatic surface of the grey monomer at the potential dimer interface (A) and of the whole dimer surface (B) is colored from red (-5 kT/e) to blue (5 kT/e). Amino acid side chains that are facing the dimer interface (C) and that are at the surface of a possible binding cavity are represented as balls and sticks. Nitrogen atoms are colored blue, oxygen atoms are red and sulfur atoms are yellow. Dashed lines are H-bonds with a maximum distance of 3.2 Å. The molecules from A, B and C are oriented equally and the monomer in figure D is rotated 45° along the y-axis. Flexible residues that were not modelled completely are highlighted by grey nametags.

The potential dimer interface was quite uncharged. This could indicate that this part is not solvent exposed but buried in the dimer interface and would support the dimerization of the protein. Besides that, the interface lacks any cavities and has only a low amount of potential functionally relevant amino acids. In general about two thirds of the residues that participate in catalysis are charged and one third are polar residues, while under 10 % are aliphatic (Bartlett *et al.*, 2002), but the potential interface comprised almost 50 % of aliphatic residues like ILE, LEU, VAL and ALA (Figure 39 C). The charged and polar residues are mainly distributed along the α2 and α3 helix including the already mentioned Q33 and N36 (Figure 39 C). However, most of those residues would participate in the dimerization and can therefore not be of functional relevance. An interesting part of PA2723 is the negatively charged pit between the α1 and the α3 helix (Figure 39 D). It is on the other side of the interface, is independent from the other monomer and is therefore not influenced by the dimerization. The most mentionable residues are H8, as HIS are most abundant in active sites (18 % of catalytic residues) (Bartlett *et al.*, 2002), Y22, which is in H-bonding distance to the HIS side chain, and C24 in the immediate

vicinity of these two residues. HIS and TYR side chains often participate in acid/base catalysis and HIS is known to activate catalytic water molecules, cofactors or other residues, while TYR often stabilizes transition states. CYS most often acts as a nucleophile during catalysis (Bartlett *et al.*, 2002). To see if this arrangement is important for the function of other enzymes the amino acid pattern search for substructures and motifs (ASSAM) server was run. It compares the 3D pattern of the input amino acids with the structures deposited in the PDB (Nadzirin *et al.*, 2012). In this case, H8, Y22, C24 and D25 were input. Several hits with near identical arrangement of respective residues were determined. The residues were found to be also sandwiched between an α-helix and a β-strand as in PA2723. However, the equivalent residues in other proteins were buried either in the protein or not near the active or ligand-binding site. Therefore, they were either not comparable to the situation in PA2723 or did not give new hints towards the function of the protein. Unfortunately, this was also true for cases were equivalent residues participated in ligand or metal binding. In most ligand binging sites HIS, TYR, CYS and ASP were part of a long tunnel that buried the ligand in the protein. Such a scenario would not be possible for PA2723 as the residues are exposed. Therefore, it stays unclear if the residues H8, Y22, C24 and D25, which are often found in enzyme active centers, participate in an enzymatic reaction, in ligand binding or if they just stabilize the overall structure. Other residues that are abundant in active sites like D55, R79 and E85, R75 interact with each other via salt bridges and might thus stabilize the overall structure. Four negatively charged residues along the surface of the α1 helix create a charged patch at the protein surface and could be of functional relevance, i.e. for a protein-protein interaction.

To derive functional relevant information from the structure, the coordinates were forwarded to the SPRITE-server (Nadzirin *et al.*, 2012). This revealed only one relevant pattern, as most identified motifs did not participate in ligand binding or catalysis of the respective proteins. The only conclusive hit was found in levansucrase (EC 2.4.1.10, PDB-ID: 1OYG, (Meng & Fütterer, 2003)). These bacterial proteins catalyze the synthesis of the polysaccharide levan. Relevant residues that are arranged as in PA2723 are the nucleophile D86 (equal to D55 in PA2723), the transition state stabilizer D247 (equal to D25 in PA2723) and the proton donor/acceptor E342 (equal to E85 in PA2723). The active site and the identified pattern of levansucrase are at the

bottom of a deep binding tunnel that is enclosed by several residues that mediate sugar binding (Martínez-Fleites *et al.*, 2005; Meng & Fütterer, 2003; Wuerges *et al.*, 2015). Since the much smaller PA2723 does not have a deep binding tunnel and lacks other residues that are important for sugar binding it is quite doubtful that PA2723 could fulfill a function comparable to the levansucrase.

4.1.4 Conclusion and Outlook

The experiments for the functional characterization of PA2721 delivered serval approaches for follow up experiments to identify the physiological role of this class III βαβββ-module protein. The comparative phenotypic characterization of the PAO1 *PA2721*::Tn mutant and the wt demonstrated that PA2721 plays no role for proper swimming and swarming motility and for the secretion of secondary metabolites like pyocyanin. The protein played no major role during central metabolism but might be involved in the proper catabolism of glycyl-L-proline if it is the only available carbon source. Glycyl-L-proline was not identified, as binding partner for PA2721 during a crystallographic fragment screening campaign, which seems to indicate that the protein does not directly interact with the ligand. Fragment screening identified only one out of 96 molecules that was able to bind in the potential binding tunnel of PA2721. Interestingly, this was the proline derivative N-benzyloxycarbonyl-L-proline. Since two independent experiments point to a connection between PA2721 and proline derivatives, proline metabolism is suggested as a good starting point to search for compounds that interact with the protein or are processed by it.

Chemical sensitivity assays indicated that PA2721 might indeed participate in the mediation of resistance mechanisms, since the PAO1 *PA2721*::Tn mutant had an altered respiration rate in the presence of compounds with antimicrobial activity. It was not possible to suggest a clear function because the identified compounds target different sites in the bacterium. However, many compounds lead to increased oxidative stress in bacterial cells. Therefore, PA2721 could contribute to anti-oxidant defense systems. The most promising leads were captan and dichlofluanid, which both covalently modified a potential catalytically active CYS in the binding tunnel. The mechanism that leads to the covalent modification and which part of captan and

dichlofluanid bind to the protein need to be identified. Mass spectrometry analysis to determine the total protein weight after the incubation with the compounds could be conducted to identify the mass of the attached molecule. High-performance liquid chromatography (HPLC) mass spectrometry could be used to analyze the reaction products after the compounds were incubated with and without the protein and be compared to respective standard molecules to identify the reaction products and if the compounds are hydrolyzed independent of the presence of the protein. Before PA2721 can be declared as captan and dichlofluanid resistance protein, the physiological relevance needs to be clarified. The chemical sensitivity assay supports this theory since *P. aeruginosa* is more susceptible to dichlofluanid in the absence of the protein but the result for captan contrasts with this. Therefore, the assays with dichlofluanid and captan should first be repeated to exclude that one of the results was a false positive or negative. Minimal inhibitory concentrations (MIC) should also be determined. One experiment to identify if PA2721 is specifically able to mediate the resistance towards both compounds would be a spot plate assay. For this, the protein could be expressed from a plasmid in *E. coli* cell cultures that are applied onto an agar plate supplemented with dichlofluanid or captan to assess if *E. coli* acquires resistance. Before one can identify a connection between all results from the PMs, the interaction with captan and dichlofluanid and the fragment screening the PMs with the other identified compounds also need to be repeated to exclude any false positives. Further, it is necessary to perform a rescue experiment with these compounds to see if the wt phenotype can be reconstituted by expression of PA2721 from a transformed plasmid in the PAO1 *PA2721*::Tn mutant. This could proof that the phenotype is solely caused by the loss of PA2721 and not by a spontaneous mutation in another gene. It would also rule out that the transposon insertion influences the expression of the downstream gene *PA2722* and be caused by a reduced amount of PA2722.

Next to the results that were obtained for PA2721, successful purification strategies for high amounts of pure recombinantly expressed PA2722 and PA2723 were established during this study. The high-resolution crystal structure of the dimeric PA2722 had the characteristic β-tent fold found in the Gfa/CENP-V-like protein family. This study did not find indications that the

glutathione formaldehyde activating function is conserved in PA2722, since the conducted experiments found no evidence for the interaction with glutathione. The only functionally characterized member of the Gfa-like protein family in prokaryotes has an alternative dimerization mode to PA2722 and a distinct glutathione-binding pocket. Therefore, it is likely that PA2722 fulfills a function that is independent of glutathione. PA2722 could even be part of a protein-protein complex, like the human CENP-V protein that also contains a predicted Gfa-like domain. Since PA2722 will not have the same target as the human protein, a pulldown assay with pseudomonal crude extract or a yeast two-hybrid screen could be applied to identify a potential protein interaction partner.

Crystallographic analysis of the unpredictable structure of PA2723 revealed that the protein does not display a novel fold but consists of a dimer of two R3H-like domains, which seems to be the first example of such a protein since R3H-like domains are usually part of multimeric proteins. Since the nucleic acid binding R3H-motif is not conserved in PA2723, it was not possible to suggest a potential function for PA2723. Especially in this case, a structure based functional prediction was very difficult, since the surface revealed no clear binding cavity for small molecules. A crystallographic fragment-based screening as performed with PA2721 would be an approach for an experimental surface mapping to discover residues or patches that are important for small molecule binding. However, the PA2723 crystals have to be checked if they meet the requirements for a fragment screening. It should also be considered that PA2723 may not interact with small molecules but with other proteins. A protein interaction partner could be identified by a pulldown assay in which PA2723 is immobilized to a matrix and exposed to *P. aeruginosa* cell lysate to bait a protein that has an affinity to PA2723. Alternatively, a yeast two-hybrid screen as suggested for PA2722 could also be applied here. The physiological role of PA2722 and PA2723 could also be investigated in microbiological assays as done for PA2721 with transposon insertion mutants that are available for both genes in the PA14 background.

4.2 PA1672

The class III βαββββ-module protein PA1672 (13.5 kDa, 126 aa) is encoded in an ORF that is not part of a bigger operon according to Wurtzel *et al.*, 2012. The structure of the homodimeric protein was initially determined and bioinformatically analyzed in a preceding study (Vit, 2015)

but no leads towards a potential function of PA1672 have been derived. Recently, the crystal structure of the βαβββ-module-containing protein Rv0577 (MW: 27 kDa, 261 aa) from *Mycobacterium tuberculosis* was discussed in the literature (PDB-ID: 3OXH, Buchko *et al.*, 2017). It belongs to the monomeric type that encodes four βαβββ-modules per protein chain with distinct binding sites. One site contained the conserved aromatic residues from class II proteins, but the second site had none of the conserved aromatic and metal-complexing residues and can be assigned to class III. Therefore, the focus was on the comparison between PA1672 and the second class III-like site of Rv0577 (Rv0577_S2, aa 141-261). The sequences that participate in each binding site were aligned individually to the sequence of PA1672 (Figure 40).

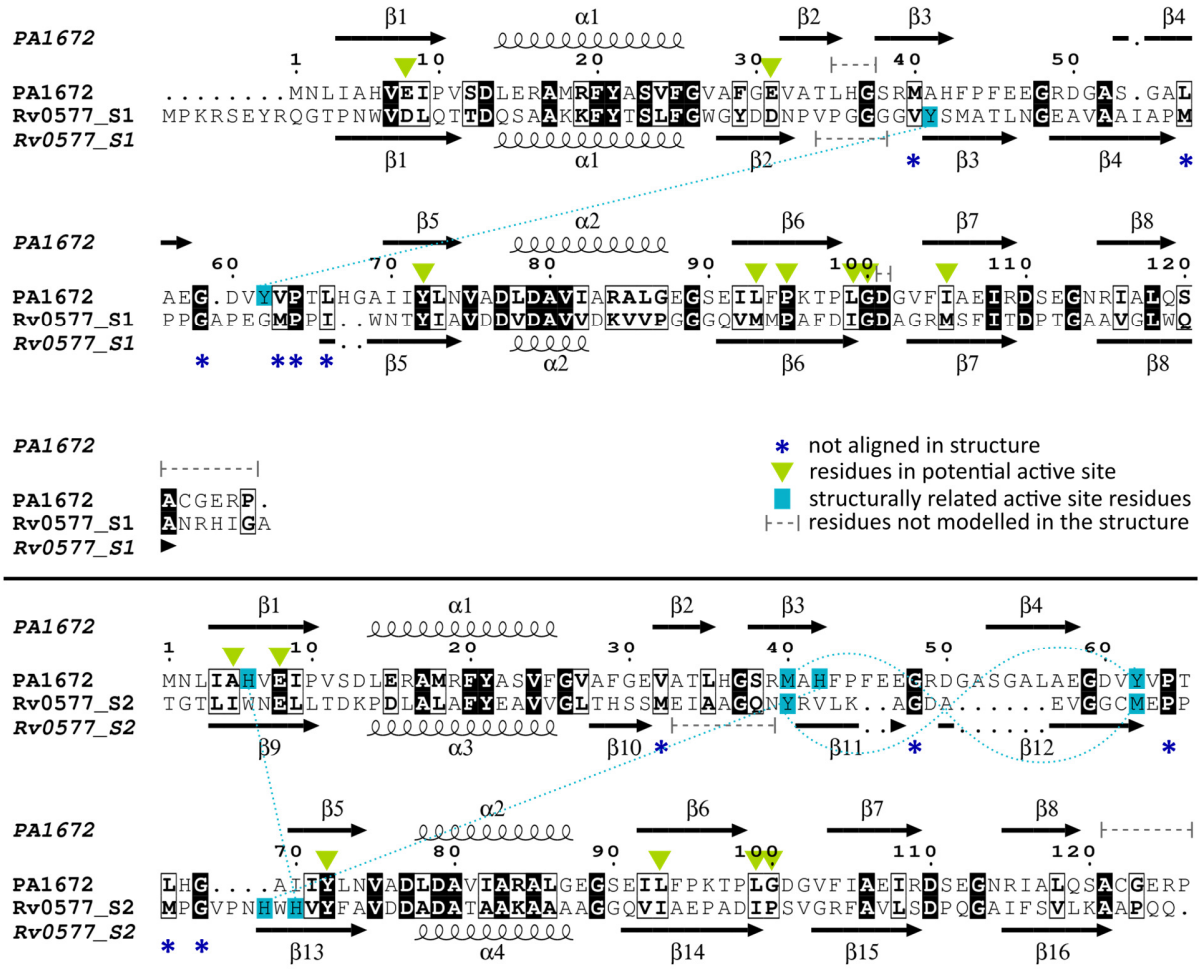

Figure 40: Sequence alignments of PA1672 with Rv0577_S1 (upper panel) and Rv0577_S2 (lower panel). Sequences were aligned with Clustal Omega (Li *et al.*, 2015) and colored with ESPript 3.0 (Robert & Gouet, 2014).

The sequence of PA1672 is not homologous (seq-ID:~20 %) to both sites of Rv0577 but based on the conserved βαββββ-fold the overall structures align fairly well (Figure 41 A, RMSD: 3.6 Å). However, only 6 of the conserved residues (Figure 40) point into the potential binding sites and most of them are aliphatic or hydrophobic amino acids, suggesting that these do not participate in enzyme catalysis but might rather contribute to ligand binding (Bartlett *et al.*, 2002; Holliday *et al.*, 2009). Conserved residues that could participate in catalysis (Bartlett *et al.*, 2002) are the polar Y72 and the negatively charged E8 from PA1672, which align with Y80 and D16 in the first binding site of Rv0577 (Rv0579_S1; Figure 40, upper panel) and with Y208 and E148 in the second (Rv0577_S2; Figure 40, lower panel). The direct comparison of all amino acids flanking the potential binding sites revealed that PA1672 has some similarities to Rv0755_S2 that were not conserved in the sequence alignment and that are not present in Rv0755_S1 (Figure 41).

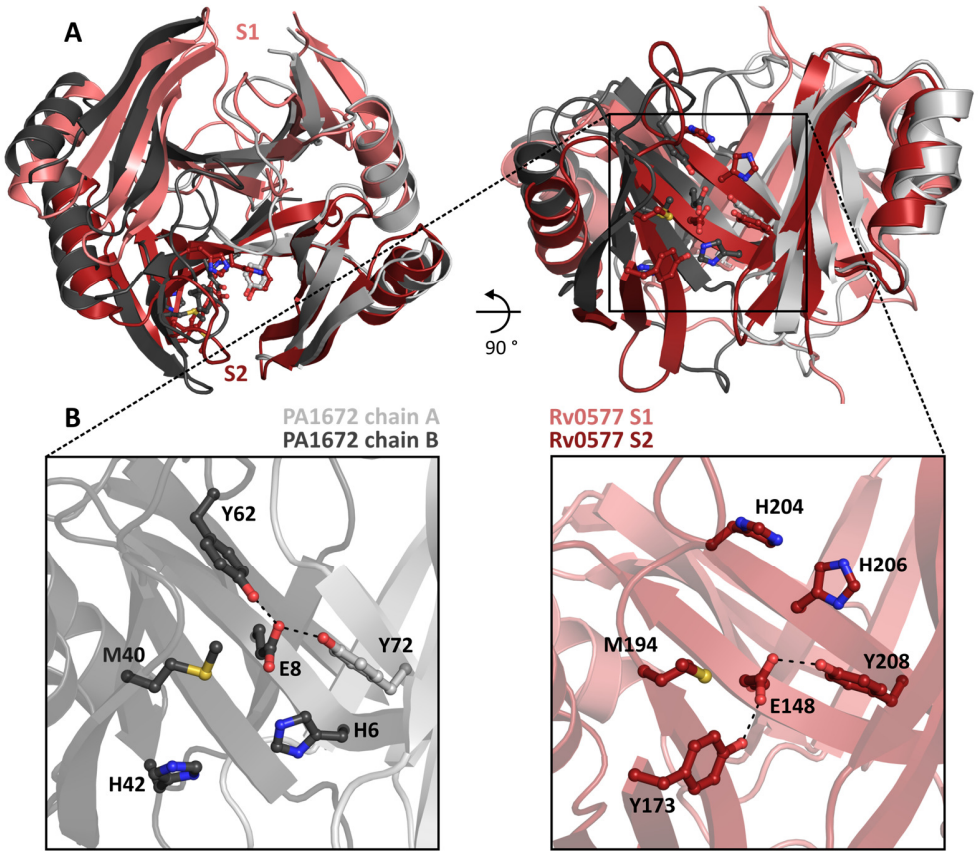

Figure 41: Crystal structures of βαββββ-module-containing proteins PA1672 (Vit, 2015) and Rv0577 (PDB-ID:3OXH, Buchko *et al.*, 2017). A) Overlay of the tertiary structures in different orientations (RMSD: 3.6 Å). B) Detailed insight in the aligned potential binding sites of PA1672 and Rv0577_S2. All figures show the binding sites of the monomeric Rv0577 in light (S1) and dark (S2) red, the monomers of PA1672 in light (chain A) and dark (chain B) grey and related amino acid residues from PA1672 and Rv0577 S2 are shown as balls and sticks. Dashed lines represent H-bonds with a maximum distance 3.2 Å.

In the structures, M40 of PA1672 aligns with M149 from Rv0577. Two HIS residues and a further TYR residue that is in H-bonding distance to the conserved GLU side chain are also present in both structures (Figure 41 B). They create a mirror-inverted but conserved amino acid pattern in both potential active sites. Since, HIS belongs to the most abundant catalytic residues together with charged amino acids, followed by residues with polar groups (Bartlett *et al.*, 2002), this pattern might play a crucial role in the function of both proteins. The rest of both binding sites are dominated by hydrophobic and unpolar aromatic amino acids that are partially aligning with each other (Figure 40, lower panel). Independent of the low sequence identity, these structural similarities between PA1672 and the second binding site of Rv0577 point to a similar function. Unfortunately, the molecular function of Rv0577 is not yet known, but the protein is secreted by *M. tuberculosis* (Rosenkrands *et al.*, 2000) and overexpressed during tuberculosis infections such that it is also discovered in the sputum of tuberculosis patients (Huard *et al.*, 2003). Moreover, Rv0577 was shown to interact with human Toll-like receptor 2 (TLR2), which leads to an altered immune response (Byun *et al.*, 2012). Since, Rv0577 has two distinct binding sites and is probably able to fulfill several functions, it is difficult to suggest which of the mentioned roles of Rv0577 could also be carried out by PA1672.

4.2.1 Phenotyping of a PA14 *PA1672*::Tn mutant

The physiological role of PA1672 was propped by comparative analysis of the PA14 wt and the *PA1672* transposon insertion mutant in the PA14 background (PA14 *PA1672*::Tn, Figure 42). The PA14 *PA1672*::Tn mutant from Liberati *et al.*, 2006 was kindly provided by Prof. S. Häußler of the HZI. PCR and sequencing of the PCR product confirmed the *MAR2xT7* transposon in the ORF of *PA1672* at bp 185 as stated by the manufacturer (Liberati *et al.*, 2006).

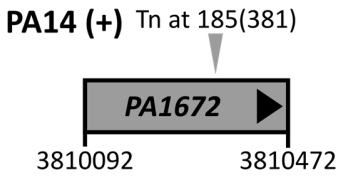

Figure 42: ORF of *PA14_42870,* which is the PA14 homologue of *PA1672* from PAO1. The genomic localization given in bp was derived from pseudomonas.com (Winsor *et al.*, 2016). The transposon insertion site (Tn) of the PA14 *PA1672*::Tn mutant used in this study is indicated by a grey arrow. The position of the insertion in the ORF is given in units of bp and the total length of the gene in brackets.

The phenotypes of the bacteria were characterized towards planktonic growth, swimming and swarming motility and on Phenotype MicroArrays™ towards the utilization of carbon-sources and towards their chemical sensitivity for antimicrobial compounds.

4.2.1.1 Planktonic growth and motility

The mutant had comparable planktonic growth and was able to migrate through the low-viscous swimming agar to a similar extent as the wt (Figure 43 A/B/D). A strong reduction of the swarming motility was observed (Figure 43 C/D). In contrast to the swarming negative-control (PA14 *rhlR*::Tn), the swarming colony of PA14 *PA1672*::Tn was able to migrate a small distance away from the point of inoculation but was unable to build out the characteristic tendrils that give the wt PA14 swarming colonies the characteristic pattern (Figure 43 C/E).

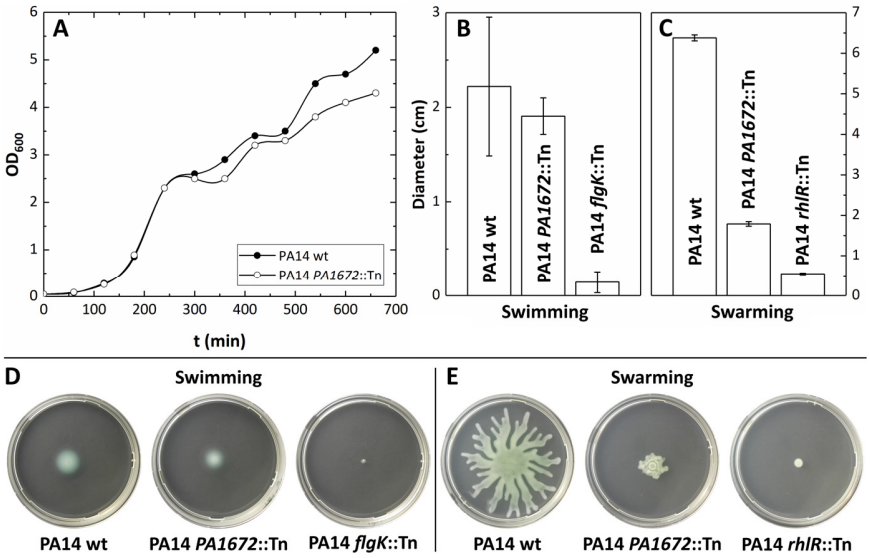

Figure 43: Phenotypic characterization of a *P. aeruginosa* PA14 *PA1672* transposon insertion mutant (PA14 *PA1672*::Tn) in comparison to the respective wild type (PA14 wt) and a swimming (PA14 *flgK*::Tn) and swarming (PA14 *rhlR*::Tn) deficient mutant. A) Planktonic growth curves of the mutant and the wt. Displayed is the increase of the optical density of the cell cultures measured at 600 nm (OD_{600}) over time (t (min)). The bacteria were incubated in LB medium under shaking conditions at 37 °C. B/C) The diameters of swimming and swarming colonies were determined from three independent experiments, after incubation for 19 (swimming) and 18 h (swarming) at 37 °C. Error bars represent the deviation calculated from the mean triplicates. D/E) Examples of the respective swimming (Figure S2) and swarming colonies (Figure S3).

Swarming motility is dependent on a properly functioning flagellum, type IV pili and the production and secretion of rhamnolipids (Köhler *et al.*, 2000). In contrast to that, swimming is only dependent on flagellar movement. Since the PA1672 mutant exhibited the same surface coverage as the wt during swimming assays (Figure 43 B/D) the protein is unlikely to influence

the proper movement of the flagellum. Type IV pili also play a crucial role during biofilm formation for the initial adherence of the bacteria (Gellatly & Hancock, 2013) so that mutant strains that are deficient in type IV pili formation fail to develop a biofilm (O'Toole & Kolter, 1998). However, the PA1672 mutant exhibited a thick biofilm layer at the interface between the bacterial culture and air attached to the glass wall of the beaker during planktonic growth experiments. This was not discovered during planktonic growth of the wt and the other PA14 Tn mutants, indicating that *PA1672*::Tn has an upregulated biofilm phenotype. This phenotype is contraindicative to any connection between PA1672 and the proper function of the type IV pili and may indicate that PA1672 rather influences the production or secretion of rhamnolipids. Rhamnolipids are glycolipidic surface-active agents (surfactants). They are essential as wetting agent, reducing the surface tension between the bacterium and the environment to enable the movement over the surface (Kearns, 2010). The amphiphilic molecules are constituted of one (monorhamnolipids) or two (dirhamnolipids) hydrophilic rhamnose groups and a hydrophobic 3-(3-hydroxyalkanoyloxy)alkanoic acid (HAA) moiety (Soberón-Chávez *et al.*, 2005). The HAA precursors of rhamnolipids are also secreted by the bacterium and also exhibit a crucial role during swarming motility (Déziel *et al.*, 2003). Interestingly, if the rhamnolipid secretion is completely suppressed, the swarming motility is also abolished, but if only HAAs are secreted, the swarming phenotype is not completely abolished but significantly reduced compared to the wt (Déziel *et al.*, 2003). Since this resembles the swarming phenotype of PA14 *PA1672*::Tn, which is only reduced, and not completely abolished as in the PA14 *rhlR*::Tn negative control, the discovered phenotype of PA14 *PA1672*::Tn might be connected to a reduced level of rhamnolipids while HAAs are produced.

The reduced motility phenotype in connection with an increased biofilm formation indicates that the mutant promotes the sessile lifestyle of *P. aeruginosa* (Rasamiravaka *et al.*, 2015), since such a phenotype was discovered before for components that participate in the inverse regulation of biofilm formation and swarming motility (Caiazza *et al.*, 2007; Li *et al.*, 2017). However, this inverse regulation is a complex network to which a variety of complex bacterial systems contribute, such as the quorum sensing system, two-component regulatory system pathways such as *GacS/GacA* (Rasamiravaka *et al.*, 2015) or chemotaxis-related regulatory

pathways (Caiazza *et al.*, 2007) together with others and probable yet unidentified systems. The complexity of the regulatory pathways for motility and biofilm behavior, which are not even fully understood today, makes it impossible to suggest a precise function for the PA1672 protein from these findings and requires further investigations.

4.2.1.2 Phenotypic MicroArrays™ - carbon source utilization

Phenotypic MicroArrays™ were performed to analyze the ability of PA14 *PA1672*::Tn to catabolize different compounds as sole carbon source. The PA1672 mutant was not able to metabolize 13 carbon sources as effectively as the wt since the mutant was unable to reach the same respiration activity in the stationary phase (Figure 44).

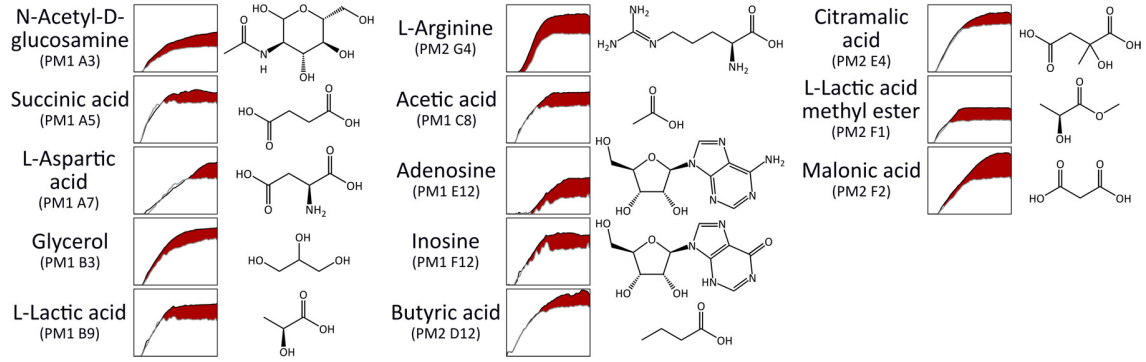

Figure 44: Carbon source utilization Phenotype MicroArrays™ of PA14 *PA1672*::Tn. Displayed are the respiration curves of PA14 *PA1672*::Tn (grey) in comparison to the wt strain (black). The red color is highlighting the reduced phenotype of the mutant. The values in parentheses describe the number of the respective Phenotype MicroArray™ and of the wells containing the compound. The respiration curves were obtained by plotting the measured absorbance in arbitrary units from 0-400 detected at 490 nm (y-axes) against the incubation time from 0-48 h (x-axes). To highlight the deficiency of the mutant, the area between the respiration curves was colored red. The chemical structures of the respective compounds were obtained from the PubChem database (Kim *et al.*, 2016) and visualized with ChemDraw Professional 17.0.

Since the compounds belong to several chemical classes, including purine nucleosides (inosine, adenosine), amino acids (aspartic acid, arginine), carbon acids, glycerol and the monosaccharide N-acetyl-D-glucosamine, it would be very difficult to deduce the actual reaction that influences the breakdown of those compounds and might go back to PA1672. To narrow down the possibilities, the interaction of these compounds with the PA1672 protein was examined by a TSA as described in section 4.2.2.

4.2.1.3 Phenotypic MicroArrays™ - chemical sensitivity

The chemical sensitivity of PA14 *PA1672*::Tn towards 240 compounds with antimicrobial activity was also tested with PMs. This revealed significant phenotypic differences. The mutant displayed a better respiration rate on 14 compounds and a decreased rate when incubated on 12 compounds in comparison to the wt (Figure 45). However, to suggest a physiological role for PA1672 the common connection between the compounds' antibacterial mechanism has to be identified. Based on their chemical structure or their site of action, some compounds can be differentiated in functional groups. Since the distinct groups target different sites in bacteria, it is challenging to derive a physiological function for PA1672.

One big functional group, for example, comprises membrane active agents that destroy the membrane integrity and cause cell leakage, leading to death. Among them are the last resort peptide antibiotic Polymyxin B (Evans *et al.*, 1999), the detergent lauryl sulfobetaine and the organic acid caprylate (Royce *et al.*, 2013). Phenolic compounds also increase the membrane permeability, such as chloroxylenol (McDonnell & Russell, 1999), 2-phenylphenol (Hugo & Bloomfield, 1971) and gallic acid (Borges *et al.*, 2013). Hexachlorophene is another phenolic compound that can disturb the membrane integrity but its primary antimicrobial action is the inhibition of the membrane-bound electron transport chain (McDonnell and Russell, 1999). The antimicrobial activity of 8-hydroxyquinoline is due to its metal-chelating properties for bivalent cations. It depletes metals that are essential for metabolism on the one hand and cations that are important for stabilizing the negative charge of the membrane surface on the other (Prachayasittikul *et al.*, 2013). Albeit the membrane active compounds have the same target, they induce contrasting phenotypes: whereas polymyxin B, chloroxylenol and 2-phenylphenol inhibit the respiration of the *PA1672*::Tn mutant, the others increase the phenotype in comparison to the wt (Figure 45). That some functionally similar compounds induce opposing phenotypes makes the interpretation of the PM assays difficult. The β-lactam antibiotics cefsoludin, azlocillin and nafcillin also induced opposing phenotypes. Despite all inhibit the bacterial cell wall synthesis by covalent modification of the penicillin-binding protein that catalyzes the peptidoglycan cross-linkage (Kong *et al.*, 2010), *PA1672*::Tn is more susceptible to azlocillin and nafcillin but more resistant to cefsoludin (Figure 45).

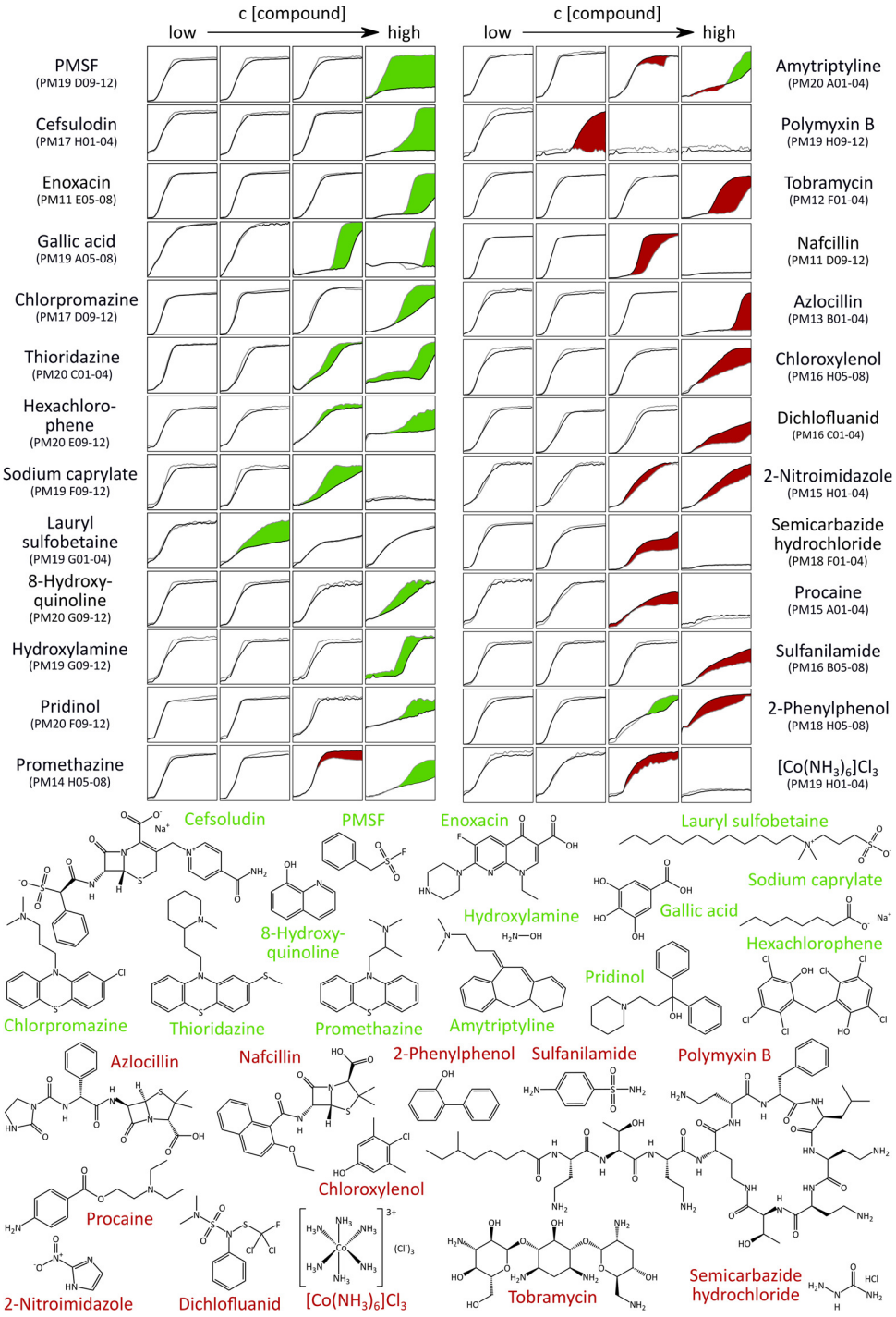

Figure 45: Chemical sensitivity Phenotype MicroArrays™ of PA14 *PA1672*::Tn. Displayed are the overlaid respiration curves of the wt (black) and the mutant (grey) that were incubated on four concentrations of substances with potential antibacterial function, that induced significant changes between the wt and the mutant. The values in parentheses describe the number of the respective Phenotype Microarray™ and of the wells containing the compound. The respiration curves were obtained by plotting the measured absorbance in arbitrary units from 0-400 detected at 490 nm (y-axes) against the incubation time from 0-48 h (x-axes). To highlight the differences, the area between the respiration curves was colored green if the mutant respired better than the wt or red if the respiration of the mutant was inhibited. The chemical structures were obtained from the PubChem database (Kim *et al.*, 2016) and visualized with ChemDraw Professional 17.0.

Other compounds that act on a variety of targets are for example the aminoglycoside antibiotic tobramycin, which blocks the protein biosynthesis by the inhibition of ribosomes (Bendush & Weber, 1976; Brogden *et al.*, 1976). The fluoroquinolone antibiotic enoxacin inhibits DNA replication by direct interaction with the DNA-unwinding gyrase and topoisomerase IV (Drlica, 1999). The antimicrobial activity of dichlofluanid is based on its reactivity against sulfhydryl groups (Schuphan *et al.*, 1981). It can react with glutathione and cause depletion of the bacterial glutathione pool, which ultimately increases the oxidative stress (Masip *et al.*, 2006). Phenylmethylsulfonyl fluoride (PMSF) is a serine protease inhibitor (Fahrney & Gold, 1963). *P. aeruginosa* PAO1 encodes the two potential serine proteases MucD and PA3535 (EprS). The secreted protease MucD degrades human interleukin-8, which helps to protect the bacteria against the human immune response (Okuda *et al.*, 2011). EprS was demonstrated to activate host inflammation by activation of human protease-activated receptors (Kida *et al.*). Since the human targets of the proteases are not available, it was not possible to find an explanation for the gain of function phenotype that is induced by the inhibition of serine proteases by PMSF in the PM. Further, it was not possible to suggest how serine proteases and PA1672 interplay with each other such that this open question remains to be elucidated in another study. Another detected compound, sulfanilamide, is a sulfonamide antibiotic. It is a substrate analog to para-aminobenzoic acid (PABA) (Woods, 1940) and thus a competitive inhibitor of folic acid production, which is an important cosubstrate during purine and pyrimidine synthesis (Stokstad & Jukes, 1987).

Another aspect that needs to be considered with respect to deriving a function of PA1672 from these PM data are the results from PMs conducted with the other transposon mutants of βαββββ-module genes in the PA14 background (Figure S4). The comparison with the respiration curves from PA14 *PA4183*::Tn (Figure 54), *PA1358*::Tn (Figure 59 A) and *PA4518*::Tn (Figure 67 A) revealed that enoxacin, polymyxin B, azlocillin, 2-phenylphenol and lauryl sulfobetaine caused significant changes in several mutants. Tobramycin and chloroxylenol even caused changes in all tested PA14 mutants. This could indicate that the function of all four class III βαββββ-proteins are at some point affecting each other or that the inserted transposon itself is responsible for the altered phenotype in comparison to the wt. Therefore, these results should

be regarded and discussed with caution. One group of compounds exclusively altered the respiration of the *PA1672*::Tn mutant. It contains the structurally related phenothiazines chlorpromazine, promethazine and thioridazine as well as amitriptyline, pridinol and procaine (Figure 45). They are human therapeutics that act on receptors or ion channels and are used as antidepressants, muscle relaxants or local anesthetics. Albeit their antimicrobial activity has been confirmed on a wide range of bacteria (Hendricks *et al.*, 2003; Ramu & Ramu, 1992; Schmidt & Rosenkranz, 1970), the actual cause of it is not well understood. They also mediate opposing phenotypes in the mutant, which is more susceptible to procaine but less susceptible to the others (Figure 45). Therefore, no connection between the function of PA1672 and these human therapeutics could be made.

4.2.2 Phenothiazines interact with PA1672

To identify a precise enzymatic function from the phenotypic changes, the respective compounds were tested in *in vitro* interaction studies with the recombinantly expressed PA1672 protein (Figure S1). The first experiment was a TSA to identify compounds that cause a significant change in the proteins T_m (ΔT_m) upon binding. A TSA was conducted with all available compounds (Figure 46).

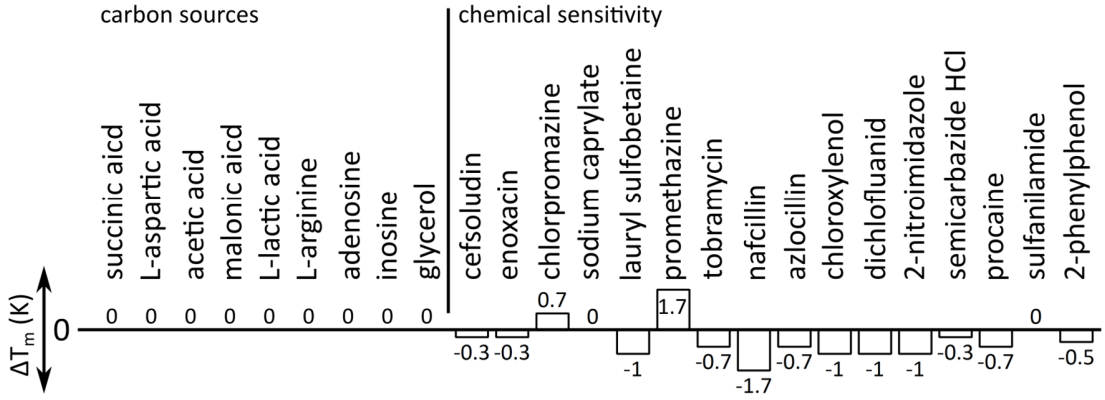

Figure 46: Result of the TSA to analyze the influence of compounds, identified in Phenotype MicroArrays™ with carbon sources and chemical sensitivity with the PA14 *PA1672*::Tn, on the thermal stability of the isolated protein PA1672. Changes in thermal stability (ΔT_m) of PA1672, that were caused upon incubation with the respective compounds in comparison to the reference T_m of 59 °C, measured under the same buffer conditions but without the compounds. ΔT_m were determined by averaging 3 independent experiments.

This revealed that none of the carbon sources altered the thermal stability of the protein, which has a T_m of 59 °C in the reference condition. This indicates that the carbon sources are not

directly interacting with PA1672 under the tested conditions. Five compounds from the chemical sensitivity assay induced a significant Δ T_m of ± 1 ° and were further tested in MST experiments together with the compounds that only caused changes of ± 0.7 °. Most of the tested compounds did not yield a significant change in the MST signal or a sigmoidal binding curve, indicating that these compounds do not interact with the protein under the tested conditions. However, the related compounds promethazine and chlorpromazine decreased the fluorescence signal. A SD-test (3.2.4.4) confirmed that the fluorescence change is caused by a binding event such that the interaction of chlorpromazine and promethazine with PA1672 was corroborated by this method. To derive the dissociation constant (K_D), both compounds were titrated against PA1672 (Figure 47 A/B). The K_D could only be estimated from the derived curves since the saturation baseline was not measurable. Both had rather a low affinity with a K_D of 335 ± 12 µM for chlorpromazine and 382 ± 19 µM for promethazine. Due to the low affinity of promethazine and chlorpromazine, the concentration of the compounds had to be increased to reach saturation of the protein. Unfortunately, saturation was not accurately measurable since the compounds started to unspecifically change the fluorescence at concentrations higher than 1.25 mM for promethazine and 0.625 mM for chlorpromazine. Additional ITC-experiments were performed to verify binding without covalent labelling of the protein. This confirmed the low affinity binding of chlorpromazine and promethazine to PA1672 but a sigmoidal curve, required to derive a reliable K_D, was also not established for this experiment (Figure 47 C-F). In the case of ITC-experiments, the concentration of the binding partner in the cell has to be at least 10 times higher than the K_D to derive an evaluable curve (Buurma & Haq, 2007). This means that according to the K_D derived from MST a concentration of roughly 4 mM PA1672 would have been required. To achieve this, the amount of 100 mg of protein would have been necessary for each measurement, which could not be provided.

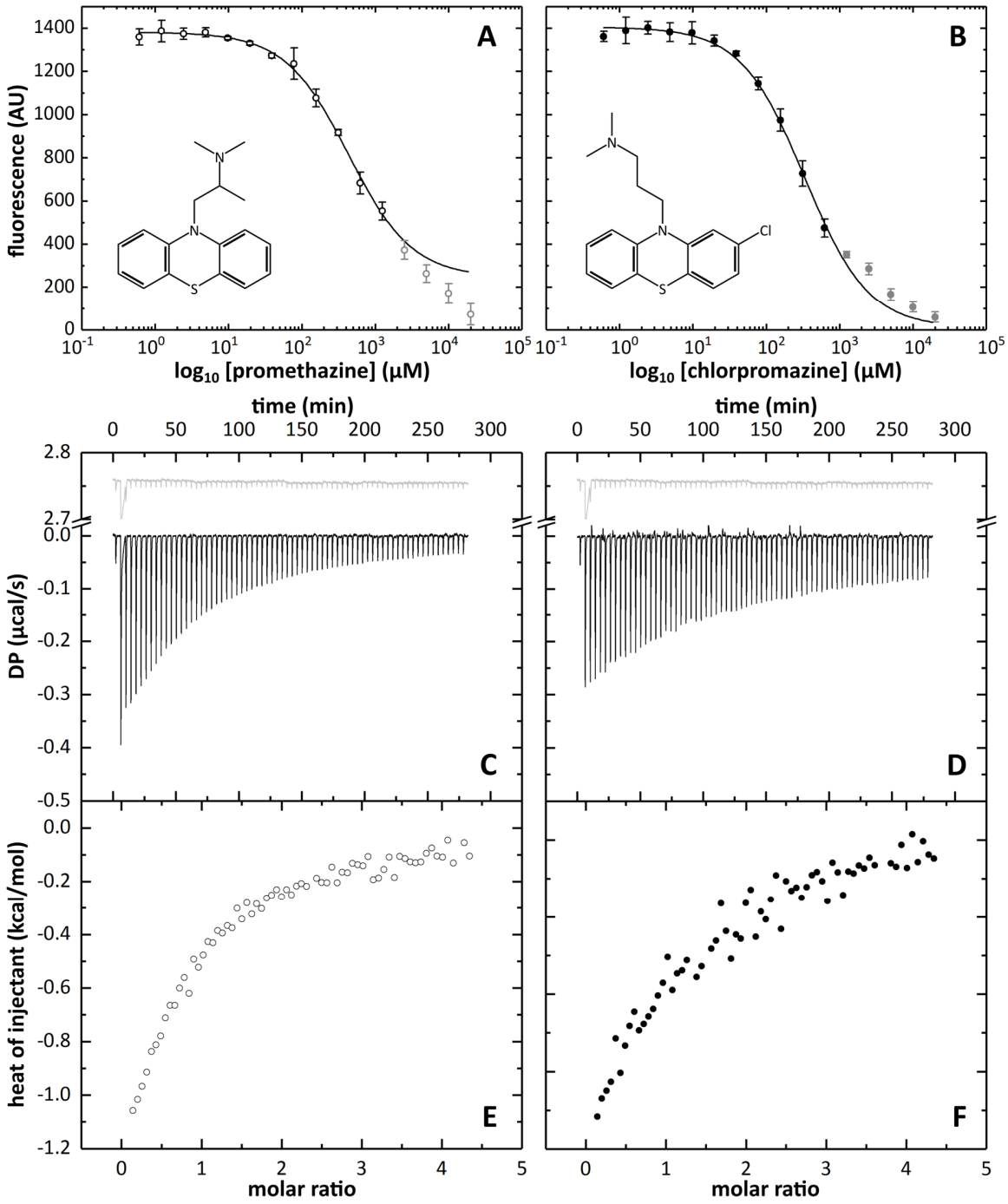

Figure 47: MST- (A/B) and ITC- (C-F) experiments of PA1672 with promethazine (○) and chlorpromazine (●). A/B) Titration of promethazine (K_D: 382 ± 19 µM) and chlorpromazine (K_D: 335 ± 12 µM) against Cy5-NHS-labeled PA1672. The collected data points that were not considered for curve fitting are represented in grey. Error bars represent the deviation calculated from the mean triplicates. The data were evaluated with the MO.Affinity Analysis software v2.15 (NanoTemper Technologies GmbH). C-F) Titration of promethazine and chlorpromazine against unlabeled PA1672. C/D) Raw data of the titration of the compounds (black) and of the buffer reference (grey) against PA1672. ITC profiles were evaluated with Origin7 (OriginLab Corp.).

A complex crystal structure with the identified compounds could have helped to suggest an enzymatic function. Unfortunately, the PA1672 crystal was not reproducible for soaking experiments and cocrystallization gave no or not diffracting crystals. Regardless, the biophysical experiments above indicate that the phenothiazine compounds chlorpromazine and promethazine are direct binding partners of PA1672. However, it remains necessary to identify if PA1672 can use them as a substrate and turn them over or if these ligands might represent substrate analogues that might not be able to bind as effectively as the actual substrate and could explain the weak affinity. Based on these ligands it would also be possible to screen for compounds with a similar chemical structure to identify ligands with a higher affinity that might lead to the actual substrate of PA1672. Phenothiazines are histamine analogues that inhibit the histamine H_1-receptor in human cells (H_1-antihistamines) by competitive interaction with the receptor (Simons & Simons, 2011). Therefore, the natural compound histamine that plays a major role during inflammation and immunomodulation (Simons & Simons, 2011) is considered as good starting point for a substrate search for PA1672.

4.2.3 Conclusion and Outlook

The phenotypic characterization delivered many starting points for follow-up experiments that might lead to the functional characterization of the βαβββ-module protein PA1672. With the Phenotypic MicroArrays™ the most promising lead was discovered, since the interaction between PA1672 and the phenothiazines chlorpromazine and promethazine was demonstrated with two independent methods. Phenothiazines are histamine analogues that inhibit the histamine H_1-receptor in human cells (H_1-antihistamines) by competitive interaction with the receptor (Simons & Simons, 2011). Therefore, the natural compound histamine that plays a major role during inflammation and immunomodulation (Simons & Simons, 2011), is considered as a good starting point for a substrate search for PA1672. Interestingly histamine indirectly enhances the sensitivity of endothelial cells towards gram-negative cell wall components since it induces the expression of the human Toll-like receptors (TLR) 2 and 4 (Talreja *et al.*, 2004). TLR are a central part of the innate immune system that sense the invasion of pathogens by recognition of conserved bacterial particles and transduce signals that lead to the secretion of cytokines (Kumar *et al.*, 2011). Cytokines of the Interleukin type (IL) such as IL-6 or IL-8 again trigger

the immune response and inflammation to combat the bacterial infections (Akdis *et al.*, 2011; Li *et al.*, 2001). To establish a successful infection, *P. aeruginosa* developed several mechanisms to evade the human immune response. One of them is the formation of biofilms that protects the bacterial aggregates (Alhede *et al.*, 2014). Active anti-immune mechanisms are mediated by secreted proteases that degrade human immune signal proteins. One example is the already mentioned secreted protease MucD that degrades IL-8 and therefore helps to reduce immune signaling (Okuda *et al.*, 2011). If histamine indeed interacts with PA1672 a similar mechanism is also imaginable for PA1672, since it is encoded in the genomic neighborhood of the second type 6 secretion system (H2-T6SS) and has a conserved active site amino acid pattern with the βαββββ-module protein Rv0577 that is a virulence factor of *M. tuberculosis*. Accordingly, PA1672 could be secreted to the host cell via the T6SS and degrade histamine to reduce the histamine mediated production of TLR 2 and 4 to evade the immune response. To promote this hypothesis, one has to conduct further experiments that proof the interaction or the reaction between PA1672 and histamine and the secretion of PA1672.

A further idea for the physiological function of PA1672 takes the reduced swarming motility in combination with an enhanced biofilm formation phenotype that was discovered in the PA14 *PA1672*::Tn mutant into consideration. If PA1672 is not secreted it could bind histamine that diffuses into the bacterial cytoplasm after host infection. PA1672 could then fulfil a sensor-like function to promote the sessile lifestyle with reduced motility and enhanced biofilm production. The first step to substantiate the involvement of PA1672 in swarming motility and biofilm formation would be a complementation experiment of the PA14 *PA1672*::Tn mutant with a plasmid that expresses the PA1672 protein. If the complemented bacterium is able to swarm in the same extend as the wt, the swarming deficiency would indeed have been caused by the disruption of the *PA1672* gene.

4.3 Open reading frame PA4183

The structurally uncharacterized class III βαββββ-module protein PA4183 (155 aa, 17.2 kDa (Gasteiger *et al.*, 2005)) was a subject of a preceding study (Vit, 2015). There, the full-length protein was insoluble during recombinant expression in *E. coli* but a successful purification strategy was established for an N-terminally truncated version (Vit, 2015). The truncated PA4183 lacks the

first 15 aa and is referred to as PA4183$^{16\text{-}155}$ (140 aa, 15.6 kDa (Gasteiger *et al.*, 2005)). According to Wurtzel *et al.*, 2012 *PA4183* is encoded in an operon with the upstream gene *PA4184* (Figure 48).

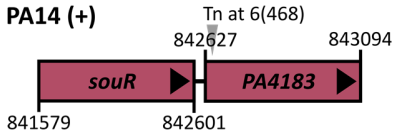

Figure 48: ORFs *PA4183* and *souR* in the *P. aeruginosa* PA14 strain. The actual locus ID of the *PA4183* homologue in the PA14 strain is *PA14_09780*. Operon organization and genomic localizations are derived from pseudomonas.com (Winsor *et al.*, 2016). The verified transposon insertion site (Tn) of the PA14 *PA4183*::Tn mutant from Liberati *et al.*, 2006 is indicated by a grey arrow. The position of the insertion in the gene is given in units of bp. The total length of the gene is given in brackets.

PA4184 (340 aa, 38 kDa (Gasteiger *et al.*, 2005)) is a two-domain transcriptional regulator from the glutamine amidotransferase I-like (GATR) subfamily. It was recently identified as sarcosine oxidation and utilization regulator (SouR) (Willsey & Wargo, 2016). Willsey & Wargo, 2016, found out that SouR induces the expression of genes coding for proteins that are required for the catabolism of sarcosine (N-methylglycine) in response to sarcosine and that this regulator is essential for bacterial growth if sarcosine is the only available C- and N-source. Further, they conducted a growth assay with a *PA4183* transposon mutant in a PA14 background offering sarcosine as sole C-/N- source. This mutant displayed a growth defect compared to reference strains but was less sensitive than the *souR*-deficient mutant. This indicates that PA4183 is not essential but involved in the sarcosine catabolism to achieve its optimal utilization (Willsey & Wargo, 2016). Therefore, the sarcosine catabolism served as a starting point to search for potential substrates of PA4183 to reveal its function.

4.3.1 Background information for sarcosine metabolism

Sarcosine occurs in the natural habitat of *P. aeruginosa* or as metabolism intermediate during the breakdown of glyphosate, creatine, carnitine or choline (Kishore & Jacob, 1987; Meadows & Wargo, 2018; Nimmo-Smith & Appleyard, 1956; Wargo & Hogan, 2009; Wargo *et al.*, 2008). An overview of the sarcosine pathway and the enzymes so far identified to participate in its breakdown are displayed in Figure 49. SouR was identified to directly up-regulate the transcription of the *sox*-operon, which contains the genes coding for the heterotetrameric sarcosine oxidase SoxBDAG, the serine hydroxymethyltransferase GlyA1 and the formyltetrahydrofolate deformylase PurU2 (Willsey & Wargo, 2016). The sarcosine oxidase catalyzes the FAD- and

FMN-dependent oxidative demethylation of sarcosine to glycine by transformation of the methyl group to tetrahydrofolate (THF). Under THF-limited conditions, H_2O serves as alternative methyl group acceptor and formaldehyde is produced (Wagner & Jorns, 1997). In both cases, the final electron acceptor is O_2, which is reduced to H_2O_2. To cope with the cytotoxic effects of formaldehyde, SouR also upregulates the expression of the formaldehyde detoxification genes *fdhA, adhC* and *PA3628* (Willsey & Wargo, 2016), which code for the glutathione-independent (FdhA) and the glutathione-dependent formaldehyde dehydrogenase (AdhC) as well as for a S-formylglutathione hydrolase (PA3628).

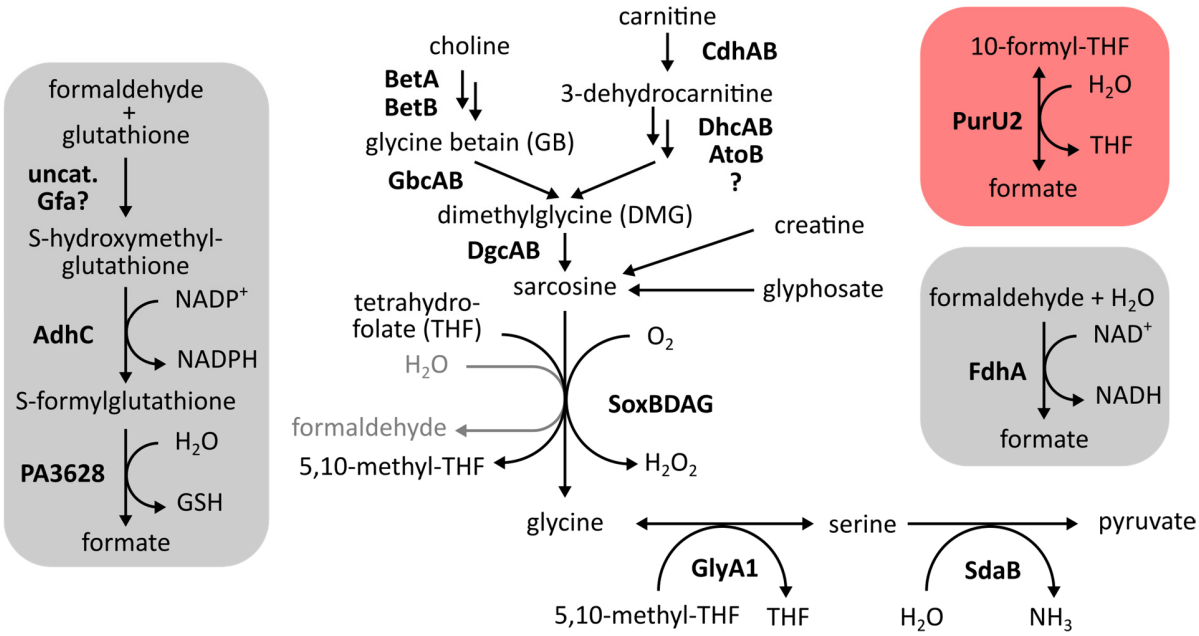

Figure 49: Excerpt from the sarcosine metabolism and the formaldehyde detoxification pathway under the transcriptional regulation of SouR (grey boxes) from *P. aeruginosa*. The red box displays the reaction catalyzed by PurU2, which is, with GlyA1 and SoxBDAG, encoded in the *sox*-operon and controlled by SouR. Characterized enzymes, which participate in the pathway are shown in bold letters. The diagram is adapted from Willsey & Wargo, 2016 and Meadows & Wargo, 2018.

4.3.2 Potential interaction of PA4183 with compounds from the sarcosine pathway

To find indications for the function of PA4183 and its involvement in the sarcosine metabolism, evidence for the interaction with possible substrates or ligands (Figure 50) from the sarcosine pathway (Figure 49) were searched. A TSA was conducted with the previously purified PA4183$^{16\text{-}155}$ (Vit, 2015) to identify compounds that alter the T_m.

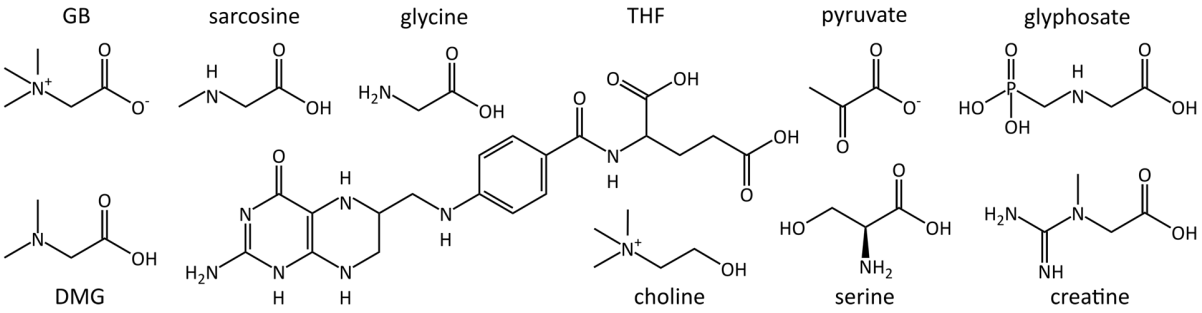

Figure 50: Ligands from the sarcosine metabolism, which were tested in a TSA with PA4183$^{16\text{-}155}$ and in MST-experiments with His$_6$-PA4183$^{16\text{-}155}$. The chemical structures were obtained from the PubChem database (Kim *et al.*, 2016) and visualized with ChemDraw Professional 17.0.

None of the tested compounds changed the T_m of PA4183$^{16\text{-}155}$, which was 48 °C in SEC buffer. This was verified by MST experiments conducted with the recombinantly expressed His$_6$-labelled version of the protein, His$_6$-PA4183$^{16\text{-}155}$ (Figure S1), where no binding curves were observed. Since none of the compounds from the central sarcosine pathway interacts with the protein, one approach to identify a binding partner would be to extend the search for compounds in pathways that are branching of from the sarcosine metabolism. In addition, the pathways that detoxify the harming side products of sarcosine demethylation, as formaldehyde should be taken into consideration. The search for a potential binding partner could be facilitated by identifying the tertiary structure of PA4183, because the location of the active sites of βαβββ-proteins is well conserved and would give a detailed insight into the substrate or ligand binding site.

4.3.3 From crystallization to structure refinement

Since PA4183$^{16\text{-}155}$ has two MET residues, a SeMET-labelled version of PA4183$^{16\text{-}155}$ (PA4183$^{16\text{-}155}$ MSE, Figure S1) was recombinantly expressed and used for crystallization to solve the phase problem through experimental phasing. During initial crystallization of PA4183$^{16\text{-}155}$ MSE, many big and well-shaped crystals were discovered but did not or poorly diffract. The only condition from which well-diffracting crystals emerged contained 1 M K/Na tartrate, 0.2 M $LiSO_4$ and 0.1 M CHES pH 9.5 (Figure 51 A). With a crystal (Figure 51 C) that had an overall resolution of 1.8 Å, Se-SAD data were collected. The anomalous signal went to a resolution of

2.9 Å and was sufficient to solve the phase problem (Table 18). The SeMET structure was refined to an R_{cryst} of 15.3 % and an R_{free} of 17.7 % (Table 18). Based on the initial crystallization condition crystals of the native PA4183$^{16\text{-}155}$ could be reproduced and optimized (Figure 51 B).

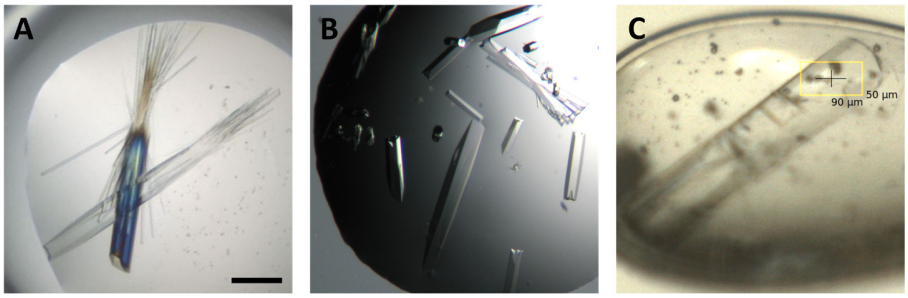

Figure 51: PA4183$^{16\text{-}155}$ crystals. A) Crystals of SeMET-labelled protein in 1 M K/Na tartrate, 0.2 M $LiSO_4$ and 0.1 M CHES pH 9.5 from JCSG Core IV A5 (Qiagen). Scale bar: 200 µm. B) Native PA4183$^{16\text{-}155}$ crystals in 0.7 M K/NA tartrate, 0.2M $LiSO_4$, 0.1 M CHES pH 9.6. C) SeMET-labelled protein crystal during data collection at SLS (PSI, Villigen, Switzerland).

A data set with a resolution of 1.52 Å was collected from a crystal grown in 0.7 M K/NA tartrate, 0.2M $LiSO_4$, 0.1 M CHES pH 9.6. The native structure was solved by MR with the SeMET model and refined to an R_{cryst} and an R_{free} of 13.9 % and 15.5 % (Table 18). Both structures contained four protein chains in the ASU, which corresponds to a rather high Matthews coefficient (Matthews, 1968) of 3.3 Å/Da concomitant with a high solvent content of 63 %. The SeMET-labelled and the native protein structure were identical, therefore only the native, higher resolution structure was discussed. The electron density of the native protein was well interpretable for the vast part of the protein structure. In protein chain A, only the final C-terminal residue could not be modelled, which was also not interpretable in the other chains due to missing electron density. Some residues from the N-terminus were not modelled in the other chains, due to missing electron density. In chain B, the first five amino acids are missing, including the extra amino acids GLY and HIS that remained after removal of the purification tag. In chain C and D, the first four amino acids are missing.

Table 18: Data collection, processing and refinement statistics for SeMet-labelled (PA4183$^{16-155}$ MSE) and native PA4183$^{16-155}$.

Data collection and processing	**PA4183$^{16-155}$ MSE**	**PA4183$^{16-155}$**
Beamline[†]/detector	X06DA, SLS/Pilatus 2M-F	BL14.2, BESSYII/MarCCD
Wavelength (Å)	0.97901	0.91841
Temperature (K)	100	100
Crystal-detector distance (mm)	155	170
Rotation range per image (°)	0.1	0.25
Total rotation range (°)	720	90
Space group	$P3_221$	$P3_221$
a, b, c (Å)	155.52 155.52 59.35	155.49 155.49 59.52
α, β, γ (°)	90 90 120	90 90 120
Mosaicity (°)[#]	0.08	0.10
Resolution range (Å)	47.18 - 1.80 (1.84-1.80)	47.26-1.52 (1.55-1.52)
Total No. of reflections	3097174 (172775)	682412 (20968)
No. of unique reflections	75818 (4439)	126391(6076)
Completeness (%)	100 (99.5)	99.8 (98.0)
Multiplicity	40.9 (38.9)	5.4 (5.3)
Mean I/σ(I)	22.7 (2.1)	19.1 (2.0)
CC1/2[+]	99.9 (77.9)	99.9 (79.5)
R_{pim}[$]	2.9 (36.9)	2.1 (36.9)
R_{meas}[$]	18.6 (231.8)	4.5 (61.9)
Wilson B factor (Å^2)	19.8	17.6
Anom. completeness	100 (99.4)	
Anom. multiplicity	20.7 (19.5)	
Refinement		
Resolution limit (Å)	47.18 - 1.80	47.26-1.52
Completeness (%)	99.97	99.81
Final R_{cryst} (%)	15.3	13.9
Final R_{free} (%)	17.7	15.5
No. of non-H atoms		
Protein	4249	4501
Solvent water/buffer	753/64	963/52
Total	5066	5516
R.m.s. deviations		
Bonds (Å)	0.009	0.017
Angles (°)	1.289	1.512
Average B factors (Å2)		
Protein	29	28
Solvent water/buffer	42/52	43/32
Ramachandran plot		
Favored regions (%)	98.5	97.61
Outliers (%)	0	0.37
MolProbity score[‡]	1.06	1.41

Values in parentheses are for the highest resolution shell. [†]BESSYII (HZB, Berlin, Germany), SLS (PSI, Villigen, Switzerland). [#] Value as reportet by *AIMLESS* (Evans & Murshudov, 2013). [+]CC1/2 as reported by (Karplus & Diederichs, 2012), [$] $R_{pim} = \Sigma_{hkl} (1/(N-1))^{1/2} \Sigma_i | I_i(hkl) - \langle I(hkl) \rangle | / \Sigma_{hkl} \Sigma_i I_i(hkl)$; $R_{meas} = \Sigma_{hkl} (N/(N-1))^{1/2} \Sigma_i | I_i(hkl) - \langle I(hkl) \rangle | / \Sigma_{hkl} \Sigma_i I_i(hkl)$, where N is the number of observations of the reflection with index hkl and I_i is the intensity of its ith observation (Weiss, 2001). [‡] *MolProbity* score as reported by *MolProbity* (Chen *et al.*, 2010).

4.3.4 Topology of the PA4183 dimer

The crystal structure of PA4183$^{16\text{-}155}$ revealed the typical βαββββ-fold where one monomer contains two βαββββ-motifs in this case formed by β_2-α_1-β_3-β_4-β_5 and β_6-α_3-β_7-β_8-β_9 (Figure 52 A/B). PA4183$^{16\text{-}155}$ forms a dimer in solution as confirmed by a DLS analysis. It calculated a MW of 28 kDa, which corresponding to twice the theoretical MW of the monomer. Therefore, the four protein chains in the ASU do not represent a higher-order oligomer. The stable dimer was established by the less common back-to-back dimerization form (Figure 52 C).

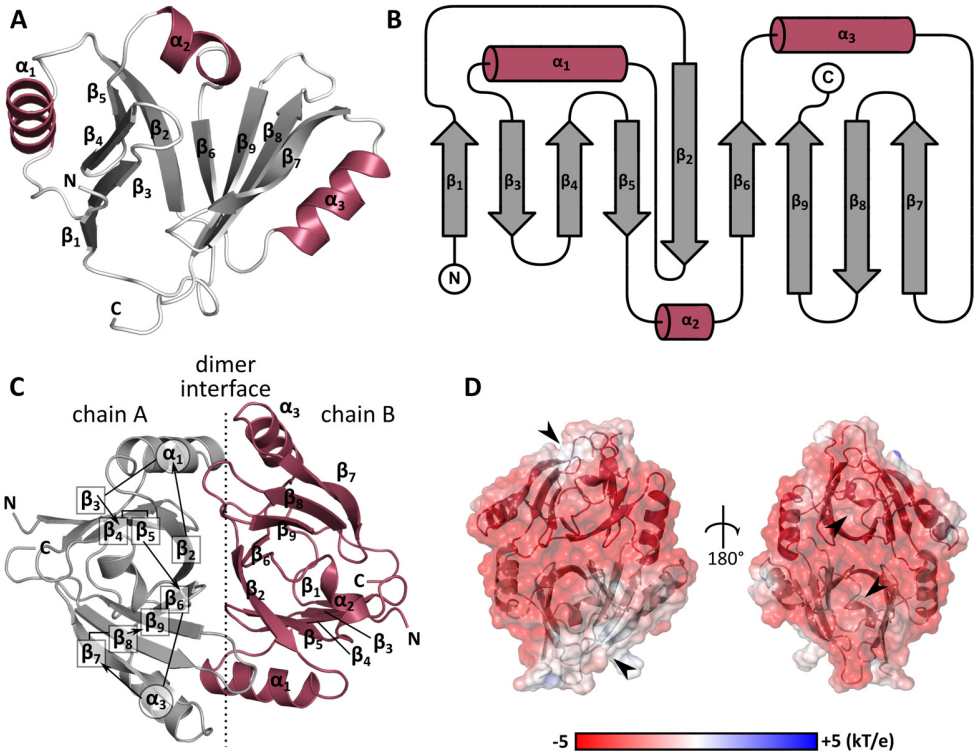

Figure 52: Protein X-ray structure of PA4183$^{16\text{-}155}$. A/B) Topology of a PA4183$^{16\text{-}155}$ monomer as 3D-arrangement (A) and as schematically representation (B) drawn with TopDraw (Bond, 2003). The secondary structure elements are colored differently. C) Architecture of the stable dimer. The chains are colored differently and a dashed line indicates the interface that is formed by back-to-back contacts according to Bergdoll *et al.*, 1998. The secondary structure elements are numbered from N- to C-terminus. D) Electrostatic surface of the PA4183$^{16\text{-}155}$ dimer in two distinct orientations, as calculated by the PDB2PQR server Version 2.0.0 (Dolinsky *et al.*, 2004). Black arrows are indicating the openings to the potential binding sites.

The topology of the monomer is dominated by the characteristic U-shaped antiparallel β-sheet (Figure 52). It is built up by eight β-strands β_2-β_9 of the duplicated βαββββ-motif and the additional β_1-strand at the truncated N-terminus. Another additional secondary structure element is the α_2-helix that connects both motifs. Regarding the electrostatic potential of the dimer, it

is quite striking that the surface is dominated by a negative charge, which is only interrupted by a rather uncharged patch (Figure 52 D).

4.3.5 Potential active site of PA4183

In the back-to-back dimerization, a single protein chain forms the potential active site. Here it is an L-shaped tunnel that stretches through the half-barrel (Figure 53 A).

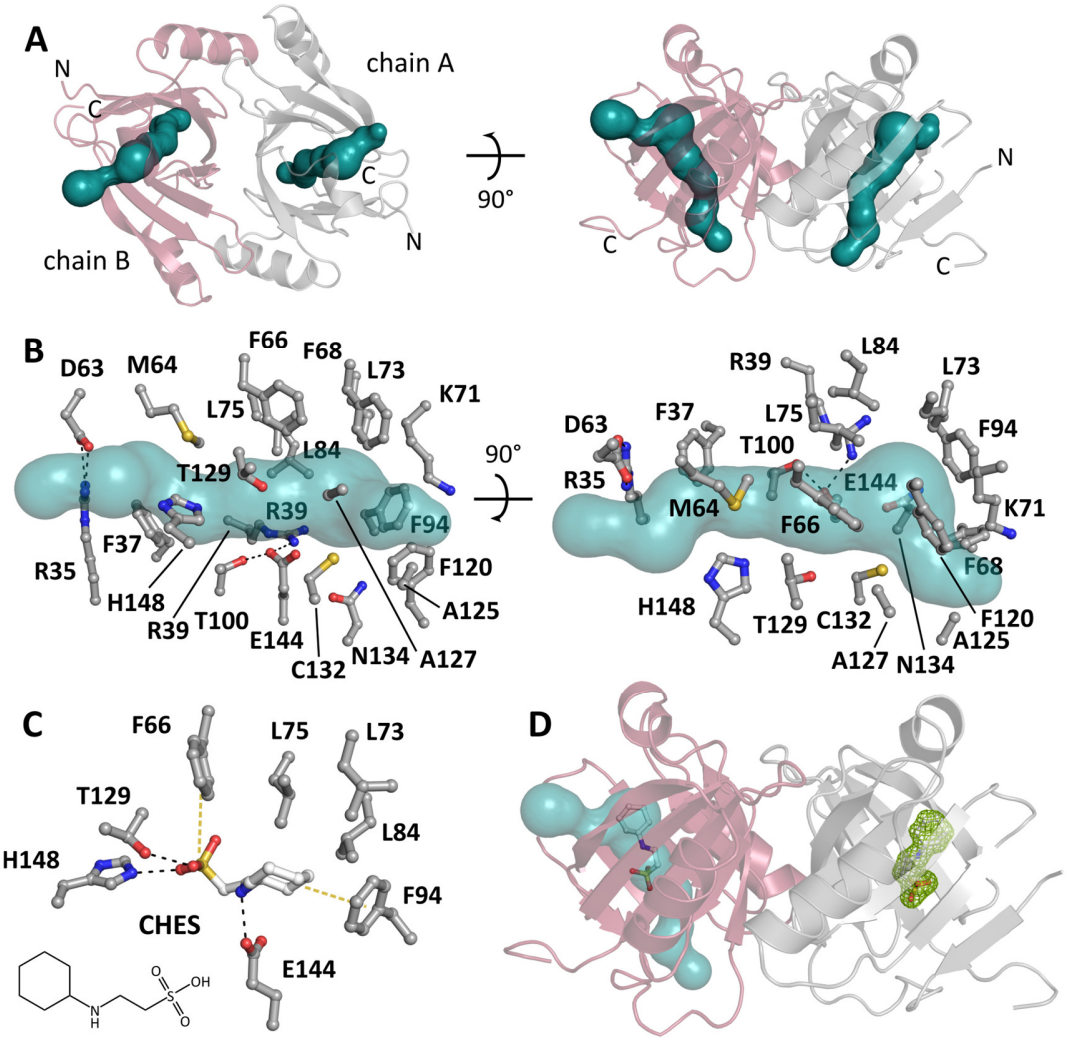

Figure 53: Potential active site of PA4183$^{16\text{-}155}$. The surface of the potential binding tunnel (teal) was visualized with Caver3.0 (Chovancova *et al.*, 2012). A) PA4183$^{16\text{-}155}$ protein dimer with distinct colored chains displayed in different orientations. B) Amino acid side chains of monomer A, which flank the potential binding tunnel. They are represented as balls and sticks in two orientations. Oxygen atoms are red, nitrogen blue and sulfur yellow. Dashed lines represent H-bonds with a maximum distance of 3.2 Å. C) Binding site of a CHES molecule. The residues that stabilize CHES are represented as balls and sticks in two orientations. Oxygen atoms are displayed in red, nitrogen in blue and sulfur in yellow. Black dashed lines represent H-bonds with a maximum distance of 3.2 Å. Yellow dashed lines indicate π-alkyl and π-sulfur interactions. The chemical structure of CHES was obtained from the PubChem database (Kim *et al.*, 2016) and visualized with ChemDraw Professional 17.0. D) Localization of CHES molecules in the protein dimer. The left monomer shows the position of CHES in the binding tunnel. The right monomer shows the unbiased mFo-DFc difference e^--density as green mesh with a contour level of 2.5 σ.

The most abundant catalytic residues in proteins are HIS and CYS (Bartlett *et al.*, 2002), which are also found in the potential PA4183 active site as H148 and C132 (Figure 53 B). Especially the CYS seems to be a promising candidate for an enzymatic active residue as it is close to E143, which is in turn in H-bonding distance to R39 and T100 two more amino acids that often have catalytic importance (Holliday *et al.*, 2009). Conspicuous is also the location of C132 at the kink of the L-shaped tunnel close to one end of the tunnel. Opposite to the kink and to C132, is a cove formed by aliphatic and hydrophobic side chains (Figure 53 B). The rest of the tunnel is also abundant in aliphatic and hydrophobic side chains (Figure 53 B). Since uncharged and non-polar residues do usually not participate in catalysis (Bartlett *et al.*, 2002; Holliday *et al.*, 2009), they might play an important role for binding of the potential substrate. Interestingly the tunnel entrance close to this hydrophobic cove is positioned in the uncharged patch found at the proteins electrostatic surface (Figure 52 D) and might indicate a functionally relevant connection.
The binding tunnel of each molecule in the ASU was occupied with extra mFo-DFc e^--density that was well interpretable with a *N*-cyclohexyl-2-aminoethanesulfonic acid (CHES) molecule from the crystallization buffer (Figure 53 D). The CHES molecule is stabilized by H-bonds formed between two distinct oxygen of the ligand's sulfonic acid moiety, the side chains of H148 and T129 and between the side chain of E144 and the proton of the ligand's amine. The sulfhydryl group is further stabilized by π-sulfur interaction with F66. The nonpolar cyclohexyl part of CHES interacts with the nonpolar kink of the binding tunnel and is stabilized by a π -alkyl interaction with F94 (Figure 53 C). The presence of the buffer molecule gives another starting point for the PA4183 substrate search. Since CHES must share some structural and chemical similarities with the substrate that enabled the binding of the molecule a search for other molecules based on the architecture of the buffer ingredient might deliver new potential ligands for PA4183 that can be tested in binding assays.

4.3.6 Bioinformatic characterization of the PA4138$^{16-155}$ crystal structure

Due to the conserved overall structure of the βαβββ-module-containing protein family, a structure-based search for functionally related proteins to derive a possible function for PA4183 seemed unpromising. Indeed, an analysis performed with PDBeFold-server (Krissinel & Henrick, 2004) returned 10 distinct hits, but none of them provided new leads towards the function of

PA4183 as most of the proteins were uncharacterized and/or the architecture of the potential active sites were not conserved to the one of PA4183. Despite this, a search for amino acid patterns in 3D space was conducted with the SPRITE-server (Nadzirin *et al.*, 2012). This was supposed to identify patterns in PA4183, which are similar to functionally important patterns from structures deposited in the PDB, independent of similarities in the sequence or the overall fold. The SPRITE-analysis based on the PA4183$^{16\text{-}155}$ dimer returned 31 hits, of which most were not interesting as the discovered motifs were located on the protein surface. Only two hits implied residues in the potential binding tunnel. Part of the first hit was H148 together with S28 and L11 that are close by. They were arranged in similar fashion as three analogous residues (S18, H20, L22) that participate in the DNA interaction of the DNA-binding protein ArtA (PDB-ID: 3GXQ; Ni *et al.*, 2009). However, it is very unlikely that these residues can mediate the interaction between PA4183 and DNA as the SER and the HIS sidechains are both hidden in the protein and not accessible for DNA molecules. They are also not in H-bonding distance as it is the case in ArtA (Ni *et al.*, 2009). The second motif was very interesting as it contained C132, N134 and A127 (Figure 53 B). The analogous amino acids identified by SPRITE were located on the NADP-dependent, glyceraldehyde 3-phosphate (G3P) dehydrogenase (GAPN). Its ASP (N145) is involved in the binding of the substrate G3P, which is covalently attacked by the respective CYS (C284) (PDB-ID: 2ESD; D'Ambrosio *et al.*, 2006). Unfortunately, the other amino acid side chains, three ARG and a TYR, which stabilize G3P in GAPN, are absent in PA4183$^{16\text{-}155}$ and make the binding of G3P rather unlikely. To be certain, a binding study like ITC or MST must be performed.

4.3.7 Characterization of PA14 *PA4183*::Tn with Phenotype MicroArrays™

Since the experiments above did not lead to the functional characterization of PA4183 the physiological role of the protein was further investigated with PM. The PA14 transposon insertion mutant (PA14 *PA4183*::Tn) from Liberati *et al.*, 2006 used here was kindly provided by Prof. S. Häußler from the HZI. The integrity of the mutant was confirmed by PCR and sequencing of the PCR product. The insertion site of the *MAR2xT7* transposon in the ORF of *PA4183* was discovered at bp 6 (Figure 48) in agreement with the manufacturer's information (Liberati *et al.*, 2006).

4.3.7.1 Carbon source utilization assay

PMs were performed to test the ability of the PA14 *PA4183*::Tn mutant to utilize different carbon compounds as sole energy source with the intention to find other C-sources besides sarcosine that are not metabolized as effectively as by the wt but deliver an explanation for the reduced ability of the transposon mutant to grown on sarcosine. Unfortunately, the respiration curves of the wt and the mutant on all tested C-sources were congruent (Figure S4) and gave no further lead to the physiological function of PA4183. However, this assay confirmed that the wt and the PA14 *PA4183*::Tn are both able to use pyruvate as sole carbon source without inhibition of the phenotype (Figure S4, PM2 H8) as shown before in a cell density based planktonic growth assay by Willsey & Wargo, 2016.

4.3.7.2 Chemical sensitivity assay

The chemical sensitivity assay identified 11 compounds that induced a significant change in the respiration rates of the PA14 *PA4183*::Tn mutant in comparison to the wt (Figure 54). The mutant had a more activated metabolism upon incubation with enoxacin and compound 48/80. A clearly reduced phenotype was visible on chlorodinitrobenzene, polymyxin B, pheneticillin, chloroxylenol and azlocillin. Tobramycin, 2-phenylphenol, nafcillin and $SbCl_3$ only caused a slight extension of the lag-phase. The comparison with the results obtained from the PMs with the other PA14 βαβββ-module gene mutants (Figure S4) revealed that $SbCl_3$ is the only compound that exclusively has an impact on the phenotype of the *PA4183*::Tn mutant. $SbCl_3$ was shown to replace Zn^{2+}-ions complexed in enzymes and proteins, like the nucleic acid binding zinc-finger domains, which can lead to the loss of crucial cellular functions and result in cell death (Demicheli *et al.*, 2008; Frézard *et al.*, 2012). Like other toxic cations it has a high affinity for sulfhydryl groups and can thus deplete GSH and directly promote oxidative stress in the bacterial cells (Nies, 1999). A direct interaction between $SbCl_3$ and PA4183 is rather unlikely since the protein lacks metal-complexing residues. If the phenotypes that were caused by the rest of the compounds are directly connected to the disruption of the *PA4183* gene and therefore to the function of PA4183 must be further evaluated.

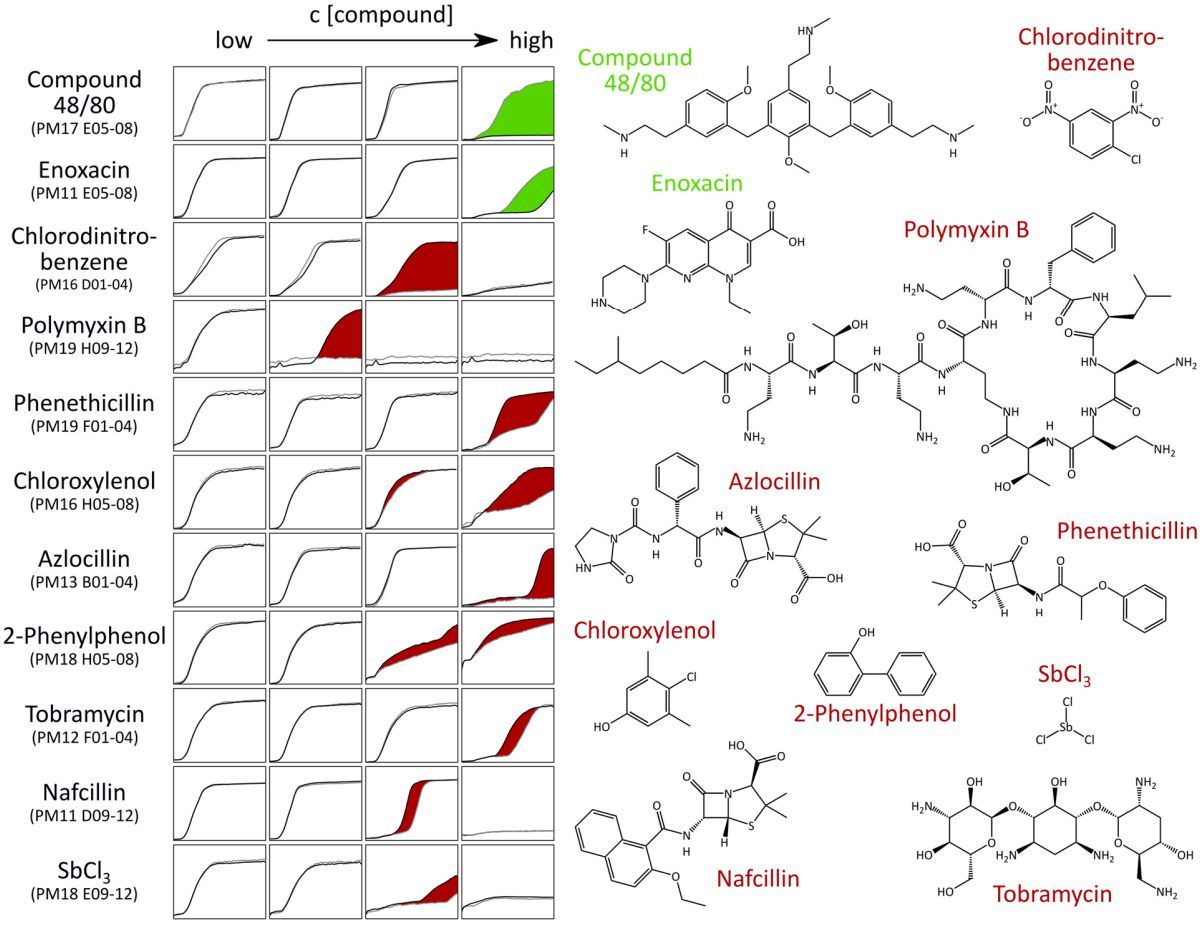

Figure 54: Chemical sensitivity Phenotype MicroArrays™ of PA14 *PA4183*::Tn. Displayed are the overlaid respiration curves of the PA14 wt (black) and the mutant (grey), which were incubated on four concentrations of substances with potential antibacterial function, that induced significant changes between the wt and the mutant. The values in parentheses describe the number of the respective Phenotype Microarray™ and of the wells containing the compound. The respiration curves were obtained by plotting the measured absorbance in arbitrary units from 0-400 detected at 490 nm (y-axes) against the incubation time from 0-48 h (x-axes). To highlight the differences, the area between the respiration curves was colored green if the mutant respired better than the wt or red if the respiration of the mutant was inhibited. The chemical structures were obtained from the PubChem database (Kim *et al.*, 2016) and visualized with ChemDraw Professional 17.0.

Taken together, the PM results make it rather challenging to suggest a physiological role for PA4183, since a common connection between the compounds' antibacterial mechanisms must be identified, which are divers and partially not fully understood. Chloroxylenol and 2-phenylphenoly are, for example, suggested to target the bacterial membrane based on the general mechanism identified for phenolic compounds. They can permeabilize the membrane and introduce cell leakage and lysis. Besides that, phenolic compounds can denature cytoplasmic proteins that lead to the inhibition of essential cellular functions (McDonnell & Russell, 1999). The aminoglycoside antibiotic tobramycin inhibits protein synthesis (Bendush & Weber, 1976; Brog-

den *et al.*, 1976) while enoxacin is a fluoroquinolone antibiotic that inhibits enzymes required for DNA replication (Drlica, 1999). The β-lactam antibiotics phenethicillin, azlocillin and nafcillin inhibit peptidoglycan synthesis and therefore cell proliferation (Kong *et al.*, 2010). Compound 48/80 is a synthetic stimulant of eukaryotic mast cell granulation (Lagunoff *et al.*, 1983). The antibacterial activity of compound 48/80 was confirmed (Lenney *et al.*, 1977) and said to induce cell membrane permeability (Hall *et al.*, 1983; Nakao *et al.*, 2011). The mechanism is supposed to be similar to that of polymyxin antibiotics. Both have a cationic amphiphilic character at physiological pH due to their abundant amino groups combined with hydrophobic moieties. This enables the interaction with the negatively charged membrane surface and the integration and pore formation in the membrane. The compound can then pass through the pores and act on the cytoplasmic membrane to induce lethal cell leakage (Brogden, 2005; Vaara, 1992). However, the *PA4183*::Tn mutant has contrasting sensitivity to compound 48/80 and polymyxin B, since it displayed a reduced phenotype on polymyxin B and an enhanced phenotype on compound 48/80. This indicates that these compounds either do not act on the same target at the bacterial membrane or that one of them has another activity, for example on targets in the cytoplasm.

4.3.8 Analysis of interaction between PA4183 and compounds discovered from chemical sensitivity PM

The compounds that altered the phenotype of the PA4183 mutant in comparison to the wt were tested in thermal shift and MST assays to find evidence for a direct interaction with the protein. In the TSA, the untagged PA4183$^{16\text{-}155}$ (Vit, 2015) was incubated with the available compounds. Enoxacin, chloroxylenol and nafcillin induced significant increase in the proteins T_m (Figure 55). To see if this increase is caused by an actual interaction with the protein, the compounds were tested in an MST experiment. For this, a His_6-tagged version of PA4183 (His_6-PA4183$^{16\text{-}155}$, Figure S1) was used to fluorescently label the protein with a His-reactive dye as the only lysine residue (K71) of PA4183$^{16\text{-}155}$ that could have been labeled with a primary amine reactive dye was close to the potential active site (Figure 53 B) such that the label might have blocked the binding tunnel. In contrast to this, the N-terminus points away from the active site (Figure 53 A) such that the risk of an interference with the potential binding site is diminished.

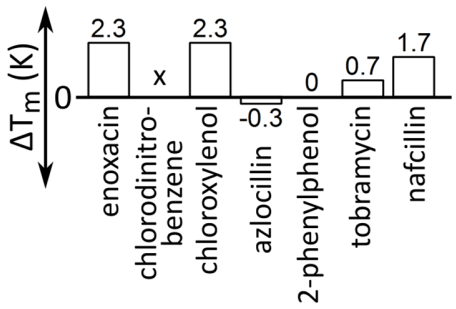

Figure 55: Result of the TSA to analyze the influence of compounds, identified in Phenotype MicroArrays™ with the PA14 *PA4183*::Tn, on the thermal stability of the isolated protein PA4183$^{16\text{-}155}$. Changes in thermal stability (ΔT_m) of PA4183$^{16\text{-}155}$, which were caused upon incubation with the respective compounds in comparison to the reference T_m of 48 °C, measured under the same buffer conditions but without the compounds. ΔT_m were determined by averaging 3 independent experiments.

Since the TSA melting curve of PA4183$^{16\text{-}155}$ with chlorodinitrobenzene was not interpretable this compound was also tested with MST. However, with none of the tested ligands a sigmoidal binding curve could be recorded. This means either that these compounds indeed do not bind or that the used conditions prevented the actual binding event. Besides, it is also possible that the His_6-tag, which elongates the N-terminus by 17 aa, folds back on the protein and might then interfere with binding. Therefore, to get a clearer statement about the binding of these compounds, one should consider a method that does not require the labeling of the protein, such as e.g. ITC. Considering the distinct chemical structures of the compounds, it is very unlikely that they are all able to bind to PA4183$^{16\text{-}155}$.

4.3.9 Conclusion and Outlook

The class III βαββββ-module-containing protein PA4183 is expressed in one operon with the sarcosine oxidization and utilization regulator SouR (Wurtzel *et al.*, 2012). Albeit it was shown that PA4183 is involved in the effective degradation of sarcosine when this compound serves as the sole carbon and nitrogen source (Willsey & Wargo, 2016), this study could not find evidence for a direct interaction between PA4183 and compounds from the central sarcosine catabolism. Further, no growth deficiencies were observed if other carbon sources are the sole energy source for the PA14 *PA4183*::Tn mutant. This could mean that PA4183 is not involved in central metabolic pathways and only indirectly connected to the sarcosine degradation. Therefore, the search for a potential substrate of PA4183 could be extended to the pathways that neutralize the toxic side products that are generated during sarcosine demethylation, like formaldehyde or H_2O_2.

The chemical sensitivity assays revealed that the PA14 *PA4183*::Tn mutant has an altered resistance to compounds with antimicrobial activity than the wt. Therefore, the function of PA4183 might in fact be linked to the mediation of resistance mechanisms. Since a direct interaction of the change-inducing compounds could not be confirmed, it is not possible to suggest a physiological function for PA4183 from this. The compounds have distinct targets in bacterial cells and a collective link that could be connected to PA4183 was not identified. To confirm the results and to eliminate false positives the PM should be repeated with the compounds that induced phenotypic changes. MICs should be determined as well, with a stepwise dilution series of the respective change inducing compounds. In addition, it must be confirmed that the phenotypes are only caused by the lack of the functional PA4183 protein. The chemical sensitivity assay with the identified compounds must be performed as a rescue experiment. For this, the protein is expressed from a plasmid in the PA14 *PA4183*::Tn mutant. If this returns the wt phenotype with the PA14 *PA4183*::Tn mutant, the destruction of PA4183 is solely responsible for the discovered changed respiration rates. Otherwise, it is possible that a spontaneous mutation in other genes occurred or that the presence of the transposon itself is responsible for the phenotypes. Such an experiment should also be considered for the growth of the PA14 *PA4183*::Tn mutant on sarcosine as sole carbon source since Willsey & Wargo, 2016 used the same transposon mutant from Liberati *et al.*, 2006. This would rule out that the transposon insertion in the *PA4183* gene has a negative impact on the expression of SouR and delivers an explanation if PA4183 really plays a role during sarcosine catabolism.

The high-resolution crystal structure of the homodimeric PA4183$^{16\text{-}155}$ gave detailed insight into a further class III βαβββ-module-containing protein that has the less common back-to-back dimerization form. The cocrystallized CHES buffer molecule, which was complexed in the conserved putative ligand-binding site delivers a new lead towards a potential substrate of PA4183, since it must share chemical similarities with the natural ligand that enable the interaction with the protein. The chemical structure of CHES could be put into a virtual screening for natural compounds with similar structure and the hits could be used for a ligand screen with PA4183$^{16\text{-}155}$ i.e. in a TSA or an MST screen to identify molecules that interact with the protein.

4.4 Open reading frames PA1358 – PA1359

The crystal structure of PA1358 (Figure 56 A) was published in the PDB (ID: 1U7I, Osipiuk, J., *et al.*, to be published) without functional data, structure discussion or associated publication. In contrast to the other class III βαβββ-module-containing proteins, the potential active site of PA1358 is a wide-open cleft (Figure 56 B).

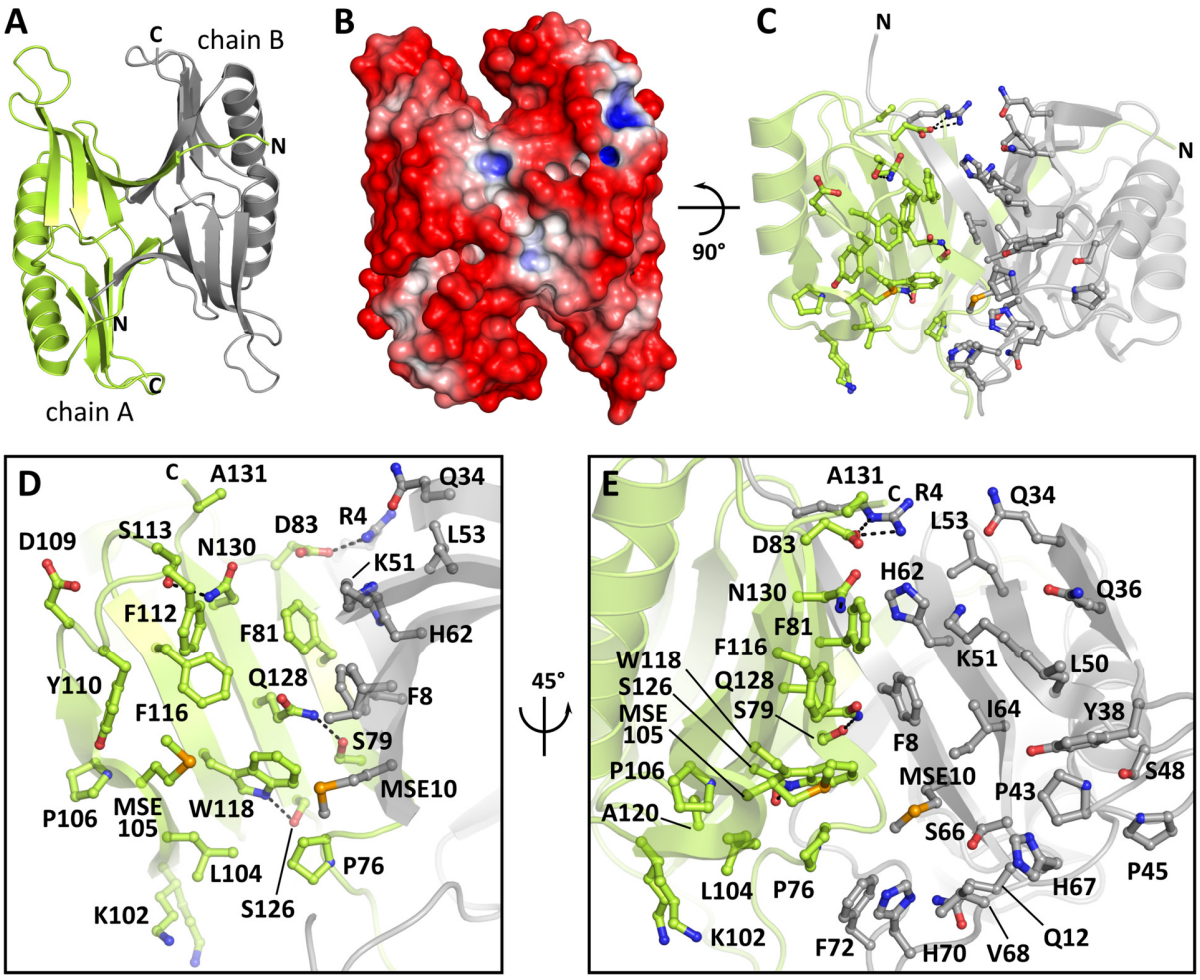

Figure 56: Crystal structure of the PA1358 dimer (PDB-ID: 1U7I, Osipiuk, J., *et al.*, to be published). A) The protein chains are colored in green (chain A) and grey (chain B). B) The electrostatic surface of PA1358 is colored from red (-5 kT/e) to blue (5 kT/e) as calculated by the PDB2PQR server Version 2.0.0 (Dolinsky *et al.*, 2004). C) Overview of side chains flanking the potential binding cleft. D/E) Detailed insight in the potential binding cleft of PA1358 in different orientations. Side chains are represented as balls and sticks. Oxygen atoms are colored in red, nitrogen in blue and selenium in orange. Dashed lines refer to H-bonds with a maximum distance of 3.2 Å.

It is not certain that this is also the case in solution since the loop regions on the tip of the cleft are involved in crystal contacts to symmetry-related molecules. This could stabilize the otherwise flexible loops that might in solution close off the cleft. In the crystal structure, all residues

that potentially participate in ligand binding are solvent exposed in the cleft, which has a rather negatively charged electrostatic surface (Figure 56 A-C). The amino acid side chains that flank the potential binding cleft and might thus be important for ligand binding or catalysis are displayed in Figure 56 D/E. Catalytically inactive side chains from five PHE, four PRO, two MET, one LEU and one ILE residues dominate the cleft (Holliday *et al.*, 2009). They might be important for stable interaction with the ligand or stabilize a potential reaction intermediate. However, there are also three HIS residues. Histidines are the most abundant catalytically active residues in proteins (Bartlett *et al.*, 2002), and are candidates that could mediate an enzymatic reaction. Especially H62 seems promising, since it is surrounded by other residues that often participate in catalysis (Bartlett *et al.*, 2002) such as K51, D83, R4 or Q34 (Figure 56 E). To derive a lead towards the protein function, the structure was compared against the PDB database with the PDBe-fold server (Krissinel & Henrick, 2004). The best among more than 100 hits came from a homologous *Bacillus cereus* protein (PDB-ID: 3OMS) with a sequence identity of 53 % and a similar potential active site. Since the function of this protein is also not identified, this does not aid functional characterization of PA1358. The rest of the hits were also inconclusive because sequence similarities, especially in binding site regions, were not detected. The gene of *PA1358* is predicted to be transcribed in an operon with the upstream ORF *PA1359* (Mao *et al.*, 2014). PA1359 is a 218 aa protein with an estimated MW of 23.9 kDa (Gasteiger *et al.*, 2005).

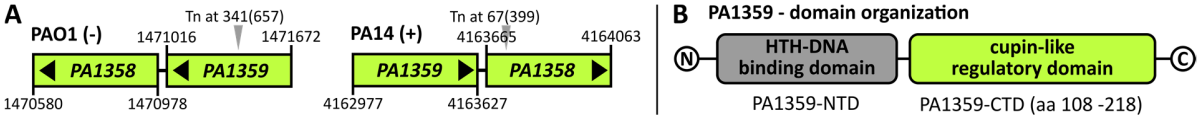

Figure 57: A) Operon organization and genomic localization of ORF *PA1358* and *PA1359* from *P. aeruginosa strains* PAO1 and the homologous genes in strain PA14 as derived from pseudomonas.com (Winsor *et al.*, 2016). The locus ID of the gene homologous to *PA1359* is *PA14_46710* in the PA14 strain and to *PA1358* it is *PA14_46720*. The transposon insertion sites (Tn) of the PAO1 *PA1359*::Tn mutant (left) and the PA14 *PA1358*::Tn mutant (right) used in this study are indicated by a grey arrow. The position of the insertion in the ORF is given in units of bp and the total length of the gene in brackets. B) Domain organization of the predicted transcriptional regulator PA1359 as predicted by a Blast analysis (Altschul *et al.*, 1997).

A protein Blast analysis (Altschul *et al.*, 1997) classified PA1359 as putative two domain transcriptional regulator of the xenobiotic response element (XRE)-family with an N-terminal conserved helix-turn-helix 3 (HTH) DNA-binding domain (PF01381) and a C-terminal conserved cupin 2 regulatory domain (PF07883). This operon was predicted to be a type II toxin-antitoxin (TA) system (Sevin & Barloy-Hubler, 2007). TA systems can regulate the persistence of bacterial

cells that allows them to survive stressful conditions, such as under exposure to antibiotics or in a dormant state with greatly reduced metabolism (Deter *et al.*, 2017). In the type II TA system, both the toxin and the antitoxin are proteins that interact with each other, to neutralize the harming effect of the toxin under standard conditions (Hall *et al.*, 2017). During stress response the antitoxin level decreases and the toxin is set free. It can then target the respective component of the bacterial cell (Deter *et al.*, 2017). Most antitoxins are two domain proteins that are coded upstream of the toxin gene, with an N-terminal DNA-binding domain that often has a HTH-motif and a C-terminal domain that interacts with the toxin (Chan *et al.*, 2016) which is consistent with the predicted domain organization of PA1359. Based on this, PA1358 would function as toxin while PA1359 would be the antitoxin in case they are a type II TA system.

4.4.1 Phenotyping

To identify the physiological roles of PA1358 and PA1359 and to find evidence for the predicted TA system, the phenotypes of transposon insertion mutants in both genes (Figure 57) were compared to the wt in planktonic growth and motility assays. The *PA1358* transposon insertion mutant was only verified in the PA14 background (PA14 *PA1358*::Tn). PA14 *PA1358*::Tn manufactured by Liberati *et al.*, 2006 was kindly provided by Prof. S. Häußler of the HZI. PCR and sequencing of the PCR product confirmed the *MAR2xT7* transposon in the ORF of *PA1358* at bp 67 (Figure 57 A) as stated by the manufacturer (Liberati *et al.*, 2006). The *PA1359* mutant was only available in the PAO1 background (PAO1 *PA1359*::Tn) from Held *et al.*, 2012 and kindly provided by Prof. S. Häußler of the HZI. The IS*phoA*/hah transposon was confirmed in the *PA1359* ORF at the supposed bp 341 (Figure 57 A) (Held *et al.*, 2012) by PCR and sequencing of the PCR product. The direct comparison of the mutants was not possible since they were not available in the same parental strain. PA1358 was also overexpressed in PA14 wt background from an arabinose inducible plasmid to demonstrate the possible toxicity of the protein. The behavior of the PA14 *PA1358*::Tn, compared to the wt, was further characterized using Phenotypic MicroArrays™.

4.4.1.1 Planktonic growth and motility

In this case, planktonic growth assays were performed to identify the toxicity of PA1358 in the absence of the potential antitoxin assuming that the PAO1 *PA1359*::Tn mutant shows distinct growth defects in comparison to the wt. However, the mutant deficient in PA1359 had comparable growth to the wt under standard conditions (Figure 58 A).

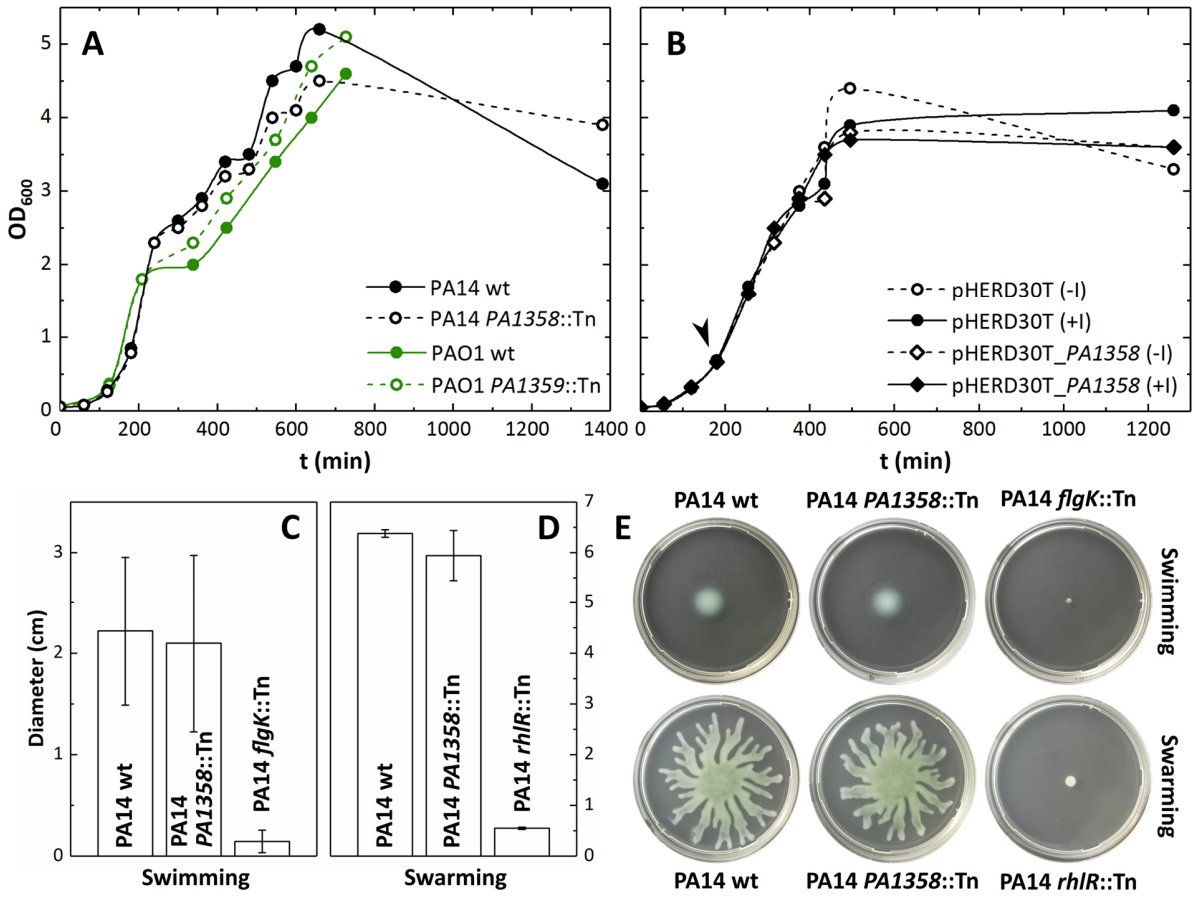

Figure 58: A) Planktonic growth curves of a PA14 *PA1358*::Tn mutant, the PA14 wt, a PAO1 *PA1359*::Tn mutant and the PAO1 wt. B) Planktonic growth curves of *P. aeruginosa* PA14 wt transformed with pHERD30T and pHERD30T_*PA1358*. After 180 min as indicated by the arrow the cultures were split and one portion of PA14 pHERD30T and PA14 pHERD30T_*PA1358* was induced (+I) with 0.1 % arabinose the others were not induced (pHERD30T (-I) and pHERD30T_*PA1358* (-I). A/B) Displayed is the increase of the optical density of the cell cultures measured at 600 nm (OD_{600}) over time (t (min)). The bacteria were incubated in LB medium under shaking conditions at 37 °C. C/D) The diameter of swimming and swarming colonies from PA14 *PA1358*::Tn mutants, PA14 wt and the negative controls PA14 *flgK*::Tn and PA14 *rhlR*::Tn were determined from three independent experiments, after incubation for 19 (swimming) and 18 h (swarming) at 37 °C. Error bars represent the deviation calculated from the mean triplicates. E) Examples of the respective swimming (Figure S2) and swarming colonies (Figure S3).

Since the PA1359 gene is located upstream in the genome, it is possible that the introduction of the transposon influences the transcription of PA1358 negatively and thus the level of protein in the cell, such that the toxicity of PA1358 cannot be developed. To ensure a high level of

PA1358 protein an arabinose inducible plasmid containing the gene for PA1358 was introduced to the PA14 wt strain to identify possible toxic effects caused by the accumulation of PA1358 in the bacterium. In addition, no striking growth differences were displayed between the mutant overexpressing PA1358 and the reference strain (Figure 58 B). Both results indicate that PA1358 has no cytotoxic effects if it is more abundant than PA1359, which does not support the hypothesis of PA1358 and PA1359 acting as a TA system.

Further, the growth assays did not support the identification of the physiological function of PA1358, as the behavior of PA14 *PA1358*::Tn mutant was well comparable to the wt in planktonic growth assays (Figure 58 A) as well as in the swimming and swarming motility assays (Figure 58 C/D/E). PA14 *PA1358*::Tn colonies had no morphological differences to the wt on LB agar plates and both developed the same level of greenish color after reaching high cell densities during planktonic and solid growth. These findings rule out that PA1358 participates in basic cellular functions or in the production and secretion of secondary metabolites like pyocyanin or pyoverdine that are responsible for the characteristic color (Pierson & Pierson, 2010).

4.4.1.2 Characterization of PA14 *PA1358*::Tn with Phenotype MicroArrays™

To identify the physiological function of PA1358, Phenotype MicroArrays™ were conducted in a comparative analysis of the PA14 *PA1358*::Tn mutant and the PA14 wt. The PA14 *PA1358*::Tn mutant had no significant differences to the wt when 190 distinct compounds served as sole carbon sources (Figure S4). In contrast to this, significant phenotypic changes were spotted in the chemical sensitivity assay (Figure 59). The PA14 *PA1358*::Tn mutant was less susceptible to hydroxylamine, azlocillin, enoxacin and 2-phenylphenol and more susceptible to chloroxylenol, oxacillin, tobramycin, phenethicillin and lauryl sulfobetaine (Figure 59 A). Of these, oxacillin was the only compound that caused a change only in the PA14 *PA1358*::Tn mutant and not in the other class III βαβββ gene mutants in the PA14 background (Figure S4). This could indicate that most effects are not caused by the deficiency of PA1358 but by the presence of the transposon itself.

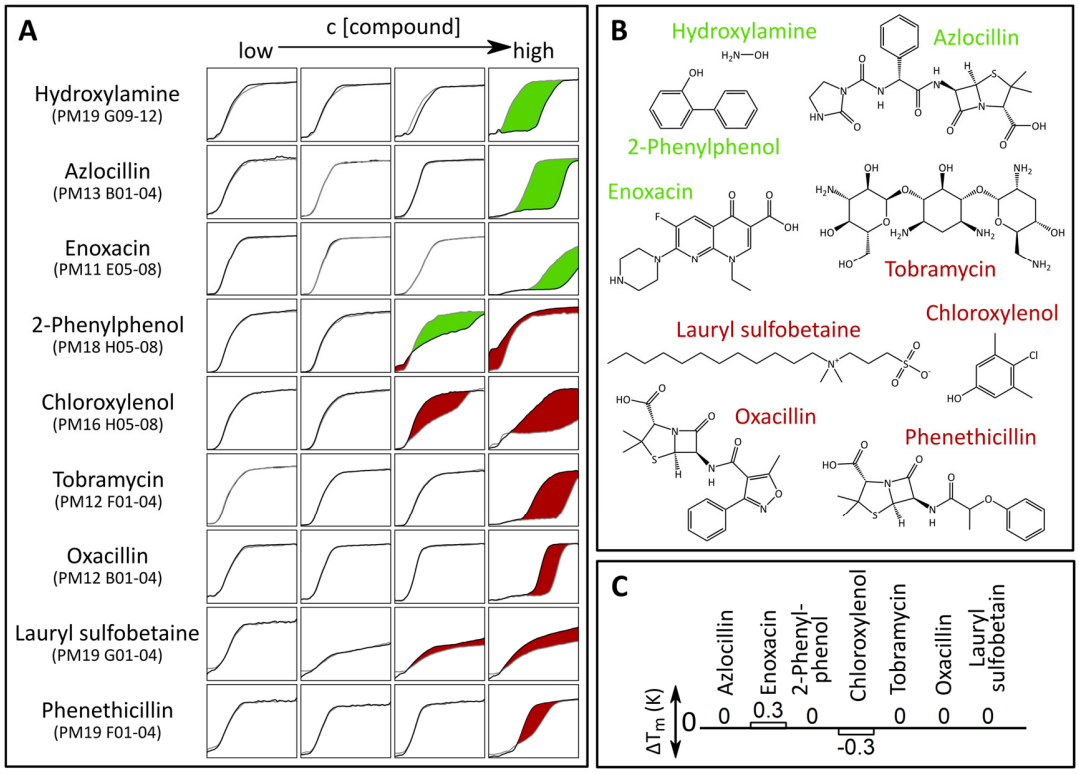

Figure 59: Chemical sensitivity Phenotype MicroArrays™ of PA14 *PA1358::*Tn. A) Overlaid respiration curves of the wt (black) and the mutant (grey) that were incubated on four concentrations of substances with potential antibacterial function, which induced significant changes between the wt and the mutant. The values in parentheses describe the number of the respective Phenotype Microarray™ and of the wells containing the compound. The respiration curves were obtained by plotting the measured absorbance in arbitrary units from 0-400 detected at 490 nm (y-axes) against the incubation time from 0-48 h (x-axes). To highlight the differences, the area between the respiration curves was colored green if the mutant respired better than the wt or red if the respiration of the mutant was inhibited. B) The chemical structures were obtained from the PubChem database (Kim *et al.*, 2016) and visualized with ChemDraw Professional 17.0. C) Changes in thermal stability (ΔT_m (K)) of PA1358 (T_m: 62°C) as measured with a TSA. ΔT_m were determined by averaging 3 independent experiments.

Oxacillin is a β-lactam antibiotic like phenethicillin and azlocillin, which inhibit peptidoglycan synthesis by covalent modification of the penicillin binding protein (Kong *et al.*, 2010). It is rather unlikely that PA1358 mediates the resistance to oxacillin only, but not to other β-lactam antibiotics. Since the other compounds have a variety of antimicrobial functions, it is not possible to draw simple conclusions from the PM results with respect to the physiological role of PA1358. If the direct interaction between one compound and PA1358 could be determined, the PM results could still deliver a hint towards the function of PA1358. Therefore, a TSA was conducted with the recombinantly expressed PA1358 protein (Figure S1) and the identified compounds. The melting temperature of PA1358 in buffer was 62 °C and was not significantly altered by any of the tested compounds (Figure 59 C). This suggests that none of them interacts with the protein under the tested conditions or at least that a potential interaction does not

stabilize the protein such that a change in T_m occurs. The latter could be investigated by the application of other methods like MST or ITC.

4.4.2 Interaction of PA1358 and PA1359-CTD

To further corroborate that PA1358 and PA1359 are not a type II TA system, as indicated by the microbiological assays, the direct interaction of both proteins was supposed to be tested. Since, the full-length PA1359 protein could not be expressed in *E. coli*, the successfully purified regulatory domain PA1359-CTD (4.4.3; Figure S1), which interacts with the toxin in related systems (Chan *et al.*, 2016), was used. An ITC experiment was conducted were PA1358 was titrated against PA1359-CTD but did not indicate any binding (Figure 60 A/B), showing that PA1358 and PA1359-CTD do not form a complex under the tested conditions. Further, an analytical SEC was conducted were a 1:1 mixture of PA1358 and PA1359-CTD and solutions with the separate proteins as reference was run over the column. Since PA1358 (14.8 kDa) and PA1359-CTD (12.9 kDa) have similar MWs and both are dimeric in solution, their elution volume is also similar (Figure 60 C; V_e: 14 and 14.2 ml). The same elution volume (14.1 ml) was discovered for the mixture of both proteins that eluted in one peak. Based on the similar MW of both proteins and the increased A_{280} of the peak, the mixture likely eluted as one peak that contained both proteins separately. Therefore, the analytical SEC does also not support complex formation between PA1358 and PA1359-CTD. Taken together it is rather unlikely that PA1358 and PA1359 can form a complex.

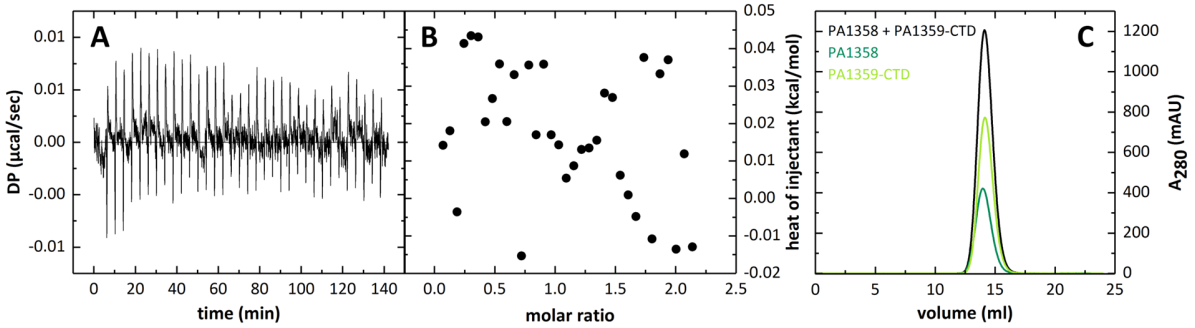

Figure 60: Possible interaction of PA1358 with PA1359-CTD. A/B) Titration of 1 mM PA1358 to 0.1 mM PA1359-CTD in an ITC-experiment as analyzed with Origin 7 (OriginLab Corp.). A) ITC raw data, displaying the measured differential thermal power (DP) in µcal/sec over time. B) Injection heat in kcal/mol plotted against the molar ratio of PA1358 and PA1359-CTD C) Elution profiles of the analytical SEC performed with a S75 10/300GL (GE Healthcare) in SEC-buffer. 100 µM of PA1358 (dark green) and PA1359-CTD (light green) and an equimolar mixture (black) of 100 µM of each protein were applied separately.

4.4.3 Construct design and purification of PA1359-CTD

The N-terminally His_6-tagged full-length protein was insoluble when expressed in *E. coli*. Therefore, a construct for the mere expression of the C-terminal domain (CTD) was designed, as recombinantly expressed DNA-binding proteins tend to aggregate in *E. coli*. The domain boundaries of PA1359 were set by analyzing a high-confidence 3D-structure prediction (80 % of the protein were modelled with 100 % confidence, no prediction for the first 40 aa) from the Phyre[2] server (Kelley *et al.*, 2015) and a secondary structure prediction performed with PSIPRED (Buchan *et al.*, 2013). The final expression construct for the PA1359-CTD ranged from aa 108 to 218 and was soluble expressed with an N-terminal His_6-tag. During a three-step purification, the tag was removed and the 12.9 kDa PA1359-CTD was isolated in high purity (Figure S1) and used for setting up crystallization screens.

4.4.4 From crystallization of PA1359-CTD to structure refinement

A well-diffracting crystal (d_{min}= 1.65 Å) of PA1359-CTD grew in the initial screen in 0.1 M Tris pH 8.5, 8 % (w/v) PEG8000 (JCSGII well A12, Figure 61 A). The phase problem was solved by the molecular replacement (MR) pipeline Balbes (Long *et al.*, 2008).

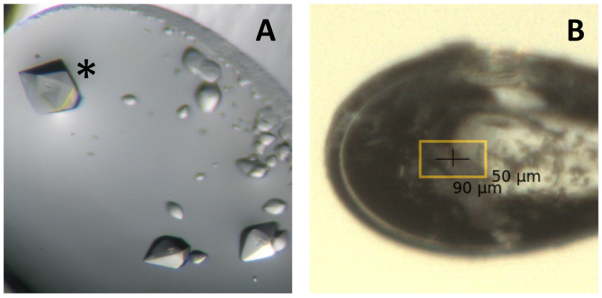

Figure 61: Crystals of PA1359-CTD grown in 0.1 M Tris pH 8.5, 8 % (w/v) PEG8000 A) Crystals in the crystallization drop. The asterisk marks the best diffracting crystal used for data collection. B) Crystal during data collection at SLS.

Two molecules of PA1359-CTD were present in the ASU (Figure 62 B), which has a solvent content of roughly 53 % as derived from the Matthews coefficient of 2.56 Å/Da (Matthews, 1968). The electron density for the vast part of the two protein molecules were well interpretable. However, no electron density was observed for the nine N-terminal residues from chain A and for the five N-terminal residues from chain B. The remaining structure was refined to an R_{cryst}

of 16.4 % and an R_{free} of 19 %. Table 19 contains the detailed data collection, processing and structure refinement statistics.

Table 19: Statistics for data collection, processing and structure refinement of PA1359-CTD

Data collection and processing		Refinement	
Beamline[†]/detector	X06DA, SLS/Pilatus 2M-F	**Resolution limit (Å)**	19.96-1.65
Wavelength (Å)	1	**Completeness (%)**	99.98
Temperature (K)	100	**Final R_{cryst} (%)**	16.4
Crystal-detector distance (mm)	150	**Final R_{free} (%)**	19.0
Rotation range per image (°)	0.1	**No. of reflections**	
Total rotation range (°)	360	**Working set**	33731
Exposure time per image (s)	0.1	**Test set**	1588
Space group	$P6_122$	**No. of non-H atoms**	
a, b, c (Å)	70.78 70.78 184.09	**Protein**	1724
α, β, γ (°)	90 90 120	**Solvent water/buffer**	188/24
Mosaicity (°)[#]	0.12	**Total**	1936
Resolution range (Å)	19.96-1.65 (1.68-1.65)	**R.m.s. deviations**	
Total No. of reflections	1267110 (63467)	**Bonds (Å)**	0.007
No. of unique reflections	33824 (1626)	**Angles (°)**	0.855
Completeness (%)	99.9 (100)	**Average *B* factors (Å²)**	
Multiplicity	37.5 (39.0)	**Protein**	40
Mean I/σ(I)	28.8 (1.7)	**Solvent water/buffer**	54/73
CC1/2[+]	100 (61.3)	**Ramachandran plot**	
R_{pim}[$]	1.3 (44.5)	**Favored regions (%)**	98.56
R_{meas}[$]	7.7 (280)	**Outliers (%)**	0
Wilson B-factor (Å²)	26.1	***MolProbity* Score[‡]**	1.29

Values in parentheses are for the highest resolution shell, [†]SLS: Swiss Light Source (PSI, Villigen, Schweiz). [#]Value as reportet by *AIMLESS* (Evans & Murshudov, 2013). [+]CC1/2 as reported by (Karplus & Diederichs, 2012). [$]$R_{pim} = \Sigma_{hkl}\,(1/(N-1))^{1/2}\,\Sigma_i \mid I_i(hkl) - \langle I(hkl)\rangle \mid / \Sigma_{hkl}\,\Sigma_i\, I_i(hkl)$; $R_{meas} = \Sigma_{hkl}\,(N/(N-1))^{1/2}\,\Sigma_i \mid I_i(hkl) - \langle I(hkl)\rangle \mid / \Sigma_{hkl}\,\Sigma_i\, I_i(hkl)$, where N is the number of observations of the reflection with index hkl and I_i is the intensity of its i^{th} observation (Weiss, 2001). [‡]*MolProbity* Score as reported by *MolProbity* (Chen *et al.*, 2010).

4.4.5 Overall structure of PA1359-CTD

The structure of PA1359-CTD revealed that it is a member of the RmlC-like cupin superfamily with one cupin domain per chain. One monomer consists of 10 β-strands (Figure 62 A). Four of these strands (β_3, β_{10}, β_5, β_8) form an antiparallel β-sheet that faces a second four-stranded (β_4, β_9, β_6, β_7) antiparallel β-sheet, together a small β-barrel is formed. This topology (Figure 62 A) represents the basic, conserved jelly roll or cupin-fold (Dunwell, 1998; Richardson, 1981). According to the core fold, there are two additional β-sheets, β_1 and β_2. These strands perform a domain swapping or β-strand exchange with the second protein chain in the ASU in a way that one of the core β-sheets is extended to a 6-stranded (β_1, β_2, β_3, β_{10}, β_5, β_8) antiparallel β-sheet (Figure 62 B). The resulting dimer is very likely stable in solution as this strand exchange is stabilized by several H-bonds that are formed between the backbone atoms of β_2- and β_3-strands

of both monomers (Figure 62 B, right). The monomers are further connected by salt bridges between the sidechains of R104 (chain B) and E18 (chain A), between E18 (chain B) and R105 (chain A) and between E44 (chain B) and the backbone of H15 (chain A) (Figure 62 A, right).

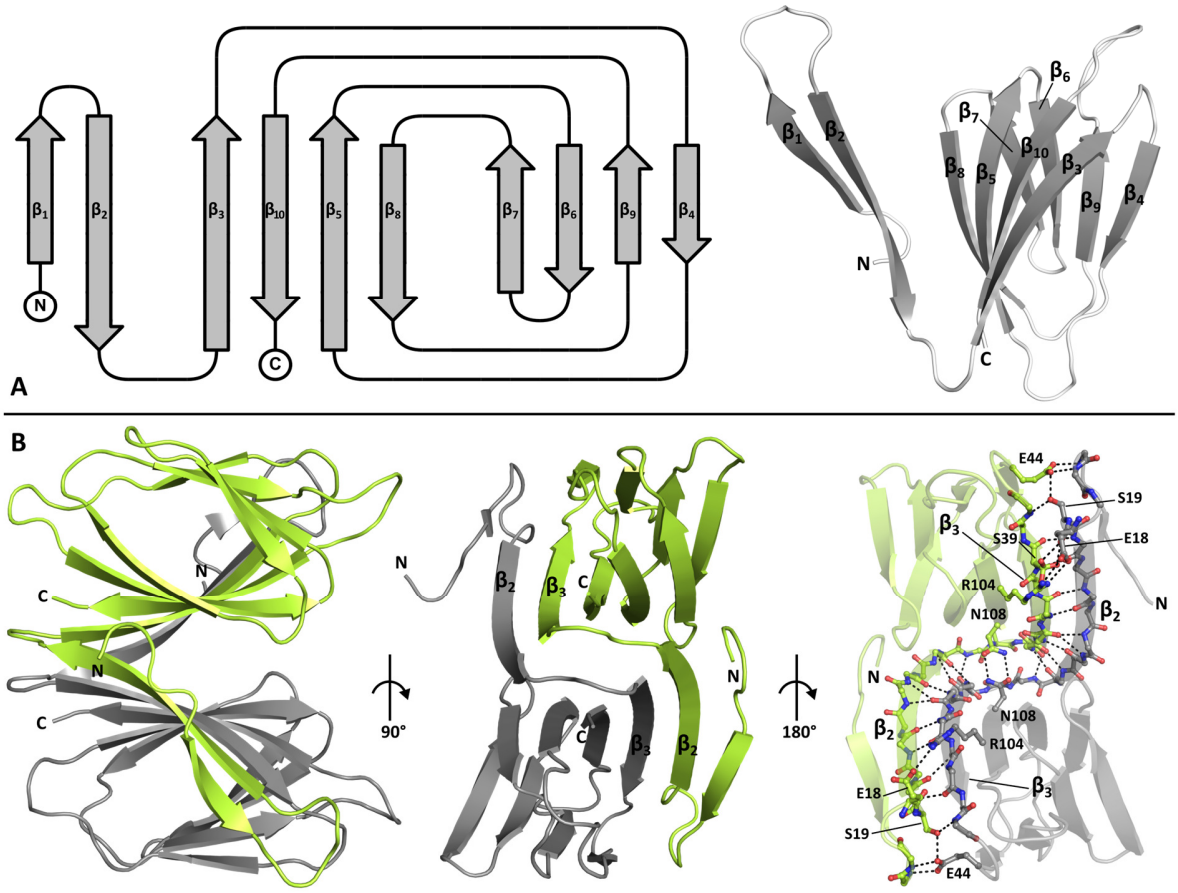

Figure 62: Architecture of PA1359-CTD. A) Topology of PA1359-CTD chain A. The β-strands are numbered from N- to C-term. The left image shows a schematic representation of secondary structure elements edited with TopDraw (Bond, 2003). The right image shows one monomer of PA1359-CTD. B) Content of the ASU. Chain A is colored green. Chain B is colored grey. The right image displays H-bonds, and salt bridges that connect both chains in the ASU.

A DLS experiment calculated a MW of 26.5 kDa, which matched the theoretical MW (25.7 kDa) of a PA1359-CTD dimer and confirmed this oligomerization state in solution. This is underpinned by an analysis with the 'Protein interfaces, surfaces and assemblies' service PISA (Krissinel and Henrick, 2007), which suggests assembly of the ASU as being stable in solution, based on the calculated value of 18 kcal/mol for the free energy of assembly dissociation (ΔG^{diss}), as ΔG^{diss}-values above zero determine assemblies as thermodynamically stable. Furthermore, the

interface area of this dimer is 1625 Å^2, which makes 25 % of the overall surface area of 6534 Å^2 and with this is at least twice as big as interfaces between other symmetry related chains.

4.4.6 Putative ligand binding site of PA1359-CTD

The structure was analyzed to identify hints towards a possible regulatory molecule that alters the affinity of the potential transcriptional regulator PA1359 towards DNA. An analysis with the PDBe-fold server (Krissinel and Henrick, 2004) returned more than 300 hits that did not deliver new leads, as the cupin fold is highly conserved while the sequence is not. Actually, the cupins have been reported as being the functionally most diverse known protein superfamily with 18 distinct functional classes (Dunwell *et al.*, 2004). Derived from the conserved structure, the potential binding site of PA1359-CTD for a small molecule is proposed to lie between the two β-sheets facing each other (Figure 63 B). The so-formed binding cavity has a negative electrostatic surface (Figure 63) and is flanked by the amino acid side chains represented in Figure 63 A.

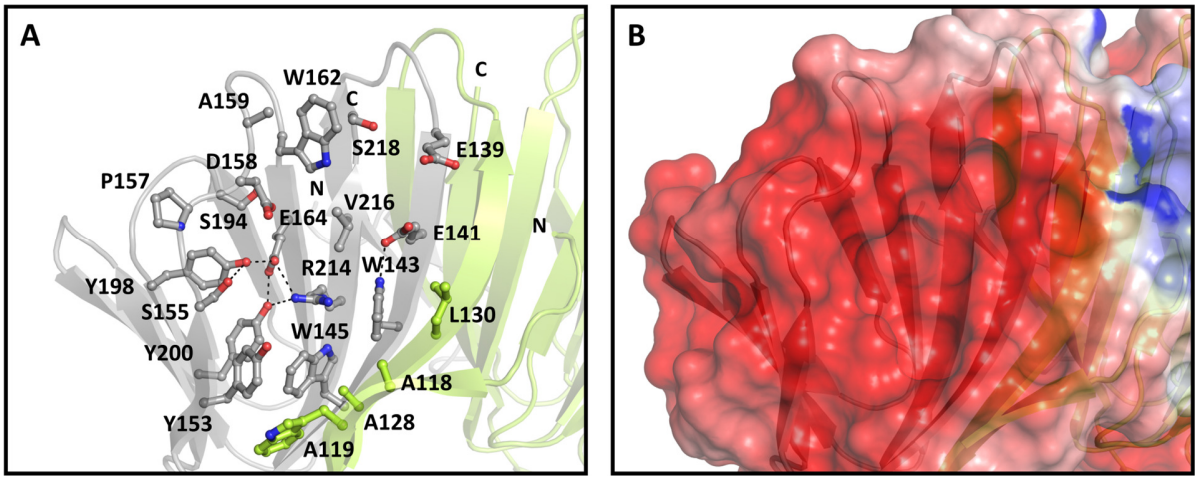

Figure 63: Putative ligand binding site of the PA1359-CTD dimer. The monomers are colored differently. A) Amino acid side chains flanking the potential ligand binding site are represented as balls and sticks. The numbering of the amino acid residues refers to their position in the full-length protein. Oxygen atoms are colored red and nitrogen atoms are blue. H-bonds with a maximum distance of 3.2 Å are displayed as dashed lines. B) The electrostatic surface of the potential ligand binding site of PA1359-CTD is colored from red to blue (-5 to 5 kT/e) as calculated by the PDB2PQR server Version 2.0.0 (Dolinsky *et al.*, 2004).

To get an idea of the potential position of the N-terminal DNA-binding domain, PA1359-CTD was superimposed with the two best hits that were used to make the structural prediction with the PHYRE^2-server (Kelley *et al.*, 2015). They were chosen as they resulted in the highest confidential model (100 % confidence at 80 % sequence coverage) and had the same two-domain

architecture as PA1359. One was the crystal structure from a potential HTH_3 family transcriptional regulator from *Vibrio cholerae* (PDB-ID: 1Y9Q; Kumaran, D., *et al.* to be published). The other structure is a hydroxypropylphosphonic acid epoxidase from *Streptomyces wedmorenis* with a catalytically active CTD and an HTH-fold containing NTD (PDB-ID: 2BNO, McLuskey *et al.*, 2005). Both structures contained the conserved C-terminal cupin fold that formed a dimer like PA1359-CTD. While the transcriptional regulator from *V. cholerae* formed a dimer in solution (Figure 64 A, PDB-ID: 1Y9Q, Kumaran, D., *et al.* to be published), the epoxidase formed a more complex homotetramer (Figure 64 B) (PDB-ID: 2BNO; McLuskey *et al.*, 2005). The structural alignments revealed that the potential molecule binding site of PA1359 could be blocked (Figure 64 C) or influenced (Figure 64 D) by the N-terminal domain such that the structure of the full-length protein is required to get an impression of all amino acid residues that are necessary for regulator binding.

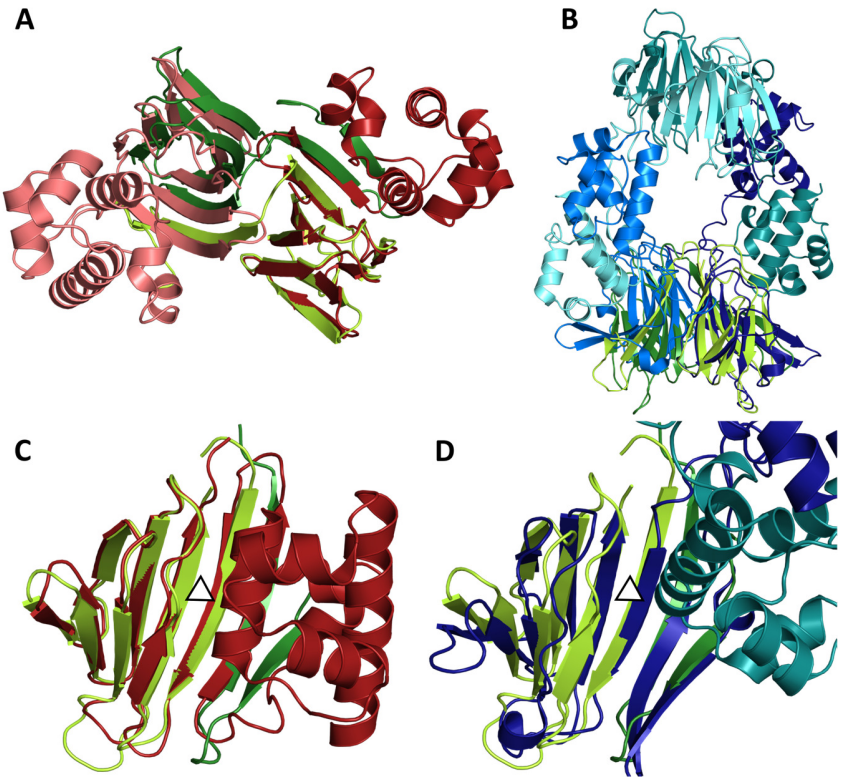

Figure 64: Superposition of PA1359-CTD (green) with structurally related proteins. A) Superposition with the homodimeric HTH_3 family transcriptional regulator (red) from *Vibrio cholerae* (PDB-ID: 1Y9Q; Kumaran, D., *et al.* to be published). B) Superposition with the homotetrameric hydroxypropylphosphonic acid epoxidase (blue) from *Streptomyces wedmorenis* (PDB-ID: 2BNO; McLuskey *et al.*, 2005). C/D) Magnification of the potential ligand-binding site of the respective cupin domain. The triangles indicate the potential ligand-binding site. Monomers of multimeric proteins are shown in different shades of green (PA1359-CTD), red (PDB-ID: 1Y9Q) or blue (PDB-ID: 2BNO).

4.4.7 Conclusion and Outlook

The ORF coding for the class III βαββββ-module-containing protein PA1358 and the probable transcriptional regulator PA1359 was predicted to be a type II TA-system with PA1358 as toxin and PA1359 as the antitoxin. However, there was no evidence to confirm the toxicity of PA1358 in the absence of PA1359 in the microbiological assays. Further, it was not possible to confirm the formation of a complex between PA1358 and the regulatory domain of PA1359, which would be expected from type II TA-system proteins. These results indicate that the prediction was not accurate and that PA1358 and PA1359 most probably fulfill another function.

The phenotypic characterization of the PA14 *PA1358*::Tn mutant provided no evidence that PA1358 plays a major role in the central metabolism of the bacterium and in the tested motility forms. Since the PA14 *PA1358*::Tn mutant had an altered metabolic rate in the chemical sensitivity assay, the protein might, as expected, participate in the mediation of resistance towards compounds with antimicrobial activity. Since no interaction was discovered between PA1358 and the identified compounds, further experiments must be conducted to suggest a precise function of PA1358. At first, the phenotypes from the chemical sensitivity assays should be confirmed by repeating the experiment and by determination of MICs, since the manufacturer does not provide the concentration of the compounds in the PM. Further, it must be clarified if the phenotypes are only caused by the lack of the functional PA1358 protein, if a spontaneous mutation in other genes occurred, or if the presence of the transposon itself is responsible for the phenotypes. As described for the other proteins investigated here, the chemical sensitivity assay with the identified compounds must be repeated as a rescue experiment in which the protein is expressed from a plasmid in the PA14 *PA1358*::Tn. If the phenotype of the PA14 *PA1358*::Tn mutant is reversed by the introduction of functional protein, the loss of PA1358 is confirmed to be responsible for a detected change in respiration rates.

The purification of the regulatory domain of PA1359 was first described in this study. The crystal structure of PA1359-CTD gave new insights in an undiscovered protein from the very diverse cupin fold superfamily. However, no hypothesis about the nature of a regulatory molecule can be made from the crystal structure, since the potential binding site is probably also built up by

the missing DNA binding domain. Therefore, more effort should be put in the soluble expression of the full-length PA1359 protein. The solubility could be enhanced if the full-length protein is expressed with different purification tags, such as MBP- or T7-lysozyme at the N- and/or at the C-termini.

4.5 PA4518

The ORF of *PA4518* in the *P. aeruginosa* genome is alone expressed in a single-gene transcriptional unit (Wurtzel *et al.*, 2012), and the crystal structure of the homodimeric class III βαββββ-module protein PA4518 (15.3 kDa, 141 aa) was determined in an earlier study (Vit, 2015). The precise analysis of the 3D arrangement of amino acids flanking the potential ligand-binding site did not provide any indications concerning a potential function or molecule interacting with PA4518 (Vit, 2015). Therefore, the physiological role of PA4518 was investigated by comparative analysis of the *PA4518* transposon insertion mutant (PA14 *PA4518*::Tn) with the wt. The PA14 *PA4518*::Tn was manufactured by Liberati *et al.*, 2006 and kindly provided by Prof. S. Häußler from the HZI. PCR and sequencing of the PCR product confirmed the *MAR2xT7* transposon in the ORF of *PA4518* at bp 63 (Figure 65 A) as stated by the manufacturer (Liberati *et al.*, 2006). The phenotype of PA14 *PA4518*::Tn was characterized with motility and planktonic growth assays and with Phenotype MicroArrays™.

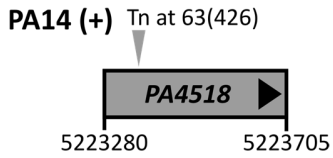

Figure 65: ORF of *PA4518* in the *P. aeruginosa* PA14 strain. The actual locus ID of the *PA4518* homologue in the PA14 strain is *PA14_58620*. The genomic localization given in bp of the gene was derived from pseudomonas.com (Winsor *et al.*, 2016). The transposon insertion site (Tn) of the PA14 *PA4518*::Tn mutant used in this study is indicated by a grey arrow. The position of the insertion in the ORF is given in units of bp and the total length of the gene in brackets.

4.5.1 Motility and planktonic growth of PA14 *PA4518*::Tn

Swimming, swarming (Figure 66 B-E) and planktonic growth (Figure 66 A) assays with PA14 *PA4518*::Tn pointed out that the mutant had comparable features as the wt. In addition to this, both strains developed the same characteristic green color when reaching high cell densities during planktonic growth and during solid growth on LB plates, indicating that they can produce comparable amounts of pyocyanin and pyoverdine. There were also no obvious morphological

differences between the colonies on agar plates. These findings indicated that the protein does not interfere in basic cellular functions and the production of the most abundant secondary metabolites, pyocyanin and pyoverdine under the tested conditions.

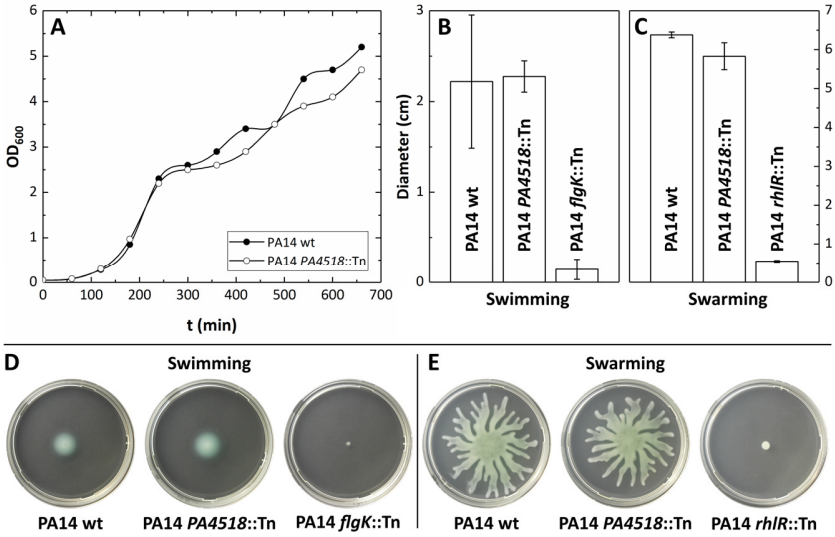

Figure 66: Phenotypic characterization of a *P. aeruginosa* PA14 PA4518 transposon insertion mutant (PA14 *PA4518*::Tn) in comparison to the respective wild type (PA14 wt) and a swimming (PA14 *flgK*::Tn) and swarming (PA14 *rhlR*::Tn) deficient mutant. A) Planktonic growth curves of the mutant and the wt. Displayed is the increase of the optical density of the cell cultures measured at 600 nm (OD_{600}) over time (t (min)). The bacteria were incubated in LB-medium under shaking conditions at 37 °C. B/C) The diameter of swimming and swarming colonies was determined from three independent experiments, after incubating for 19 (swimming) and 18 h (swarming) at 37 °C. Error bars represent the deviation calculated from the mean triplicates. D/E) Examples of the respective swimming and swarming colonies.

4.5.2 Characterization of PA14 *PA4518*::Tn with Phenotype MicroArrays™

The identification of the physiological role of PA4518 was further investigated with Phenotype MicroArrays™. The PA14 *PA4518*::Tn was incubated on 190 different carbon sources and on 240 distinct compounds with antimicrobial activity. The comparison of the respiration curves between the mutant and the wt (Figure S4) revealed no significant changes in the carbon source utilization assay, but some differences occurred in the chemical sensitivity assay. Four compounds induced an increased and six compounds induced a reduced respiration phenotype (Figure 67). Most of the compounds were also discovered in the PMs with the other PA14 mutants where their antimicrobial activity was already discussed. Polymyxin B (Evans *et al.*, 1999), compound 48/80 (Hall *et al.*, 1983; Lenney *et al.*, 1977; Nakao *et al.*, 2011) and chloroxylenol (McDonnell and Russell, 1999) target the membrane and increase its permeability. Azlocillin and phenethicillin are β-lactam antibiotics that inhibit the cell wall synthesis (Kong *et al.*, 2010).

Chlorodinitrobenzene (Habig *et al.*, 1974; Vuilleumier, 1997) and dichlofluanid (Schuphan *et al.*, 1981) are suggested to deplete the glutathione pool and thus increase the oxidative stress (Masip *et al.*, 2006). The aminoglycoside antibiotic tobramycin inhibits protein synthesis (Bendush & Weber, 1976; Brogden *et al.*, 1976). Ruthenium red and 5-fluoroorotic acid exclusively alter the respiration rate in the PA14 *PA4518*::Tn mutant (Figure 67 A, Figure S4).

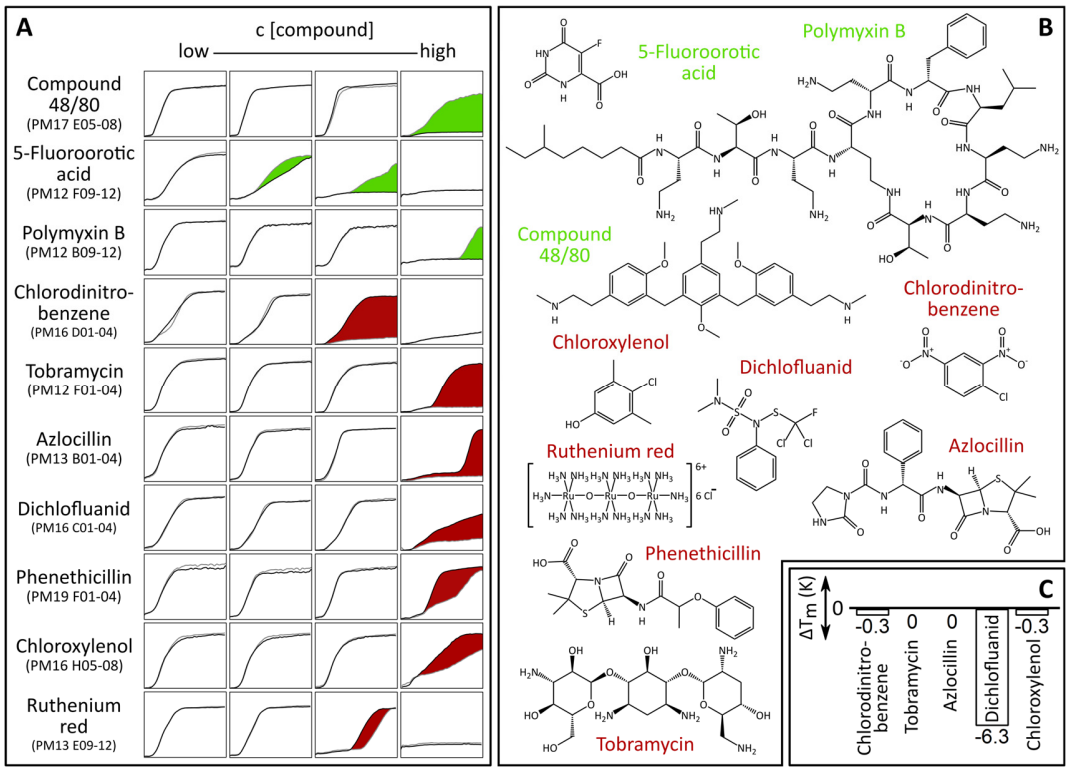

Figure 67: Chemical sensitivity Phenotype MicroArrays™ of PA14 *PA4518*::Tn. A) Displayed are the overlaid respiration curves of the wt (black) and the mutant (grey) that were incubated on four concentrations of substances with potential antibacterial function that induced significant changes between the wt and the mutant. The values in parentheses describe the number of the respective Phenotype Microarray™ and of the wells containing the compound. The respiration curves were obtained by plotting the measured absorbance in arbitrary units from 0-400 detected at 490 nm (y-axes) against the incubation time from 0-48 h (x-axes). To highlight the differences, the area between the respiration curves was colored green if the mutant respired better than the wt or red if the respiration of the mutant was inhibited. B) The chemical structures were obtained from the PubChem database (Kim *et al.*, 2016) and visualized with ChemDraw Professional 17.0. C) TSA results: changes in thermal stability (ΔT_m (K)) of PA4518 (T_m: 59°C) that were determined by averaging 3 independent experiments.

Ruthenium red is a histological stain that can interact with several Ca^{2+}-binding proteins in eukaryotes (Charuk *et al.*, 1990; Yamada *et al.*, 2000). The antimicrobial mechanism is not understood but ruthenium red was identified to bind to the bacterial Ca^{2+}-binding protein FtsZ and induce its bundling to protofilaments (Santra *et al.*, 2004). FtsZ bundling plays an important role during cell division (Koppelman *et al.*, 2004; Margolin, 2003) and therefore, ruthenium red

might interfere with proper proliferation of bacteria. 5-fluoroorotic acid is an analog of orotic acid and inhibits the enzymes of the pyrimidine synthesis pathway that use orotic acid as natural substrate, explaining the toxic effect towards bacteria (Krungkrai *et al.*, 1992). The PM identified compounds with antimicrobial activity mediated by various mechanisms. They could not be connected to suggest a physiological role for PA4518 that explains the observed phenotypes introduced by all compounds. Since it cannot be ruled out that PA4518 directly interacts with one of the compounds, the possible binding of the isolated PA4518 with the available compounds was investigated by a TSA and MST experiments. For this, the recombinantly expressed protein was purified by Vanessa Hering as described before (Vit, 2015) (Figure S1). In the TSA, dichlofluanid was the only compound that significantly affected the T_m of PA4518, which is 59 °C in SEC buffer by -6.3 K (Figure 67 C). The following MST experiment with dichlofluanid did not result in a binding curve, indicating that the compound does not interact with PA4518 under the tested conditions.

4.5.3 Conclusion and Outlook

The comparative analysis of the PA14 *PA4518*::Tn mutant phenotype with the PA14 wt revealed that the protein plays no role during central metabolism and during swimming and swarming motility. The higher susceptibility of the PA14 *PA4518*::Tn mutant to antibacterial compounds suggests that the class III βαββββ-module protein plays a role during the mediation of resistance towards toxic compounds as shown for other βαββββ-module proteins. However, no further hypotheses about a potential mechanism can be derived since the direct interaction with the compounds was not detectable and PA4518 might participate in a more common resistance mechanism. Before a reliable statement about the function of PA4518 can be made, the results from the chemical sensitivity assay have to be confirmed by repeating the experiment and by determination of MICs. Further, it must be demonstrated that the phenotype is only caused by the disruption of the *PA4518* gene and the resulting lack of the PA4518 protein and not by spontaneous mutations in other genes or by the presence of the transposon. This can be done in a rescue experiment in which a protein expression plasmid containing the *PA4518* ORF is introduced in the PA14 *PA4518*::Tn mutant and the phenotype of the change inducing com-

pounds is investigated. If the phenotype of the complemented PA14 *PA4518*::Tn mutant reflects the phenotype of the wt, the loss of PA4518 is responsible for a detected change in respiration rates.

5 Supplement

5.1 Protein purification

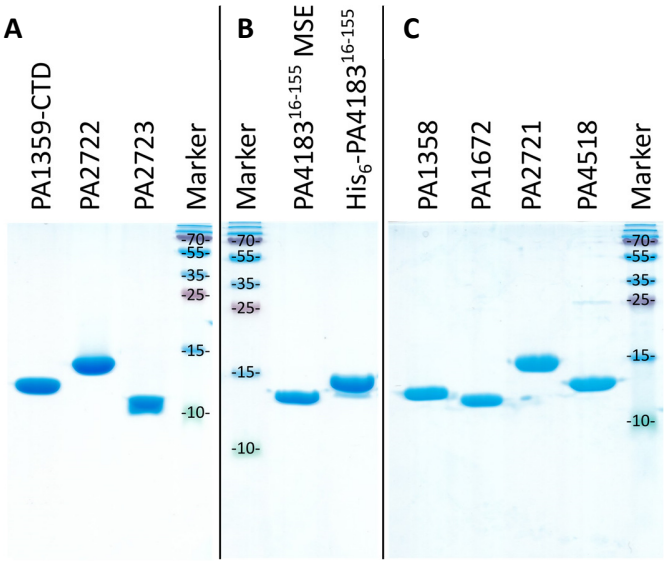

Figure S1: Final purities of proteins isolated during this study. Displayed is a 18 % SDS-gel. 4 µg protein were loaded on each lane and stained with InstantBlue™ (expedeon). The marker was PageRuler™ Plus Prestained Protein Ladder, #26620 (Thermo Fisher Scientific). A) Protein constructs that were first isolated during this study. B) Purity of PA4183$^{16-155}$ MSE produced for phasing the crystal structure and His$_6$-PA4183$^{16-155}$ utilized in MST experiments. C) Purity of proteins used and purified during this study, with before described purification protocols. PA4518 was purified by Vanessa Hering under supervision of the author.

5.2.1 Swimming and swarming motility assays

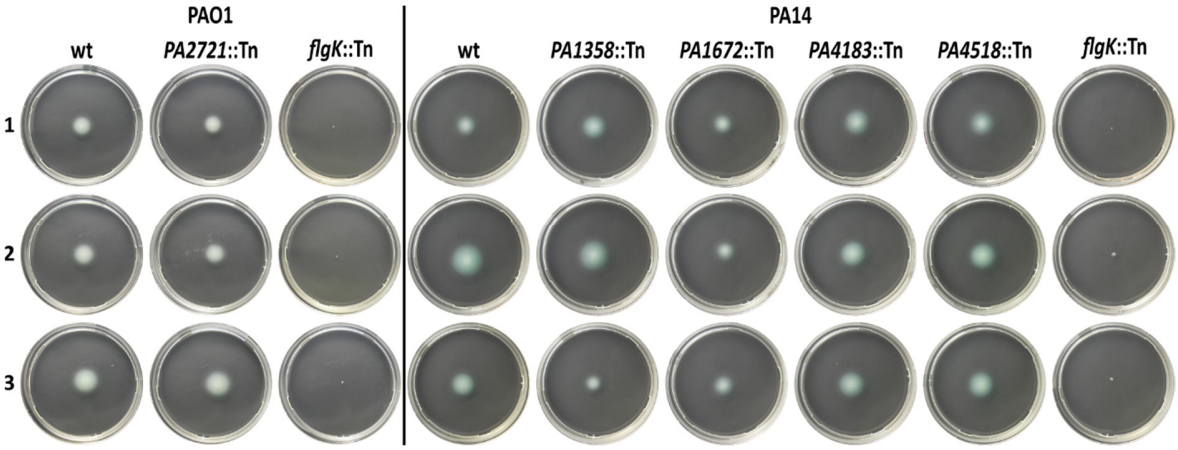

Figure S2: Swimming motility assays**.** Displayed are three independent biological replicates of the βαββββ transposon mutants in comparison with the respective wt and swimming deficient transposon mutant.

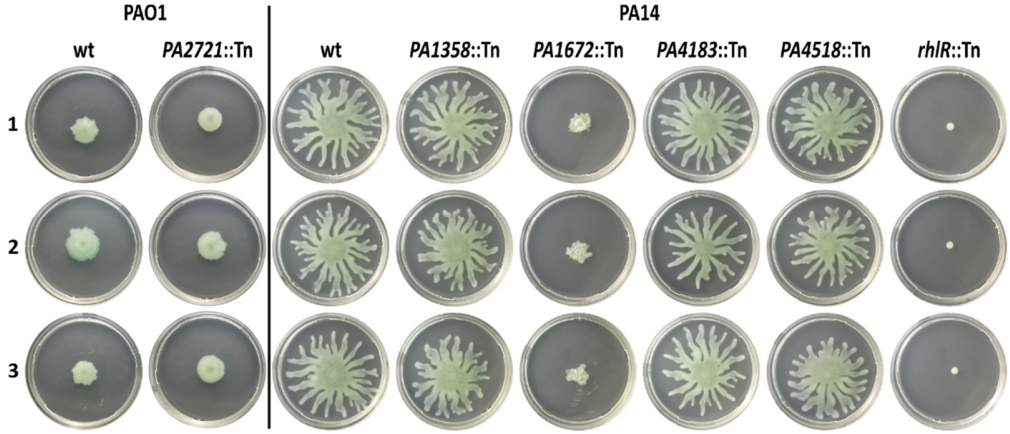

Figure S3: Swarming motility assays. Displayed are three independent biological replicates of the βαββββ transposon mutants in comparison with the respective wt and swimming deficient transposon mutant.

5.2.2 Phenotype MicroArrays™ (PM)

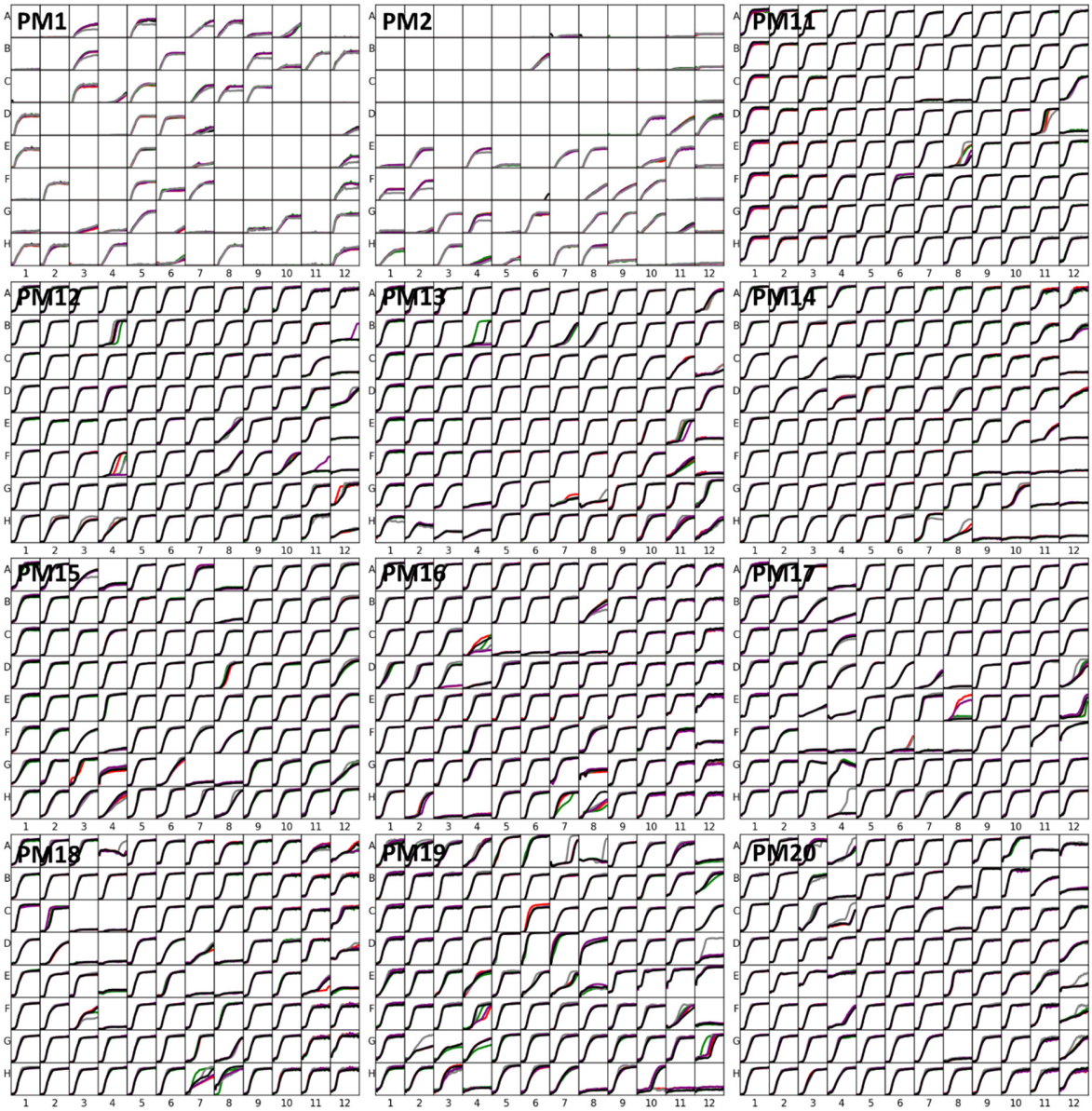

Figure S4: Phenotype MicroArrays™ of PA14 mutants *PA1358*::Tn (green), *PA1672*::Tn (grey), *PA4183*::Tn (red), *PA4518*::Tn (purple) in comparison to the PA14 WT (black). The respiration curves were obtained by plotting the measured absorbance (490 nm) in arbitrary units from 0-400 (y-axes) against the incubation time from 0-48 h (x-axes). Plates PM1 and PM2 contained different carbon sources and PM11-PM20 contained chemical compounds with antimicrobial activity in four different concentrations that are increasing from left to right (wells 1-4, 5-8 and 9-12 contain the same compound.

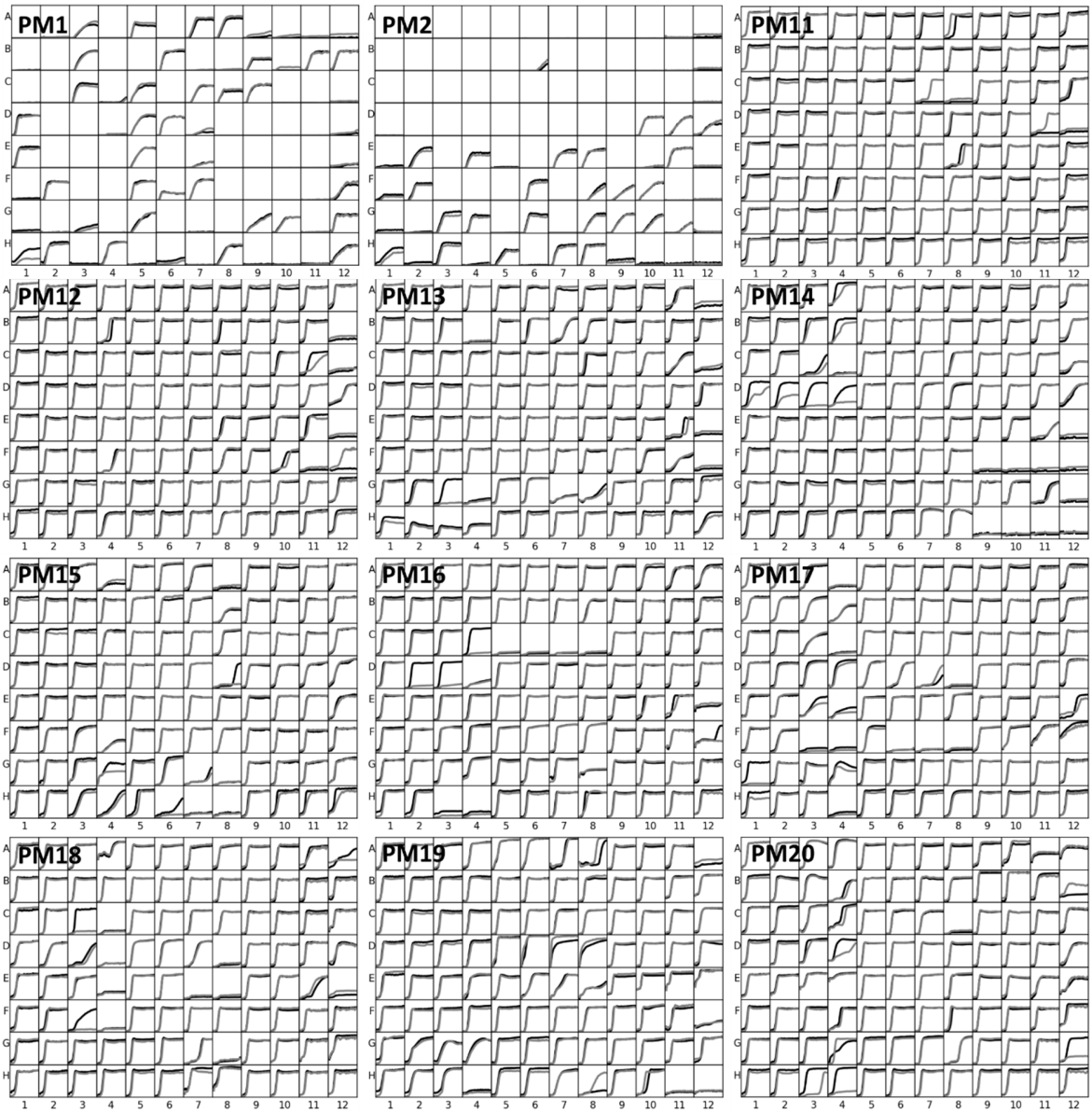

Figure S5: Phenotype MicorArrays™ of PAO1 WT (black) and *PA2721*::Tn mutant (grey). The respiration curves were obtained by plotting the measured absorbance (490 nm) in arbitrary units from 0-400 (y-axes) against the incubation time from 0-48 h (x-axes). Plates PM1 and PM2 contained different carbon sources and PM11-PM20 contained chemical compounds with antimicrobial activity in four different concentrations that are increasing from left to right (wells 1-4, 5-8 and 9-12 contain the same compound.

5.3 Supporting information for open reading frame PA2721-PA2723

5.3.1 Supporting information for PA2723

Figure S6: Secondary structure prediction of PA2723 by PSIPRED server **(Buchan *et al.*, 2013)**.

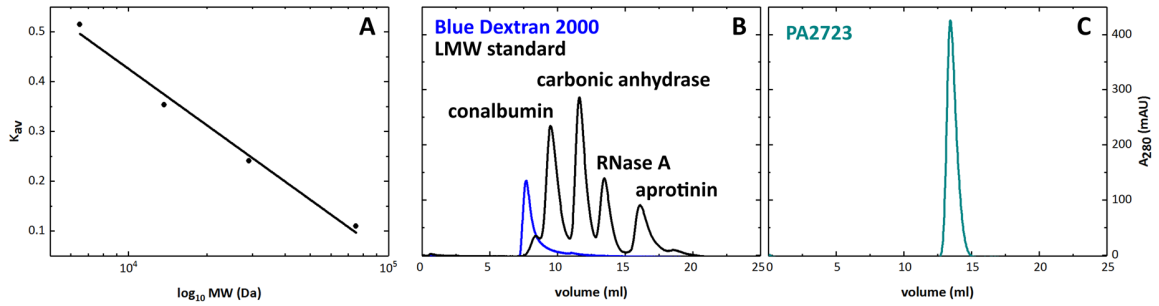

Figure S7: Determination of the oligomerization state of PA2723 by analytical SEC with a Superdex^{TM} 75 10/300 GL (GE Healthcare) in SEC-buffer. A) Calibration curve calculated after equation 2 using the elution volumes (V_e) from the LMW standard. B) Elution profiles of the LMW standard proteins and Blue dextran. The void volume (V_0) correspond to the V_e of Blue dextran 7.7 ml. The other V_e that were used for calculating the calibration curve are 9.48 ml for conalbumin, 11.62 ml for carbonic anhydrase, 13.46 ml for RNase A and 16.09 ml for aprotinin. C) Elution profile of PA2723. V_e is 13.5ml, which corresponds to a MW of 15.1 kDa.

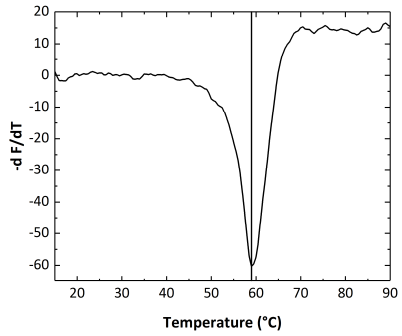

Figure S8: TSA of PA2723. Displayed is the negative derivative curve. The melting temperature of PA2723 is defined at the minimum of the derivative curve and is 59 °C in SEC buffer.

5.3.2 Supporting information for PA2722

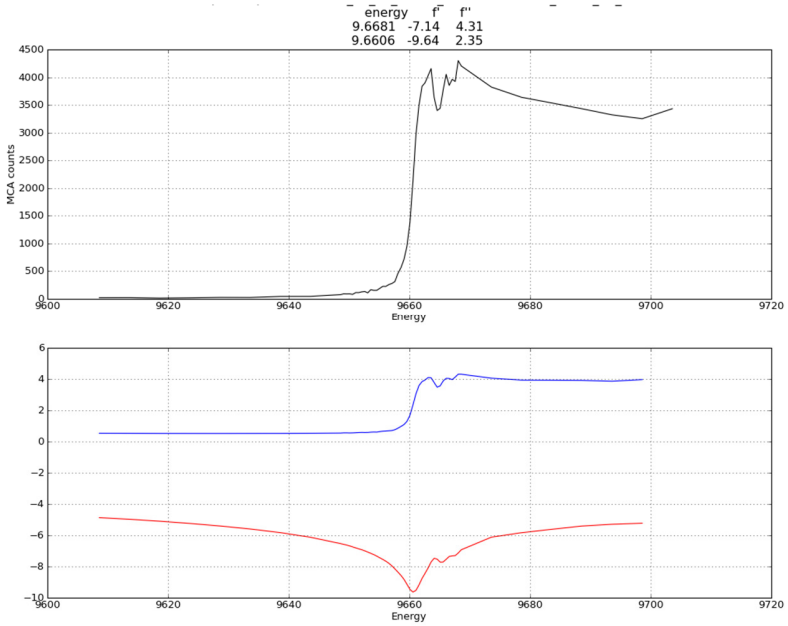

Figure S9: Fluorescence scan with the PA2722 crystal from BESSY II, BL14.2 to confirm the presence of Zn^{2+}-ions and to identify the peak wavelength for SAD-data collection.

5.3.3 Statistics of PA2721 crystals soaked with dichlofluanid and captan

Table S1: Full data collection, processing and refinement statistics of PA2721 crystals soaked with each 1.5 mM dichlofluanid & captan for 24 h.

Data collection & processing	Dichlofluanid	Captan
Beamline	BL14.2, BESSY II	home source
Detector	Pilatus 2M	Saturn944+
Wavelength (Å)	0.9184	1.54187
Temperature (K)	100	100
Exposure time per image (s)	0.3	10
Rotation range per image (°)	0.1	0.5
Total rotation range (°)	360	100
Crystal-detector distance (mm)	127	50
Space group	$P2_1$	$P2_1$
a,b,c (Å)	42.88 55.09 58.98	42.57 54.78 56.57
α,β,γ (°)	90.00 95.87 90.00	90.00 95.31 90.00
Resolution range (Å)	42.65-1.46 (1.48-1.46)	39.27 - 2.1 (2.16-2.1)
Mosaicity (°)[#]	0.33	0.36
Total No. of reflections	315008 (15711)	31243 (2411)
No. of unique reflections	47017 (2254)	14431 (1122)
Multiplicity	6.7	2.1
Completeness (%)	99.1 (97.2)	90.6 (57.6)
Mean I/σ(I)	20.2 (2.1)	7.3 (1.7)
CC1/2[+]	99.9 (85.6)	99.7 (70)
R_{meas} (%)[¥]	4.5 (106.4)	8.3 (58.7)
R_{pim} (%)[$]	1.7 (39.8)	5.5 (39.0)
Wilson B-factor (Å²)	16.2	25.7
Matthews coefficient	2	1.9
Solvent content (%)	38	34
Molecules per ASU	2	2

Refinement	Dichlofluanid	Captan
Space group	$P2_1$	$P2_1$
Resolution limits (Å)	42.65-1.46	39.27-2.1
Completeness (%)	98.8	94.5
Final R_{cryst} (%)	15.59	23.29
Final R_{free} (%)	17.6	26.59
No. of reflections		
Working set	46921	14411
Test set	2301	738
No. of non-H atoms		
Protein	2470	2364
Solvens	387	125
Total	2857	2489
R.m.s. deviations		
Bonds (Å)	0.007	0.002
Angles (°)	0.844	0.435
Average *B* factors (Å²)		
Protein	25.36	34.78
Solvens	38.89	36.34
Ramachandran plot		
Favoured regions (%)	97.8	96.1
Outliers (%)	0	0.32
MolProbity score[‡]	1.03	1.38

Values in parentheses are for the highest resolution shell, [†] BESSYII (HZB, Berlin, Germany), home source: MicroMax™ 007 HF rotating Cu-anode X-ray generator with a Saturn 944+ CCD detector (Rigaku, Tokyo, Japan), [#] Value as reported by *AIMLESS* (Evans and Murshudov, 2013). [+] CC1/2 as reported by (Karplus and Diederichs, 2012), [$] $R_{pim} = \Sigma_{hkl} (1/(N-1))^{1/2} \Sigma_i | I_i(hkl) - < I(hkl) > | / \Sigma_{hkl} \Sigma_i I_i(hkl)$ (Weiss, 2001); [¥] $R_{meas} = \Sigma_{hkl} (N/(N-1))^{1/2} \Sigma_i | I_i(hkl) - < I(hkl) > | / \Sigma_{hkl} \Sigma_i I_i(hkl)$, where N is the number of observations of the reflection with index hkl and I_i is the intensity of its i^{th} observation (Weiss, 2001). [‡] *MolProbity* score as reported by *MolProbity* (Chen *et al.*, 2010).

5.3.4 Crystallographic fragment screening with PA2721

Table S2: Summary of processing and refinement statistics[¥] of fragment screening data sets processed in SG P1.

Data set ID[§]	Completeness (%)	ISa	Res. (Å)	R_{work} (%)	R_{free} (%)	R.m.s. deviations bonds (Å)	R.m.s. deviations angles (°)
1	93.8 (91.0)	33.4	1.5	15.34	19.48	0.009	1.218
3	95.8 (93.3)	32.5	1.53	16.78	22.17	0.010	1.228
4	74.8 (75.2)	38.7	1.6	19.49	27.22	0.011	1.265
5	85.0 (85.4)	37.7	1.7	18.14	23.01	0.011	1.317
7	77.6 (79.4)	36.6	1.26	20.36	25.53	0.011	1.274
9	93.5 (90.7)	32.4	1.31	18.1	21.83	0.009	1.242
12	94.2 (92.0)	23.2	1.69	26.33	34.16	0.015	1.554
15	86.2 (84.9)	26.3	1.34	22.61	25.61	0.011	1.323
16	93.3 (91.9)	38.1	1.63	16.6	20.11	0.010	1.270
18	92.6 (88.6)	18.0	1.68	28.25	37.33	0.016	1.604
19	93.5 (91.6)	35.6	1.45	14.33	18.29	0.009	1.205
20	85.5 (87.6)	42.7	1.51	15.61	21.15	0.009	1.195
25	93.1 (90.8)	25.3	1.45	23.12	26.6	0.011	1.362
26	92.7 (87.4)	19.6	1.5	23.26	27.71	0.012	1.345
28	94.6 (93.8)	38.5	1.59	14.54	19.69	0.009	1.178
32	92.4 (91.2)	36.8	1.35	21.04	26.28	0.010	1.271
34	93.1 (92.3)	30.5	1.52	19.87	23.78	0.011	1.285
37	94.1 (91.8)	28.8	1.45	20.41	26.22	0.011	1.319
40	95.1 (92.0)	31.9	1.35	20.08	24.51	0.010	1.236
46	92.4 (90.7)	35.7	1.33	19.09	23.8	0.010	1.253
47	93.6 (91.5)	37.8	1.37	17.83	23.25	0.010	1.230
49	94.9 (93.2)	25.9	1.67	20.64	25.55	0.012	1.361
50	75.6 (77.2)	31.3	1.69	20.22	26.89	0.012	1.304
51	93.7 (91.2)	31.6	1.36	17.46	22.09	0.009	1.204
52	94.2 (92.3)	31.1	1.49	16.34	20.93	0.009	1.219
55	84.2 (86.5)	45.1	1.76	21.13	28.1	0.012	1.353
58	86.0 (86.4)	26.2	1.48	23.78	28.84	0.013	1.391
59	93.8 (90.9)	33.2	1.55	16.74	22.55	0.011	1.237
62	92.0 (90.8)	29.8	1.3	22.74	26.97	0.010	1.316
63	93.5 (90.6)	32.8	1.43	23.76	28.83	0.012	1.393
64	94.6 (90.3)	28.8	1.61	20.98	26.01	0.012	1.374
65	92.4 (88.8)	31.8	1.47	25.74	30.09	0.013	1.444
66	78.5 (79.2)	37.5	1.28	23.21	28.76	0.010	1.235
67	93.3 (90.3)	29.7	1.37	25.13	31.5	0.012	1.366
71	93.9 (89.8)	34.3	1.6	18.72	22.82	0.012	1.326
73	92.5 (87.3)	27.7	1.59	24.11	31.4	0.013	1.404
75	77.9 (79.8)	43.7	1.29	18.78	23.72	0.009	1.242
77	94.1 (89.8)	26.7	1.57	15.37	20.07	0.010	1.209
86	93.9 (92.5)	32.8	1.5	14.29	19.11	0.009	1.181
87	84.3 (83.1)	37.4	1.6	22.53	29.92	0.013	1.362
88	76.6 (78.9)	40.1	1.48	25.78	34.7	0.013	1.399
91	93.0 (88.6)	29.6	1.8	21.12	27.75	0.013	1.399
94	90.5 (87.6)	24.8	1.8	23.49	30.85	0.014	1.470
96	90.3 (87.5)	36.8	1.38	18.92	24.59	0.010	1.268
98	94.5 (93.3)	31.0	1.89	16.52	22.35	0.012	1.293
120	92.5 (90.7)	36.0	1.39	18.31	22.98	0.009	1.261
123[¤]	94.7 (92.0)	15.2	2.0	19.88	27.06	0.008	0.977

[§]The data set ID refers to the ID of the soaked fragments. Data sets 1-120 were collected at beamline 14.2, BESSYII (HZB). [¥]Processing statistics (Completeness (%), Isa value and Resolution (Res. (Å)) as calculated by XDSAPPv2.99 or v2.0 (Krug *et al.*, 2012; Sparta *et al.*, 2016). Refinement statistics as calculated by phenix.refine (Adams *et al.*, 2010) through the HZB automated refinement pipeline. [¤]Data set 123 was measured at the home source. Processing statistics as calculated by XDS (Kabsch, 2010) and Aimless (Winn *et al.*, 2011). Refinement statistics as calculated by phenix.refine (Adams *et al.*, 2010).

Table S3: Summary of processing[¥] and refinement[†] statistics of fragment screening data sets processed in space group $P2_1$.

Data set ID[§]	Completeness (%)	ISa	Res. (Å)	R_{work} (%)	R_{free} (%)	R.m.s. deviations bonds (Å)	R.m.s. deviations angles (°)
2	94.3 (92.5)	44.1	1.5	20.55	24.21	0.011	1.324
6	95.0 (94.0)	42.9	1.38	17.33	21.68	0.008	1.189
8	92.2 (68.9)	13.6	1.41	24.36	30.94	0.011	1.320
10	94.4 (93.8)	50.9	1.47	16.0	20.17	0.009	1.171
11	96.8 (96.9)	35.8	1.5	17.74	22.25	0.009	1.168
14	96.1 (96.4)	45.2	1.77	19.07	24.02	0.010	1.251
17	93.9 (92.6)	35.2	1.38	16.85	21.87	0.008	1.180
21	95.4 (95.3)	39.6	1.46	18.12	22.93	0.009	1.155
30	96.6 (94.3)	29.6	1.56	14.42	20.47	0.008	1.154
31	98.9 (98.4)	27.4	1.44	21.1	24.03	0.010	1.313
33	95.0 (93.2)	20.7	2.13	18.31	26.5	0.013	1.330
35	94.2 (93.3)	38.6	1.28	17.2	20.61	0.008	1.206
36	97.2 (96.8)	28.9	1.54	18.72	23.81	0.010	1.139
39	96.4 (94.5)	37.4	1.29	19.1	23.75	0.009	1.211
41	99.2 (97.5)	35.8	1.2	21.82	24.34	0.009	1.236
44	91.7 (90.2)	37.1	1.4	16.64	20.1	0.008	1.201
45	91.8 (89.1)	40.6	1.51	15.44	21.67	0.009	1.119
53	94.0 (92.1)	40.6	1.42	16.16	20.5	0.008	1.196
54	98.8 (97.7)	37.9	1.4	18.45	22.61	0.009	1.167
57	96.5 (95.3)	38.1	1.49	17.44	22.31	0.009	1.204
60	94.7 (93.6)	46.6	1.48	16.2	21.69	0.009	1.207
61	95.6 (94.0)	33.1	1.25	18.83	21.02	0.008	1.212
69	95.3 (91.9)	44.4	1.43	18.79	22.29	0.009	1.242
70	96.0 (92.8)	21.1	1.48	20.06	25.88	0.011	1.241
72	96.3 (96.3)	50.7	1.44	17.78	22.67	0.008	1.131
76	95.3 (94.7)	48.8	1.72	24.39	30.86	0.014	1.447
78	94.0 (74.6)	31.7	1.04	20.85	23.84	0.008	1.177
79	95.2 (94.6)	43.7	1.4	16.95	21.27	0.008	1.165
80	96.1 (94.5)	37.3	1.34	18.1	21.96	0.009	1.230
85	94.4 (94.2)	26.8	1.56	15.95	22.77	0.009	1.158
89	95.5 (95.6)	41.5	1.55	21.43	25.07	0.011	1.231
90	96.5 (94.1)	36.9	1.31	17.73	21.72	0.008	1.161
93	95.8 (94.3)	41.4	1.27	19.23	24.7	0.009	1.170
99	98.6 (96.9)	23.2	1.51	18.22	24.14	0.010	1.221
101	95.1 (93.6)	37.9	1.33	16.99	20.16	0.008	1.164
102	94.6 (92.6)	29.7	1.3	19.64	23.34	0.008	1.174
122	96.7 (96.3)	34.9	1.28	15.65	18.27	0.008	1.201
124	96.4 (95.7)	41.1	1.45	17.53	21.68	0.008	1.128
125	96.5 (95.3)	19.2	1.6	18.56	24.66	0.010	1.183
13[¤]	96.0 (93.0)	17.4	2.0	25.94	34.01	0.015	1.281
29	95.8 (92.4)	49.6	1.9	17.90	22.55	0.005	0.747
43	94.2 (69.2)	47.7	2.0	19.37	23.70	0.005	0.836
56	91.5 (59.3)	31.7	2.0	19.53	23.05	0.005	1.243
68	97.7 (81.2)	28.3	2.0	20.09	24.02	0.010	1.128
82	97.4 (95.8)	39.2	2.1	20.20	23.99	0.015	1.868
97	92.2 (65.8)	54.5	1.8	19.95	24.41	0.014	1.359
100	100 (100)	20.4	2.0	18.32	23.62	0.007	0.942
121	96.9 (93.8)	30.4	1.9	21.04	22.49	0.006	0.974

[§]The data set ID refers to the ID of the fragments soaked into the crystal. Data sets 2-125 were collected at beamline BL14.2, BESSY II (HZB). [¥]Processing statistics (Completeness (%), Isa value and Resolution (Res., (Å)) as calculated by XDSAPP v2.99 or v2.0 (Krug *et al.*, 2012; Sparta *et al.*, 2016). Refinement statistics as calculated by phenix.refine (Adams *et al.*, 2010) through the HZB automated refinement pipeline. [¤]Data sets 13-121 were measured at the home source. Processing statistics as calculated by XDS (Kabsch, 2010) and Aimless (Winn *et al.*, 2011). Refinement statistics as calculated by phenix.refine (Adams *et al.*, 2010). Data sets with fragment screening hits are marked green.

Table S4: Data collection and processing statistics of PA2721 fragment screening hits (8, 10, 61 & 100) and of input models for HZB phasing and refinement pipeline (90, 19).

Data set ID	8	10	61	90	19	100
Beamline/detector[†]	BL14.2, BESSY II/Pilatus 2M					home source
Wavelength (Å)	0.9184					1.54187
Temperature (K)	100					100
Exposure time per image (s)		0.2				10
Rotation range per image (°)		0.1				0.5
Total rotation range (°)	160	120	120	160	220	360
Crystal-detector distance (mm)	115	127	144	136	115	40
Space group	$P2_1$	$P2_1$	$P2_1$	$P2_1$	P1	$P2_1$
a,b,c (Å)	42.75 55.18 56.65	42.42 55.01 56.27	42.83 54.59 57.22	42.41 54.88 56.35	56.51 69.06 69.64	42.20 54.96 56.17
α,β,γ (°)	90.0 93.69 90.0	90 95.68 90	90 93.97 90	90.0 95.72 90.0	104.31 93.1 93.37	90 95.41 90
Resolution range (Å)	42.66-1.30 (1.38-1.30)	42.21-1.47 (1.56-1.47)	39.45-1.25 (1.33-1.25)	42.2-1.31 (1.39-1.31)	44.77-1.45 (1.54-1.45)	42.01-2.0 (2.05-2.00)
Mosaicity (°)[#]	0.102	0.174	0.064	0.155	0.153	0.19
Total No. of reflections	192660	96044	160205	180982	370918	127492
No. of unique reflections	63991	41696	69630	59727	169345	17448
Multiplicity	3.0	2.3	2.3	3.0	2.2	7.1
Completeness (%)	98.6 (97.9)	94.4 (93.8)	95.6 (94.0)	96.5 (94.1)	93.5 (91.6)	100.0 (100.0)
Mean I/σ(I)	11.74 (2.45)	18.09 (2.40)	11.00 (1.61)	12.64 (0.84)	13.08 (2.41)	7.2 (1.8)
CC1/2[+]	99.8 (79.1)	100.0 (83.7)	99.9 (63.5)	99.9 (44.8)	99.9 (80.3)	98.4 (58.6)
R_{meas} (%)[¥]	6.6 (54.3)	3.5 (49.1)	5.8 (72.9)	5.2 (147.4)	5.6 (47.2)	31.7 (149.3)
Wilson B-factor (Å^2)	16.97	24.99	18.2	23.6	19.84	11.8
Isa	24.06	50.93	33.12	36.89	35.59	20.41
Matthews coefficient	1.9	1.9	1.9	1.9	1.9	1.9
Solvent content (%)	35	35	35	35	34	34
Molecules per ASU	2	2	2	2	8	2

Values in parentheses are for the highest resolution shell, [†]BESSYII (HZB, Berlin, Germany), home source: MicroMax™ 007 HF rotating Cu-anode X-ray generator with a Saturn 944+ CCD detector (Rigaku, Tokyo, Japan), [#]Value as reported by *AIMLESS* (Evans and Murshudov, 2013). [+]CC1/2 as reported by (Karplus and Diederichs, 2012), [¥]$R_{meas} = \Sigma_{hkl} (N/(N-1))^{1/2} \Sigma_i | I_i(hkl) - < I(hkl) > | / \Sigma_{hkl} \Sigma_i I_i(hkl)$, where N is the number of observations of the reflection with index hkl and I_i is the intensity of its i^{th} observation (Weiss, 2001).

Table S5: Refinement statistics of PA2721 fragment screening hits (8, 10, 61&100) and of input models for HZB phasing and refinement pipeline (90 & 19).

Data set ID	8	10	61	90	100	19
Space group	$P2_1$	$P2_1$	$P2_1$	$P2_1$	$P2_1$	P1
Resolution limits (Å)	39.49-1.30	39.24-1.47	39.45-1.25	35.46-1.31	27.96-2.0	39.32-1.45
Completeness (%)	98.6	94.44	95.57	96.51	99.99	93.50
Final R_{cryst} (%)	13.98	16.62	14.80	23.18	18.02	18.27
Final R_{free} (%)	15.41	18.69	16.93	26.19	23.12	20.61
No. of reflections						
Working set	63984	41683	69614	59696	17432	169271
Test set	2101	2084	2100	2100	793	2099
No. of non-H atoms						
Protein	2508	2544	2516	2335	2447	9727
Fragment	38	36	11	-	9	-
Solvens	462	297	419	139	244	1152
Total	3008	2877	2946	2474	2700	10879
R.m.s. deviations						
Bonds (Å)	0.005	0.003	0.007	0.004	0.005	0.008
Angles (°)	0.953	0.697	0.951	0.651	0.842	1.164
Average *B* factors (Å^2)						
Protein	14.0	26.96	17.18	22.17	19.09	15.05
Fragment	17.22	41.63	17.12	-	14.92	-
Solvens	31.67	39.78	33.62	29.18	28.56	23.85
Ramachandran plot						
Favoured regions (%)	96.5	97.1	95.9	96.41	95.2	97.8
Outliers (%)	0	0	0	0	0	0.08
MolProbity score‡	1.23	1.24	1.22	1.06	1.43	1.15

‡ *MolProbity* score as reported by *MolProbity* (Chen *et al.*, 2010).

Table S6: Gene names of homologs in *P. aeruginosa* strains PAO1 and PA14

PAO1	PA14
PA1358	PA14_46720
PA1359	PA14_46710
PA1672	PA14_42870
PA2721	PA14_28960
PA2722	PA14_28950
PA2723	PA14_28940
PA4183	PA14_09780
PA4184	PA14_09770
PA4518	PA14_58620

6 References

Adams, P.D., Afonine, P.V., Bunkóczi, G., Chen, V.B., Davis, I.W., Echols, N., Headd, J.J., Hung, L.-W., Kapral, G.J., Grosse-Kunstleve, R.W., McCoy, A.J., Moriarty, N.W., Oeffner, R., Read, R.J., Richardson, D.C., Richardson, J.S., Terwilliger, T.C., and Zwart, P.H. (2010). PHENIX: a comprehensive Python-based system for macromolecular structure solution. Acta Crystallogr. D Biol. Crystallogr. *66*, 213–221.

Akdis, M., Burgler, S., Crameri, R., Eiwegger, T., Fujita, H., Gomez, E., Klunker, S., Meyer, N., O'Mahony, L., Palomares, O., Rhyner, C., Quaked, N., Schaffartzik, A., Van De Veen, W., Zeller, S., Zimmermann, M., and Akdis, C.A. (2011). Interleukins, from 1 to 37, and interferon-γ: Receptors, functions, and roles in diseases. J. Allergy Clin. Immunol. *127*, 701-721.e70.

Alexander, C.G., Wanner, R., Johnson, C.M., Breitsprecher, D., Winter, G., Duhr, S., Baaske, P., and Ferguson, N. (2014). Novel microscale approaches for easy, rapid determination of protein stability in academic and commercial settings. Biochim. Biophys. Acta BBA - Proteins Proteomics *1844*, 2241–2250.

Alhede, M., Bjarnsholt, T., Givskov, M., and Alhede, M. (2014). Chapter One - *Pseudomonas aeruginosa* Biofilms: Mechanisms of Immune Evasion. In Advances in Applied Microbiology, S. Sariaslani, and G.M. Gadd, eds. (Academic Press), pp. 1–40.

Altschul, S.F., Madden, T.L., Schäffer, A.A., Zhang, J., Zhang, Z., Miller, W., and Lipman, D.J. (1997). Gapped BLAST and PSI-BLAST: a new generation of protein database search programs. Nucleic Acids Res. *25*, 3389–3402.

Anyan, M.E., Amiri, A., Harvey, C.W., Tierra, G., Morales-Soto, N., Driscoll, C.M., Alber, M.S., and Shrout, J.D. (2014). Type IV pili interactions promote intercellular association and moderate swarming of *Pseudomonas aeruginosa*. Proc. Natl. Acad. Sci. U. S. A. *111*, 18013–18018.

Armstrong, R.N. (2000). Mechanistic Diversity in a Metalloenzyme Superfamily. Biochemistry (Mosc.) *39*, 13625–13632.

Barrueco, C., and de la Peña, E. (1988). Mutagenic evaluation of the pesticides captan, folpet, captafol, dichlofluanid and related compounds with the mutants TA102 and TA104 of *Salmonella typhimurium*. Mutagenesis *3*, 467–480.

Bartlett, G.J., Porter, C.T., Borkakoti, N., and Thornton, J.M. (2002). Analysis of Catalytic Residues in Enzyme Active Sites. J. Mol. Biol. *324*, 105–121.

Bendush, C.L., and Weber, R. (1976). Tobramycin Sulfate: A Summary of Worldwide Experience from Clinical Trials. J. Infect. Dis. *134*, S219–S234.

Bergdoll, M., Eltis, L.D., Cameron, A.D., Dumas, P., and Bolin, J.T. (1998). All in the family: structural and evolutionary relationships among three modular proteins with diverse functions and variable assembly. Protein Sci. Publ. Protein Soc. *7*, 1661–1670.

Bernat, B.A., Laughlin, L.T., and Armstrong, R.N. (1997). Fosfomycin resistance protein (FosA) is a manganese metalloglutathione transferase related to glyoxalase I and the extradiol dioxygenases. Biochemistry (Mosc.) *36*, 3050–3055.

Biswas, S., Brunel, J.-M., Dubus, J.-C., Reynaud-Gaubert, M., and Rolain, J.-M. (2012). Colistin: an update on the antibiotic of the 21st century. Expert Rev. Anti Infect. Ther. *10*, 917–934.

Bleves, S., Viarre, V., Salacha, R., Michel, G.P.F., Filloux, A., and Voulhoux, R. (2010). Protein secretion systems in *Pseudomonas aeruginosa*: A wealth of pathogenic weapons. Int. J. Med. Microbiol. IJMM *300*, 534–543.

Blundell, M.R., and Wild, D.G. (1969). Inhibition of bacterial growth by metal salts. A survey of effects on the synthesis of ribonucleic acid and protein. Biochem. J. *115*, 207–212.

Bochner, B. (1989). Breathprints at the microbial level. ASM News. *55*, 536-539.

Bochner, B.R. (2009). Global phenotypic characterization of bacteria. Fems Microbiol. Rev. *33*, 191–205.

Bond, C.S. (2003). TopDraw: a sketchpad for protein structure topology cartoons. Bioinforma. Oxf. Engl. *19*, 311–312.

Borges, A., Ferreira, C., Saavedra, M.J., and Simões, M. (2013). Antibacterial Activity and Mode of Action of Ferulic and Gallic Acids Against Pathogenic Bacteria. Microb. Drug Resist. *19*, 256–265.

Brogden, K.A. (2005). Antimicrobial peptides: pore formers or metabolic inhibitors in bacteria? Nat. Rev. Microbiol. *3*, 238–250.

Brogden, R.N., Pinder, R.M., Sawyer, P.R., Speight, T.M., and Avery, G.S. (1976). Tobramycin: a review of its antibacterial and pharmacokinetic properties and therapeutic use. Drugs *12*, 166–200.

Buchan, D.W.A., Minneci, F., Nugent, T.C.O., Bryson, K., and Jones, D.T. (2013). Scalable web services for the PSIPRED Protein Analysis Workbench. Nucleic Acids Res. *41*, W349–W357.

Buchko, G.W., Kim, H., Myler, P.J., Terwilliger, T.C., and Kim, C.-Y. (2012). Chemical shift assignments for Rv0577, a putative glyoxylase associated with virulence from *Mycobacterium tuberculosis*. Biomol. NMR Assign. *6*, 43–46.

Buchko, G.W., Echols, N., Flynn, E.M., Ng, H.-L., Stephenson, S., Kim, H.-B., Myler, P.J., Terwilliger, T.C., Alber, T., and Kim, C.-Y. (2017). Structural and Biophysical Characterization of the *Mycobacterium tuberculosis* Protein Rv0577, a Protein Associated with Neutral Red Staining of Virulent Tuberculosis Strains and Homologue of the *Streptomyces coelicolor* Protein KbpA. Biochemistry (Mosc.) *56*, 4015–4027.

Buurma, N.J., and Haq, I. (2007). Advances in the analysis of isothermal titration calorimetry data for ligand–DNA interactions. Methods *42*, 162–172.

Byun, E.-H., Kim, W.S., Kim, J.-S., Jung, I.D., Park, Y.-M., Kim, H.-J., Cho, S.-N., and Shin, S.J. (2012). *Mycobacterium tuberculosis* Rv0577, a novel TLR2 agonist, induces maturation of dendritic cells and drives Th1 immune response. FASEB J. Off. Publ. Fed. Am. Soc. Exp. Biol. *26*, 2695–2711.

Caiazza, N.C., Merritt, J.H., Brothers, K.M., and O'Toole, G.A. (2007). Inverse Regulation of Biofilm Formation and Swarming Motility by *Pseudomonas aeruginosa* PA14. J. Bacteriol. *189*, 3603–3612.

Cameron, A.D., Olin, B., Ridderström, M., Mannervik, B., and Jones, T.A. (1997). Crystal structure of human glyoxalase I-evidence for gene duplication and 3D domain swapping. EMBO J. *16*, 3386–3395.

Cattoni, D.I., Chara, O., Kaufman, S.B., and Flecha, F.L.G. (2015). Cooperativity in Binding Processes: New Insights from Phenomenological Modeling. PLOS ONE *10*, e0146043.

Chan, W.T., Espinosa, M., and Yeo, C.C. (2016). Keeping the Wolves at Bay: Antitoxins of Prokaryotic Type II Toxin-Antitoxin Systems. Front. Mol. Biosci. *3*, 9.

Charuk, J.H.M., Pirraglia, C.A., and Reithmeier, R.A.F. (1990). Interaction of ruthenium red with Ca^{2+}-binding proteins. Anal. Biochem. *188*, 123–131.

Chayen, N.E. (2004). Turning protein crystallization from an art into a science. Curr. Opin. Struct. Biol. *14*, 577–583.

Chayen, N.E., and Saridakis, E. (2008). Protein crystallization: from purified protein to diffraction-quality crystal. Nat. Methods *5*, 147–153.

Chen, V.B., Arendall, W.B., Headd, J.J., Keedy, D.A., Immormino, R.M., Kapral, G.J., Murray, L.W., Richardson, J.S., and Richardson, D.C. (2010). MolProbity: all-atom structure validation for macromolecular crystallography. Acta Crystallogr. D Biol. Crystallogr. *66*, 12–21.

Chovancova, E., Pavelka, A., Benes, P., Strnad, O., Brezovsky, J., Kozlikova, B., Gora, A., Sustr, V., Klvana, M., Medek, P., Biedermannova, L., Sochor, J., and Damborsky, J. (2012). CAVER 3.0: a tool for the analysis of transport pathways in dynamic protein structures. PLoS Comput. Biol. *8*, e1002708.

D'Ambrosio, K., Pailot, A., Talfournier, F., Didierjean, C., Benedetti, E., Aubry, A., Branlant, G., and Corbier, C. (2006). The First Crystal Structure of a Thioacylenzyme Intermediate in the ALDH Family: New Coenzyme Conformation and Relevance to Catalysis. Biochemistry (Mosc.) *45*, 2978–2986.

DeLano, W. (2002). The PyMOL Molecular Graphics System (2002) DeLano Scientific, Palo Alto, CA, USA. http://www.pymol.org.

Deller, M.C., and Rupp, B. (2015). Models of protein–ligand crystal structures: trust, but verify. J. Comput. Aided Mol. Des. *29*, 817–836.

Demicheli, C., Frézard, F., Mangrum, J.B., and Farrell, N.P. (2008). Interaction of trivalent antimony with a CCHC zinc finger domain: potential relevance to the mechanism of action of antimonial drugs. Chem. Commun. *0*, 4828–4830.

Deter, H.S., Jensen, R.V., Mather, W.H., and Butzin, N.C. (2017). Mechanisms for Differential Protein Production in Toxin–Antitoxin Systems. Toxins *9*.

Déziel, E., Lépine, F., Milot, S., and Villemur, R. (2003). rhlA is required for the production of a novel biosurfactant promoting swarming motility in *Pseudomonas aeruginosa*: 3-(3-hydroxyalkanoyloxy)alkanoic acids (HAAs), the precursors of rhamnolipids. Microbiology *149*, 2005–2013.

Dolinsky, T.J., Nielsen, J.E., McCammon, J.A., and Baker, N.A. (2004). PDB2PQR: an automated pipeline for the setup of Poisson-Boltzmann electrostatics calculations. Nucleic Acids Res. *32*, W665-667.

Drlica, K. (1999). Mechanism of fluoroquinolone action. Curr. Opin. Microbiol. *2*, 504–508.

Dunwell, J.M. (1998). Cupins: A New Superfamily of Functionally Diverse Proteins that Include Germins and Plant Storage Proteins. Biotechnol. Genet. Eng. Rev. *15*, 1–32.

Dunwell, J.M., Purvis, A., and Khuri, S. (2004). Cupins: the most functionally diverse protein superfamily? Phytochemistry *65*, 7–17.

Emsley, P., Lohkamp, B., Scott, W.G., and Cowtan, K. (2010). Features and development of Coot. Acta Crystallogr. D Biol. Crystallogr. *66*, 486–501.

Evans, P.R., and Murshudov, G.N. (2013). How good are my data and what is the resolution? Acta Crystallogr. D Biol. Crystallogr. *69*, 1204–1214.

Evans, M.E., Feola, D.J., and Rapp, R.P. (1999). Polymyxin B sulfate and colistin: old antibiotics for emerging multiresistant gram-negative bacteria. Ann. Pharmacother. *33*, 960–967.

Fahrney, D.E., and Gold, A.M. (1963). Sulfonyl Fluorides as Inhibitors of Esterases. I. Rates of Reaction with Acetylcholinesterase, α-Chymotrypsin, and Trypsin. J. Am. Chem. Soc. *85*, 997–1000.

Favero, M.S., Carson, L.A., Bond, W.W., and Petersen, N.J. (1971). *Pseudomonas aeruginosa*: growth in distilled water from hospitals. Science *173*, 836–838.

Feldman, M., Bryan, R., Rajan, S., Scheffler, L., Brunnert, S., Tang, H., and Prince, A. (1998). Role of flagella in pathogenesis of *Pseudomonas aeruginosa* pulmonary infection. Infect. Immun. *66*, 43–51.

Fenwick, M.K., Philmus, B., Begley, T.P., and Ealick, S.E. (2011). Toxoflavin Lyase Requires a Novel 1-His-2-Carboxylate Facial Triad,. Biochemistry (Mosc.) *50*, 1091–1100.

Fielding, A.J., Kovaleva, E.G., Farquhar, E.R., Lipscomb, J.D., and Que, L. (2011). A hyperactive cobalt-substituted extradiol-cleaving catechol dioxygenase. J. Biol. Inorg. Chem. JBIC Publ. Soc. Biol. Inorg. Chem. *16*, 341–355.

Filloux, A., and Ramos, J.-L. (2014). Pseudomonas Methods and Protocols (New York, NY: Springer New York).

Frézard, F., Silva, H., Pimenta, A.M. de C., Farrell, N., and Demicheli, C. (2012). Greater binding affinity of trivalent antimony to a CCCH zinc finger domain compared to a CCHC domain of kinetoplastid proteins. Metallomics *4*, 433–440.

Galardini, M., Mengoni, A., Biondi, E.G., Semeraro, R., Florio, A., Bazzicalupo, M., Benedetti, A., and Mocali, S. (2014). DuctApe: a suite for the analysis and correlation of genomic and OmniLog™ Phenotype Microarray data. Genomics *103*, 1–10.

Gasteiger, E., Hoogland, C., Gattiker, A., Duvaud, S., Wilkins, M., Appel, R., and Bairoch, A. (2005). Protein Identification and Analysis Tools on the ExPASy Server. In The Proteomics Protocols Handbook, J. Walker, ed. (Humana Press), pp. 571–607.

Gatasheh, M.K., Kannan, S., Hemalatha, K., and Imrana, N. (2017). Proflavine an acridine DNA intercalating agent and strong antimicrobial possessing potential properties of carcinogen. Karbala Int. J. Mod. Sci. *3*, 272–278.

Gellatly, S.L., and Hancock, R.E.W. (2013). *Pseudomonas aeruginosa*: new insights into pathogenesis and host defenses. Pathog. Dis. *67*, 159–173.

Goenrich, M., Bartoschek, S., Hagemeier, C.H., Griesinger, C., and Vorholt, J.A. (2002). A Glutathione-dependent Formaldehyde-activating Enzyme (Gfa) from *Paracoccus denitrificans* Detected and Purified via Two-dimensional Proton Exchange NMR Spectroscopy ,. J. Biol. Chem. *277*, 3069–3072.

Grishin, N.V. (1998). The R3H motif: a domain that binds single-stranded nucleic acids. Trends Biochem. Sci. *23*, 329–330.

Habig, W.H., Pabst, M.J., and Jakoby, W.B. (1974). Glutathione S-Transferases THE FIRST ENZYMATIC STEP IN MERCAPTURIC ACID FORMATION. J. Biol. Chem. *249*, 7130–7139.

Haiko, J., and Westerlund-Wikström, B. (2013). The Role of the Bacterial Flagellum in Adhesion and Virulence. Biology *2*, 1242–1267.

Hall, A.M., Gollan, B., and Helaine, S. (2017). Toxin–antitoxin systems: reversible toxicity. Curr. Opin. Microbiol. *36*, 102–110.

Hall, J.B., Hino, G.N., Inouye, L., Nada, A., Lau, C.K.H., and Read, G.W. (1983). Antimicrobial action of compound 48/80—II. Mechanism of action. Biochem. Pharmacol. *32*, 449–453.

Hall, S., McDermott, C., Anoopkumar-Dukie, S., McFarland, A.J., Forbes, A., Perkins, A.V., Davey, A.K., Chess-Williams, R., Kiefel, M.J., Arora, D., and Grant, G.D. (2016). Cellular Effects of Pyocyanin, a Secreted Virulence Factor of *Pseudomonas aeruginosa*. Toxins *8*, 236-250.

Han, S., Eltis, L.D., Timmis, K.N., Muchmore, S.W., and Bolin, J.T. (1995). Crystal Structure of the Biphenyl-Cleaving Extradiol Dioxygenase from a PCB-Degrading *Pseudomonad*. Science *270*, 976–980.

He, P., and Moran, G.R. (2009). We two alone will sing: the two-substrate α-keto acid-dependent oxygenases. Curr. Opin. Chem. Biol. *13*, 443–450.

He, P., and Moran, G.R. (2011). Structural and mechanistic comparisons of the metal-binding members of the vicinal oxygen chelate (VOC) superfamily. J. Inorg. Biochem. *105*, 1259–1272.

Held, K., Ramage, E., Jacobs, M., Gallagher, L., and Manoil, C. (2012). Sequence-Verified Two-Allele Transposon Mutant Library for *Pseudomonas aeruginosa* PAO1. J. Bacteriol. *194*, 6387–6389.

Hendricks, O., Butterworth, T.S., and Kristiansen, J.E. (2003). The in-vitro antimicrobial effect of non-antibiotics and putative inhibitors of efflux pumps on *Pseudomonas aeruginosa* and *Staphylococcus aureus*. Int. J. Antimicrob. Agents *22*, 262–264.

Holliday, G.L., Mitchell, J.B.O., and Thornton, J.M. (2009). Understanding the Functional Roles of Amino Acid Residues in Enzyme Catalysis. J. Mol. Biol. *390*, 560–577.

Holm, L., and Laakso, L.M. (2016). Dali server update. Nucleic Acids Res. *44*, W351-355.

Holm, L., and Rosenström, P. (2010). Dali server: conservation mapping in 3D. Nucleic Acids Res. *38*, W545–W549.

Honda, Z., Suzuki, T., and Honda, H. (2009). Identification of CENP-V as a novel microtubule-associating molecule that activates Src family kinases through SH3 domain interaction. Genes Cells *14*, 1383–1394.

Hopkinson, R.J., Leung, I.K.H., Smart, T.J., Rose, N.R., Henry, L., Claridge, T.D.W., and Schofield, C.J. (2015). Studies on the Glutathione-Dependent Formaldehyde-Activating Enzyme from *Paracoccus denitrificans*. PLOS ONE *10*, e0145085.

Huard, R.C., Chitale, S., Leung, M., Lazzarini, L.C.O., Zhu, H., Shashkina, E., Laal, S., Conde, M.B., Kritski, A.L., Belisle, J.T., Kreiswirth, B.N., Lapa e Silva, J.R., and Ho, J.L. (2003). The *Mycobacterium tuberculosis* complex-restricted gene cfp32 encodes an expressed protein that is detectable in tuberculosis patients and is positively correlated with pulmonary interleukin-10. Infect. Immun. *71*, 6871–6883.

Hugo, W.B., and Bloomfield, S.F. (1971). Studies on the mode of action of the phenolic antibacterial agent fentichlor against *Staphylococcus aureus* and *Escherichia coli*. II. The effects of fentichlor on the bacterial membrane and the cytoplasmic constituents of the cell. J. Appl. Bacteriol. *34*, 569–578.

Hunter, S., Apweiler, R., Attwood, T.K., Bairoch, A., Bateman, A., Binns, D., Bork, P., Das, U., Daugherty, L., Duquenne, L., *et al.* (2009). InterPro: the integrative protein signature database. Nucleic Acids Res. *37*, D211–D215.

Huschmann, F.U., Linnik, J., Sparta, K., Ühlein, M., Wang, X., Metz, A., Schiebel, J., Heine, A., Klebe, G., Weiss, M.S., and Mueller U. (2016). Structures of endothiapepsin-fragment complexes from crystallographic fragment screening using a novel, diverse and affordable 96-compound fragment library. Acta Crystallogr. Sect. F Struct. Biol. Commun. *72*, 346–355.

Huynh, K., and Partch, C.L. (2015). Current Protocols in Protein Science. Curr. Protoc. Protein Sci. Editor. Board John E Coligan Al *79*, 28.9.1-28.9.14.

Hyldgaard, M., Mygind, T., Vad, B.S., Stenvang, M., Otzen, D.E., and Meyer, R.L. (2014). The antimicrobial mechanism of action of epsilon-poly-l-lysine. Appl. Environ. Microbiol. *80*, 7758–7770.

Jarrell, K.F., and McBride, M.J. (2008). The surprisingly diverse ways that prokaryotes move. Nat. Rev. Microbiol. *6*, 466–476.

Jaudzems, K., Jia, X., Yagi, H., Zhulenkovs, D., Graham, B., Otting, G., and Liepinsh, E. (2012). Structural Basis for 5'-End-Specific Recognition of Single-Stranded DNA by the R3H Domain from Human Sμbp-2. J. Mol. Biol. *424*, 42–53.

Javor, G.T. (1983). Depression of adenosylmethionine content of *Escherichia coli* by thioglycerol. Antimicrob. Agents Chemother. *24*, 860–867.

Jelesarov, I., and Bosshard, H.R. (1999). Isothermal titration calorimetry and differential scanning calorimetry as complementary tools to investigate the energetics of biomolecular recognition. J. Mol. Recognit. *12*, 3–18.

Jeong, Y., Kim, J., Kim, S., Kang, Y., Nagamatsu, T., and Hwang, I. (2003). Toxoflavin Produced by *Burkholderia glumae* Causing Rice Grain Rot Is Responsible for Inducing Bacterial Wilt in Many Field Crops. Plant Dis. *87*, 890–895.

Jerabek-Willemsen, M., Wienken, C.J., Braun, D., Baaske, P., and Duhr, S. (2011). Molecular Interaction Studies Using Microscale Thermophoresis. ASSAY Drug Dev. Technol. *9*, 342–353.

Jerabek-Willemsen, M., André, T., Wanner, R., Roth, H.M., Duhr, S., Baaske, P., and Breitsprecher, D. (2014). MicroScale Thermophoresis: Interaction analysis and beyond. J. Mol. Struct. *1077*, 101–113.

Josenhans, C., and Suerbaum, S. (2002). The role of motility as a virulence factor in bacteria. Int. J. Med. Microbiol. *291*, 605–614.

Kabsch, W. (2010). XDS. Acta Crystallogr. D Biol. Crystallogr. *66*, 125–132.

Kalawy-Fansa, E. (2010). Untersuchungen an Glyoxalase I/Bleomycin Resistenz-Proteinen aus *Pseudomonas aeruginosa* PAO1. Master Thesis. MPI Dortmund.

Karplus, P.A., and Diederichs, K. (2012). Linking crystallographic model and data quality. Science *336*, 1030–1033.

Kearns, D.B. (2010). A field guide to bacterial swarming motility. Nat. Rev. Microbiol. *8*, 634–644.

Kelley, L.A., Mezulis, S., Yates, C.M., Wass, M.N., and Sternberg, M.J.E. (2015). The Phyre2 web portal for protein modeling, prediction and analysis. Nat. Protoc. *10*, 845–858.

Kibbe, W.A. (2007). OligoCalc: an online oligonucleotide properties calculator. Nucleic Acids Res. *35*, W43-46.

Kida, Y., Taira, J., Yamamoto, T., Higashimoto, Y., and Kuwano, K. EprS, an autotransporter protein of Pseudomonas aeruginosa, possessing serine protease activity induces inflammatory responses through protease-activated receptors. Cell. Microbiol. *15*, 1168–1181.

Kim, G., Weiss, S.J., and Levine, R.L. (2014). Methionine oxidation and reduction in proteins. Biochim. Biophys. Acta *1840*, 901–905.

Kim, S., Thiessen, P.A., Bolton, E.E., Chen, J., Fu, G., Gindulyte, A., Han, L., He, J., He, S., Shoemaker, B.A., Wang, J., Yu, B., Zhang, J., and Bryant, S.H. (2016). PubChem Substance and Compound databases. Nucleic Acids Res. *44*, D1202–D1213.

King, G.F., Crossley, M.J., and Kuchel, P.W. (1989). Inhibition and active-site modelling of prolidase. Eur. J. Biochem. *180*, 377–384.

Kishore, G.M., and Jacob, G.S. (1987). Degradation of glyphosate by *Pseudomonas sp.* PG2982 via a sarcosine intermediate. J. Biol. Chem. *262*, 12164–12168.

Klockgether, J., and Tümmler, B. (2017). Recent advances in understanding *Pseudomonas aeruginosa* as a pathogen. F1000Research *6*.

Köhler, T., Curty, L.K., Barja, F., van Delden, C., and Pechère, J.-C. (2000). Swarming of *Pseudomonas aeruginosa* Is Dependent on Cell-to-Cell Signaling and Requires Flagella and Pili. J. Bacteriol. *182*, 5990–5996.

Kong, K.-F., Schneper, L., and Mathee, K. (2010). Beta-lactam Antibiotics: From Antibiosis to Resistance and Bacteriology. APMIS Acta Pathol. Microbiol. Immunol. Scand. *118*, 1–36.

Koppelman, C.-M., Aarsman, M.E.G., Postmus, J., Pas, E., Muijsers, A.O., Scheffers, D.-J., Nanninga, N., and Blaauwen, T.D. (2004). R174 of *Escherichia coli* FtsZ is involved in membrane interaction and protofilament bundling, and is essential for cell division. Mol. Microbiol. *51*, 645–657.

Krissinel, E., and Henrick, K. (2004). Secondary-structure matching (SSM), a new tool for fast protein structure alignment in three dimensions. Acta Crystallogr. D Biol. Crystallogr. *60*, 2256–2268.

Krissinel, E., and Henrick, K. (2007). Inference of macromolecular assemblies from crystalline state. J. Mol. Biol. *372*, 774–797.

Krug, M., Weiss, M.S., Heinemann, U., and Mueller, U. (2012). XDSAPP: a graphical user interface for the convenient processing of diffraction data using XDS. J. Appl. Crystallogr. *45*, 568–572.

Krungkrai, J., Krungkrai, S.R., and Phakanont, K. (1992). Antimalarial activity of orotate analogs that inhibit dihydroorotase and dihydroorotate dehydrogenase. Biochem. Pharmacol. *43*, 1295–1301.

Kumar, H., Kawai, T., and Akira, S. (2011). Pathogen Recognition by the Innate Immune System. Int. Rev. Immunol. *30*, 16–34.

Kyaw, B.M., Champakalakshmi, R., Sakharkar, M.K., Lim, C.S., and Sakharkar, K.R. (2012). Biodegradation of Low Density Polythene (LDPE) by *Pseudomonas Species*. Indian J. Microbiol. *52*, 411–419.

Laemmli, U.K. (1970). Cleavage of structural proteins during the assembly of the head of bacteriophage T4. Nature *227*, 680–685.

Lagunoff, D., Martin, T.W., and Read, G. (1983). Agents that Release Histamine from Mast Cells. Annu. Rev. Pharmacol. Toxicol. *23*, 331–351.

Laitaoja, M., Valjakka, J., and Jänis, J. (2013). Zinc coordination spheres in protein structures. Inorg. Chem. *52*, 10983–10991.

Lee, J.K., Lee, Y.S., Park, Y.K., and Kim, B.S. (2005). Alterations in the GyrA and GyrB subunits of topoisomerase II and the ParC and ParE subunits of topoisomerase IV in ciprofloxacin-resistant clinical isolates of *Pseudomonas aeruginosa*. Int. J. Antimicrob. Agents *25*, 290–295.

Lenney, J.F., Siddiqui, W.A., Schnell, J.V., Furusawa, E., and Read, G.W. (1977). Antimicrobial action of compound 48/80 against protozoa, bacteria, and fungi. J. Pharm. Sci. *66*, 702–705.

Levenberg, B., and Linton, S.N. (1966). On the biosynthesis of toxoflavin, an azapteridine antibiotic produced by *Pseudomonas cocovenenans*. J. Biol. Chem. *241*, 846–852.

Levine, R.L., Mosoni, L., Berlett, B.S., and Stadtman, E.R. (1996). Methionine residues as endogenous antioxidants in proteins. Proc. Natl. Acad. Sci. U. S. A. *93*, 15036–15040.

Li, M.Z., and Elledge, S.J. (2007). Harnessing homologous recombination in vitro to generate recombinant DNA via SLIC. Nat. Methods *4*, 251–256.

Li, K., Yang, G., Debru, A.B., Li, P., Zong, L., Li, P., Xu, T., Wu, W., Jin, S., and Bao, Q. (2017). SuhB Regulates the Motile-Sessile Switch in *Pseudomonas aeruginosa* through the Gac/Rsm Pathway and c-di-GMP Signaling. Front. Microbiol. *8*.

Li, W., Cowley, A., Uludag, M., Gur, T., McWilliam, H., Squizzato, S., Park, Y.M., Buso, N., and Lopez, R. (2015). The EMBL-EBI bioinformatics web and programmatic tools framework. Nucleic Acids Res. *43*, W580-4.

Li, Y., Chi, L., Stechschulte, D.J., and Dileepan, K.N. (2001). Histamine-induced production of interleukin-6 and interleukin-8 by human coronary artery endothelial cells is enhanced by endotoxin and tumor necrosis factor-alpha. Microvasc. Res. *61*, 253–262.

Liberati, N.T., Urbach, J.M., Miyata, S., Lee, D.G., Drenkard, E., Wu, G., Villanueva, J., Wei, T., and Ausubel, F.M. (2006). An ordered, nonredundant library of *Pseudomonas aeruginosa* strain PA14 transposon insertion mutants. Proc. Natl. Acad. Sci. U. S. A. *103*, 2833–2838.

Lister, P.D., Wolter, D.J., and Hanson, N.D. (2009). Antibacterial-Resistant *Pseudomonas aeruginosa*: Clinical Impact and Complex Regulation of Chromosomally Encoded Resistance Mechanisms. Clin. Microbiol. Rev. *22*, 582–610.

Long, F., Vagin, A.A., Young, P., and Murshudov, G.N. (2008). BALBES: a molecular-replacement pipeline. Acta Crystallogr. D Biol. Crystallogr. *64*, 125–132.

Lupas, A.N., Zhu, H., and Korycinski, M. (2015). The Thalidomide-Binding Domain of Cereblon Defines the CULT Domain Family and Is a New Member of the β-Tent Fold. PLoS Comput. Biol. *11*.

Lupi, A., Rossi, A., Vaghi, P., Gallanti, A., Cetta, G., and Forlino, A. (2005). N-benzyloxycarbonyl-l-proline: An in vitro and in vivo inhibitor of prolidase. Biochim. Biophys. Acta BBA - Mol. Cell Res. *1744*, 157–163.

Mao, X., Ma, Q., Zhou, C., Chen, X., Zhang, H., Yang, J., Mao, F., Lai, W., and Xu, Y. (2014). DOOR 2.0: presenting operons and their functions through dynamic and integrated views. Nucleic Acids Res. *42*, D654-659.

Margolin, W. (2003). Bacterial Division: The Fellowship of The Ring. Curr. Biol. *13*, R16–R18.

Martin, T.W., Dauter, Z., Devedjiev, Y., Sheffield, P., Jelen, F., He, M., Sherman, D.H., Otlewski, J., Derewenda, Z.S., and Derewenda, U. (2002). Molecular Basis of Mitomycin C Resistance in *Streptomyces*. Structure *10*, 933–942.

Martínez-Fleites, C., Ortíz-Lombardía, M., Pons, T., Tarbouriech, N., Taylor, E.J., Arrieta, J.G., Hernández, L., and Davies, G.J. (2005). Crystal structure of levansucrase from the Gram-negative bacterium *Gluconacetobacter diazotrophicus*. Biochem. J. *390*, 19–27.

Maruyama, M., Kumagai, T., Matoba, Y., Hayashida, M., Fujii, T., Hata, Y., and Sugiyama, M. (2001). Crystal Structures of the Transposon Tn5-carried Bleomycin Resistance Determinant Uncomplexed and Complexed with Bleomycin. J. Biol. Chem. *276*, 9992–9999.

Masip, L., Veeravalli, K., and Georgiou, G. (2006). The many faces of glutathione in bacteria. Antioxid. Redox Signal. *8*, 753–762.

Matthews, B.W. (1968). Solvent content of protein crystals. J. Mol. Biol. *33*, 491–497.

Mavrodi, D.V., Bonsall, R.F., Delaney, S.M., Soule, M.J., Phillips, G., and Thomashow, L.S. (2001). Functional Analysis of Genes for Biosynthesis of Pyocyanin and Phenazine-1-Carboxamide from *Pseudomonas aeruginosa* PAO1. J. Bacteriol. *183*, 6454–6465.

Mavrodi, D.V., Blankenfeldt, W., and Thomashow, L.S. (2006). Phenazine Compounds in Fluorescent *Pseudomonas Spp.* Biosynthesis and Regulation. Annu. Rev. Phytopathol. *44*, 417–445.

McCoy, A.J., Grosse-Kunstleve, R.W., Adams, P.D., Winn, M.D., Storoni, L.C., and Read, R.J. (2007). Phaser crystallographic software. J. Appl. Crystallogr. *40*, 658–674.

McDonnell, G., and Russell, A.D. (1999). Antiseptics and Disinfectants: Activity, Action, and Resistance. Clin. Microbiol. Rev. *12*, 147–179.

McLuskey, K., Cameron, S., Hammerschmidt, F., and Hunter, W.N. (2005). Structure and reactivity of hydroxypropylphosphonic acid epoxidase in fosfomycin biosynthesis by a cation- and flavin-dependent mechanism. Proc. Natl. Acad. Sci. U. S. A. *102*, 14221–14226.

McPherson, A., and Gavira, J.A. (2013). Introduction to protein crystallization. Acta Crystallogr. Sect. F Struct. Biol. Commun. *70*, 2–20.

Meadows, J.A., and Wargo, M.J. (2018). Transcriptional Regulation of Carnitine Catabolism in *Pseudomonas aeruginosa* by CdhR. MSphere *3*.

Megadi, V.B., Tallur, P.N., Mulla, S.I., and Ninnekar, H.Z. (2010). Bacterial degradation of fungicide captan. J. Agric. Food Chem. *58*, 12863–12868.

Meng, G., and Fütterer, K. (2003). Structural framework of fructosyl transfer in *Bacillus subtilis* levansucrase. Nat. Struct. Biol. *10*, 935–941.

Michalska, M., and Wolf, P. (2015). *Pseudomonas* Exotoxin A: optimized by evolution for effective killing. Front. Microbiol. *6*.

Moradali, M.F., Ghods, S., and Rehm, B.H.A. (2017). *Pseudomonas aeruginosa* Lifestyle: A Paradigm for Adaptation, Survival, and Persistence. Front. Cell. Infect. Microbiol. *7*.

Moriarty, N.W., Grosse-Kunstleve, R.W., and Adams, P.D. (2009). Electronic Ligand Builder and Optimization Workbench (eLBOW): a tool for ligand coordinate and restraint generation. Acta Crystallogr. D Biol. Crystallogr. *65*, 1074–1080.

Mueller, U., Darowski, N., Fuchs, M.R., Förster, R., Hellmig, M., Paithankar, K.S., Pühringer, S., Steffien, M., Zocher, G., and Weiss, M.S. (2012). Facilities for macromolecular crystallography at the Helmholtz-Zentrum Berlin. J. Synchrotron Radiat. *19*, 442–449.

Mueller, U., Förster, R., Hellmig, M., Huschmann, F.U., Kastner, A., Malecki, P., Pühringer, S., Röwer, M., Sparta, K., Steffien, M., Zocher, G., and Weiss, M.S. (2015). The macromolecular crystallography beamlines at BESSY II of the Helmholtz-Zentrum Berlin: Current status and perspectives. Eur. Phys. J. Plus *130*, 141.

Myara, I., Charpentier, C., and Lemonnier, A. (1984). Prolidase and prolidase deficiency. Life Sci. *34*, 1985–1998.

Nadzirin, N., Gardiner, E.J., Willett, P., Artymiuk, P.J., and Firdaus-Raih, M. (2012). SPRITE and ASSAM: web servers for side chain 3D-motif searching in protein structures. Nucleic Acids Res. *40*, W380–W386.

Nakao, S., Komagoe, K., Inoue, T., and Katsu, T. (2011). Comparative study of the membrane-permeabilizing activities of mastoparans and related histamine-releasing agents in bacteria, erythrocytes, and mast cells. Biochim. Biophys. Acta BBA - Biomembr. *1808*, 490–497.

Neculai, A.M., Neculai, D., Griesinger, C., Vorholt, J.A., and Becker, S. (2005). A dynamic zinc redox switch. J. Biol. Chem. *280*, 2826–2830.

Ni, L., Jensen, S.O., Ky Tonthat, N., Berg, T., Kwong, S.M., Guan, F.H.X., Brown, M.H., Skurray, R.A., Firth, N., and Schumacher, M.A. (2009). The *Staphylococcus aureus* pSK41 plasmid-encoded ArtA protein is a master regulator of plasmid transmission genes and contains a RHH motif used in alternate DNA-binding modes. Nucleic Acids Res. *37*, 6970–6983.

Nies, D.H. (1999). Microbial heavy-metal resistance. Appl. Microbiol. Biotechnol. *51*, 730–750.

Niesen, F.H., Berglund, H., and Vedadi, M. (2007). The use of differential scanning fluorimetry to detect ligand interactions that promote protein stability. Nat. Protoc. *2*, 2212–2221.

Nikaido, H. (2003). Molecular Basis of Bacterial Outer Membrane Permeability Revisited. Microbiol. Mol. Biol. Rev. *67*, 593–656.

Nimmo-Smith, R.H., and Appleyard, G. (1956). Studies with a *Pseudomonad* able to Grow with Creatine as Main Source of Carbon and Nitrogen. Microbiology *14*, 336–350.

Nocek, B., Cuff, M., Evdokimova, E., Edwards, A., Joachimiak, A., and Savchenko, A. (2006). 1.6 A crystal structure of a PA2721 protein from *Pseudomonas aeruginosa*--a potential drug-resistance protein. Proteins *63*, 1102–1105.

Oberthuer, D., Knoška, J., Wiedorn, M.O., Beyerlein, K.R., Bushnell, D.A., Kovaleva, E.G., Heymann, M., Gumprecht, L., Kirian, R.A., Barty, A., *et al.* (2017). Double-flow focused liquid injector for efficient serial femtosecond crystallography. Sci. Rep. *7*, 44628.

Oda, K., Matoba, Y., Noda, M., Kumagai, T., and Sugiyama, M. (2010). Catalytic mechanism of bleomycin N-acetyltransferase proposed on the basis of its crystal structure. J. Biol. Chem. *285*, 1446–1456.

Okuda, J., Hayashi, N., Minagawa, S., Gotoh, N., and Tanabe, S. (2011). Degradation of interleukin 8 by the serine protease MucD of *Pseudomonas aeruginosa*. J. Infect. Chemother. *17*, 782–792.

O'Toole, G.A., and Kolter, R. (1998). Flagellar and twitching motility are necessary for *Pseudomonas aeruginosa* biofilm development. Mol. Microbiol. *30*, 295–304.

Page, R., and Peti, W. (2016). Toxin-antitoxin systems in bacterial growth arrest and persistence. Nat. Chem. Biol. *12*, 208–214.

Pei, J., Kim, B.-H., and Grishin, N.V. (2008). PROMALS3D: a tool for multiple protein sequence and structure alignments. Nucleic Acids Res. *36*, 2295–2300.

Pendleton, J.N., Gorman, S.P., and Gilmore, B.F. (2013). Clinical relevance of the ESKAPE pathogens. Expert Rev. Anti Infect. Ther. *11*, 297–308.

Pettersen, E.F., Goddard, T.D., Huang, C.C., Couch, G.S., Greenblatt, D.M., Meng, E.C., and Ferrin, T.E. (2004). UCSF Chimera--a visualization system for exploratory research and analysis. J. Comput. Chem. *25*, 1605–1612.

Philmus, B., Abdelwahed, S., Williams, H.J., Fenwick, M.K., Ealick, S.E., and Begley, T.P. (2012). Identification of the Product of Toxoflavin Lyase: Degradation via a Baeyer–Villiger Oxidation. J. Am. Chem. Soc. *134*, 5326–5330.

Pierson, L.S., and Pierson, E.A. (2010). Metabolism and function of phenazines in bacteria: impacts on the behavior of bacteria in the environment and biotechnological processes. Appl. Microbiol. Biotechnol. *86*, 1659–1670.

Popp, M. (2013). Charakterisierung von PA3127 und PA3128 aus *Pseudomonas aeruginosa* PAO1. Master Thesis. Universität Bayreuth.

Prachayasittikul, V., Prachayasittikul, S., Ruchirawat, S., and Prachayasittikul, V. (2013). 8-Hydroxyquinolines: a review of their metal chelating properties and medicinal applications. Drug Des. Devel. Ther. *7*, 1157–1178.

Puel, O., Galtier, P., and Oswald, I.P. (2010). Biosynthesis and Toxicological Effects of Patulin. Toxins *2*, 613–631.

Qiu, D., Damron, F.H., Mima, T., Schweizer, H.P., and Yu, H.D. (2008). PBAD-based shuttle vectors for functional analysis of toxic and highly regulated genes in *Pseudomonas* and *Burkholderia spp.* and other bacteria. Appl. Environ. Microbiol. *74*, 7422–7426.

Rahden-Staroń, I., Szumiło, M., and Ziemkiewicz, P. (1994). The effects of captan and captafol on different bacterial strains and on c-mitosis in V79 Chinese hamster fibroblasts. Acta Biochim. Pol. *41*, 45–55.

Ramu, A., and Ramu, N. (1992). Reversal of multidrug resistance by phenothiazines and structurally related compounds. Cancer Chemother. Pharmacol. *30*, 165–173.

Rasamiravaka, T., Labtani, Q., Duez, P., and El Jaziri, M. (2015). The Formation of Biofilms by Pseudomonas aeruginosa: A Review of the Natural and Synthetic Compounds Interfering with Control Mechanisms.

Reddy, V.Y., Desorchers, P.E., Pizzo, S.V., Gonias, S.L., Sahakian, J.A., Levine, R.L., and Weiss, S.J. (1994). Oxidative dissociation of human alpha 2-macroglobulin tetramers into dysfunctional dimers. J. Biol. Chem. *269*, 4683–4691.

Rhodes, G. (2006). Crystallography Made Crystal Clear, Third Edition: A Guide for Users of Macromolecular Models (Amsterdam: Academic Press).

Richardson, J.S. (1981). The Anatomy and Taxonomy of Protein Structure. Adv. Protein Chem. *34*, 167–339.

Rife, C.L., Pharris, R.E., Newcomer, M.E., and Armstrong, R.N. (2002). Crystal structure of a genomically encoded fosfomycin resistance protein (FosA) at 1.19 A resolution by MAD phasing off the L-III edge of Tl(+). J. Am. Chem. Soc. *124*, 11001–11003.

Robert, X., and Gouet, P. (2014). Deciphering key features in protein structures with the new ENDscript server. Nucleic Acids Res. *42*, W320–W324.

Rodríguez, D.D., Grosse, C., Himmel, S., González, C., de Ilarduya, I.M., Becker, S., Sheldrick, G.M., and Usón, I. (2009). Crystallographic ab initio protein structure solution below atomic resolution. Nat. Methods *6*, 651–653.

Rosenkrands, I., Weldingh, K., Jacobsen, S., Hansen, C.V., Florio, W., Gianetri, I., and Andersen, P. (2000). Mapping and identification of *Mycobacterium tuberculosis* proteins by two-dimensional gel electrophoresis, microsequencing and immunodetection. Electrophoresis *21*, 935–948.

Royce, L.A., Liu, P., Stebbins, M.J., Hanson, B.C., and Jarboe, L.R. (2013). The damaging effects of short chain fatty acids on *Escherichia coli* membranes. Appl. Microbiol. Biotechnol. *97*, 8317–8327.

Rupp, B. (2009). Biomolecular Crystallography: Principles, Practice, and Application to Structural Biology (New York, NY: Garland Science).

Rybtke, M.T., Jensen, P.Ø., Høiby, N., Givskov, M., Tolker-Nielsen, T., and Bjarnsholt, T. (2011). The implication of *Pseudomonas aeruginosa* biofilms in infections. Inflamm. Allergy Drug Targets *10*, 141–157.

Santra, M.K., Beuria, T.K., Banerjee, A., and Panda, D. (2004). Ruthenium red-induced bundling of bacterial cell division protein, FtsZ. J. Biol. Chem. *279*, 25959–25965.

Sasikaran, J., Ziemski, M., Zadora, P.K., Fleig, A., and Berg, I.A. (2014). Bacterial itaconate degradation promotes pathogenicity. Nat. Chem. Biol. *10*, 371–377.

Schmidt, R.M., and Rosenkranz, H.S. (1970). Antimicrobial activity of local anesthetics: lidocaine and procaine. J. Infect. Dis. *121*, 597–607.

Schuphan, I., Westphal, D., Haque, A., and Ebing, W. (1981). Biological and Chemical Behavior of Perhalogenmethylmercapto Fungicides: Metabolism and in Vitro Reactions of Dichlofluanid in Comparison with Captan. In Sulfur in Pesticide Action and Metabolism, (AMERICAN CHEMICAL SOCIETY), pp. 85–96.

Seidel, S.A.I., Wienken, C.J., Geissler, S., Jerabek-Willemsen, M., Duhr, S., Reiter, A., Trauner, D., Braun, D., and Baaske, P. (2012). Label-Free Microscale Thermophoresis Discriminates Sites and Affinity of Protein–Ligand Binding. Angew. Chem. Int. Ed. *51*, 10656–10659.

Sevin, E.W., and Barloy-Hubler, F. (2007). RASTA-Bacteria: a web-based tool for identifying toxin-antitoxin loci in prokaryotes. Genome Biol. *8*, R155.

Sievers, F., Wilm, A., Dineen, D., Gibson, T.J., Karplus, K., Li, W., Lopez, R., McWilliam, H., Remmert, M., Söding, J., Thompson, J.D., and Higgins, D.G. (2011). Fast, scalable generation of high-quality protein multiple sequence alignments using Clustal Omega. Mol. Syst. Biol. *7*, 539–539.

Silby, M.W., Winstanley, C., Godfrey, S.A.C., Levy, S.B., and Jackson, R.W. (2011). *Pseudomonas genomes*: diverse and adaptable. FEMS Microbiol. Rev. *35*, 652–680.

Silva, M.S., Gomes, R.A., Ferreira, A.E.N., Freire, A.P., and Cordeiro, C. (2013). The glyoxalase pathway: the first hundred years… and beyond. Biochem. J. *453*, 1–15.

Silver, L.L. (2017). Fosfomycin: Mechanism and Resistance. Cold Spring Harb. Perspect. Med. *7*, a025262.

Simons, F.E.R., and Simons, K.J. (2011). Histamine and H1-antihistamines: celebrating a century of progress. J. Allergy Clin. Immunol. *128*, 1139-1150.

Soberón-Chávez, G., Lépine, F., and Déziel, E. (2005). Production of rhamnolipids by *Pseudomonas aeruginosa*. Appl. Microbiol. Biotechnol. *68*, 718–725.

Sparta, K.M., Krug, M., Heinemann, U., Mueller, U., and Weiss, M.S. (2016). XDSAPP2.0. J. Appl. Crystallogr. *49*, 1085–1092.

Stokstad, E.L.R., and Jukes, T.H. (1987). Sulfonamides and Folic Acid Antagonists: A Historical Review. J. Nutr. *117*, 1335–1341.

Sukdeo, N., Clugston, S.L., Daub, E., and Honek, J.F. (2004). Distinct classes of glyoxalase I: metal specificity of the Yersinia pestis, *Pseudomonas aeruginosa* and *Neisseria meningitidis* enzymes1. Biochem. J. *384*, 111–117.

Tadeu, A.M.B., Ribeiro, S., Johnston, J., Goldberg, I., Gerloff, D., and Earnshaw, W.C. (2008). CENP-V is required for centromere organization, chromosome alignment and cytokinesis. EMBO J. *27*, 2510–2522.

Talreja, J., Kabir, M.H., B Filla, M., Stechschulte, D.J., and Dileepan, K.N. (2004). Histamine induces Toll-like receptor 2 and 4 expression in endothelial cells and enhances sensitivity to Gram-positive and Gram-negative bacterial cell wall components. Immunology *113*, 224–233.

Taylor, G.L. (2010). Introduction to phasing. Acta Crystallogr. D Biol. Crystallogr. *66*, 325–338.

Terwilliger, T.C., Bunkóczi, G., Hung, L.-W., Zwart, P.H., Smith, J.L., Akey, D.L., and Adams, P.D. (2016). Can I solve my structure by SAD phasing? Anomalous signal in SAD phasing. Acta Crystallogr. Sect. Struct. Biol. *72*, 346–358.

Thorn, A., and Sheldrick, G.M. (2013). Extending molecular-replacement solutions with SHELXE. Acta Crystallogr. D Biol. Crystallogr. *69*, 2251–2256.

Tosa, T., and Pizer, L.I. (1971a). Biochemical Bases for the Antimetabolite Action of l-Serine Hydroxamate. J. Bacteriol. *106*, 972–982.

Tosa, T., and Pizer, L.I. (1971b). Effect of Serine Hydroxamate on the Growth of *Escherichia coli*. J. Bacteriol. *106*, 966–971.

Turra, G.L., Agostini, R.B., Fauguel, C.M., Presello, D.A., Andreo, C.S., González, J.M., and Campos-Bermudez, V.A. (2015). Structure of the novel monomeric glyoxalase I from *Zea mays.* Acta Crystallogr. D Biol. Crystallogr. *71*, 2009–2020.

Umeyama, T., and Horinouchi, S. (2001). Autophosphorylation of a Bacterial Serine/Threonine Kinase, AfsK, Is Inhibited by KbpA, an AfsK-Binding Protein. J. Bacteriol. *183*, 5506–5512.

Unterholzner, S.J., Poppenberger, B., and Rozhon, W. (2013). Toxin–antitoxin systems. Mob. Genet. Elem. *3*.

Vaara, M. (1992). Agents that increase the permeability of the outer membrane. Microbiol. Rev. *56*, 395–411.

Vallee, B.L., and Auld, D.S. (1993). Zinc: biological functions and coordination motifs. Acc. Chem. Res. *26*, 543–551.

Valot, B., Guyeux, C., Rolland, J.Y., Mazouzi, K., Bertrand, X., and Hocquet, D. (2015). What It Takes to Be a *Pseudomonas aeruginosa*? The Core Genome of the Opportunistic Pathogen Updated. PLoS ONE *10*.

van Ditmarsch, D., Boyle, K.E., Sakhtah, H., Oyler, J.E., Nadell, C.D., Déziel, É., Dietrich, L.E.P., and Xavier, J.B. (2013). Convergent Evolution of Hyperswarming Leads to Impaired Biofilm Formation in Pathogenic Bacteria. Cell Rep. *4*, 697–708.

Vit, K.A. (2015). Structural and Functional Studies on βαβββ-Module Resistance Proteins from Pseudomonas aeruginosa PAO1 and Structural Insights into Mycobacterial Ergothioneine Biosynthesis. Dissertation. Technische Universität Carolo-Wilhelmina zu Braunschweig.

Vuilleumier, S. (1997). Bacterial glutathione S-transferases: what are they good for? J. Bacteriol. *179*, 1431–1441.

Wagner, M.A., and Jorns, M.S. (1997). Folate Utilization by Monomeric versus Heterotetrameric Sarcosine Oxidases. Arch. Biochem. Biophys. *342*, 176–181.

Wainwright, M. (2001). Acridine—a neglected antibacterial chromophore. J. Antimicrob. Chemother. *47*, 1–13.

Wargo, M.J., and Hogan, D.A. (2009). Identification of genes required for *Pseudomonas aeruginosa* carnitine catabolism. Microbiology *155*, 2411–2419.

Wargo, M.J., Szwergold, B.S., and Hogan, D.A. (2008). Identification of Two Gene Clusters and a Transcriptional Regulator Required for *Pseudomonas aeruginosa* Glycine Betaine Catabolism. J. Bacteriol. *190*, 2690–2699.

Weber, I. (2011). Biochemische und strukturelle Untersuchungen zu Glyoxalase I/Bleomycinresistenzproteinen aus Pseudomonas aeruginosa PAO1. Bachelor Thesis. Universität Bayreuth.

Weiss, M.S. (2001). Global indicators of X-ray data quality. J. Appl. Crystallogr. *34*, 130–135.

Wilk, P., Uehlein, M., Kalms, J., Dobbek, H., Mueller, U., and Weiss, M.S. (2017). Substrate specificity and reaction mechanism of human prolidase. FEBS J. *284*, 2870–2885.

Willsey, G.G., and Wargo, M.J. (2016). Sarcosine Catabolism in *Pseudomonas aeruginosa* Is Transcriptionally Regulated by SouR. J. Bacteriol. *198*, 301–310.

Winn, M.D., Ballard, C.C., Cowtan, K.D., Dodson, E.J., Emsley, P., Evans, P.R., Keegan, R.M., Krissinel, E.B., Leslie, A.G.W., McCoy, A., McNicholas, S.J., Murshudov, G.N., Pannu, N.S., Potterton, E.A., Powell, H.R., Read, R.J., Vagin, A., and Wilson, K.S. (2011). Overview of the CCP4 suite and current developments. Acta Crystallogr. D Biol. Crystallogr. *67*, 235–242.

Winsor, G.L., Griffiths, E.J., Lo, R., Dhillon, B.K., Shay, J.A., and Brinkman, F.S.L. (2016). Enhanced annotations and features for comparing thousands of *Pseudomonas genomes* in the *Pseudomonas* genome database. Nucleic Acids Res. *44*, D646-653.

Wolfe, N.L., Zepp, R.G., Doster, J.C., and Hollis, R.C. (1976). Captan hydrolysis. J. Agric. Food Chem. *24*, 1041–1045.

Woods, D.D. (1940). The Relation of p-aminobenzoic Acid to the Mechanism of the Action of Sulphanilamide. Br. J. Exp. Pathol. *21*, 74–90.

Wright, A.J. (1999). The Penicillins. Mayo Clin. Proc. *74*, 290–307.

Wuerges, J., Caputi, L., Cianci, M., Boivin, S., Meijers, R., and Benini, S. (2015). The crystal structure of *Erwinia amylovora* levansucrase provides a snapshot of the products of sucrose hydrolysis trapped into the active site. J. Struct. Biol. *191*, 290–298.

Wurtzel, O., Yoder-Himes, D.R., Han, K., Dandekar, A.A., Edelheit, S., Greenberg, E.P., Sorek, R., and Lory, S. (2012). The Single-Nucleotide Resolution Transcriptome of *Pseudomonas aeruginosa* Grown in Body Temperature. PLoS Pathog *8*, e1002945.

Yamada, A., Sato, O., Watanabe, M., Walsh, M.P., Ogawa, Y., and Imaizumi, Y. (2000). Inhibition of smooth-muscle myosin-light-chain phosphatase by Ruthenium Red. Biochem. J. *349*, 797–804.

Yu, S. (2009). Assesment of Pseudomonas Quinolone Signal Response Protein PqsE and Preliminary Funcitonal Annotation of Hypothetical Protein PA0803 from *Pseudomonas aeruginosa*. Dissertation. MPI Dortmund.

Yu, S., Vit, A., Devenish, S., Mahanty, H.K., Itzen, A., Goody, R.S., and Blankenfeldt, W. (2011). Atomic resolution structure of EhpR: phenazine resistance in *Enterobacter agglomerans* Eh1087 follows principles of bleomycin/mitomycin C resistance in other bacteria. BMC Struct. Biol. *11*, 33.

Zhao, W.-H., and Hu, Z.-Q. (2010). β-Lactamases identified in clinical isolates of *Pseudomonas aeruginosa*. Crit. Rev. Microbiol. *36*, 245–258.

Zheng, H., Chruszcz, M., Lasota, P., Lebioda, L., and Minor, W. (2008). Data mining of metal ion environments present in protein structures. J. Inorg. Biochem. *102*, 1765–1776.

Zheng, H., Chordia, M.D., Cooper, D.R., Chruszcz, M., Müller, P., Sheldrick, G.M., and Minor, W. (2014). Validation of metal-binding sites in macromolecular structures with the CheckMyMetal web server. Nat. Protoc. *9*, 156.

Zheng, H., Cooper, D.R., Porebski, P.J., Shabalin, I.G., Handing, K.B., and Minor, W. (2017). CheckMyMetal: a macromolecular metal-binding validation tool. Acta Crystallogr. Sect. Struct. Biol. *73*, 223–233.

Danksagung

Hiermit möchte ich allen Menschen, die mich während der letzten Jahre begleitet und unterstützt haben und somit zum Gelingen meiner Doktorarbeit beigetragen haben ein herzliches Dankeschön aussprechen:

meinem Mentor **Prof. Dr. Wulf Blankenfeldt**, für die Betreuung meiner Doktorarbeit, in der er mir die Möglichkeit gegeben hat dieses abwechslungsreiche und herausfordernde Thema zu bearbeiten, sowie für seine fachliche Unterstützung und den wissenschaftlichen Freiraum,

Prof. Dr. Susanne Engelmann, für die Übernahme der Zweitkorrektur,

Prof. Michael Hust, für die Übernahme des Vorsitzes meiner Prüfungskomission,

den Mitgliedern meines *Thesis Committees* **Prof. Dr. Mark Brönstrupp** und **Prof. Dr. Susanne Häußler** für die hilfreichen Diskussionen und Prof. Dr. Susanne Häußler außerdem, für die Bereitstellung der *P. aeruginosa* Stämme,

Prof. Dr. Dietmar Schomburg von der TU Braunschweig, für die Möglichkeit in seinem Labor am BRICS sein Omnilog® System zu benutzen und **Elisabeth Majer** für technische und fachliche Unterstützung während der Versuchsdurchführung,

dem Kollaborationspartner **Dr. Manfred Weiß** vom HZB, für die Möglichkeit das *fragment based screening* durchzuführen und **Dr. Franziska Huschmann** für die Hilfe und Ratschläge während der experimentellen Durchführung,

Dr. Allegra Vit die mich als Betreuerin während meiner Masterarbeit bereits in die spannende Welt der βαβββ-Modulproteine eingeführt hat und von der ich währenddessen sehr viel lernen durfte und als Vorgänger auf diesem Projekt, für die Bereitstellung ihrer klonierten Plasmide wodurch mir der Einstieg in die Doktorarbeit erleichtert wurde,

der **HZI Graduate School GS-Fire** für die Weiterbildungsangebote und dafür das sie die Teilnahme am *Protein Structure and structur-based drug design* Kurs and der Universität Lund ermöglicht haben,

allen weiteren Kollegen, die während der letzten 4 ½ Jahre meinen Weg am HZI gekreuzt haben (Allegra, Christina, Christian, Bockto, Mihai, Andrea, Pooja, Juliane, Jan, Yafei, Maurice, Peer, Stefan, Thomas, JR, Ute, Manuela, Angelika, Simone, Claudia, Konrad, Kevin und die

Leute von SBAU und RPEX) und teilweise zu Freunden geworden sind, allen voran der Franken-Connection (Nina & Flo), dafür das alle stets ein offenes Ohr und gute Ratschläge hatten, für die technische Unterstützung im Labor und vor allem im IT-Bereich, für die schöne Arbeitsatmosphäre und natürlich für den Spaß bei der Arbeit. Davon möchte ich vor allem denjenigen danken, die auch außerhalb der Arbeit stets für einen Spaß zu haben waren, für die gemeinsamen Unternehmungen und dafür, dass ihr die letzten Jahre in Braunschweig zu einer unvergesslichen Zeit gemacht habt, die ich sehr vermissen werde.

Ein besonderer Dank gilt meiner Familie für ihr Verständnis und dafür, dass sie mich stets unterstützen. Vor allem möchte ich meinem Freund Flo für sein Verständnis, seine unermüdliche Unterstützung und Motivation danken.